Reconfigurable Intelligent Surface-Based Novel Transceiver Architectures and Multiple Access

by

Aymen Khaleel

A Dissertation Submitted to the
Graduate School of Sciences and Engineering
in Partial Fulfillment of the Requirements for
the Degree of

Doctor of Philosophy

in

Electrical and Electronics Engineering

KOÇ ÜNİVERSİTESİ

February 15, 2023

Reconfigurable Intelligent Surface-Based Novel Transceiver Architectures and Multiple Access

Koç University

Graduate School of Sciences and Engineering

This is to certify that I have examined this copy of a doctoral dissertation by

Aymen Khaleel

and have found that it is complete and satisfactory in all respects,
and that any and all revisions required by the final
examining committee have been made.

Committee Members:

Assoc. Prof. Dr. Ertuğrul Başar (Advisor)

Prof. Dr. Sinem Çöleri

Prof. Dr. Hüseyin Arslan

Prof. Dr. Alper Erdoğan

Prof. Dr. Ali Emre Pusane

Date:

ABSTRACT

Reconfigurable Intelligent Surface-Based Novel Transceiver Architectures and Multiple Access
Aymen Khaleel
Doctor of Philosophy in Electrical and Electronics Engineering
February 15, 2023

Over five generations of wireless communications networks, from 1G to 5G, the wireless channel was always a given system entity and not a design parameter. The wireless channel is dictated by the physical nature of the environment that contains the transmitter and receiver, the endpoints of a wireless network, which makes it random from their perspective. Hence, it cannot be manipulated, and the only way to deal with it is to compensate for its negative impact at the endpoints of the network. Recently, a new emerging technology called reconfigurable intelligent surfaces (RISs) has appeared to provide some degree of manipulation in the random wireless channel. With unprecedented capabilities, RISs somehow offer to make (even if partially) the random wireless channel as a design parameter that can be optimized jointly with the other conventional parameters to achieve a particular unified goal for the wireless network. An RIS is a metasurface in the form of a large array of passive and low-cost elements that can be controlled electronically to reshape the electromagnetic waves impinging the surface and absorb or reflect them to the opposite side. Owing to their unique properties of reconfigurability, low cost, and intelligence, recent literature envisions that RISs can find their way to integration with almost all of the existing wireless communication systems. Therefore, RISs has drawn growing attention in the wireless communication society as a promising emerging technology that can be a potential candidate for 6G and beyond wireless networks, which motivates this thesis.

In this thesis, we investigate the potential of RISs to be used in the next generation of wireless networks as an enabling technology by examining how far it will impact the network's overall performance. Our investigation is carried out by proposing new solutions that redesign existing classical wireless communications sys-

tems to include RISs in their transceiver architectures and assess their performance compared to the classical systems. Specifically, this thesis proposes the design and performance analysis of seven RIS-assisted wireless communications systems, including single user and multiple users with multiple access, which can be categorized into three parts, as follows.

In the first part of this thesis, we combine RISs with multiple-input multiple-output (MIMO) systems, where we consider vertical Bell Labs space-time (VBLAST) and Alamouti's schemes as the most common and practical MIMO schemes. For the VBLAST-based new system, an RIS is used to enhance the performance of the nulling and canceling-based sub-optimal detection procedure as well as to noticeably boost the spectral efficiency by performing index modulation (IM) at the RIS side. Furthermore, we propose an RIS-based transmitter for Alamouti's scheme that replaces the two radio frequency (RF) chains at the classical transmitter with a single RF signal generator.

In the second part, we integrate RISs into non-orthogonal multiple access (NOMA) systems, as follows. First, we propose a novel NOMA solution with RIS partitioning with the aim of enhancing spectrum efficiency by improving the ergodic rate of all users and maximizing user fairness. In the proposed system, we distribute the physical resources among users such that the base station (BS) and RIS are dedicated to serving different clusters of users, thus, reducing the mutual interference between users' clusters. Second, in order to increase the coverage area, we consider the generalized version of RISs, namely, simultaneous transmitting and reflecting RISs (STAR-RISs). In particular, we investigate the BER performance of a NOMA network assisted by a STAR-RIS, where the STAR-RIS serves multiple non-orthogonal users located on either side of the surface by utilizing the mode-switching protocol. We derive the closed-form BER expressions in perfect and imperfect successive interference cancellation cases. Furthermore, asymptotic analyses are also conducted to provide further insights into the BER behavior in the high signal-to-noise ratio region. Third, we consider general system design and physical resources allocation problems for STAR-RIS-assisted NOMA networks. In particular, we propose a novel STAR-RIS-assisted NOMA system, where unlike most of the related works, we target scalable phase shift design that requires a reduced channel estimation overhead. The proposed system aims to maximize the overall sum rate while guaranteeing the quality-of-service requirements (QoS) for individual users.

Finally, in the third part, we consider the RIS-assisted system design considering practical implementation problems associated with RISs. The first problem is the phase shift adjustment in RISs, which is associated with many issues in hardware implementation, limiting the RIS achievable gain. Therefore, we propose a low-cost, phase shift-free and novel passive beamforming (PB) scheme by only optimizing the on/off states of the RIS elements while fixing their phase shifts. The proposed PB scheme is shown to achieve the same scaling law (quadratic growth with the RIS size) for the signal-to-noise ratio as in the classical phase shift-based PB scheme, yet, with far less sensitivity to spatial correlation and phase errors. The second problem is the fact that RISs do not selectively reflect impinging electromagnetic waves; therefore, they can also reflect electromagnetic interference (EMI) from the surrounding environment to the receiver side. To solve this problem, we propose a novel EMI cancellation scheme to mitigate the impact of the EMI by exploiting its special time-domain structure and considering a clever passive beamforming method at the RIS.

For all of the proposed system designs, we assess their performance using mathematical analyses by considering different relevant performance matrices, which are validated via simulation results. Also, using comprehensive computer simulations and under different system settings, we compare the performance of the proposed systems against their state-of-the-art counterparts using the same simulation parameters to guarantee fair comparison.

The obtained mathematical and computer simulation results show that RISs have a huge potential to be a promising candidate for 6G and beyond wireless communications systems. RISs are shown to offer high degrees of freedom in terms of the system design, where they can be used as a supportive technology or main module within the existing wireless systems' architectures. Accordingly, they can offer system performance enhancement over different metrics, reduce the hardware design's complexity and cost, or even offer completely new features.

ÖZETÇE

Doktora Tez Başlığı
Aymen Khaleel
Elektrik ve Elektronik Mühendisliği, Doktora
15 Şubat 2023

Beşinci nesil (fifth generation, 5G) sistemlerine kadar, bir kablosuz haberleşme sisteminin kanalı, kontrol edilebilir bir sistem parametresi olarak değil, kablosuz ağların uç noktaları olan alıcı ve vericilerde rastgele olarak algılanan fiziksel bir sistem olarak ele tanımlanmıştır. Bu nedenle, bir haberleşme sisteminin kanalının kontrolü mümkün görülmemekte ve bunun yaratacağı olumsuz etkileri ortadan kaldırmanın tek yolu ise, ağın uç noktalarında bu etkiye müdahale etmekten geçmektedir. Son yıllarda, uyarlanabilir akıllı yüzey (reconfigurable intelligent surafaces, RIS) teknolojisi, kablosuz haberleşme kanallarına kontrol edilebilirlik yeteneği sağlamaktadır. Daha önce benzerine rastlanmamış kanalı manipüle etme yeteneğine sahip RIS teknolojisi, kablosuz ağı iyileştirmek için, iletim kanalını, diğer geleneksel parametrelerle işbirliği içinde optimize edilebilecek bir tasarım parametresi (kısmen de olsa) olarak kullanmaktadır. Bu amaçla kullanılan akıllı yüzeyler, her bir elemanı, yüzeye çarpan elektromanyetik dalgayı soğurarak veya karşı tarafa yansıtarak yeniden şekillendirmektedir. Böylece, son yıllarda yapılan çalışmalar, uyarlanabilir ve düşük maliyetli RIS'lerin neredeyse bütün mevcut kablosuz iletişim sistemleriyle entegrasyonunun sağlanabileceği öngörülmektedir. Bu nedenle, RIS teknolojisi, 6G ve ötesi kablosuz ağlar için potansiyel bir aday olabilecek, umut vadeden yeni bir teknoloji olarak büyük bir ilgi görmektedir.

Bu tez, RIS teknolojisinin yeni nesil kablosuz ağlarda kullanılma potansiyelini araştırmaktadır. Bu amaçla, bu tezde, mevcut kablosuz iletişim sistemlerinin alıcı-verici mimarilerine RIS teknolojisini dahil ederek, klasik sistemlere kıyasla performanslarını iyileştirmeye yönelik özgün sistem tasarımları ve çözümler sunulmaktadır. Özetle, bu tezde, tek kullanıcılı ve çoklu erişime sahip çok kullanıcılı yedi farklı RIS-destekli kablosuz iletişim sisteminin tasarımını ve performans analizi aşağıdaki gibi üç farklı bölümde sunulmaktadır.

Bu tezin ilk bölümünde, klasik çok-girişli çok-çıkışlı (multiple-input multiple-output, MIMO) sistemlerin başında gelen, dikey Bell laboratuvarları katmanlı uzay-zaman kodu (vertical Bell Laboratories layered space-time, VBLAST) ve Alamouti uzay-zaman kodunu, RIS ile birleştirilerek iki farklı sistem tasarımı önerilmektedir. Önerilen VBLAST-tabanlı sistemde, RIS yardımıyla, RIS'te sıfırlama ve iptal etme (nulling and cancelling)-tabanlı yarı-optimum bir algoritma kullanarak iletim ortamını iyileştirilmesi ve aynı zamanda, indis modülasyonu (index modulation, IM) tekniğine başvurularak bant verimliliğinin büyük ölçüde arttırması hedeflenmiştir. Bunun yanı sıra önerilen Alamouti şemasında, klasik verici yapısında kullanılan iki radyo frekansı (radio frequency, RF) zincirinin yerini, tek bir RF sinyal üretecinin aldığı RIS-tabanlı bir verici tasarımı önerilmektedir.

Bu tezin ikinci bölümünde, RIS teknolojisi, dik olmayan çoklu erişim (non-orthogonal multiple access, NOMA) tekniğine aşağıdaki gibi entegre edilmiştir. Bu çalışmada ilk olarak, bant verimliliğinin arttırılması, tüm kullanıcıların ergodik kapasitesini iyileştirilmesi ve kullanıcı eşitliği sağlanması amacıyla, RIS'in alt-bölümlere ayrıldığı bir RIS-tabanlı NOMA sistemi önerilmiştir. Önerilen bu sistemde, baz istasyonu (base station, BS) ve RIS farklı kullanıcı kümelerine tahsis edilerek, kullanıcı kümeleri arasındaki karşılıklı girişimin en aza inmesi sağlanmıştır. Daha sonra ise, tam kapsama alanını ulaşmak için, RIS'in genelleştirilmiş versiyonu olan eş zamanlı iletim ve yansıma (simultaneous transmission and reflection, STAR) fonksiyonlarına sahip STAR-RIS yapısı göz önünde bulundurulmuştur. Bu çalışmada, STAR-RIS yapısının mod değiştirme prensibi kullanılarak, STAR-RIS yüzeylerinin her iki tarafında konumlanmış çoklu dik-olmayan kullanıcılara hizmet verildiği bir NOMA sisteminin bit hata oranı (bit error rate, BER) incelenmiştir. Burada, mükemmel ve kusurlu ardışık girişim engelleme (successive interference cancellation, SIC) durumları için kapalı formda BER ifadelerini türetilmiştir. Ayrıca, yüksek işaret-gürültü oranı (signal-to-noise rati, SNR) bölgesindeki BER davranışı hakkında daha fazla bilgi sunmak için asimptotik analizler yapılmıştır. Bu bölümde son olarak, STAR-RIS-destekli NOMA sistemleri için genel sistem tasarımı ve fiziksel kaynak tahsisi problemleri ele alınmıştır. Özellikle, literatürdeki çalışmaların çoğundan farklı olarak, STAR-RIS destekli NOMA sistemi için, daha az kanal kestirim yükü gerektiren, ölçeklenebilir bir faz kaydırma tekniği önerilmiştir. Önerilen bu sistemde, bireysel kullanıcılar için hizmet kalitesi gereksinimleri (quality of servise, QoS)'nin arttırması garanti edilirken, toplam hızın (sum-rate) enbüyüklenmesi amaçlanmaktadır.

Bu tezin üçüncü ve son bölümünde, RIS-destekli sistem tasarımlarında karşılaşılan, RIS kaynaklı pratik uygulama problemleri göz önünde bulundurulmuştur. Bu problemlerden ilki, RIS'in donanımsal uygulamalarında birçok sorunla karşımıza çıkan ve RIS'ten elde edilebilir kazancı sınırlayan, faz kayması ayarıdır. Bunun için, RIS elemanlarının sabit faz kaymaları ürettiği varsayılarak, bu elemanların açık/kapalı durumlarını optimize eden ve düşük maliyetli, faz yeni bir pasif huzme oluşturma (passive beamforming, PB) şeması önerilmiştir. Bu çalışmada, önerilen PB şemasının, klasik faz kaymasına dayalı PB şemasında olduğu gibi sinyal-gürültü oranı için aynı ölçüde büyüme (RIS boyutuna göre ikinci dereceden büyüme)'nin elde edildiği, ancak uzamsal korelasyona ve faz hatalarına karşı çok daha dayanıklı olduğu gösterilmiştir. Bu çalışmada incelenen ve RIS-destekli pratik uygulamalarda karşılaşılan diğer bir sorun ise RIS'in, kendisine çarpan her elektromanyetik dalgayı yansıtmasıdır ki, bu ortamda yayılan herhangi bir elektromanyetik paraziti (EMI) de alıcı tarafına iletmesi anlamına gelmektedir. Bu çalışmada, bu problemi çözmek ve EMI'nin etkisini azaltmak için, özel zaman bölgesi (special time-domain) yapısından yararlanılarak ve RIS'te akıllı bir pasif huzme oluşturma tekniğine başvurularak için yeni bir EMI engelleme şeması önerilmiştir.

Önerilen tüm sistem tasarımlarının performans incelemeleri, ilgili performans matrislerini göz önünde bulundurarak yapılan detaylı matematiksel analizler ile ortaya konulmuş ve bu analizler, simülasyon sonuçlarıyla desteklenmiştir. Ayrıca, önerilen sistemlerin, kapsamlı bilgisayar simülasyonlar ile mevcut referanslara göre performans karşılaştırmaları adil sistem parametreleri gözetilerek karşılaştırılmıştır.

Sonuç olarak, tüm bu elde edilen matematiksel analizler ve bilgisayar simülasyonu sonuçları, RIS'in 6G ve ötesi kablosuz iletişim sistemleri için umut verici bir aday olma potansiyeline sahip olduğunu göstermektedir. Ayrıca, RIS'in, mevcut kablosuz sistemlerin mimarilerinde destekleyici bir teknoloji veya temel bir sistem modülü olarak kullanılabileceği, sistem tasarımı açısından büyük bir serbestlik sunduğu gösterilmiştir. Tüm bu sonuçlar göstermektedir ki, RIS teknolojisi, farklı metrikler üzerinden bir temel haberleşme sisteminin performansı iyileştirmek, donanım tasarımının karmaşıklığını ve maliyetini azaltmak ve hatta sisteme tamamen yeni nitelikler kazandırmak için kullanılabilmektedirler.

ACKNOWLEDGMENTS

In the name of Allāh, the Entirely Merciful, the Especially Merciful

All praise is due to Allāh; and blessings and peace be upon His messenger and servant, Muhammad, and upon his family and companions and whoever follows his guidance until the Day of Resurrection.

Our prophet Mohammed (peace be upon him) said: **"Whoever does not thank people has not thanked Allāh."**. Sunan Abī Dāwūd 4811. Accordingly,

I would like to express my deep gratitude to my supervisor, Assoc. Prof. Dr. Ertuğrul Başar, for his insightful guidance and constant support. Without Allāh's help and then his help, I would not have been able to write these words today. During this long journey, he taught me science, dedication, high ethical standards, and integrity.

I would also like to thank my thesis committee members, Prof. Dr. Sinem Çöleri and Prof. Dr. Hüseyin Arslan, for their encouragement and insightful comments.

My thanks and gratefulness are extended to the Scientific and Technological Research Council of Turkey (TÜBİTAK) for its financial support during the whole study years in the projects with grant numbers 117E869 and 120E401.

Finally, to my big family, especially my mother, father, aunt, and my step mother, who raised me to be who I am now, thank you for everything. To my small family, my wife, my daughters, and my sons, thank you for your love and patience. To my brothers, thank you for your unlimited support. My mother, may Allāh reward you for all the difficulties you have faced for the sake of taking care of me.

TABLE OF CONTENTS

LIST OF TABLES

LIST OF FIGURES

ABBREVIATIONS

AWGN	Additive White Gaussian Noise
BER	Bit Error Rate
BS	Base Station
CDF	Cumulative Distribution Function
CLT	Central Limit Theorem
CMs	Complex Multiplications
CSI	Channel State Information
IM	Index Modulation
LoS	Line-of-Sight
ML	Maximum Likelihood
MIMO	Multiple-Input Multiple-Output
NOMA	Non-Orthogonal Multiple Access
OP	Outage Probability
PB	Passive Beamforming
PSK	Phase Shift Keying
RIS	Reconfigurable Intelligent Surface
RF	Radio Frequency
RV	Random Variable
SEP	Symbol Error Probability
SINR	Signal-to-Interference-Plus-Noise Ratio
SISO	Single-Input Single-Output
SNR	Signal-to-Noise Ratio
STAR-RIS	Simultaneous Transmitting and Reflecting Reconfigurable Intelligent Surface
SIC	Successive Interference Cancellation

Chapter 1

INTRODUCTION

In this chapter, we first introduce the RISs technology in Section 1.1. Within this section, we provide a conceptual structure example for the RIS in Section 1.1.1, the signal model in Section 1.1.2, practical implementation examples in Section 1.1.3, potential applications in Section 1.1.4, and finally, open research problems in Section 1.1.5. In Section 1.2, we give the motivation and main contributions of this thesis. Finally, in Section 1.3, we provide the organization of the remaining chapters of the thesis.

1.1 Reconfigurable Intelligent Surfaces

In general, metasurfaces are artificial surfaces that are fabricated to provide new physical features that do not exist in nature, hence the prefix meta. Metasurfaces obtain their specific functions based on the internal physical design of their unit cells, which form these surfaces together and in large numbers. These unit cells can be physically designed to reflect, absorb, and partially transmit/refract the incident electromagnetic (EM) wave that impinges the surface [2], see Fig. 1.1. Although having different purposes and internal designs, metasurfaces share common properties that can be described by relating them to the wavelength of the operating frequency [3], as follows. They are thin surfaces with a thickness that is much smaller than the wavelength, while the other dimensions (length and width) are significantly larger than the wavelength. Also, their construction unit cells are with dimensions that are less than the wavelength. By combining these unit cells with an active control mechanism, metasurfaces become intelligent surfaces that can perform

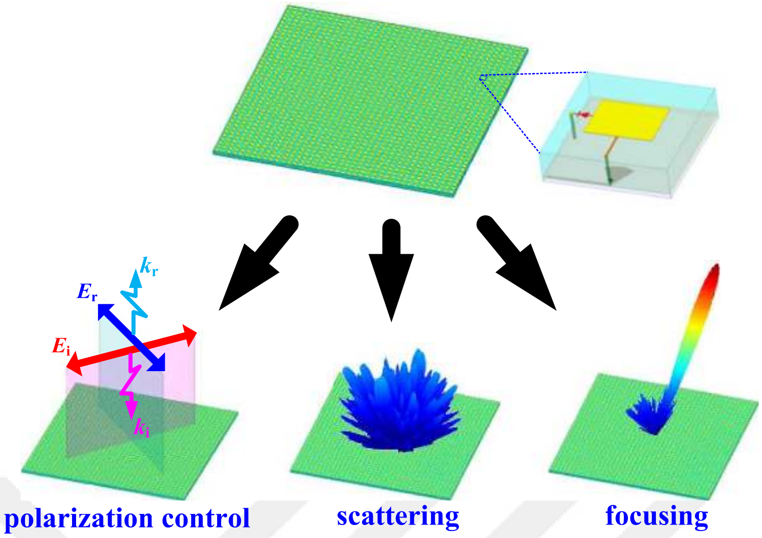

Figure 1.1: A schematic plot of a metasurface example with its different functions [1].

complex tasks in real time by acting on the impinging EM waves. In this context, a reconfigurable intelligent surface (RIS) is an artificial surface that contains an array of passive and low-cost elements, where each element can be tuned to reflect or fully absorb the electromagnetic waves impinging its surface [4]-[5].

Despite the aforementioned advantages, RISs act as reflective metasurfaces, which means that they can only serve the users located on their same side. In other words, RISs offer only half-space coverage, which limits the flexibility of deploying them. To solve this problem, recently, the novel concept of simultaneous transmitting and reflecting RISs (STAR-RISs) has been proposed [6]. Compared to conventional RISs, STAR-RISs have elements that support both electric polarization and magnetization currents yielding simultaneous control of the transmitted and reflected signals. In this way, STAR-RISs can offer full-space coverage. Furthermore, in order to enhance this full-space coverage, three main operating protocols are proposed, namely the energy splitting (ES), mode switching (MS), and time switching (TS). Specifically, for ES, all elements of the STAR-RIS are assumed to operate in transmission and reflection mode simultaneously. For MS, each element can operate in full transmis-

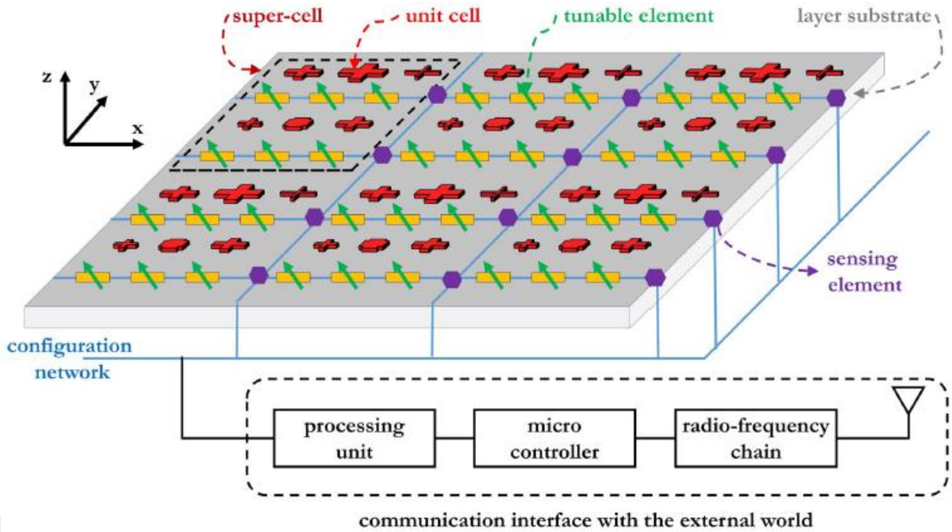

Figure 1.2: A Conceptual example of an RIS with a general structure [7].

sion or reflection mode, while in TS, all elements periodically switch between the transmission and reflection modes in an orthogonal time slots. Interested readers are referred to [7] for in-depth details on RISs.

1.1.1 A Conceptual Structure Example

Fig. 1.2 shows a conceptual structure of an RIS that is used to assist RF wireless communications. Note that this conceptual structure can be used as a general sample of RIS for system design and analysis, which applies to different real implementations of RISs. This RIS is a two-dimensional (2D) model with a thin sheet shape (thickness is much less than the wavelength), while length and width are much larger than the wavelength. It consists of tens, hundreds, or even thousands of sub-wavelength size unit cells [8]. Having this 2D shape makes it easier and cheaper for implementation and deployment compared to the 3D counterpart.

Different layers of metallic and dielectric materials are used to form the surface. In particular, the unit cells (RIS elements) are formed as patches that are printed on the dielectric material that forms a substrate. From the EM wave perspective, the unit cell can be modeled as a passive scattering element. Depending on these unit cells' microscopic design, the RIS's macroscopic reaction toward the EM waves is determined. The design details of the unit cells include the type of material, size, geometrical shape, and spacing between unit cells.

Passiveness is an essential property for RISs, which can be described as follows. First, the unit cells perform no power amplification on the impinging EM wave. Second, the unit cell performs limited and basic signal processing on the EM wave. Third, minimal power is required to tune the unit cells (reconfigure the RIS). On the other side, other types of RISs have recently emerged, such as active RISs [9] that contain amplifying unit cells, which are out of the scope of this thesis.

As shown in Fig. 1.2, the RIS needs, at least, a single RF chain to have its gateway to the other parts of the wireless network. This is essential, as the RIS needs to be remotely reconfigured by the endpoints (transmitter and receiver) of the wireless network. Furthermore, to provide control signals for different unit cells, a microcontroller with a wired/wireless communication mechanism between the cells and the controller (on-chip network type) needs to be integrated into the RIS structure.

The intelligence property of the RIS stems from its potential to reshape the EM wave for different specific purposes. This can be done by tuning (reconfiguring) the individual RIS elements, for example, to steer the reflected signals to a predetermined spatial direction. In this way, the RIS control (tuning) signals associated with the elements become a design parameter for the wireless network, where it can be jointly optimized with the other parameters to achieve a particular goal for the network.

1.1.2 Signal Model

Here, we give a simple example of an RIS deployed between a transmitter and receiver, where we provide the overall signal model considering the RIS.

Consider a downlink SISO system assisted by an RIS with N-elements size, where the direct link between the source (S) and destination (D) is blocked. The received

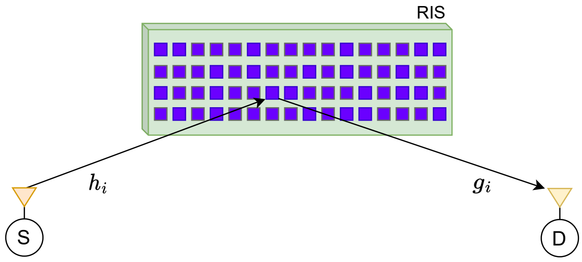

Figure 1.3: RIS-assisted S-D wireless communication.

signal at D is given by [10]

$$y = x\sqrt{P_L P}\sum_{i=1}^{N} h_i \Gamma_i g_i + n, \tag{1.1}$$

where x is the transmitted signal, P is the transmit power, and P_L is the large scale fading (path gain), which is given as [11]

$$P_L = \frac{\lambda^4}{256\pi^2 r_s^2 r_d^2}, \tag{1.2}$$

where λ is the wavelength of the operating frequency, r_s and r_d are the S-RIS and RIS-D distances in meter. Here, h_i and g_i are the S-RIS (i^{th} element) and RIS (i^{th} element)-D channel coefficients. Γ_i is the RIS (i^{th} element) reflection coefficient, $\Gamma_i = \beta_i e^{j\theta_i}$, where $\beta_i \in [0, 1]$ and $\theta_i \in [0, 2\pi)$ are the reflection amplitude (attenuation) and phase shift, respectively. Also, the additive white Gaussian noise (AWGN) sample is denoted by $n \sim \mathcal{CN}(0, \sigma^2)$. In order to maximize the signal-to-noise ratio (SNR) at D, the reflection amplitude can be set as $\beta_i = 1$ to obtain maximum reflection power (with no amplification and without reflection loss). On the other side, the phase shift can be set as $\theta_i = -\arg(h_i g_i)$ to align all the reflected signals into the same direction (zero direction in this case), obtaining constructive combining of the EM waves reaching D. Accordingly, we obtain the SNR as

$$\mathrm{SNR} = \frac{P_L P\left(\sum_{i=1}^{N} |h_i||g_i|\right)^2}{\sigma^2}. \tag{1.3}$$

From (1.3) it can be clearly seen that the SNR has a quadratic scaling behavior as a function of N.

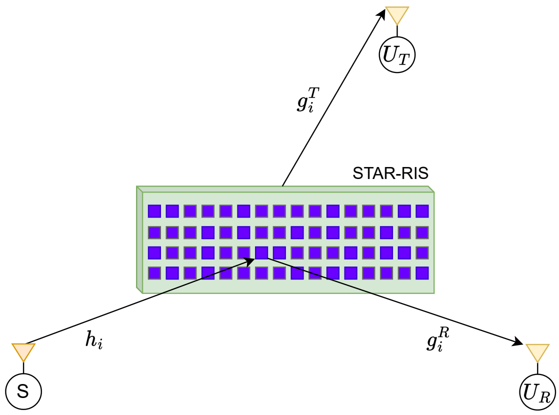

Figure 1.4: STAR-RIS-assisted wireless communications system.

In order to generalize the system model to the STAR-RIS case shown in Fig. 1.4, we note the following. The i^{th} element will be associated with two coefficients namely, reflection Γ_i^R and transmission Γ_i^T coefficients, where $|\Gamma_i^R|^2+|\Gamma_i^T|^2 \leq 1$. Here, $\Gamma_i^R = \sqrt{\beta_i^R} e^{j\theta_i^R}$, $\Gamma_i^T = \sqrt{\beta_i^T} e^{j\theta_i^T}$, where $\sqrt{\beta_i^\chi}$ and θ_i^χ, $\chi \in \{R, T\}$, are the amplitude and phase shift applied by the i^{th} element to the impinging electromagnetic wave [12]. Accordingly, the received signal at the user U_χ can be obtained by rewriting (1.1) as

$$y^\chi = x\sqrt{P_L^\chi P} \sum_{i=1}^{N} h_i \Gamma_i^\chi g_i^\chi + n. \tag{1.4}$$

In MS mode, $\beta_i^\chi \in \{0, 1\}$, where $\beta_i^\chi = 0$ and $\beta_i^\chi = 1$ correspond to the full transmission (forwarding) and full reflection of the impinging wave, respectively. In ES mode, $\beta_i^\chi \in [0, 1]$ and $\beta_i^T + \beta_i^R \leq 1$, where part of the impinging wave's energy is reflected while the other part is forwarded to the opposite direction of the surface. In TS mode, β_i^χ periodically changes between zero and unity over time. On the other side, depending on the STAR-RIS implementation method, θ_i^T and $\theta_i^R \in [0, 2\pi)$ may or may not be correlated [13], [14]. Finally, the SNR can be readily obtained from (1.4) in a form similar to (1.3).

Figure 1.5: Rfocus: Real implemntation of an RIS [8].

1.1.3 Practical Examples

Fig. 1.5 shows a practical implementation of an RIS made by researchers at Massachusetts institute of technology (MIT), USA. By using a large number (3720 elements) of low-cost antennas (a few cents each), a six square meter RIS surface is formed. Excluding the power dissipation associated with control signals, the surface itself (3720 elements) consumes no power as they do not perform any kind of amplification to the reflected signals. In this RIS setup, the authors used a majority voting algorithm where, based on the received signal strength indicator (RSSI) measurements, some of the RIS elements are set to the reflection mode while others are to the absorbing mode. In this way, the RIS performs passive beamforming to focus the signal in a specific spatial direction.

In Fig. 1.6, researchers in NTT DOCOMO, Japan, built an artificially intelligent thin layer of glass (metasurface) that contains a large number of tiny (sub-wavelength size) unit cells. The unit cells are arranged to be in periodic positions on a two-dimensional surface and covered with another layer of glass that forms a substrate.

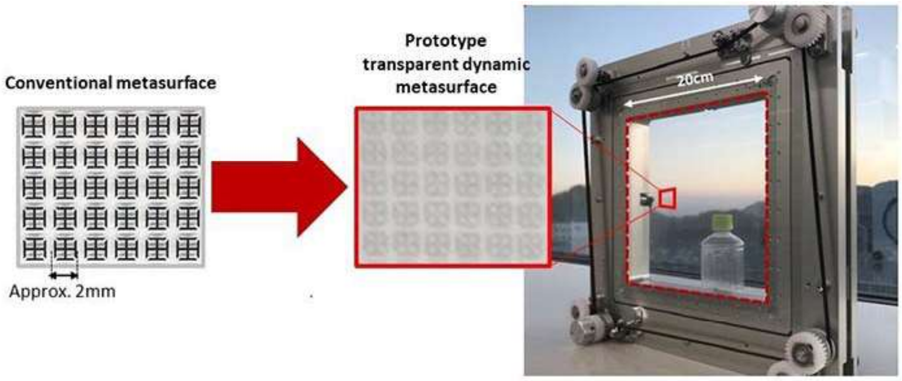

Figure 1.6: A real implementation of a transparent STAR-RIS from NTT DOCOMO [15].

In order to change the response of the surface to the impinging EM waves, the glass substrate can be moved slightly. In this way, three different dynamic responses can be achieved: Letting the EM waves fully penetrate the surface, fully reflected to the opposite side of the surface front, or partially reflecting/penetrating the surface. Considering the transparent nature of the glass, the deployment of the intelligent surface becomes less restricted in different environments. The installation of the intelligent surface provides high flexibility to fulfill different requirements; for example, it can fully block the leakage of EM waves in the opposite direction due to security. Also, due to its transparency, it can be installed in crowded areas such as buildings or vehicles, where the intelligent surface does not block the line-of-sight (LoS) of people.

1.1.4 Potential Applications

Considering its unprecedented capabilities, RISs have found their way for almost all wireless communications systems, where they have envisioned to be integrated with the existing systems for a variety of purposes, see Fig. 1.7. The author in [10] used an RIS to achieve ultra-reliable communication by remarkably enhancing the SNR at the receiver side. In [17], the index modulation (IM) concept is applied to an RIS to

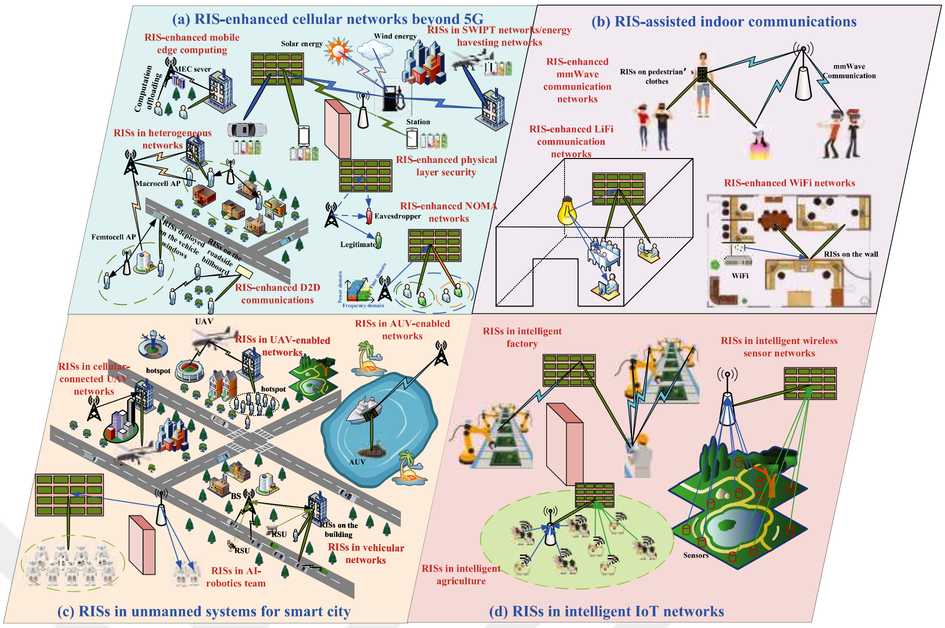

Figure 1.7: RIS envisioned applications in wireless networks [16].

simultaneously enhance the SNR and convey additional bits through the indices of the RIS elements. RISs can also be used to replace (reduce) some of the RF chains as in [18], where the authors redesigned the transmitter of Alamouti's scheme to have a single RF signal generator instead of two dedicated RF chains. In the same context, the authors in [19] moved the modulation process from the transmitter to the RIS side by manipulating the RIS reflection coefficients. Furthermore, in [20] and [21], the authors used, respectively, the RIS and the simultaneous transmitting and reflecting intelligent surface (STAR-RIS), to assist non-orthogonal-multiple-access (NOMA) networks through novel partitioning schemes. In particular, the authors divided the RIS elements among users to maximize user fairness and enhance the overall sum rate. In [22] and [23], the authors considered mobile edge computing networks where they used RISs to enhance the quality of service (QoS) and latency performance. In [24], the authors proposed the deployment of multiple RISs to work as signal reflection hubs in a device-to-device wireless network, where the RISs phase shifts along with the other network paramters are jointly optimized to maximize the uplink sum rate. Considering the physical layer security, in [25], the RIS is proposed to be used to improve the secrecy rate by smartly adjusting the RIS phase shifts to enhance the SNR for the legitimate user while degrading it for the eavesdropper. The RIS in [26] is proposed to be deployed at the boundary of the cellular network to support cell-edge users and reduce the interference effect from adjacent networks. By exploiting the RIS high passive beamforming gain, the authors in [27] utilized RIS to maximize the sum-power received by energy harvesting receivers. In [28], by jointly optimizing the unmanned aerial vehicle (UAV) trajectory and the phase shifts associated with RIS passive beamforming, the average achievable rate is maximized. An extensive literature review of RIS potential applications can be found in [7] and [29] for interested readers.

1.1.5 Open Research Problems

Most of the RIS literature relies on simplified mathematical models that facilitate building a tractable mathematical framework to deal with RIS from the wireless communications perspective. However, these simplified models might not be enough to accurately describe the physical nature behind the operation of the RIS. This, in turn, adversely affects the real implementation of the RIS to match the mathematical expectations. For example, the mathematical model adopted by most of the RIS literature deals with the cell units as individual scatterers isolated from each other, while, in reality, they have mutual coupling [30], [31]. Also, unlike real implementation [32], [33], in the current adopted models, the reflection coefficient of each cell unit is considered to have reflection amplitude and phase shift that are independent of each other. The reaction between the unit cell and the angle of the indecent wave [34] is also not taken into account in most of the works in the RIS literature.

Considering the performance limit of RISs, most of the works in the literature focus on the SNR maximization [10]; however, it has been shown in [35] that RIS can both enhance the SNR and embed more information bits. This raises a fundamental question on the best strategy to use the RIS within a wireless network. Also, since most of the literature adopts simplified signal models for the proposed RIS-assisted systems, it is hard to reveal the real practical potential of this emerging technology compared to the other existing ones.

The passive beamforming gain is an essential feature RISs have, which is performed by smartly adjusting the phase shifts of the individual unit cells. Knowing the channel state information (CSI) associated with the links between these cells and the network endpoints, therefore, is a necessity for the passive beamforming process. However, due to the passiveness of RISs, which is an advantage from the power consumption perspective, the channel estimation process becomes a bottleneck on the achievable gain of RISs as they do not have the sensing and processing capability to estimate the channel. Therefore, the channel estimation needs to be carried out at the wireless network endpoints. In addition, considering a large number of these unit cells, the channel estimation overhead becomes even more challenging. Accordingly, a balance needs to be struck between the achievable beamforming gain and the cost of channel estimation overhead needs to be paid in front [36]. Although many studies have considered the channel estimation problem [37, 38, 39, 40], yet, it is still one of the main research problems associated with RISs that need to be further investigated.

1.2 Thesis Motivation and Contributions

Based on the introduction of the RIS technology provided in the previous sections, it can be seen that they have unique capabilities that can be utilized to enhance the performance of existing wireless communications systems or even redesign them in a more efficient way in terms of hardware complexity and cost. Furthermore, due to their low implementation cost, energy efficiency, and ease of deployment, they have high flexibility to be integrated into different wireless systems and to perform a wide range of functions. Motivated by these remarkable advantages, this thesis examines the potential of RISs in the 6G and beyond wireless communications systems by proposing several wireless system designs that include RISs in their transceiver architectures and compare their performance with the classical systems.

The main contributions of this thesis can be summarized as follows.

- We propose an RIS-based transmitter for Alamuti's scheme, where we replace the two RF chains in the classical transmitter with a single RF signal generator. The new design preserves Alamouti's scheme diversity order and enhances the bit error rate (BER) performance. Furthermore, theoretical analysis and simulation results show that the same concept can be generalized to space-time block code (STBC) systems. In other words, in a large-scale MIMO setup, our scheme can replace a large number of RF chains at the transmitter side with a single RF signal generator.[1]

- We propose an RIS-assisted and IM-based VBLST system, where an RIS is used to enhance the performance of the nulling and canceling-based sub-optimal detection procedure as well as to noticeably boost the spectral efficiency by conveying extra bits through the adjustment of the phases of the RIS elements.

- We integrate RISs into non-orthogonal multiple access (NOMA) systems, where we partition the RIS into sub-surfaces to serve different users with the aim of enhancing spectrum efficiency by improving the ergodic rate of all users and maximizing user fairness.

- In order to increase the coverage area, we consider the generalized version of RISs, namely, STAR-RISs to assist NOMA networks. For the considered system, we derive the closed-form BER expressions in perfect and imperfect successive interference cancellation cases. Furthermore, asymptotic analyses are also conducted to provide further insights into the BER behavior in high SNR regions.

[1] Our proposed RIS-based transmitter for Alamouti's scheme has been implemented in an experimental setup by independent researchers in [41], where the authors have confirmed the feasibility of our proposed theoretical solution.

- We propose a novel STAR-RIS-assisted NOMA system, where unlike most of the related works, we target scalable phase shift design that requires a reduced channel estimation overhead. We utilize the STAR-RIS to maximize the sum rate while guaranteeing individual QoS requirements for different users.

- In order to avoid the passive beamforming (PB) losses due to the hardware implementation issues associated with the RIS phase shift adjustment, we propose an alternative PB scheme. In particular, we propose a low-cost and phase shift-free PB scheme by only optimizing the on/off states of the RIS elements while fixing their phase shifts. The proposed PB scheme is shown to achieve the same scaling law (quadratic growth with the RIS size) for the SNR as in the classical phase shift-based PB scheme, yet, with far less sensitivity to spatial correlation and phase errors.

- In order to mitigate the negative impact of electromagnetic interference (EMI) associated with RISs, we propose an EMI cancellation scheme to enhance the signal-to-interference-plus-noise ratio (SINR) performance at the receiver side.

1.3 Thesis Organization and Notation

The rest of this thesis is organized as follows:

- **Chapter 2** introduces new designs for the transceiver architectures of two MIMO systems, Alamouti and VBLAST schemes. For Alamouti's scheme, we present the proposed RIS-based transmitter, explain the transmission mechanism, and derive the average symbol error probability (SEP) for phase shift keying (PSK) modulation. For VBLAST scheme, we present three different operating modes to run the RIS with the aim of enhancing the SNR and/or boosting the data rate. Next, we provide the proposed symbols detection algorithms along with their complexity analysis. Finally, using comprehensive computer simulations, we compare the proposed systems against their benchmarks.

- **Chapter 3** presents the combination of RISs and NOMA protocol. It proposes a novel NOMA solution with RIS partitioning, aiming to enhance the spectrum efficiency by improving the ergodic rate of all users, and maximizing user fairness. In particular, a new strategy is introduced to distribute the physical resources (PRs) among users such that the base station (BS) and RIS are dedicated to serve different clusters of users. Accordingly, we formulate an RIS partitioning optimization problem that mathematically characterizes the proposed PRs allocation strategy, which turns out to be a non-convex and non-linear integer programming (NLIP) problem with a combinatorial feasible set, which is challenging to solve. Therefore, a sub-optimal solution is introduced in the form of three efficient search algorithms that need to be applied sequentially, followed by their convergence and complexity analysis. Next, we derive exact and asymptotic expressions for the outage probability (OP) of the proposed system. Finally, we compare the proposed system with four different NOMA and OMA benchmark systems using comprehensive computer simulations with different user deployment scenarios.

- **Chapter 4** provides the derivations of the bit error rate (BER) for STAR-RISs-assisted NOMA networks. In particular, we derive the closed-form BER expressions in perfect and imperfect successive interference cancellation cases. Furthermore, asymptotic analyses are also conducted to provide further insights into the BER behavior in the high SNR regions. Finally, the accuracy of our theoretical analysis is validated through Monte Carlo simulations.

- **Chapter 5** proposes a novel STAR-RIS-assisted NOMA system. In particular, we propose novel algorithms to partition the STAR-RIS surface among the available user, aiming to maximize the system sum rate while guaranteeing the quality-of-service (QoS) requirements for individual users. Also, we provide the convergence and complexity analysis of the proposed algorithms and discuss their application in different user deployment scenarios. Next, we derive closed-form analytical expressions for the outage probability and its corresponding asymptotic behavior under different user deployments scenarios. Finally, Monte Carlo simulations are provided for different user deployment scenarios and under different system settings to verify the correctness of the theoretical analysis.

- **Chapter 6** investigates a practical problem inherent in RISs and proposes a novel solution to address it. First, we show that practically, the phase shift adjustment in RISs is associated with many issues in hardware implementation, limiting the RIS achievable passive beamforming (PB) gain. Accordingly, we propose a low-cost, phase shift-free and novel PB scheme by only optimizing the on/off states of the RIS elements while fixing their phase shifts. We show that the proposed PB scheme achieves the same scaling law (quadratic growth with the RIS size) for the SNR as in the classical phase shift-based PB scheme, yet, with far less sensitivity to spatial correlation and phase errors. Next, we provide a unified mathematical analysis that characterizes the performance of the proposed PB scheme, where we obtain the outage probability and ergodic rate for the considered RIS-assisted system. Finally, through comprehensive computer simulations, we show that the proposed PB scheme has a clear superiority over the classical one under different performance metrics.

- **Chapter 7** considers the electromagnetic interference (EMI) problem associated with the RIS-assisted transmission. In particular, we propose a novel EMI cancellation scheme to mitigate the impact of the EMI by exploiting its special time-domain structure and considering a clever passive beamforming method at the RIS. We introduce the considered system settings and explain our methodology to exploit these settings and propose our EMI cancellation scheme accordingly. Next, we obtain the outage probability expression of the RIS-assisted system under the proposed scheme. Finally, compared to its benchmark, we show through computer simulations that the proposed scheme achieves superior performance in terms of the average signal-to-interference-plus-noise ratio (SINR) and outage probability (OP).

- **Chapter 8** Provides thesis conclusions and shed light on useful insights obtained from its main results.

Notation: Matrices and column vectors are denoted by an upper and lower case boldface letters, respectively. $\mathbf{X} \in \mathbb{C}^{m\times k}$ denotes a complex-valued matrix $\mathbf{X}$ with $m \times k$ size, where $\mathbf{X}^T$ is the transpose and $[\mathbf{X}]_{n,\tilde{n}}$ is the $(n, \tilde{n})$-th entry. $\mathbf{0}_N$, $\mathbf{I}_N$, $\binom{m}{k}$, $\lfloor\cdot\rfloor$, $\lceil\cdot\rceil$, and $\mathrm{mod}(\cdot)$ are the N-dimensional all-zeros column vector, the $N \times N$ identity matrix, the binomial coefficient, the floor, ceiling, and modulo functions, respectively. $x \sim \mathcal{CN}(0, \sigma^2)$ stands for complex Gaussian distributed random variable (RV) with mean $\mathrm{E}[x] = 0$ and variance $\mathrm{VAR}[x] = \sigma^2$. $\mathbb{R}$, $\mathbb{Z}^+$, and $|\mathcal{S}|$ are the set of real numbers, the set of positive integer numbers, and the cardinality of the set $\mathcal{S}$, respectively.

The chapters of this thesis, Chapters 2-7, have been published or are in the process of publication, as given below.

Chapter 2

A. Khaleel and E. Basar, "Reconfigurable intelligent surface-empowered MIMO systems," in *IEEE Systems Journal*, vol. 15, no. 3, pp. 4358–4366, Aug. 2021, doi: 10.1109/JSYST.2020.3011987.

Chapter 3

A. Khaleel and E. Basar, "A novel NOMA solution with RIS partitioning," in *IEEE Journal of Selected Topics in Signal Processing*, vol. 16, no. 1, pp. 70–81, Jan. 2022, doi:10.1109/JSTSP.2021.3127725.

Chapter 4

M. Aldababsa, A. Khaleel and E. Basar, "STAR-RIS-NOMA Networks: An Error Performance Perspective," in *IEEE Communications Letters*, vol. 26, no. 8, pp. 1784-1788, Aug. 2022, doi: 10.1109/LCOMM.2022.3179731.

Chapter 5

M. Aldababsa, A. Khaleel, and E. Basar, "Simultaneous transmitting and reflecting intelligent surfaces-empowered NOMA networks," Received major revision from

IEEE Systems Journal.

Chapter 6

A. Khaleel and E. Basar, "Phase shift-free passive beamforming for reconfigurable intelligent surfaces," in *IEEE Transactions on Communications*, vol. 70, no. 10, pp. 6966-6976, Oct. 2022, doi: 10.1109/TCOMM.2022.3200670.

Chapter 7

A. Khaleel and E. Basar, "Electromagnetic interference cancellation for RIS-assisted communications," submitted to *IEEE Transactions on Vehicular Technology*.

Chapter 2

RIS-ASSISTED NEXT-GENERATION MIMO SYSTEMS

In this chapter, two new multiple-input multiple-output (MIMO) system designs using RISs are presented to enhance the performance and boost the spectral efficiency of state-of-the-art MIMO communication systems. Vertical Bell Labs layered space-time (VBLAST) and Alamouti's schemes have been considered in this study and RIS-based simple transceiver architectures are proposed. For the VBLAST-based new system, an RIS is used to enhance the performance of the nulling and canceling-based sub-optimal detection procedure as well as to noticeably boost the spectral efficiency by conveying extra bits through the adjustment of the phases of the RIS elements. In addition, RIS elements have been utilized in order to re-design Alamouti's scheme with a single radio frequency (RF) signal generator at the transmitter side and to enhance its bit error rate (BER) performance. Monte Carlo simulations are provided to show the effectiveness of our system designs and it has been shown that they outperform the reference schemes in terms of BER performance and spectral efficiency.

The rest of the chapter is organized as follows. In Section 2.1, we present the relevant literature works. In Section 2.2, we give the motivation and main contributions. For the RIS-assisted Alamouti's scheme, an overview of the proposed scheme is presented in Section 2.3. In the following subsections, we give system model and transmission mechanism in Section 2.3.1, mathematical analysis in Section 2.3.2, and simulation results in Section 2.3.3. For RIS-assisted and IM-based VBLAST scheme, an overview of the proposed scheme is presented in Section 2.4. Next in the following subsections, system model is provided in Section 2.4.1, detection algorithms in Section 2.4.2, complexity analysis in Section 2.4.3, and simulation results in Section 2.4.4. Finally, we conclude the chapter in Section 2.5.

2.1 Related Works

In this section, we provide a brief literature review of the relevant works. In the preliminary study of [10], RISs are employed for two different purposes. First, an RIS is used to realize an ultra-reliable communication scheme that operates at considerably low signal-to-noise ratio (SNR) values. While in the second scenario, an RIS is used as an access point to create virtual phase shift keying (PSK) symbols at the receiver side. The latter concept is also used to perform index modulation at the receiver side [35]. Considering a dual-hop communication scenario, the authors in [42] proposed an RIS-based space shift keying system where the RIS is used as a reflector which is positioned between a transmitter with multiple antennas and a receiver with a single antenna. In [43], the indoor multiple-user network-sharing capacity is enhanced by optimally adjusting the phases of a passive reconfigurable reflect-array to cancel the interference and enhance the users' signal quality. An energy efficient multiple-input single output (MISO) system is proposed in [44], by jointly optimizing the transmit powers of the users and the phases of RIS elements. In [45], the authors proposed an RIS-assisted simultaneous wireless information and power transfer system, where an information decoding set and energy harvesting set of single-antenna receivers are served by a multiple-antenna access point. In [46], the authors investigated the use of artificial noise in order to increase the secrecy rate in an RIS-based communication system, where a single-antenna user is served by a multiple-antenna transmitter in the presence of multi-antenna eavesdroppers. In [47] and [48], the received signal power for a MISO user is maximized by optimizing the active beamforming at the transmitter jointly with the passive beamforming at the RIS by adjusting its phase shifters. The latter concept is also used in [49], where the beamformer at the access point and RIS are jointly optimized in order to increase the spectral efficiency for an RIS-assisted multi-user MISO system. In [50], an RIS-assisted multi-user MISO system is considered with different channel types where RIS phase optimization is utilized in order to maximize the minimum signal-to-noise-and-interference ratio (SNIR). RIS is used in [51] to improve the channel rank for MIMO systems by adding additional multipaths with distinctively different spatial angles in addition to the low-rank direct channel path. RIS reflection coefficients and the transmit covariance matrix are jointly optimized in [52] in order to maximize the capacity of a point-to-point MIMO system. In [53], the authors consider the channel estimation problem in multi-user MIMO systems and propose an uplink channel estimation protocol to estimate the cascaded channel from the base station to the RIS and from the RIS to the user. The use of passive intelligent mirrors (PIM) with a multi-user MISO downlink system is investigated in [54], where the transmit powers and the PIM reflection coefficients are designed to maximize the sum-rate considering the individual quality of service for mobile users. An overview of the holographic MIMO surface is presented in [55], where the authors investigated their hardware architectures, functionalities, and characteristics. In [56], the authors exploited the deep learning reinforcement to jointly obtain the optimum beamforming matrix and the RIS phase shifts where the introduced algorithm learns directly from the environment and updates the beamforming matrix and RIS phase shifts accordingly. Based on cosine similarity theorem, a low-complexity RIS phase shift design algorithm is proposed in [57], where the RIS is used to assist a MIMO communication system. In [58] and [59], the authors investigated physical channel modeling for mmWave bands considering indoor and outdoor environments. Furthermore, the authors provided an open-source comprehensive channel simulator which can be used to examine the different channel models discussed in their work.

2.2 Motivation and Contributions

From the previous literature review, it can be seen that the use of RISs to boost the spectral efficiency and/or reliability of existing MIMO systems along with applications of index modulation (IM) is not well explored in the open literature. Against this background, two new RIS-assisted communication schemes are presented in this chapter by focusing on the integration of RISs into the existing MIMO systems in a simple and effective way. VBLAST [60] and Alamouti's schemes [61] are considered in this study as the most common and practical MIMO schemes while a generalization to other advanced MIMO signaling schemes might be possible using our concept. We summarize the main contributions of this chapter as follows:

- We propose an RIS-assisted Alamouti's scheme in which we redesign the classical Alamouti's scheme with a single RF signal generator at the transmitter side instead of two RF chains.

- Considering the RIS-assisted Alamouti's scheme, we derive the average symbol error probability (SEP) for phase shift keying (PSK) modulation with an arbitrary M modulation order.

- We show that our RIS-assisted Alamouti's scheme preserves the diversity order of the classical Alamouti's scheme and provides a significant BER performance enhancement.

- We propose an RIS-assisted and IM-based VBLAST scheme using nulling and cancelling-based sub-optimal detection with zero forcing (ZF) technique. Compared to the classical VBLAST scheme, we show that our proposed RIS-assisted and IM-based VBLAST scheme provides superior performance in terms of the spectral efficiency and the BER performance.

- For RIS-assisted and IM-based VBLAST scheme, we propose two novel nulling-based optimal and sub-optimal detectors to detect the indices of the antennas targeted by the IM.

In RIS-assisted Alamouti's scheme, at the receiver side, the classical Alamouti's detector is used to recover the transmitted symbols, assuming that the channel state information (CSI) is available at this unit. It is worth noting that, for our RIS-assisted scheme, no CSI is needed at the RIS side, which reduces the overhead for CSI acquisition and simplifies the RIS design. Compared to the blind RIS-AP scheme in [10] and the classical Alamouti's scheme, our results show that the proposed scheme provides a significant improvement in the BER performance.

Furthermore, theoretical analysis and simulations results of the RIS-assisted Alamouti's scheme show that the same concept can be generalized to space-time block code (STBC) systems. In other words, in a large scale MIMO setup, our scheme can replace a large number of RF chains at the transmitter side by a single RF signal generator. Furthermore, our RIS-assisted scheme can provide a significant BER performance enhancement while preserving the diversity order of the STBC system. In RIS-assisted and IM-based VBLAST scheme, the RIS can be operated in multiple modes with and without IM. With IM, the RIS eliminates the channel phases between a specific transmit-receive antenna pair, which is selected according to the additional information bits in an IM fashion. On the other hand, without IM, the RIS eliminates the channel phases between a fixed and predefined antenna pair in order to provide the maximum BER performance enhancement. In this scheme, the CSI between each transmit-receive antenna pair through the RIS is required at both the RIS and the receiver side. At the receiver side, the IM bits are obtained using our novel nulling-based detectors while the transmitted symbols will be detected as in the plain VBLAST scheme using ZF-based nulling and cancelling algorithm without requiring additional signal processing steps [60]. The proposed schemes are simple in design and do not require major modifications for the state-of-the-art systems. Furthermore, comprehensive computer simulations are provided in this study under realistic environment setups to assess their practical feasibility.

2.3 RIS-Assisted Alamouti's Scheme

In this section, an RIS-assisted Alamouti's scheme is proposed to enhance the BER performance and reduce the required radio frequency (RF) resources.[1] In particular, RIS elements have been utilized in order to redesign Alamouti's scheme [61] with a single RF signal generator at the transmitter side instead of two RF chains. Furthermore, to assess the performance of the proposed scheme, the average symbol error probability (SEP) has been derived for phase shift keying (PSK) modulation with

[1]The authors in [41] have confirmed the feasibility of our proposed theoretical solution by implementing the proposed RIS-based transmitter for Alamouti's scheme in an experimental setup.

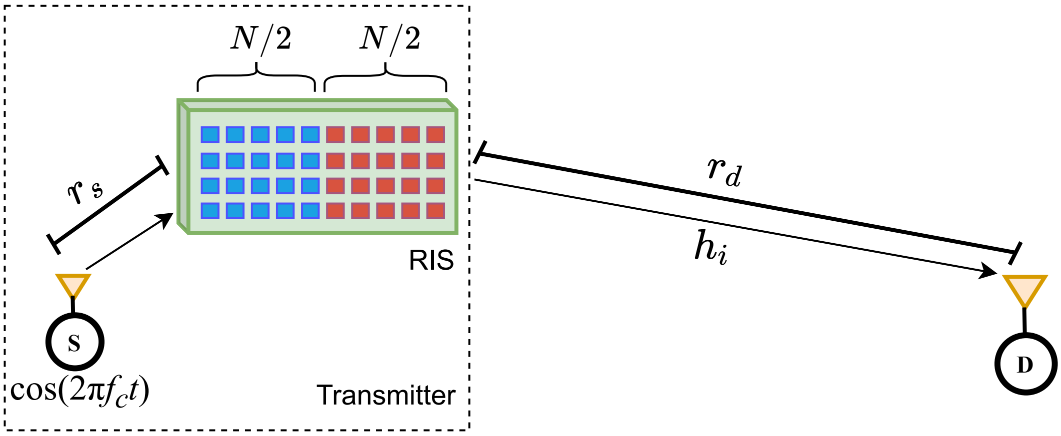

Figure 2.1: RIS-assisted Alamouti's scheme with the RIS as the transmitter.

any given M modulation order. In addition to the mathematical analysis, Monte Carlo simulations are provided to show the effectiveness of our proposed scheme, and it has been shown that it outperforms the reference schemes in terms of BER performance while preserving the same diversity order of the classical Alamouti's scheme.

2.3.1 System Model

In this section, we introduce the system model and transmission mechanism of the proposed RIS-assisted Alamouti's scheme.

In the proposed scheme, an unmodulated carrier signal is being transmitted from a low-cost RF signal generator close to the source (S) unit. The RF signal generator contains an RF digital-to-analog converter with an internal memory and a power amplifier as discussed in [10]. Fig. 2.1 shows the block diagram of the proposed scheme where r_s and r_d are the distances (in meters) of S-RIS and RIS-D, respectively. r_s is selected in a way that the channel between S and RIS is assumed to be line-of-sight (LOS) dominated. In our setup, the RIS is divided into two parts each having $N/2$ elements adjusted to a common reflection phase value. Each part employs two different common reflection phase values over two time slots. The proposed system emulates the Alamouti's scheme by adjusting the phases of the

RIS elements to modify the RF carrier signal and invoke the phases of the two data symbols. In this way, the Alamouti's scheme can be redesigned with a single RF signal generator instead of two full RF chains at the transmitter side. The RIS is a blind one with respect to the CSI, while its intelligent stems from the fact that it adjusts the unmodulated RF signal to mimic the PSK symbol phases. In this study, due to the high path loss experienced by the signals reflected from the RIS, the power of the signals reflected from the RIS for two or more times is ignored and only the first reflection is considered in our signal model [47].

Let h_i denotes the small-scale fading channel coefficient between the destination (D) and i^{th} element of the RIS, we have $h_i \sim \mathcal{CN}(0,1)$ under Rayleigh fading assumption. θ_0 and θ_1 stand for the phases of two M-PSK symbols to be transmitted according to $2\log_2(M)$ bits. Assuming quasi-static fading channels, where the channels will remain constant over the two time slots, the received signal at the first time slot can be written as

$$r_0 = \sqrt{P_L}\left[\sqrt{E_s}e^{j\theta_0}\sum_{i=1}^{N/2} h_i + \sqrt{E_s}e^{j\theta_1}\sum_{i=\frac{N}{2}+1}^{N} h_i\right] + n_0, \tag{2.1}$$

where n_0 is the additive white Gaussian noise (AWGN) sample at the first time slot, $n_0 \sim \mathcal{CN}(0, N_0)$. E_s is the transmitted RF signal energy and θ_0 and θ_1 are the common RIS reflection phases for the first and second parts, respectively, for the first time slot. P_L is the total path gain (loss), and more details regarding the considered path loss model and environmental setups will be given in Section 2.3.3. According to the Alamouti's transmission scheme, in the second time slot, we obtain the following received signal by carefully adjusting the common RIS phase terms as $-(\theta_1 + \pi)$ and $-\theta_0$ for the first and second parts, respectively:

$$r_1 = \sqrt{P_L}\left[\sqrt{E_s}e^{-j(\theta_1+\pi)}\sum_{i=1}^{N/2} h_i + \sqrt{E_s}e^{-j\theta_0}\sum_{j=\frac{N}{2}+1}^{N} h_i\right] + n_1, \tag{2.2}$$

where $n_1 \sim \mathcal{CN}(0, N_0)$. Defining $s_0 = \sqrt{E_s} e^{\theta_0}$, $s_1 = \sqrt{E_s} e^{\theta_1}$, $A_0 = \sqrt{P_L} \sum_{i=1}^{N/2} h_i$ and $A_1 = \sqrt{P_L} \sum_{i=\frac{N}{2}+1}^{N} h_i$, (2.1) and (2.2) can be re-expressed as

$$r_0 = s_0 A_0 + s_1 A_1 + n_0, \tag{2.3}$$

$$r_1 = -s_1^* A_0 + s_0^* A_1 + n_1, \tag{2.4}$$

where s_0 and s_1 stand for two virtual M-PSK symbols to be delivered to the receiver and M is the modulation order. As in the classical Alamouti's scheme, the combiner will construct the combined signals as follows:

$$\tilde{s_0} = r_0 A_0^* + r_1^* A_1 = (|A_0|^2 + |A_1|^2) s_0 + A_0^* n_0 + A_1 n_1^*, \tag{2.5}$$

$$\tilde{s_1} = r_0 A_1^* - r_1^* A_0 = (|A_0|^2 + |A_1|^2) s_1 - A_0 n_1^* + A_1^* n_0. \tag{2.6}$$

Then, $\tilde{s}_0$ and $\tilde{s}_1$ will be passed to the maximum likelihood (ML) detector to estimate s_0 and s_1.

2.3.2 Mathematical Analysis

In this section, we provide the mathematical analysis of the proposed scheme.

Considering the symmetry of s_0 and s_1, the instantaneous received SNR per symbol can be obtained as

$$\gamma = \frac{(|A_0|^2 + |A_1|^2) E_s}{N_0}. \tag{2.7}$$

Considering $h_i \sim \mathcal{CN}(0, 1)$, we obtain A_0 and $A_1 \sim \mathcal{CN}(0, P_L \frac{N}{2})$. Consequently, γ becomes a central chi-square distributed random variable with four degrees of freedom with the following MGF [62]:

$$M_\gamma(s) = \left(\frac{1}{1 - \frac{s P_L N E_s}{2N_0}} \right)^2. \tag{2.8}$$

From (2.8), the average symbol error probability (SEP) for M-PSK signaling can be obtained as [63]

$$P_e = \frac{1}{\pi} \int_0^{(M-1)\pi/M} \left(\frac{1}{1 + \left(\frac{\sin(\pi/M)^2}{\sin(\eta)^2} \right) \frac{P_L N E_s}{2N_0}} \right)^2 d\eta, \tag{2.9}$$

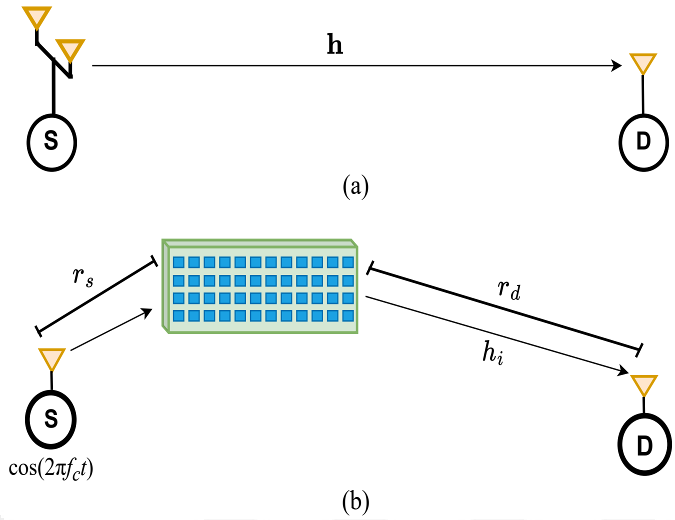

Figure 2.2: (a) Classical Alamouti's scheme. (b) RIS-AP scheme.

which can be simplified for BPSK as

$$P_e = \frac{1}{\pi}\int_0^{\pi/2}\left(\frac{1}{1+\frac{P_L N E_s}{2N_0 \sin(\eta)^2}}\right)^2 d\eta. \tag{2.10}$$

From (2.9), we observe that a transmit diversity of order two is still achieved by this scheme due to the fact that the RIS mimics a similar transmission methodology to the Alamouti's scheme over two time slots and preserves its orthogonality. Furthermore, the transmitted symbols have an SNR amplification achieved by the combination of the signals reflected from the RIS, where the SNR is enhanced by a factor of N, as seen from (2.10).

2.3.3 Simulation Results

In this section, exhaustive computer simulations are provided for the proposed scheme against its counterparts. We consider realistic setups and path loss models where both transmitter and receiver located in an indoor environment and Fig. 2.2 shows the block diagrams of the benchmark schemes. In all simulations, the SNR is defined to be E_s/N_0. Furthermore, perfect CSI is assumed to be available for the proposed and benchmark scheme at the receiver side only. Figs. 2.2 (a) and (b) show the system setups for the classical Alamouti and RIS-AP schemes, where the S-D channel is assumed to follow a Rayleigh fading (i.e., consist of a non-LOS link). For the RIS-AP scheme shown in Fig. 2.2 (b), the S-D transmission path is assumed to be fully blocked by obstacles and the only transmission path is through the RIS, where the S-RIS path is LOS dominated and the RIS-D path follow Rayleigh fading [10].

For classical Alamouti scheme, where there is no RIS, the path loss is calculated for an operating frequency of 1.8 GHz, as follows [64]

$$P_L^{(S-D)}(R)[\text{dB}] = 42.7 + 20\log_{10} R + 13.8 \tag{2.11}$$

where $R = 9.85$ m is the S-D separation distance, 42.7 dB is the path loss at one meter distance, and 13.8 dB corresponds to the path loss of two walls each having 6.9 dB of path loss.

For the RIS-assisted Alamouti and RIS-AP schemes, the S-RIS-D path loss, P_L, is calculated as follows [11]

$$P_L^{(S-RIS-D)} = \frac{\lambda^4}{256\pi^2 r_s^2 r_d^2} \tag{2.12}$$

where λ is the wavelength of the operating frequency (1.8 GHz), $r_s = 1$ m, and $r_d = 9$ m. Fig. 2.3.3 illustrates the BER performance of the RIS-assisted Alamouti's scheme versus the classical Alamouti's scheme for a 2×1 MISO system and the blind case of RIS-AP in [10]. We observe that a second order transmit diversity is achieved using a single RF signal generator thanks to the RIS. Furthermore, the influence of the number of RIS elements on the BER performance is shown to be significant, where a 10 dB gain is achieved with 64 RIS elements. As it can be verified from (2.10), the increase of the number of RIS elements enhances the BER performance linearly, where a 3 dB gain is achieved by doubling N. Hence, the RIS-assisted Alamouti's scheme outperforms the classical Alamouti's scheme in terms of the BER performance and the required RF resources on the transmitter side. Also, compared to the blind scheme of RIS-AP in [10], we see that the proposed scheme clearly shines out by a diversity of order two due to the orthogonality of Alamouti's transmission matrix.

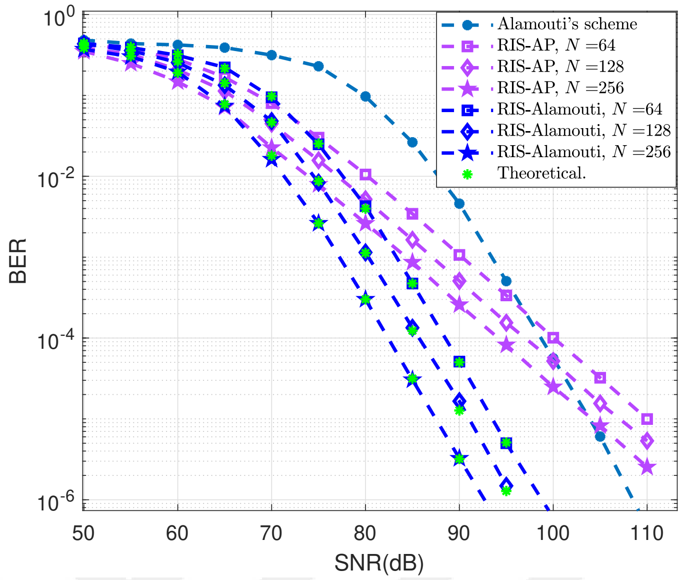

Figure 2.3: BER performance of RIS-assisted Alamouti's scheme versus 2×1 classical Alamouti's scheme and RIS-AP (blind) scheme, with different N values and BPSK.

2.4 RIS-Assisted and IM-Based VBLAST System

In this section, an RIS is proposed to be integrated into the well-known VBLAST MIMO system. In particular, an RIS is used to enhance the performance of the VBLAST nulling and canceling-based sub-optimal detection procedure, as well as to noticeably boost spectral efficiency by conveying extra bits through the adjustment of the phases of the RIS elements (IM). In order to cope with the different requirements of communications channels, three different operating modes are proposed to run the RIS. At the receiver side, we propose two novel algorithms for symbols detection along with their computational complexity analysis. Through Monte Carlo simulations, we show the superiority of our proposed RIS-assisted and IM-based VBLAST scheme over the benchmark one in terms of BER performance and spectral efficiency.

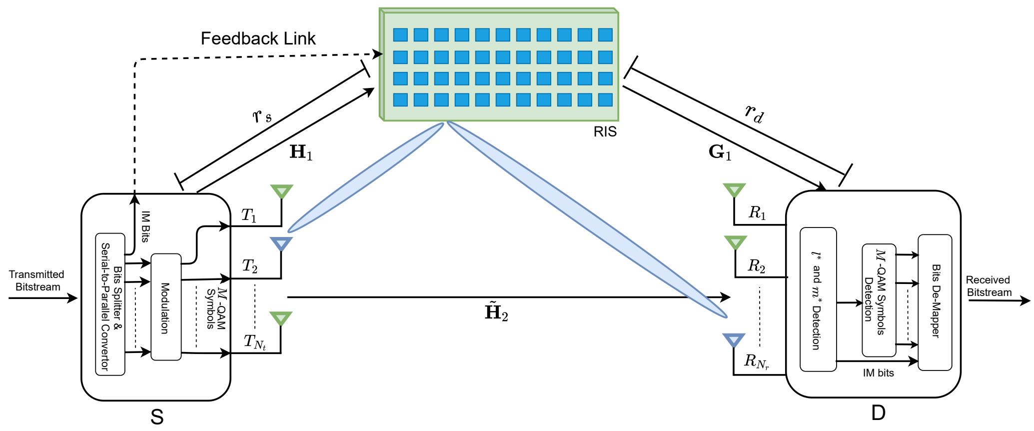

Figure 2.4: RIS-assisted and IM-based $N_t \times N_r$ VBLAST scheme.

2.4.1 System Model

In this section, the system model of the proposed RIS-assisted and IM-based VBLAST scheme is presented, where we explain the process of integrating the RIS into the VBLAST MIMO system to end up with three different operating modes for the RIS module.

The proposed scheme is assumed to utilize the RIS through a feedback link to eliminate the channel phases between a transmit-receive antenna pair. Instead of randomly selecting it, this transmit-receive antenna pair is selected according to the bits incoming to the RIS from S through the feedback link, in IM fashion. This means that the proposed scheme benefits from the RIS in an effective way. Consequently, with the help of the RIS, the proposed scheme provides a significant BER performance enhancement and an effective boost in the spectral efficiency compared to the classical VBLAST scheme. The proposed scheme is shown in Fig. 2.4, where an $N_t \times N_r$ VBLAST system is being operated along with an RIS with N reflecting elements. The RIS-assisted and IM-based VBLAST scheme can be operated in three different modes namely, i) full IM mode, ii) partial-IM mode, and iii) enhancing mode. In what follows, we describe these three operating modes.

In the full-IM mode, at the transmitter side, the IM-based mapping and transmission can be described as follows. The incoming bits will be divided into two groups, the first group of $N_t \log_2 M$ bits will be used to select N_t independent M-QAM symbols to be transmitted from the available N_t transmitting antennas at S, as in classical VBLAST scheme.

The second group of $\log_2 (N_t N_r)$ bits, where $N_t N_r$ is assumed to be an integer power of two and corresponds to the all possible transmit-receive antenna combinations, is sent through a feedback link from S to the RIS. The RIS uses these incoming bits to select the indices of the transmit and receive antennas, shown by l^* and m^*, corresponding to a $T_{l^*} - R_{m^*}$ pair of antennas, respectively. According to the CSI associated with the selected antenna pair, the phase shifts of the RIS elements will be adjusted to make the T_{l^*}-RIS-R_{m^*} equivalent channel phases equal to zero. Consequently, the signals transmitted from T_{l^*} and reflected from the RIS will constructively combine to provide SNR amplification at R_{m^*}. The overall spectral efficiency of the system becomes $N_t \log_2 M + \log_2 (N_t N_r)$ bits per channel use (bpcu).

In the partial-IM mode, the transmission procedure is the same as in the full-IM mode except that a smaller set of the transmit-receive antenna combinations is used to convey the IM bits. That is, the index of the targeted transmit antenna is determined first and the same index is used for the targeted receive antenna, $T_{l^*} - R_{l^*}$. Hence, there are only $\log_2 N_t$ possible combinations that can be used to convey the IM bits. The resulting spectral efficiency under this mode will be $N_t \log_2 M + \log_2 N_t$ bpcu, where the motivation here is to sacrifice spectral efficiency gained by IM in order to further enhance the BER performance through increasing the reliability of IM bits.

Finally, in the enhancing mode, IM is not performed at all and therefore, there is no need for a feedback link between S and D, instead, a fixed and predefined antenna pair will always be targeted by the RIS for the elimination of channel phases. Consequently, the best BER performance is achieved while preserving the same spectral efficiency for classical VBLAST, $N_t \log_2 M$. For all operating modes, we assume that perfect CSI is available at the both RIS and receiver side. The acquisition of CSI in RIS-based systems is discussed in [53], [65], [66]. We describe our scheme with an example.

Example: A 4×4 RIS-assisted VBLAST system operated in the full-IM mode with QPSK modulation transmits the bitstream of [00 01 10 11 00 01] as follows. The first 8 bits are modulated to 4 QPSK symbols and transmitted, in parallel, from the available 4 transmit antennas. The remaining 4 bits are used by the RIS to select the pair $T_1 - R_2$, since we implement the following mapping rule: $00 \rightarrow 1$ and $01 \rightarrow 2$. The RIS adjusts the reflection phases to eliminate the channel phases between T_1 and R_2. Here, we assume that the adjustment of the phases of the RIS elements and the M-QAM symbols' transmission from S are being performed simultaneously. On the other hand, the receiver tries to first estimate the indices of the selected antennas, and then successively detects the N_t independent M-QAM symbols.

For an $N_t \times N_r$ VBLAST system assisted by an RIS with N reflectors, the vector of the received signals $\mathbf{r} \in \mathbb{C}^{N_r \times 1}$ can be written as [67]

$$\mathbf{r} = \left[\sqrt{P_{L1}}\mathbf{G}_1^T \mathbf{\Theta} \mathbf{H}_1 + \sqrt{P_{L2}}\tilde{\mathbf{H}}_2\right]\mathbf{x} + \mathbf{n} = \mathbf{V}\mathbf{x} + \mathbf{n}, \tag{2.13}$$

where $\mathbf{H}_1 \in \mathbb{C}^{N \times N_t}$, $\mathbf{G}_1 \in \mathbb{C}^{N \times N_r}$ are the S-RIS and RIS-D, uncorrelated Rician fading channel matrices, respectively. The S-D channel matrix $\tilde{\mathbf{H}}_2 \in \mathbb{C}^{N_r \times N_t}$ is a random matrix where its elements are independent and identically distributed (i.i.d) complex Gaussian random variables (RVs) with zero mean and unit variance, $\sim \mathcal{CN}(0, 1)$. K is the Rician factor standing for the ratio of LOS and NLOS power and $\mathbf{\Theta} = \mathrm{diag}(e^{j\Phi_1}, ..., e^{j\Phi_n}, ..., e^{j\Phi_N})$ is the matrix of RIS reflection phases. In theory, each RIS element can be adjusted to any arbitrary phase shift, $\Phi_n \in [0, 2\pi)$, however, this is challenging to implement in practice. Therefore, in implementation, the RIS elements are being designed so that they can be adjusted to a finite number of discrete phase shifts. Hence, assuming uniform quantization for the interval $[0, 2\pi)$, the phase shift associated with each RIS element can be controlled by b bits that correspond to $Z = 2^b$ possible different phase shifts belong to the finite set $\mathcal{F} = \{0, \Delta\Phi, ..., \Delta\Phi(Z-1)\}$, where $\Delta\Phi = \frac{2\pi}{Z}$ [68]. $\mathbf{x} \in \mathbb{C}^{N_t \times 1}$ is the vector of transmitted M-QAM symbols, $\mathbf{V} \in \mathbb{C}^{N_r \times N_t}$ is the S-RIS-D and S-D equivalent channel matrix and $\mathbf{n} \in \mathbb{C}^{N_r \times 1}$ is the vector of AWGN noise samples. P_{L1} and P_{L2} are the total path losses for S-RIS-D and S-D transmission paths, respectively, and more details are given in Section 2.4.4. The received signal by the m^{th} receiving antenna (R_m) can be represented as

$$r_m = \left[\sqrt{P_{L1}}\mathbf{g}_m^T \boldsymbol{\Theta}\mathbf{H}+\mathbf{h}_2\right]\mathbf{x} + n_m, \tag{2.14}$$

where $\mathbf{h}_2 = \sqrt{P_{L2}}\tilde{\mathbf{h}}_2$ and $\tilde{\mathbf{h}}_2 \in \mathbb{C}^{1\times N_t}$ is the S-D channel vector for the m^{th} receiving antenna. $\mathbf{g}_m \in \mathbb{C}^{N\times 1}$ is the RIS-D channel vector for the m^{th} receiving antenna, and n_m is the AWGN sample with $n_m \sim \mathcal{CN}(0, N_0)$. Expanding (2.14), we have

$$r_m = \sqrt{P_{L1}}\sum_{l=1}^{N_t}\left[\sum_{i=1}^{N} h_i^{(l)} e^{j\Phi_i} g_i^{(m)}\right] x^{(l)} + \mathbf{h}_2\mathbf{x} + n_m, \tag{2.15}$$

where $h_i^{(l)} = \alpha_i^l e^{-j\theta_i^{(l)}}$ is the S (l^{th} transmitting antenna)-RIS (i^{th}element) channel coefficient and $g_i^{(m)} = \beta_i^m e^{-j\Psi_i^{(m)}}$ is RIS (i^{th}element)-D (m^{th} receiving antenna) channel coefficient. In this way, in order to eliminate the phases of the S-RIS-D channel between the antenna pair $T_{l^*} - R_{m^*}$, elements' phases of the RIS are adjusted as $\Phi_i = \theta_i^{(l^*)} + \Psi_i^{(m^*)}$, and (2.15) can be re-expressed for the $(m^*)^{th}$ receive antenna as

$$\begin{aligned} r_{m^*} = \sqrt{P_{L1}}&\left[\left[\sum_{i=1}^{N}\alpha_i^{l^*}\beta_i^{m^*}\right]x^{(l^*)} + \sum_{l=1,l\neq l^*}^{N_t-1}\left[\sum_{i=1}^{N} h_i^{(l)} e^{j\Phi_i} g_i^{(m^*)}\right]x^{(l)}\right] \\ &+ \mathbf{h}_2\mathbf{x} + n_{m^*}. \end{aligned} \tag{2.16}$$

(2.16) can be interpreted as follows. The first term illustrates the amplification gained by the constructive combining of the signals reflected from the RIS and belongs to the symbol $x^{(l^*)}$. This constructive combining will result in an SNR gain of N^2 for this symbol as in [10]. Hence, the BER performance of this symbol will be boosted up and consequently, it will be the strongest symbol where the nulling and canceling algorithm starts with. This also means that the error propagation from the first symbol to the remaining ones will be significantly mitigated and the overall BER performance will be improved. The second term shows the destructive interference of the signals reflected from the RIS, which belongs to the other symbols. Finally, the third term corresponds to the interference received by the $(m^*)^{th}$ receiving antenna through the S-D transmission path for all the transmitted symbols. Hence, compared to the classical VBLAST, an RIS will introduce N times extra interference for each received symbol. Nevertheless, assuming that the CSI over S-RIS-D is available at the receiver side, then this interference can be handled readily.

2.4.2 Detection Algorithms

In this section, we introduce the proposed symbols detection algorithms that need to be run at the receiver side of our proposed system.

At the receiver side, we introduce two novel nulling-based detectors to detect the transmit-receive antenna indices targeted by the RIS for channel phases elimination. According to Algorithm 1, the optimal detector performs an exhaustive search for l^* and m^* jointly, as follows. For each iteration, the detector determines $\mathbf{\Theta}^{(l,m)}$ and then constructs $\hat{\mathbf{V}}^{(l,m)}$. Next, the nulling-based procedure will be used to detect the first symbol, which has the highest SNR, assumed to be transmitted and received by the antenna pair $T_l - R_m$. Finally, the pair l and m associated with the symbol that has the minimum squared Euclidean distance will be picked as the pair l^* and m^*.

In Algorithm 1, $\hat{\mathbf{V}}^{(l,m)}$ is the index-estimated S-RIS-D and S-D equivalent channel matrix assuming the antenna pair $T_l - R_m$ was targeted by the RIS for channel phases elimination. $\mathbf{\Theta}^{(l,m)}$ is the diagonal RIS phases matrix where its i^{th} element $\Phi_i = \theta_i^{(l)} + \Psi_i^{(m)}$ corresponds to the phase elimination for the S-RIS-D channel between T_l and R_m. $(\cdot)^+$ is Moore-Penrose pseudo-inverse operator, $(\hat{\mathbf{V}}^{(l,m)})^+ = (\hat{\mathbf{V}}^{(l,m)})^\dagger(\hat{\mathbf{V}}^{(l,m)}(\hat{\mathbf{V}}^{(l,m)})^\dagger)^{-1}$, where $(\cdot)^\dagger$ is the Hermitian operator. $(\mathbf{W}^{(l,m)})_j$ is the j^{th} row of $\mathbf{W}^{(l,m)}$. k_l is the index of the row, which has the minimum squared Euclidean norm, of the matrix $\mathbf{W}^{(l,m)}$, corresponding to the symbol with the highest SNR. $(\mathbf{W}^{(l,m)})_{k_l}$ is the k_l^{th} row of $\mathbf{W}^{(l,m)}$, y_{k_l} is the k_l^{th} symbol after nulling the interference of the other symbols. $\mathcal{Q}(\cdot)$ returns the squared Euclidean distance, $D_{l,m}$, of the closest M-QAM symbol associated with y_{k_l}. Hence, $\hat{\mathbf{V}}^{(\hat{l},\hat{m})}$ associated with the minimum distance $D_{\hat{l},\hat{m}}$ is the most likely the equivalent channel matrix

Algorithm 1 Optimal detector: Detecting the antenna indices l^* and m^* jointly.

Require: $\mathbf{H}_1$, $\tilde{\mathbf{H}}_2$ $\mathbf{G}_1$, $\mathbf{r}$, $\sqrt{P_{L1}}$, $\sqrt{P_{L2}}$

for $l = 1 : N_t$ **do**

  for $m = 1 : N_r$ **do**

    $\hat{\mathbf{V}}^{(l,m)} = \sqrt{P_{L1}}\mathbf{G_1}^T\mathbf{\Theta}^{(l,m)}\mathbf{H}_1 + \sqrt{P_{L2}}\tilde{\mathbf{H}}_2$

    $\mathbf{W}^{(l,m)} = (\hat{\mathbf{V}}^{(l,m)})^+$

    $k_l = \underset{j\in\{1,2,..N_t\}}{\arg\min} \left|\left|(\mathbf{W}^{(l,m)})_j\right|\right|^2$ {Ordering}

    $\mathbf{s}_{k_l} = (\mathbf{W}^{(l,m)})_{k_l}$

    $y_{k_l} = \mathbf{s}_{k_l}^T\mathbf{r}$ {Nulling}

    $D_{l,m} = \mathcal{Q}(y_{k_l})$

  end for

end for

$\{\hat{l}, \hat{m}\} = \underset{\substack{l\in\{1,2,..N_t\} \\ m\in\{1,2,..N_r\}}}{\arg\min} D_{l,m}$

$\hat{\mathbf{V}} = \sqrt{P_{L1}}\mathbf{G_1}^T\mathbf{\Theta}^{(\hat{l},\hat{m})}\mathbf{H}_1 + \sqrt{P_{L2}}\tilde{\mathbf{H}}_2$

return $\hat{\mathbf{V}}$

that corresponds to the current adjustment of the RIS phases. By estimating l^* and m^*, the IM bits conveyed by the adjustment of the RIS phases will be obtained.

In order to reduce the complexity of the detector proposed in Algorithm 1, the receiving antenna index, m^*, can be detected using a greedy detector instead of the joint exhaustive search for l^* and m^*. In this way, m^* can be detected by finding the receiving antenna with the highest instantaneous energy:

$$\hat{m} = \underset{m\in\{1,2,...N_r\}}{\arg\max} |r_m|^2. \tag{2.17}$$

Next, a nulling-based procedure is used to search for l^* while fixing $\hat{m}$ found from (2.17). This detector is represented as a sub-optimal one and Algorithm 2 illustrates its detection steps.

After obtaining the S-RIS-D and S-D equivalent channel matrix, $\hat{\mathbf{V}}$, it will be used by Algorithm 3 to detect the N_t independent symbols as in the case of classical VBLAST [60]. In Algorithm 3, $\tilde{\mathcal{Q}}(\cdot)$ is the slicing function, $(\hat{\mathbf{V}})_{k_i}$ is the k_i^{th} column

Algorithm 2 Sub-optimal detector: Detecting the antenna indices l^* and m^* sequentially.

Require: $\mathbf{H}_1$, $\tilde{\mathbf{H}}_2$ $\mathbf{G}_1$, $\mathbf{r}$, $\sqrt{P_L}$, $\sqrt{P_{L2}}$

$\hat{m} = \underset{m\in\{1,2,..N_r\}}{\arg\max} \ |r_m|^2$

for $l = 1 : N_t$ **do**

$\hat{\mathbf{V}}^{(l,\hat{m})} = \sqrt{P_{L1}}\mathbf{G_1}^T\mathbf{\Theta}^{(l,\hat{m})}\mathbf{H}_1 + \sqrt{P_{L2}}\tilde{\mathbf{H}}_2$

$\mathbf{W}^{(l,\hat{m})} = (\hat{\mathbf{V}}^{(l,\hat{m})})^+$

$k_l = \underset{j\in\{1,2,..N_t\}}{\arg\min} \ \left|\left|(\mathbf{W}^{(l,\hat{m})})_j\right|\right|^2$ {Ordering}

$\mathbf{s}_{k_l} = (\mathbf{W}^{(l,\hat{m})})_{k_l}$

$y_{k_l} = \mathbf{s}_{k_l}^T\mathbf{r}$ {Nulling}

$D_l = \mathcal{Q}(y_{k_l})$

end for

$\hat{l} = \underset{l\in\{1,2,..N_t\}}{\arg\min} \ D_l$

$\hat{\mathbf{V}} = \sqrt{P_{L1}}\mathbf{G_1}^T\mathbf{\Theta}^{(\hat{l},\hat{m})}\mathbf{H}_1 + \sqrt{P_{L2}}\tilde{\mathbf{H}}_2$

return $\hat{\mathbf{V}}$

of $\hat{\mathbf{V}}$ and $(\hat{\mathbf{V}}_{\overline{k_i}})^+$ is pseudo inverse of the matrix obtained by zeroing the columns of $\hat{\mathbf{V}}$ with indices k_1, k_2, $...k_i$. Finally, $\mathbf{r}_{i+1}$ is the signal vector after subtracting the interference contribution of the previously detected symbol $\hat{x}_{k_i}$.

Algorithm 3 ZF-based successive nulling and canceling to detect the transmitted M-QAM symbols.

Require: $\hat{\mathbf{V}}$, $\mathbf{r}$

$\mathbf{r}_1 = \mathbf{r}$

$\mathbf{W}_1 = \hat{\mathbf{V}}^{+}$

$k_1 = \underset{j \in \{1,2,..N_t\}}{\arg\min} \left|\left|(\mathbf{W}_1)_j\right|\right|^2$

for $i = 1 : N_t - 1$ **do**

  $\mathbf{s}_{k_i} = (\mathbf{W}_i)_{k_i}$

  $y_{k_i} = \mathbf{s}_{k_i}^T \mathbf{r}_i$

  $\hat{x}_{k_i} = \tilde{\mathcal{Q}}(y_{k_i})$ {Slicing}

  $\mathbf{r}_{i+1} = \mathbf{r}_i - \hat{x}_{k_i}(\hat{\mathbf{V}})_{k_i}$ {Canceling}

  $\mathbf{W}_{i+1} = (\hat{\mathbf{V}}_{\overline{k_i}})^{+}$

  $k_{i+1} = \underset{j \in \{1,\ldots,N_t\} \setminus \{k_1,\ldots,k_i\}}{\arg\min} \left|\left|(\mathbf{W}_{i+1})_j\right|\right|^2$

end for

$\mathbf{s}_{k_{i+1}} = (\mathbf{W}_{i+1})_{k_{i+1}}$

$y_{k_{i+1}} = \mathbf{s}_{k_{i+1}}^T \mathbf{r}_{i+1}$

$\hat{x}_{k_{i+1}} = \tilde{\mathcal{Q}}(y_{k_{i+1}})$

return $\hat{\mathbf{x}}$

2.4.3 Complexity Analysis

This section provides the computational complexity analysis for the proposed detection algorithms. At the receiver side, first, the RIS-assisted VBLAST scheme uses Algorithm 1 or Algorithm 2 to detect the indices l^* and m^*. Second, the receiver uses Algorithm 3 to detect the N_t transmitted M-QAM symbols. Here, we calculate the computational complexity associated with Algorithms 1, 2, and 3.

Denoting the total number of complex multiplications (CMs) required by Algorithms 1, 2, and 3 as C_1, C_2, and C_3, respectively, then from Table 2.1, C_1, C_2 and

Table 2.1: Computational complexity derivation steps of nulling-based detection algorithms.

Operation	CMs
Searching for $\hat{m}$	N_r
Constructing $\hat{\mathbf{V}}^{(l,m)}$	$N_rN+N_rNN_t$
Pseudo inverse of $\hat{\mathbf{V}}^{(l,m)}$	$2N_r^2N_t+N_r^3$
Ordering	N_tN_r
Nulling	N_r
Getting $D_{l,m}$	2^M

C_3 can be calculated as follows

$$\begin{aligned} C_1 &= N_tN_r[(N_rN+N_rNN_t)+(2N_r^2N_t+N_r^3)+N_tN_r \\ &\quad +N_r+2^M], \end{aligned} \tag{2.18}$$

$$\begin{aligned} C_2 &= N_r+N_t[(N_rN+N_rNN_t)+(2N_r^2N_t+N_r^3)+N_tN_r \\ &\quad +N_r+2^M], \end{aligned} \tag{2.19}$$

$$\begin{aligned} C_3 &= (2N_r^2N_t+N_r^3)+N_tN_r+(N_t-1)[N_r+2^M+N_r \\ &\quad +(2N_r^2N_t+N_r^3)+N_tN_r]+N_r+2^M. \end{aligned} \tag{2.20}$$

In order to provide a useful insight on the overall complexity, let $N_t = N_r$. Then (2.18), (2.19), and (2.20) can be rewritten as

$$C_1 = N(N_r^3+N_r^4)+3N_r^5+N_r^4+N_r^3+N_r^2 2^M, \tag{2.21}$$

$$C_2 = N_r+N(N_r^2+N_r^3)+3N_r^4+N_r^3+N_r^2+N_r 2^M, \tag{2.22}$$

$$C_3 = 4N_r^3+3N_r^2+N_r 2^M+3N_r^4+N_r+2^M. \tag{2.23}$$

From (2.18) and (2.19), it can be seen that the number of antennas and the number of RIS reflecting elements both have a significant contribution to the computational complexity of detecting the antenna indices l^* and m^*. This is still valid even if we consider the fact that N is, practically, much larger than N_r, since the latter still has a higher exponent. From (2.21) and (2.22), the overall computational complexity

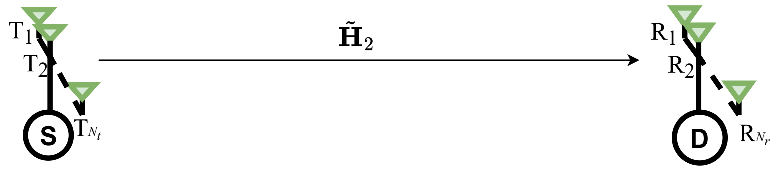

Figure 2.5: Classical VBLAST scheme.

level can be obtained as $\sim \mathcal{O}(N(N_r^3 + N_r^4) + N_r^5)$, and $\sim \mathcal{O}(N(N_r^2 + N_r^3) + N_r^4)$, for Algorithms 1 and 2, respectively. Comparing both algorithms, we observe that the overall computational complexity is dominated by that of constructing $\hat{\mathbf{V}}^{(l,m)}$. Compared to the classical VBLAST scheme, where the receiver computational complexity will be equivalent to that of Algorithm 3 only, $\sim \mathcal{O}(N_r^4)$, RIS-assisted IM-based VBLAST scheme has an extra complexity of $\sim \mathcal{O}(N(N_r^3 + N_r^4))$ and $\sim \mathcal{O}(N(N_r^2 + N_r^3))$ for Algorithms 1 and 2, respectively.

The cost of this additional complexity stems for the construction of $\hat{\mathbf{V}}^{(\hat{l},\hat{m})}$, which is required to detect the transmitted symbols and the indices of the targeted transmit-receiving antennas. In a brief, C_1 or C_2 is the additional computational complexity that is required to operate a classical VBLAST system as an RIS-assisted system.

2.4.4 Simulation Results

In this section, we provide exhaustive computer simulations to compare the proposed scheme with the benchmark one (shown in Fig. 2.5). A realistic setup of an indoor environment is considered along with its corresponding practical path loss model. SNR is defined to be E_s/N_0 for all simulations. Furthermore, for the proposed and benchmark schemes, perfect CSI is assumed to be available at the receiver side; in addition, it should also be available at the RIS side for the proposed scheme.

For the classical VBLAST scheme, the S-D channel is assumed to follow a Rayleigh fading (i.e., consist of a non-LOS link). The path loss model (1.8 GHz operating frequency) for the benchmark scheme is given in (2.11), while for RIS-

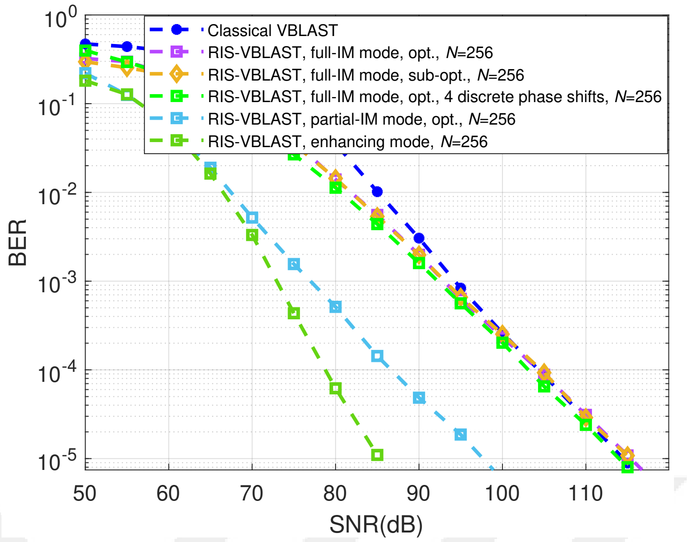

Figure 2.6: BER performance of RIS-assisted and IM-based VBLAST scheme versus classical VBLAST with 2×2 MIMO setup, BPSK, and $K = -\infty$ dB.

assisted and IM-based VBLAST scheme, P_{L1} and P_{L2} are calculated from (2.12) and (2.11), respectively. For the path loss calculations, we have $r_s = 3$ m, $r_d = 3$ m, and $R = 5.91$ m.

For the RIS-assisted and IM-based VBLAST scheme, we considered the existence and absence of a LOS component for the S-RIS, and RIS-D channels. Therefore, the simulations are performed with $K = 5$, and $-\infty$ dB, where K values can change dramatically within the same indoor environment depending on the location of the transmitter and receiver [69].

In Figs. 2.6 and 2.7, we compare RIS-assisted and IM-based VBLAST with classical VBLAST for 2×2 MIMO setup. Algorithms 1 and 2 correspond to the optimal and sub-optimal detectors for the transmit-receive antenna indices and they are denoted in Figs. 2.6 and 2.7 by “opt.” and “sub-opt.”, respectively. Here, the spectral efficiency of classical VBLAST is 2 b/s/Hz, while it is 3 and 4 b/s/Hz for the RIS-assisted and IM-based VBLAST, in partial and full-IM modes, respectively, with BPSK. Thus, the spectral efficiency for the RIS-assisted IM-based VBLAST is significantly boosted compared to the classical VBLAST due to the extra IM bits conveyed by our antenna pair selection methodology.

In Fig. 2.6 we compare the BER performance of RIS-assisted and IM-based

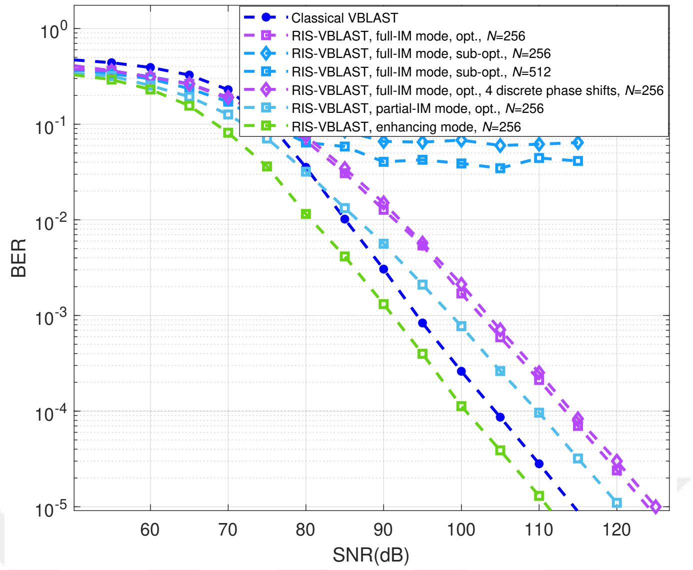

Figure 2.7: BER performance of RIS-assisted and IM-based VBLAST scheme versus classical VBLAST with 2×2 MIMO setup, BPSK, and $K = 5$ dB.

VBLAST scheme, under the Rayleigh fading assumption for the S-RIS-D transmission path, with classical VBLAST scheme. We observe that the proposed scheme operated in full-IM mode provides an improved BER at low to mid SNR values, while saturating to the BER performance of the classical VBLAST at high SNR. Nevertheless, compared to the classical VBLAST scheme, the spectral efficiency is doubled for the proposed scheme. In addition, the sub-optimal detector represented by Algorithm 2 is shown to achieve the same performance as for the optimal one, which is represented by Algorithm 1. This means that the detection process of the antenna indices can be simpler in terms of the complexity level. It can be also seen that the performance of the continuous phases adjustment can be almost achieved with only four discrete phase shifts [68], [70]. In this way, the RIS design can be simplified to control the phase shift of each element using 2-bits only.

Furthermore, the partial-IM and enhancing modes show a significant BER performance gain of 16 and 28 dB, respectively, compared to the classical VBLAST scheme. It is worth noting that, the partial-IM scheme increases the spectral efficiency by 50%.

In Fig. 2.7, the BER performance curves are shown for the RIS-assisted and

IM-based VBLAST scheme considering the existence of LOS component ($K = 5$ dB) between S and the RIS, and between the RIS and D. Compared to the classical VBLAST scheme, the impact of the LOS component on the RIS performance can be clearly seen for the proposed scheme. The full-IM and partial-IM modes need an SNR increase of 5-10 dB in order to increase the spectral efficiency by 2 and 1.5 fold, respectively. This can be explained by the lack of diversity due to the LOS component in the S-RIS and RIS-D channels. Therefore, the receiver makes more errors while detecting the targeted antenna indices, l^* and m^*. Since the construction of $\hat{\mathbf{V}}$ depends on l^* and m^*, the erroneous detection of them reflects on the detection of the M-QAM symbols. Furthermore, it can be noted that the sub-optimal (greedy) detector provides an error floor even with an RIS of 512 elements. This is, also, due to the LOS component, which makes the difference in the instantaneous energy, received by all the receiving antennas, trivial. Nevertheless, the enhancing mode still provides a BER performance gain of 4 dB compared to the classical VBLAST scheme.

Comparing the three operating modes, Fig. 2.6 and Fig. 2.7 show that the enhancing mode, where there is no IM, achieves the best BER performance. This is due to the fact that, in enhancing mode, the amplification is directed towards a fixed and predefined antenna pair. Furthermore, the proposed scheme has the flexibility to operate in one of these three modes according to the K value, hence, increase the spectral efficiency and/or enhance the BER performance accordingly.

Finally, it is worth noting that, from (2.11) and (2.12), comparing the S-RIS-D and S-D communication links, we obtain 12.29 dB additional path loss for the S-RIS-D compared to the S-D communication link, under the given separation distances. This shows that the transmission over the RIS has considerably higher path loss compared to the direct transmission without RIS. Nevertheless, the additional path loss can be compensated by choosing the proper RIS size [11], [71], as we showed in our proposed scheme.

2.5 Conclusion

In this chapter, we have proposed novel designs for the most common and practical MIMO systems, VBLAST and Alamouti's schemes, as follows.

First, an RIS-assisted Alamouti's scheme has been proposed, where the transmitter of Alamouti's scheme has been redesigned in a cost-efficient way in terms of the required RF resources. The proposed scheme achieves a remarkable performance gain in terms of the BER by providing N times SNR enhancement while preserving the diversity order of the classical Alamouti's scheme. Applying the considered concept to space-time codes in large-scale MIMO setups with a large number of antennas may show a remarkable advantage for this scheme by utilizing a single RF signal generator instead of multiple RF chains. Considering the simplicity of implementation and deployment, the proposed scheme does not require a significant reconfiguration for the existing MIMO setup, particularly in its receiver architecture, which makes it a practical and feasible alternative for future wireless systems. The design of a practical phase-shift model that captures the phase-dependent amplitude variation for the proposed scheme appears to be an interesting problem that we will consider in our future research.

Second, we have proposed a novel design for VBLAST MIMO system with the assistance of RISs. Without reconfiguring the transceiver architecture, the RIS has been integrated into the VBLAST scheme as a supportive module, which makes it a practical solution for MIMO systems. The RIS-assisted IM-based VBLAST scheme is able to provide a significant BER performance gain in addition to the noticeable increase in spectral efficiency by the smart methodology of channel phases elimination. In addition, by offering three different operating modes, the proposed scheme provide a high flexibility to deal with the different requirements of different communications channels. Investigating the channel estimation overhead effect on the proposed scheme is a promising direction for future research.

Chapter 3

A NOVEL NOMA SOLUTION WITH RIS PARTITIONING

In this chapter, we propose a novel NOMA solution with RIS partitioning, where we aim to enhance the spectrum efficiency by improving the ergodic rate of all users, and to maximize the user fairness. In the proposed system, we distribute the physical resources among users such that the base station (BS) and RIS are dedicated to serve different clusters of users. Furthermore, we formulate an RIS partitioning optimization problem to slice the RIS elements between the users such that the user fairness is maximized. The formulated problem is shown to be a non-convex and non-linear integer programming (NLIP) problem with a combinatorial feasible set, which is challenging to solve. Therefore, we exploit the structure of the problem to bound its feasible set and obtain a sub-optimal solution by sequentially applying three efficient search algorithms. Furthermore, we derive exact and asymptotic expressions for the outage probability. Simulation results clearly indicate the superiority of the proposed system over the considered benchmark systems in terms of ergodic sum-rate, outage probability, and user fairness performance.

The following sections of the chapter are given as follows. In Section 3.1 a brief background about NOMA is presented. In Section 3.2, we provide the literature studies related to our proposed solution, followed by the motivation and main contributions in Section 3.3. In Section 3.4, we introduce the system model, which provides the general system settings, users clustering, and transmission mechanism. In Section 3.5, we provide the mathematical analysis for the proposed system. Our proposed partitioning approach is introduced in Section 3.6 followed by the partitioning algorithms in Section 3.7 and their complexity analysis in Section 3.8. Special cases derived from the general system model are given Section 3.9. Simulation results for different system settings and users deployment scenarios are given in Section 3.10, and we conclude the chapter in Section 3.11.

3.1 Background

Non-orthogonal multiple access (NOMA) has received significant attention due to its ability to realize high spectral efficiency, massive connectivity, and low latency. NOMA fundamentally differs from conventional orthogonal multiple access (OMA) schemes that provide orthogonal access to users in time, frequency, code, or space. NOMA has been regarded as one of the promising technologies to address the increasing demand for high data rates, massive connectivity, and spectrum efficiency associated with fifth-generation (5G) and beyond networks [72]. The key idea in NOMA is to allocate non-orthogonal resources to serve multiple users, yielding a higher spectral efficiency while allowing some degree of interference at receivers [73]. In power-domain NOMA (PD-NOMA), multiple users' signals are superposed with different power levels in reverse order to their channels' gains. At the receiver side, successive interference cancellation (SIC) is applied by each user to recover its own signal, providing a good trade-off between system throughput and user fairness [74]. Compared to the orthogonal multiple access (OMA), it has been shown that NOMA has a superior performance in terms of the outage probability and the ergodic sum-rate [75], [76],[77]. On the other side, due to the use of higher carrier frequencies and to fulfill the verticals' specific requirements, local service areas are among the main envisioned deployment models in 5G [78]. Within this context, NOMA can play an essential role in order to efficiently exploiting the spectrum and serving higher numbers of users in such networks [79]. This is because NOMA allows the sharing of the same time/frequency/code resources between users and thus, enhances the spectrum efficiency and decreases the latency by allowing more users to be connected in the same time-frequency slot [80].

3.2 Related Works

Due to their remarkable advantages, the integration of RISs with NOMA systems is indispensable in future wireless communications to fulfill the stringent demands on data rate and connectivity [72]. Recently, the joint operation of RISs with NOMA has appeared as an appealing research direction and the combination of the hardware capabilities of RISs and the SC technique of PD-NOMA has been investigated. In [81] and [82], the rate performance and user fairness of an RIS-assisted NOMA system are optimized by maximizing the minimum decoding signal-to-interference-plus-noise ratio (SINR) of all users, which is achieved by the joint optimization of the active and passive beamforming at the BS and the RIS, respectively. The authors in [83] considered an RIS-assisted multiple-input single-output (MISO) NOMA system where the cell-center users are served by using spatial division multiple access (SDMA) and the cell-edge users are served by RISs. In [84], by considering a priority-oriented design, an RIS-assisted SISO NOMA network is proposed, where the passive beamforming weights are designed at the RIS side in order to enhance the spectrum efficiency. In [85], the energy efficiency is enhanced in a downlink RIS-assisted NOMA system by jointly optimizing the user clustering, passive beamforming, and power allocation. The user fairness is considered in [86], where the authors investigated the joint optimization of power allocation, decoding order, and the RIS phase shifts to maximize the minimum user rate considering a total power constraint. In [87], the deployment and passive beamforming design of an RIS are investigated for an RIS-assisted MISO NOMA system, in order to maximize the energy efficiency under the constraint of preserving the individual data rate requirements for users. Joint optimization for the active beamforming matrices at the BS and the reflection coefficient vector at the RIS is utilized in [88] in order to minimize the total transmit power for a multi-cluster MISO NOMA networks. In [89], a multi-cluster RIS-assisted MIMO NOMA network is considered, where by designing its passive beamforming weights, the RIS is employed in a signal cancellation mode to eliminate the inter-cluster interference. The authors in [90] and [91] used stochastic geometry to investigate the coverage probability and ergodic rate of an RIS-assisted multi-cell NOMA networks for outdoor scenarios by using Poisson cluster process (PCP) model. The authors in [92] considered the combination of joint transmission coordinated multipoint (JT-CoMP) with the RIS technology in order to enhance the cell-edge user ergodic rate performance without degrading the performance of the cell-center user. In [93], the authors investigated the impact of the coherent and the random discrete phase-shifting designs on an RIS-assisted NOMA system. Finally, the authors in [94] considered the resource allocation problem in an RIS-assisted NOMA system, and jointly optimized the channel assignments, power allocation, decoding order, and RIS reflection coefficients, in order to maximize the system throughput.

3.3 Motivation and Contributions

In light of the above discussion, it can be noted that a common physical resource (PR) allocation scheme is followed by all of the previous works, which can be summarized as follows. The BS and RIS are both used to serve all users by using a single SC message, where all users are assumed to be in the field-of-view (FoV) of the RIS. Furthermore, by adjusting its reflection coefficients, the RIS is used as a single unit to serve all users jointly. Considering this PR allocation scheme, the main factor that limits the users' performance becomes the mutual interference that underlies the SC technique, which can be seen clearly when the users are deployed randomly in and out of the FoV of the RIS. In such a users' deployment scenario, not all users share the same PR (BS and RIS) and therefore, the use of a single SC message for all users adversely affects user fairness and unnecessarily amplifies the mutual interference between the users' messages.

Against this background, we propose an RIS-assisted novel NOMA system, where a more efficient PR allocation scheme is proposed to enhance user fairness and effectively mitigate the impact of the mutual interference between users. In the proposed system, the users are grouped into two clusters, Cluster 1 (C_1) contains all the users out of the FoV of the RIS, and Cluster 2 (C_2) contains the ones inside it. The BS is dedicated to serve the users in C_1 and the RIS is portioned into sub-surfaces, where each sub-surface is exploited to serve a different user in C_2. The main contributions of this chapter can be summarized as follows:

- To the best of the authors' knowledge, this study considers the PR problem when the users are deployed in and out of the FoV of the RIS, for the first time. To address this issue, we propose a novel PR scheme that employs RIS partitioning to mitigate the mutual interference between the users in and out of the FoV of the RIS. This leads to an effective enhancement in the performance of all users in terms of ergodic rate, outage probability, fair distribution of the PRs among users, and simplifies the detection process.

- We formulate an RIS partitioning optimization problem to find a proper RIS slicing that maximizes the fairness among C_2 users. Although the fact that the formulated problem is a non-convex and non-linear integer programming (NLIP) one, we exploit the structure of the problem, specifically the nature of transmission over the RIS, to provide a sub-optimal solution with marginal performance degradation. Note that, unlike the partitioning schemes adopted in [95] and [96], to obtain a scalable optimization framework for the phase-shift adjustment of large RISs, we partition the RIS so that each sub-surface works as a modulator and beamformer simultaneously. In this way, each sub-surface sends an independent data stream to the user assigned to it independently from the other sub-surfaces.

- We derive the exact and asymptotic outage probability expressions for users in C_2. Accordingly, under the uniform partitioning scenario, we obtain the required number of RIS elements that need to be allocated for each user in C_2 to obtain a given outage probability value for all users.

- With comprehensive computer simulations, we compare our proposed system with four different benchmark schemes and show the superiority of our proposed system in terms of the ergodic sum-rate, outage probability, and user fairness.

3.4 System Model

This section introduces systems settings, users' clustering approach, and transmission mechanism for the proposed RIS partitioning based NOMA system.

Consider a downlink NOMA system where single-antenna users are served by a single-antenna BS and an RIS of $N = N_H N_V$ elements, where N_H and N_V denote the number of elements per row and per column, respectively. Note that the RIS is deployed in the direct line-of-sight (LoS) of the BS to compensate for the high path loss associated with the RIS. However, deploying the RIS in LoS with the BS makes the use of multiple antennas at the BS inefficient and justifies our use of a single antenna due to the following reasons. First, a direct LoS between the RIS and BS leads to a rank-one BS-RIS channel, where no multiplexing gain can be achieved by using multiple transmit antennas. Furthermore, under such conditions, it has been shown that the array gain vanishes as the number of users increases, irrespective of the number of transmit antennas and RIS size, and the number of users that can be efficiently served is one [97].

The users are assumed to be grouped into two clusters, C_1 with M_1 users and C_2 with M_2 users, as shown in Fig. 3.1. Note that C_1 and C_2 are the main clusters that identify the users who are out of the FoV of the RIS and served by the BS, and the ones who are in the FoV of the RIS and served by the RIS, respectively. Therefore, it is possible to use a second level of clustering inside these two main clusters [98], however, the investigation of such a scenario is out of the scope of this study.

The RIS is deployed close, yet in the far-field, to the BS in order to exploit the pure line-of-sight (LoS) channels and to make the use of a backhaul link from the BS to the RIS practical. This simplifies the system analysis, where for the near-field assumption we need to consider the distances of the individual RIS elements from the BS and thus, the effective BS antenna area and the polarization mismatch associated with each RIS element [99].

Furthermore, denoting the m^{th} user in C_2 by $\mathrm{U}_{m,2}$, perfect channel state infor-

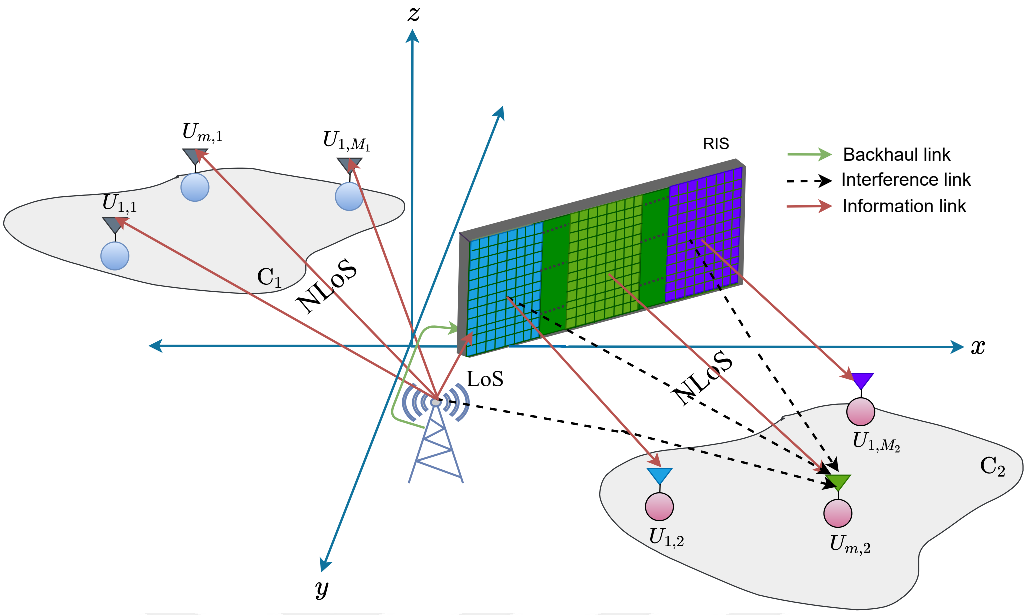

Figure 3.1: RIS partitioning based NOMA system.

mation (CSI) of the BS-RIS-$U_{m,2}$ link for all users in C_2 and the channel gains of all users in C_1 need to be available at the BS side, under the quasi-static flat-fading channels assumption. Although the fact that the perfect CSI assumption is practically challenging, nevertheless, it is adopted by the vast majority of the RIS-assisted NOMA works in the literature [97], [100], [101]. Therefore, the CSI is assumed to be obtained by using one of the proposed methods in the literature [102], [103], and thus, the performance results provided in this study can serve as an upper bound to the ones achievable in practical implementation.

Finally, instead of using a single SC message that combines all users' symbols, the C_1 and C_2 users' symbols are simultaneously transmitted over the BS direct link and the RIS reflection link, respectively, as follows.

3.4.1 The Transmission of C_1 Users' Symbols

This subsection explains the transmission mechanism for C_1 users' symbols, as follows. Let T_c denotes the duration of the channel coherence block, wherein all channels remain constant, while all channel coefficients are independent and identically distributed (i.i.d.) over different coherence blocks. Within T_c, the BS transmits x, which is the superposed signal of all symbols to be transmitted to M_1 users in C_1. As in conventional PD-NOMA, x is constructed as follows:

$$x = \sum_{m=1}^{M_1} \sqrt{P\zeta_m} x_m, \tag{3.1}$$

where P is the transmit power, ζ_m and x_m are the power allocation factor and the symbol to be transmitted to user m in C_1 ($\mathrm{U}_{m,1}$), respectively, where $\sum_{m=1}^{M_1} \zeta_m = 1$. Note that x can be represented in the form $x = ue^{-j\theta_{M_1}}$, where $u = |x|$ is the amplitude and $\theta_{M_1} = \arg(x)$ is the angle. From (3.1), it is clear that u and θ_{M_1} are both RVs, where $\theta_{M_1} \in [0, 2\pi)$ and $u \in \mathbb{R}$. Without loss of generality, in order to simplify our derivations, u is assumed to be a constant value that is equal to unity, which can be achieved by the proper design of the constellations used to obtain x_1 and x_2 for C_1 users [104], [105]. For example, consider the simple case of two users in C_1, where $x_1 \in \{\frac{t}{\sqrt{2}}(1+1j), \frac{t}{\sqrt{2}}(-1-1j)\}$ and $x_2 \in \{\frac{t}{\sqrt{2}}(1-1j), \frac{t}{\sqrt{2}}(-1+1j)\}$, then for any random values of ζ_1 and ζ_2 we obtain $u = |t|$, where $t \in \mathbb{R}$.

The signal received by each user m in C_1 is given by

$$\tilde{y}_m = \tilde{v}_m x + \tilde{z}_m, \tag{3.2}$$

where $\tilde{v}_m$ is the BS-$\mathrm{U}_{m,1}$ channel coefficient and $\tilde{z}_m$ is the additive white Gaussian noise (AWGN) sample at $\mathrm{U}_{m,1}$.

From (3.2), it can be noted that there is no interference from C_2 users' symbols received by C_1 users, due to the location of C_1 being behind the RIS. Although C_1 users still need to use SIC to recover their own signals, the SIC is performed with significantly less number of iterations due to the absence of C_2 users' interference. This simplifies the detection process and effectively reduces the error propagation associated with the SIC technique. In this way, the system performance for the M_1 users in C_1 follows the one of the conventional PD-NOMA, therefore, its analysis is omitted in this study and we focus on the system performance of C_2. Nevertheless, we still perform the numerical simulations in Section 3.10 for the users in C_1 along with C_2 users to show that the proposed system enhances the performance of both C_1 and C_2 users compared to the benchmark systems.

3.4.2 The Transmission of C_2 Users' Symbols

In this subsection, we introduce the novel transmission mechanism for C_2 users' symbols, as follows. Instead of using the SC technique to send the symbols of C_2 users in a single message from the BS, the symbol of each user m is sent over the RIS reflection link independent from the symbols belong to the other users. Therefore, the RIS is partitioned into M_2 sub-surfaces, where each sub-surface i has N_i elements and is allocated to serve a specific user m in C_2, for $i = m$, where $m = 1, 2, ...M_2$. Specifically, each sub-surface $i = m$ remodulates the same impinging signal x to reflect the $\mathrm{U}_{m,2}$ symbol over the RIS-$\mathrm{U}_{m,2}$ reflection link. Thus, by considering only a single reflection from the RIS elements [106] and within the same T_c, the signal received by each user m in C_2 can be obtained as follows:

$$y_m = \left[\mathbf{g}_{m,m}^T \boldsymbol{\Theta}_m \mathbf{h}_m + \sum\nolimits_{\substack{i=1 \\ i \neq m}}^{M_2 - 1} \mathbf{g}_{i,m}^T \boldsymbol{\Theta}_i \mathbf{h}_i + v_m\right] x + z_m, \tag{3.3}$$

where $z_m \sim \mathcal{CN}(0, \sigma^2)$ is the AWGN sample at $\mathrm{U}_{m,2}$, v_m is the BS-$\mathrm{U}_{m,2}$ channel coefficient, $v_m \sim \mathcal{CN}(0, L_m^{\mathrm{BS}})$, under Rayleigh fading assumption [97], [107], where L_m^{BS} denotes the BS-$\mathrm{U}_{m,2}$ path gain. Assuming pure LoS links [107], $\mathbf{h}_i \in \mathbb{C}^{N_i \times 1}$ is the BS-(i^{th} sub-surface) LoS channel vector with $[\mathbf{h}_i]_n = \sqrt{L^{\mathrm{RISh}}} e^{-j\psi^{(n)}}$, where L^{RISh} denote the path gain, $\psi^{(n)} = \pi(n-1)\sin\psi_A \sin\psi_E$, where ψ_E and ψ_A denote the LoS elevation and azimuth angles of arrival (AoA)s at the RIS, respectively [97]. Since the RIS is deployed in the far-field of the BS, the path gain experienced by each element is assumed to be the same, where the spacing between the elements is small compared to the BS-RIS distance. $\mathbf{g}_{i,m} \in \mathbb{C}^{N_i \times 1}$ is the RIS (i^{th} sub-surface)-$\mathrm{U}_{m,2}$ channel vector, $[\mathbf{g}_{i,m}]_n = \sqrt{L_m^{\mathrm{RISg}}} g_{i,m}^{(n)}$, where $g_{i,m}^{(n)}$ and L_m^{RISg} are the RIS (i^{th} sub-surface n^{th} element)-$\mathrm{U}_{m,2}$ small-scale fading coefficient and path gain, respectively. $g_{i,m}^{(n)} = \beta_{i,m}^{(n)} e^{-j\phi_{i,m}^{(n)}}$, where $\beta_{i,m}^{(n)}$ and $\phi_{i,m}^{(n)}$ denote the channel amplitude and phase, respectively. Thus, the overall RIS-$\mathrm{U}_{m,2}$ channel vector can be given as $\mathbf{g}_m = [\mathbf{g}_{1,m} \ ... \ \mathbf{g}_{i,m} \ ... \ \mathbf{g}_{M_2,m}]^T$, $\mathbf{g}_m \in \mathcal{CN}(\mathbf{0}_N, \mathbf{R}_{\mathrm{RIS}})$, where $\mathbf{R}_{\mathrm{RIS}} \in \mathbb{C}^{N \times N}$ is the RIS spatial correlation matrix. $\boldsymbol{\Theta}_i \in \mathbb{C}^{N_i \times N_i}$ is the matrix of reflection coefficients for the i^{th} sub-surface of the RIS, $[\boldsymbol{\Theta}_i]_n = \eta_i^{(n)} e^{j\Phi_i^{(n)}}$, where $\Phi_i^{(n)} \in [0, 2\pi)$ and $\eta_i^{(n)} = 1, \forall i, n,$

assuming full reflection[1]. In what follows, we describe the process of remodulating the impinging signal x at the RIS sub-surfaces to reflect the symbols of the C_2 users.

By properly and independently adjusting its phase shifts, each sub-surface $i = m$ performs two roles, namely, maximizing the channel gain by making the BS-RIS-$U_{m,2}$ channel phases equal to zero (passive beamforming), and remodulating the impinging signal x to reflect the symbol to be transmitted to $U_{m,2}$. Note that since the transmission of the RIS to C_2 depends on the BS transmission to C_1, the symbol rate is the same for all users in both clusters. To serve user m in C_2, the phases of the $i = m$ sub-surface are adjusted such that the phase of each element is given as

$$\Phi_m^{(n)} = \phi_{m,m}^{(n)} + \psi^{(n)} + \theta_m + \theta_{M_1}, n = 1, ..., N_m, \tag{3.4}$$

where θ_m is the phase shift keying (PSK) symbol to be transmitted to user m in C_2, furthermore, $\Phi_m^{(n)}$ is assumed to be calculated at the BS and sent to the RIS controller over a backhaul link. By considering the close distance and the LoS link between the BS and the RIS, a wired/out-band wireless backhaul link can be used without affecting the useful bandwidth used in (3.1) [109], [110]. In this way, the BS and RIS perform a joint transmission synchronized by the backhaul link as in coordinated multi-point transmission [111], where the achievable capacity of the backhaul link is assumed to be much higher than the one of the RIS-C_2 link.

The PSK modulation scheme is adopted for the users in C_2 due to the phase-dependent amplitude variation associated with the RIS reflection coefficient, where it is difficult to realize modulation schemes with a non-constant envelope [108].

According to the RIS phase adjustment in (3.4), (3.3) can be re-expressed as

$$\begin{aligned} y_m = &\sqrt{L_m^{\mathrm{RIS}}} \left[e^{j\theta_m} \sum_{n=1}^{N_m} \beta_{m,m}^{(n)} + \sum\nolimits_{\substack{i=1 \\ i \neq m}}^{M_2-1} \left[\sum_{n=1}^{N_i} \beta_{i,m}^{(n)} e^{j\bar{\Phi}_i^{(n)}} \right] \right] \\ &+ e^{j\theta_{M_1}} v_m + z_m, \end{aligned} \tag{3.5}$$

---

[1]Note that, practically, there are phase-dependent amplitude variations associated with the reflection coefficient of each RIS element [108]. However, we assume a constant reflection amplitude for the mathematical analysis simplification, as this assumption has no effect on the proposed system design.

where $L_m^{\text{RIS}} = L_m^{\text{RISh}} L_m^{\text{RISg}}$,$\bar{\Phi}_i^{(n)} = -\phi_{i,m}^{(n)} + \Phi_i^{(n)}$, $\Phi_i^{(n)}$ corresponds to the phase adjustment of the other sub-surface i for $i \in \{1, ..., M_2\} \setminus \{m\}$, and it is given by

$$\Phi_i^{(n)} = \phi_{i,i}^{(n)} + \psi^{(n)} + \theta_i + \theta_{M_1}, n = 1, ..., N_i. \tag{3.6}$$

The first three terms in (3.5) represent the amplitudes of the constructive combining, the intra-cluster, and inter-clusters interference, respectively. Furthermore, thanks to the remodulation process at the RIS, it can be noted that there is no interference from C_1 users' symbols received by C_2 users over the RIS link.

In order to detect its PSK symbol, each user m in C_2 is assumed to perform maximum likelihood (ML) detection in the presence of the interference coming from the other sub-surfaces ($i \neq m$) and the one comes from the BS, which are irremovable [112] and considered as noise. In this way, for the detection process, user m in C_2 needs to know the overall sum of the channel gains of the m^{th} sub-surface only. This, in turn, significantly reduces the training overhead and limits the spectrum efficiency degradation associated with it [37], [38]. Furthermore, by properly choosing the RIS size [113], each user m in C_2 relies on the amplification gain provided by its own sub-surface ($i = m$) to overcome the irremovable interference. Thus, the SINR for user m in C_2 to decoded its own message is given by

$$\text{SINR}_m = \frac{A_m}{I_m + \frac{1}{\rho}}, \tag{3.7}$$

where $\rho = \frac{P}{\sigma^2}$ denotes the transmit SNR, A_m and I_m denote the signal and total interference powers, respectively, and they are, from (3.5), given as

$$A_m = \left| \sqrt{L_m^{\text{RIS}}} \sum_{n=1}^{N_m} \beta_{m,m}^{(n)} \right|^2, \tag{3.8}$$

$$I_m = \left| I_{\text{RIS}} + v_m \right|^2, \tag{3.9}$$

and I_{RIS} is given by

$$I_{\text{RIS}} = \sqrt{L_m^{\text{RIS}}} \sum_{\substack{i=1 \\ i \neq m}}^{M_2 - 1} \left[\sum_{n=1}^{N_i} \beta_{i,m}^{(n)} e^{j \bar{\Phi}_i^{(n)}} \right]. \tag{3.10}$$

From (3.7), the instantaneous transmission rate for $\mathrm{U}_{m,2}$ and the sum-rate for the all M_2 users can be calculated, respectively, as follows:

$$R_m = \log_2(1 + \mathrm{SINR}_m), \tag{3.11}$$

$$R = \sum_{m=1}^{M_2} R_m = \sum_{m=1}^{M_2} \log_2(1 + \mathrm{SINR}_m). \tag{3.12}$$

In the following section we derive the outage probability for a given user m in C_2.

Remark 1. *It can be verified from* (3.2) *and* (3.5) *that the number of users in C_1 and C_2 has no effect on the performance of the users belong to the other cluster, where the BS and RIS independently serve C_1 and C_2, respectively. Furthermore, although the fact that the users in C_2 still receive interference from the users in C_1 through the BS-U_m link in addition to the sub-surfaces mutual interference, increasing the RIS size can effectively mitigate the impact of the overall interference on the users in C_2 [113]. Furthermore, the sum-rate gain provided by the proposed system does not require that the users in C_2 have different channel gains as is the case in conventional NOMA, which adds more flexibility to the system design. Finally, for the detection process, user m in C_2 needs to know the overall sum of the channel gains of the m^{th} sub-surface only, which effectively reduces the training overhead in the channel estimation of the RIS channels.*

3.5 Mathematical Analysis

This section provides the mathematical analysis of the proposed RIS partitioning based NOMA system in terms of the outage probability.

3.5.1 Outage Probability: Closed-form

In this subsection, we obtain the closed-form expression for the outage probability, as follows.

Denoting the data rate requirement for $\mathrm{U}_{m,2}$ as γ_m^*, the outage probability for $\mathrm{U}_{m,2}$ is given as [62]

$$P_m^{out} = P(R_m < \gamma_m^*) \tag{3.13}$$

By substituting (3.11) in (3.13), we obtain

$$\begin{aligned} P_m^{out} &= P\left(\log_2\left(1+\mathrm{SINR}_m\right) < \gamma_m^*\right), \\ &= P\left(\mathrm{SINR}_m < 2^{\gamma_m^*} - 1\right) \end{aligned} \tag{3.14}$$

Due to the spatial correlation between the RIS-U_m channels, and thus, the correlation through $\mathbf{\Theta}_i$, it is challenging to derive the distribution of SINR_m[114], [115][2]. Furthermore, by considering an inter-element separation of $\lambda/2$, where λ is the wavelength of the operating frequency, the spatially correlated channels become close to the i.i.d. case [116]. This approximation is verified through Monte Carlo simulations in Section 3.10, where the ergodic-rates and outage probability curves with/without correlation are shown to be close to each other. In what follows the outage probability expression is given under the i.i.d Rayleigh fading channels assumption and thus, the obtained results can serve as an upper bound for the performance of the cases where the inter-element separation is less than $\lambda/2$ and the RIS channels are highly spatially-correlated.

Proposition 1. *The closed-form outage probability expression of user m in C_2, assuming uncorrelated channels $\mathbf{R}_{RIS} = \mathbf{I}_N$, is given by*

$$\begin{aligned} P_m^{out} = 1 - \mathcal{Q}_{\frac{1}{2}}\left(\frac{\mu_1}{s_1}, \sqrt{\frac{y}{s_1^2}}\right) + \left(\frac{s_2^2}{s_1^2+s_2^2}\right)^{\frac{1}{2}} exp\left(\frac{y}{2s_2^2}\right) \\ \times\, exp\left(-\frac{\mu_1^2}{2(s_1^2+s_2^2)}\right)\mathcal{Q}_{\frac{1}{2}}\left(\frac{\mu_1}{s_1}\sqrt{\frac{s_2^2}{s_1^2+s_2^2}}, \sqrt{\frac{y(s_1^2+s_2^2)}{s_1^2 s_2^2}}\right), \end{aligned} \tag{3.15}$$

where $\mathcal{Q}_k$ is the k^{th} order generalized Marcum Q-function [117], $y = \frac{2^{\gamma_m^*}-1}{\rho}$, $\mu_1 = \sqrt{L_m^{RIS}}N_m\frac{\sqrt{\pi}}{2}$, $s_1^2 = L_m^{RIS}N_m\frac{4-\pi}{4}$, and $s_2^2 = 0.5(2^{\gamma_m^*}-1)(L_m^{RIS}(N-N_m)+L_m^{BS})$.

[2]In [114] and [115] a deterministic equivalent and moment matching approaches have been considered, respectively, to obtain the outage probability under spatially correlated channels. However, these works do not consider the intelligent phase shift adjustment.

Proof: From (3.14), we obtain

$$\begin{aligned} P_{\text{out}} &= \left(\frac{A_m}{I_m + \frac{1}{\rho}} < 2^{\gamma_m^*} - 1 \right) \\ &= P\left(Y < y\right) \end{aligned} \tag{3.16}$$

where $Y = A_m - \bar{I}_m$, $y = \frac{2^{\gamma_m^*}-1}{\rho}$, and $\bar{I}_m$ is given by

$$\bar{I}_m = (2^{\gamma_m^*} - 1)I_m = |\sqrt{(2^{\gamma_m^*} - 1)}(I_{\text{RIS}} + v_m)|^2. \tag{3.17}$$

From (3.16), we note that the outage probability is equivalent to the cumulative distribution function (CDF) of Y. In order to find the CDF of Y, we first find the distribution of the RVs A_m and $\bar{I}_m$, as follows. By considering (3.8), we note that $\beta_{m,m}^{(n)}$ is a Rayleigh distributed RV with a mean $\text{E}[\beta_{m,m}^{(n)}] = \sqrt{\pi}/2$, and a variance $\text{VAR}[\beta_{m,m}^{(n)}] = (4 - \pi)/4$. According to the central limit theorem (CLT), for $N_m >> 1$, the term inside the squared parenthesis is a Gaussian RV, $\sim \mathcal{N}(\sqrt{L_m^{\text{RIS}}} N_m \frac{\sqrt{\pi}}{2}$, $L_m^{\text{RIS}} N_m \frac{4-\pi}{4})$. Thus, A_m is a non-central chi-square (χ^2) RV with one degree of freedom. Likewise, by considering (3.10), for $N - N_m >> 1$, I_{RIS} is a Gaussian RV, $I_{\text{RIS}} \sim \mathcal{CN}(0, L_m^{\text{RIS}}(N - N_m))$. Consequently, the constant-scaled sum of the two independent Gaussian RVs in (3.17), $\sqrt{(2^{\gamma_m^*} - 1)}(I_{\text{RIS}} + v_m)$, is a Gaussian RV, $\sim \mathcal{CN}(0, (2^{\gamma_m^*} - 1)(L_m^{\text{RIS}}(N - N_m) + L_m^{\text{BS}})$. Thus, $\bar{I}_m$ is a central χ^2 RV with two degrees of freedom, and consequently, Y is the difference of a non-central and central independent χ^2 RVs, where its CDF is given in (3.15) [118]. This completes the proof of Proposition 1. ■

Proposition 1 expresses the outage probability as a function of the transmit SNR and the ratio of $\sqrt{L_m^{\text{RIS}}} N_m$ to $\sqrt{L_m^{\text{RIS}}}(N - N_m)$ plus $\sqrt{L_m^{\text{BS}}}$, where these parameters reflect the amplification gain, the sub-surfaces interference, and the BS interference powers, respectively. To get more insight, we give the following corollaries that follow from Proposition 1.

3.5.2 Outage Probability: Asymptotic analysis

This subsection provides useful engineering insight into the proposed system performance from the asymptotic behavior perspective. In what follows, we introduce two important corollaries based on Proposition 1.

Corollary 1. *The Asymptotic behaviour of the outage probability can be obtained, for $\rho \to \infty$ or $y \to 0$, as*

$$P_m^{\infty} = \left(\frac{s_2^2}{s_1^2+s_2^2}\right)^{\frac{1}{2}} exp\left(-\frac{\mu_1^2}{2(s_1^2+s_2^2)}\right), \tag{3.18}$$

Proof: The proof follows directly from Proposition 1 by letting $y = 0$, where $Q_{\frac{1}{2}}(a, 0) = 1, \forall a$ [117]. ■

From Corollary 1, at high SNR, the outage probability performance improves exponentially with the ratio of the amplification gain to the overall interference associated with the RIS sub-surfaces and the BS links.

Corollary 2. *Consider the case where the RIS is uniformly partitioned between $M_2 + 1$ users in C_2, where $N_m = N_i = N/(M_2 + 1), \forall i, m$, $\sqrt{L_m^{RIS}} M_2 N_m >> L_m^{BS}$, and $\rho \to \infty$, then, the outage probability is given by*

$$P_m^{\infty} = \left(\frac{2M_2}{2M_2+4-\pi}\right)^{\frac{1}{2}} exp\left(-\frac{\pi N_m}{2(2M_2+4-\pi)}\right), \tag{3.19}$$

for $M_2 >> 1$, (3.19) can be simplified to

$$P_m^{\infty} \approx exp\left(-\frac{\pi N_m}{4M_2}\right). \tag{3.20}$$

Thus, for a given P_m^{∞}, the required N_m for each user in C_2 can be obtained as

$$N_m \approx \lceil -\frac{4M_2}{\pi} \ln(P_m^{\infty}) \rceil. \tag{3.21}$$

Proof: The proof follows directly from Corollary 1 by letting $s_2^2 = 0.5(\sqrt{L_m^{\mathrm{RIS}}}(N - N_m) + L_m^{BS}) \approx 0.5\sqrt{L_m^{\mathrm{RIS}}} M_2 N_m$, where, without loss of generality, $\gamma_m^* = 1$ bit per channel use (bpcu). ■

Corollary 2 shows the outage probability performance at high SNR by considering only the mutual sub-surfaces interference impact. The BS link interference impact can be ignored by assuming large RIS size N and/or $L_m^{\mathrm{BS}} >> L_m^{\mathrm{RIS}}$. It can clearly be seen from (3.20) that the outage probability performance improves exponentially in proportion to the ratio of the sub-surface size allocated to user m to the number of the other served users (M_2). Although increasing N_m for each user, and hence increasing N, increases the number of the interferer signals received by each user, the outage probability still decreases exponentially for all users. This can be explained by the fact that the interference is of the incoherent type where the interferer signals are combined constructively/destructively in a random way.

Remark 2. *Interestingly, the impact of the mutual sub-surfaces' interference between users can be effectively mitigated by increasing the overall RIS size for a given M_2 number of users in C_2. This is in contrast to the case of using SC, where increasing the transmit power has no effect on the mutual interference between the superposed symbols.*

3.5.3 Outage Probability: Rician fading channels

The outage probability in (3.15) can be generalized to the case where all the links, BS-RIS, BS-U$_m$, and RIS-U$_m$ are Rician fading channels. In this case, by considering the same derivation steps provided in the proof of Proposition 1, we obtain Y to be the difference of two independent and non-central chi-square random variables, which has the following characteristic function (CF)[119]

$$\Psi_Y(w) = \frac{\exp\left(\frac{jw\mu_A^2}{1-2jw\sigma_A^2}\right)\exp\left(\frac{-jw\mu_I^2}{1+2jw\sigma_I^2}\right)}{(1-2jw\sigma_A^2)^{0.5}(1+2jw\sigma_I^2)}, \tag{3.22}$$

where (μ_A,σ_A) and (μ_I, σ_I) are the mean and standard deviation pairs of A_m and $\bar{I}_m$, respectively. Thus, by using Gil-Pelaez's inversion formula, P_m^{out} can be obtained as follows [120]

$$P(Y < y) = \frac{1}{2} - \int_0^\infty \frac{\Im\{e^{-jwy}\Psi_Y(w)\}}{w\pi}dw, \tag{3.23}$$

where the integration needs to be evaluated numerically with a suitable upper limit to avoid errors associated with the numerical calculations.

3.6 RIS Partitioning Approach

In this section, we provide the approach we used to partition the RIS among C_2 users in order to maximize user fairness. Since each sub-surface of the RIS is allocated to serve a different user, each user m in C_2 receives a huge number of interferer signals from the other sub-surfaces allocated to the other users. Therefore, a proper number of reflecting elements (N_m) needs to be allocated for each user in order to guarantee maximum user fairness among them. In the following two subsections, we first formulate the number of RIS elements allocation problem and then introduce our proposed solution by dividing the main problem into three subproblems.

3.6.1 Problem Formulation

In order to achieve maximum user fairness, we formulate an optimization problem where the Jain's fairness index [121] is the objective function to be maximized and $N_1, ..., N_m, ..., N_{M_2}$ are the decision variables to be determined, as follows:

$$\text{(P1)}: \max_{N_1,...,N_m,...,N_{M_2}} \quad \frac{\left(\frac{1}{M_2}\sum_{m=1}^{M_2}\bar{R}_m\right)^2}{\frac{1}{M_2}\sum_{m=1}^{M_2}\bar{R}_m^2}, \tag{3.24a}$$

$$\text{s.t.} \quad \sum_{m=1}^{M_2} N_m = N,\ N_m \in \{1, ..., N-(M_2-1)\}, \forall m, \tag{3.24b}$$

where $\bar{R}_m = \mathbb{E}[R_m]$ is the ergodic rate of $U_{m,2}$, $\mathbb{E}[\cdot]$ is the statistical expectation operator over all the random channel realizations.

(P1) is NLIP problem with a non-convex feasible set represented by the constraint (3.24b) that has combinatorial growth as N increases. This makes (P1) a non-convex combinatorial optimization problem which is very challenging to solve if we consider the fact that a LIP is generally a non-deterministic polynomial-time (NP) hard problem [122]. IP optimization problems are usually solved by using branch-and-bound with the relaxation of the integrality constraint on the decision variables [123], which is, in this case, invalid for N_m, the number of RIS elements allocated to $U_{m,2}$. On the other side, considering the exhaustive search solution, the complexity lies in the explosively large size of the feasible set represented by the constraint (3.24b) which has $\binom{N-1}{M_2-1}$ feasible points. This implies that the required searching loops to scan all the feasible points are at a complexity level of $\mathcal{O}((N-1)^{\min(M_2-1,N-M_2)})$, or $\mathcal{O}((N-1)^{M_2-1})$ if we considered the fact that $N >> M_2$.

3.6.2 Proposed Solution

In order to shrink the size of the feasible set and thus, make the exhaustive search a practical method to solve (P1), we exploit the structure of the problem, specifically the nature of the transmission over the RIS, to bound the feasible set in (3.24b), as follows.

First, the number of RIS elements (N_m) allocated to any user m in C_2 cannot be randomly small, otherwise, the irremovable interference power from the other sub-surfaces overwhelms the amplification power from the m^{th} sub-surface. Motivated by the so-called interference temperature [124], a signal-to-interference power constraint (SIPC)[112] needs to be considered to protect each user $\mathrm{U}_{m,2}$ from the interference belong to the other users. Based on the SIPC threshold, there is a minimum number of RIS elements N_{thr} that can be allocated for any user m in C_2 to protect it from the interference power associated with the remaining part of the RIS $(N - N_{thr})$. This means that the feasible set in (3.24b) needs to have N_{thr} (rather than unity) as the minimum element in the set, which in turn shrinks the size of the feasible set to $\binom{N-N_{thr}-1}{M_2-1}$ feasible points. Second, instead of considering a step size of one between any two successive elements in the feasible set of (3.24b), an adjustable step size b is considered, which reduces the feasible set further to $\binom{\frac{N-N_{thr}}{b}-1}{M_2-1}$ feasible points, where $\frac{N-N_{thr}}{b}$ needs to be an integer. Third, as in the power allocation of classical PD-NOMA, more RIS elements need to be allocated to the user with the weakest RIS-$\mathrm{U}_{m,2}$ channel gain. Hence, the users need to be ordered according to their distances from the RIS, where $\mathrm{U}_{m,2}$ is the m^{th} farthest user from the RIS and thus, the user with the m^{th} weakest RIS-$\mathrm{U}_{m,2}$ channel gain. By considering the previously mentioned three bounding modifications on the feasible set in (3.24b), (P1) can be reformulated to obtain the following new optimization problem:

$$(\text{P1.1}): \max_{N_1,\ldots,N_m,\ldots,N_{M_2}} \quad \frac{(\frac{1}{M_2}\sum_{m=1}^{M_2}\bar{R}_m)^2}{\frac{1}{M_2}\sum_{m=1}^{M_2}\bar{R}_m^2}, \tag{3.25a}$$

$$\text{s.t.} \sum_{m=1}^{M_2} N_m = N,\ N_m \in \mathcal{N},\ \forall m, \text{where } \mathcal{N} = \{N_{thr}, N_{thr}$$

$$+ 1b, N_{thr} + 2b, ..., N - N_{thr}(M_2 - 1)\}, \mathcal{N} \subset \mathbb{Z}^+, \tag{3.25b}$$

$$N_1 \geq N_2 ... \geq N_{M_2}. \tag{3.25c}$$

By considering (P1.1), it can be observed that the combinatorial growth of the feasible set of (P1) is significantly limited by the three modifications considered on the constraint (3.24b), which in turn effectively reduces the search space. In what follows, we formulate two new optimization problems to find the proper N_{thr} and b for (P1.1):

$$(\text{P1.1.1}): \min \quad N_{thr}, \tag{3.26a}$$

$$\text{s.t.} \ P(A_m|_{N_m=N_{thr}} \leq q\,|I_{\text{RIS}}|_{M_2=2,i\neq m}|^2) \leq \epsilon \tag{3.26b}$$

$$M_2 N_{thr} \leq N. \tag{3.26c}$$

Here, the motivation behind the constraint (3.26b) can be explained by the fact that from each user $\text{U}_{m,2}$ perspective, the RIS appears to be partitioned into two parts, the first part (with N_{thr} elements) that amplifies the signal of $\text{U}_{m,2}$, and the second part (with $N - N_{thr}$ elements) where the interference associated with the other users comes from. Thus, regardless of the noise and the BS-$\text{U}_{m,2}$ interference, the constraint (3.26b) ensures that for any user $\text{U}_{m,2}$ with N_{thr} RIS elements allocation, there is a low probability $\epsilon << 1$ that the interference power associated with the $N-N_{thr}$ part can be higher (by a factor of q) than the amplification power associated with the N_{thr} part. The two parameters ϵ and q need to be adjusted according to the size of the RIS and the number of users in C_2. Furthermore, the probability given in (3.26b) can be obtained from (3.18) by letting $L_m^{\text{BS}} = 0$ and $\gamma_m^* = 1$, as it is illustrated in Algorithm 4. The constraint (3.26c) ensures that for a given N, N_{thr} needs to have a small enough value such that all the M_2 users can have (at least) the same allocation of N_{thr} RIS elements, otherwise, N need to be increased. In what follows we formulate an optimization problem to find the proper step size b for (P1.1).

$$
\begin{aligned}
\text{(P1.1.2)}: \quad & \max \quad b, && \text{(3.27a)}\\
& \text{s.t.} \quad \bar{R}_m^{(N_{thr}+b)} - \bar{R}_m^{(N_{thr})} \leq \bar{r}, && \text{(3.27b)}\\
& \qquad\;\; b \leq N - M_2 N_{thr}, && \text{(3.27c)}
\end{aligned}
$$

where $\bar{R}_m^{(N_{thr}+b)}$ and $\bar{R}_m^{(N_{thr})}$ are obtained from (3.11) with simple modifications, as illustrated in Algorithm 5.

After determining N_{thr} in (P1.1.1), in (P1.1.2) we aim to find the maximum increment b that can be added to N_{thr} to get, accordingly, an ergodic rate increment upper-bounded by $\bar{r}$ b/s/Hz. Thus, b corresponds to the step size of the exhaustive search that ensures a maximum of $\bar{r}$ ergodic-rate resolution. In (3.27b), due to the fact that the users in C_2 experience different SNR values and different BS-$\text{U}_{m,2}$ interference power levels, the ergodic rate difference is calculated in the absence of the noise and the BS-$\text{U}_{m,2}$ interference effects. In this way, b determined from (P1.1.2) ensures that in the presence of noise and BS-$\text{U}_{m,2}$ interference, the search resolution to solve (P1.1) does not exceed $\bar{r}$, for all users. Hence, $\bar{r}$ needs to be adjusted according to the RIS size and number of users in C_2. In what follows, we introduce the search algorithms to solve (P1.1.1), (P1.1.2), and consequently, solve (P1.1).

3.7 RIS Partitioning Algorithms

In this section, we introduce the solution algorithms for (P1.1.1), (P1.1.2), and consequently, (P1.1).

Note that Algorithm 6 is the main algorithm to solve the main problem (P1.1) and obtain the RIS sub-optimum partition $N_1, N_2, ..., N_{M_2}$. Nevertheless, Algorithms 4, 5, and 6 need to be applied in order, where Algorithm 4 is used first to solve the subproblem (P1.1.1) and obtain N_{thr}, which is the input of Algorithm 5. In the same way, Algorithm 5 is used to solve the subproblem (P1.1.2) and obtain b, then, N_{thr} and b are used as inputs to Algorithm 6, which can be summarized as follows.

Algorithm 4 Solves (P1.1.1) to find N_{thr}.

Require: L_m^{RIS}, M_2, N, q, ϵ.

Initialize $N_{thr} = 1, m = 1, i = 2$.

repeat

$\mu_m = \sqrt{L_m^{\mathrm{RIS}}} N_{thr} \frac{\sqrt{\pi}}{2}$, $s_m^2 = L_m^{\mathrm{RIS}} N_{thr} \frac{4-\pi}{4}$, $s_i^2 = 0.5 L_m^{\mathrm{RIS}} q (N - N_{thr})$.

The probability in (3.26b) can be obtained from (3.18):
$P_m^{\infty} = \left(\frac{s_i^2}{s_m^2 + s_i^2} \right)^{\frac{1}{2}} \exp\left(-\frac{\mu_m^2}{2(s_m^2 + s_i^2)} \right)$.

$N_{thr} = N_{thr} + 1$.

while $P_m^{\infty} <= \epsilon$ and $M_2 N_{thr} \leq N$.

return $N_{thr} = N_{thr} - 1$.

Algorithm 5 Solves (P1.1.2) to find the step size b.

Require: N, N_{thr}, $\bar{r}$, $\beta_{m,m}^{(n)}$, $\beta_{i,m}^{(n)}$, $\bar{\Phi}_i^n$, $\forall n$, and for any m and i such that $i \neq m$.

Initialize $b = 1$.

$\bar{R}_m^{(N_{thr})} = \mathbb{E}\left[\log_2 \left(1 + \frac{A_m|_{N_m = N_{thr}}}{|I_{\mathrm{RIS}}|_{N_i = N - N_{thr}}|^2} \right) \right]$. Perform the expectation over 10^4 random channel realizations [125].

repeat

$\bar{R}_m^{(N_{thr}+b)} = \mathbb{E}\left[\log_2 \left(1 + \frac{A_m|_{N_m = N_{thr}+b}}{|I_{\mathrm{RIS}}|_{N_i = N - N_{thr} - b}|^2} \right) \right]$.

$\bar{r}_{diff} = \bar{R}_m^{(N_{thr}+b)} - \bar{R}_m^{(N_{thr})}$.

$b = b + 1$.

while $\bar{r}_{diff} \leq \bar{r}$ and $b \leq N - M_2 N_{thr}$.

return $b = b - 1$.

Algorithm 6 RIS partitioning algorithm to solve (P1.1)

Require: b, N_{thr}, N, M_2, L_m^{RIS}, ρ, v_m, $\beta_{i,m}^{(n)}$, $\phi_{i,m}^{(n)}$, $\bar{\Phi}_i^n$, $\forall i, n, m$.

Construct the set $\mathcal{N}$ in the constraint (3.25b).

According to the constraint (3.25b), construct the set $\mathcal{S}$ by finding all the solutions of $\sum_{m=1}^{M_2} N_m = N$, and excluding the ones that do not satisfy (3.25c). Thus, $\mathcal{S} = \{\tilde{\mathcal{S}}^{(1)}, ..., \tilde{\mathcal{S}}^{(s)}, ...\tilde{\mathcal{S}}^{(|\mathcal{S}|)}\}$, where $\tilde{\mathcal{S}}^{(s)} = \{N_1^{(s)}, ..., N_m^{(s)}, ...N_M^{(s)}\}$ corresponds to the RIS partition s, $\tilde{\mathcal{S}}^{(s)} \subset \mathcal{N}$, $\forall s$.

Construct the new sets $\mathcal{R}^{(1)}, ..., \mathcal{R}^{(s)}, ..., \mathcal{R}^{(|\mathcal{S}|)}$, where $\mathcal{R}^{(s)} = \{\emptyset\}$, $\forall s$.

for $s = 1 : |\mathcal{S}|$ **do**

  for $m = 1 : M_2$ **do**

    $R_m = \mathbb{E}\left[\log_2\left(1 + \frac{A_m}{I_m + \frac{1}{\rho}}\right)\right]$, where $N_i,\ N_m \in \tilde{\mathcal{S}}^{(s)}$, $\forall i,\ m$. Perform the expectation over 10^4 random channel realizations.

    $\mathcal{R}^{(s)} = \mathcal{R}^{(s)} \cup \{R_m\}$.

  end for

end for

Construct a new set $\mathcal{J} = \{\emptyset\}$.

for $s = 1 : |\mathcal{S}|$ **do**

  $J = \frac{(\frac{1}{M_2}\sum_{m=1}^{M_2} R_m)^2}{\frac{1}{M_2}\sum_{m=1}^{M_2} R_m^2}$, where $R_m \in \mathcal{R}^{(s)}, \forall m$.

  $\mathcal{J} = \mathcal{J} \cup \{J\}$.

end for

$j^* = \underset{j=1:|\mathcal{J}|}{\arg\max}\ \mathcal{J}^{(j)}$

return $\tilde{\mathcal{S}}^{(j^*)} = \{N_1^*, N_2^*, ..., N_m^*, ..., N_{M_2}^*\}$.

First, the set $\mathcal{S}$ is constructed according to the constraints (3.25b) and (3.25c). The elements of $\mathcal{S}$ are the possible partitions the RIS can be partitioned into. When $b = 1$ is used in (3.25b), $\mathcal{S}$ contains all the possible partitions and the solution of the algorithm is a globally optimal solution, otherwise, for $b > 1$, the solution is a sub-optimal one. Second, for each partition s in $\mathcal{S}$, the ergodic transmission rate $\bar{R}_m$ for the all M_2 users are calculated and stored in the set $\mathcal{R}^{(s)}$. Third, for each partition s, Jain's index is calculated from $\mathcal{R}^{(s)}$ and stored in the set $\mathcal{J}$. Finally, the partition j^* associated with the maximum Jain's index is chosen as the optimum partition, and the set $\tilde{\mathcal{S}}^{(j^*)}$ contains the optimum number of RIS elements N_m^* needs to be allocated to each user m in C_2.

3.8 Complexity and Convergence Analysis

In this section, we provide the convergence and complexity analysis of the three proposed algorithms, as follows.

The convergence of the three algorithms is guaranteed as all algorithms have a predetermined finite number of iterations. Specifically, Algorithms 4 and 5 have $\bar{I}_1 = N/M_2$ and $\bar{I}_2 = N - M_2N_{thr}$ maximum number of iterations, respectively. Likewise, Algorithm 6 has a maximum upper bound number of iterations $\bar{I}_3 = 2\binom{\frac{N-N_{thr}}{b}-1}{M_2-1}$, which can be verified from the constraints (3.25b) and (3.25c) of (P1.1).

From the convergence analysis above, the computational complexity for Algorithm i, $i \in \{4,5,6\}$, can be given as $\mathcal{O}(\bar{C}_i\bar{I}_i)$, where $\bar{C}_i$ is the computational complexity of the functions inside the loops and $\bar{I}_i$ is the number of iterations for all loops, which is given above for each algorithm. By considering the required number of complex multiplications (CMs) as a metric, we obtain $N^2 + N$ as the number of CMs required to construct A_m and I_m/I_{RIS} in Algorithms 4 and 5, where we considered the vector-matrix multiplication form given in (3.3). Consequently, for Algorithm 5, we obtain $\bar{I}_2(N^2+N) = (N - M_2N_{thr})(N^2+N)$ required number of CMs, hence, a complexity level of $\mathcal{O}_2(N^3)$. Likewise, for Algorithm 6, we have $0.5\bar{I}_3(N^2+N) = \binom{\frac{N-N_{thr}}{b}-1}{M_2-1}(N^2+N)$, hence, a complexity level of $\mathcal{O}_2(N^2\binom{\frac{N-N_{thr}}{b}-1}{M_2-1})$, where we considered only the first loop that requires CMs. For Algorithm 4, which has no CMs, the complexity level associated with $\bar{C}_1$ depends on the type of the used algorithm.

Remark 3. *Note that the partitioning process (Algorithms 4, 5, and 6) needs to be updated only when the RIS size N, transmit power P, number of users M_2 in C_2, or the distances of users from the RIS/BS changes. This significantly reduces* *the computational complexity cost associated with performing these algorithms as the mentioned parameters slowly change with time. Furthermore, a minimum data rate requirement for all or individual users can be straightforwardly included in the algorithms. Particularly, such a constraint can be included in Algorithm 4 to replace the constraint* (3.26b).

3.9 Special Cases with Different Number of Users in Clusters

Here, in addition to the general case introduced in Section 3.4, we consider the system performance analysis for particular cases in order to shed some light on the performance of the proposed system under different settings, as follows.

3.9.1 All Users Are Located in C_2

In this scenario $M_1 = 0$, and the same transmission mechanism described in Section 3.4 is used here with the following single modification. Since there are no users in C_1, the BS is assumed to transmit $x = \sqrt{P}\bar{x}$, where $\bar{x}$ is a predetermined symbol. Thus, assuming v_m is known at the receiver side, the signal $v_m\bar{x}$ received by each user m in C_2 over the BS-$\mathrm{U}_{m,2}$ link can be removed readily. Furthermore, over the RIS-$\mathrm{U}_{m,2}$ link, each sub-surface $i = m$ of the RIS remodulates $\bar{x}$ to reflect the PSK symbol to be transmitted to $\mathrm{U}_{m,2}$, as described in Section 3.4. Without loss of generality, an unmodulated carrier signal can be sent from the BS and, in this case, the BS can be compensated by a single RF signal generator (SG), which simplifies the transmitter architecture. Furthermore, R_m and P_m^{out} can be obtained from (3.11) and (3.15), respectively, by letting $v_m = 0$ ($L_m^{\mathrm{BS}} = 0$). Likewise, for the asymptotic behaviour at high SNR, $P_{\mathrm{out}}^{\infty}$ can be directly obtained from (3.19) and (3.20) by considering the uniform partitioning of the RIS elements to guarantee maximum user fairness.

3.9.2 Each Cluster Has a Single User

In this scenario, $\mathrm{U}_{1,1}$ and $\mathrm{U}_{1,2}$ are the only users in C_1 and C_2, respectively. Therefore, the BS transmits $x = \sqrt{P}x_1$, and $\mathrm{U}_{1,1}$ experience the same performance in a SISO system. On the other side, the RIS (as a single unit) remodulates x and reflects the PSK symbol to be transmitted to $\mathrm{U}_{1,2}$, as described in Section 3.4. Since the whole surface is allocated for $\mathrm{U}_{1,2}$, R_1, P_m^{out}, and P_m^{∞} can be obtained from (3.11), (3.15), and (3.18), respectively, by omitting the sub-surfaces interference term $I_{\text{RIS}} = 0$ and letting $N_1 = N$.

3.10 Simulation Results

In this section, we provide computer simulation results for the proposed scheme against the following four benchmark schemes: the time division multiple access (TDMA) as an OMA scheme, where the BS serves, with full power P, each user in its time slot with/without the RIS. PD-NOMA scheme, where the SC message is constructed as in (3.1). Finally, the RIS-assisted SISO NOMA scheme proposed in [81], [82][3]. For TDMA and classical NOMA schemes, in order to achieve maximum user fairness, we optimize the time and power allocation, respectively, at the transmitter side using exhaustive search. In order to guarantee a fair comparison, we consider the maximum fairness between users as the common threshold for all schemes, while the comparison lies in the ergodic transmission rates and outage probability performance. In the following subsections, we first introduce the considered simulation parameters and system settings, then we provide simulation results for the proposed search algorithms, special cases introduced in Section 3.9, and the general case introduced in Section 3.4, respectively.

3.10.1 Simulation Parameters and System Settings

In this subsection, we describe the path loss models and other considered simulation parameters. For the BS-$\mathrm{U}_{m,c}$ link, where c denotes the cluster number, we obtain the path loss as $(L_{m,c}^{\text{BS}})^{-1} = C_0\,(d_{m,c}/D_0)^{\alpha}$ [106], where $C_0 = -30$ dB is the path gain at the reference distance $D_0 = 1$ m, $d_{m,c}$ is the BS-$\mathrm{U}_{m,c}$ distance, and $\alpha = -3.5$ is the

[3]This work does not consider the spatial correlation for the RIS channels in the obtained power allocation solution. Nevertheless, spatially correlated channels are used in our simulations of this benchmark scheme.

Table 3.1: Users' distances for different deployment scenarios.

Users' deployment	$d_{1,1}$, $r_{1,1}$	$d_{2,1}$, $r_{2,1}$	$d_{1,2}$, $r_{1,2}$	$d_{2,2}$, $r_{2,2}$
$M_1 = 0$, $M_2 = 2$	-	-	150, 146	100, 104
$M_1 = 1$, $M_2 = 1$	150, 146	-	100, 104	-
$M_1 = 2$, $M_2 = 2$	150, 154	100, 104	250, 254	200, 204

path gain exponent. For the BS-RIS-U$_{m,2}$ link, we consider that the RIS is located in the far-field with respect to the BS by ensuring that $r_s = \lceil \frac{N\lambda}{2} \rceil$ [19], thus, we obtain the path loss (with maximum gain RIS elements) as $(L_m^{\text{RIS}})^{-1} = \lambda^4/(256\pi^2 r_s^2 r_m^2)$ [11], where r_s and r_m are the BS-RIS (the center point) and the RIS (the center point)-U$_{m,2}$ distances, all in meters, respectively. Due to the small spacing distances between the RIS elements compared to r_s and r_m, we consider r_s and r_m for the path loss calculations, consequently, the path losses for all the RIS elements are considered the same. In Table 3.1, we give the users' distances from the BS and RIS, for different deployment scenarios, which are the used distances in our simulations, unless stated otherwise. The entries of the spatial correlation matrix are given as $[\mathbf{R}_{\text{RIS}}]_{n,\tilde{n}} = \text{sinc}\left(2\left\|\mathbf{u}_n - \mathbf{u}_{\tilde{n}}\right\|/\lambda\right),\ n, \tilde{n} = 1, ..., N$ [116], where λ is calculated for a 1.8 Ghz operating frequency, $\text{sinc}(a) = \sin(\pi a)/(\pi a)$ is the sinc function, $\mathbf{u}_n = [0,\ i(n)d_l, \tilde{i}(n)d_w\ ]^T$, where $i(n)$, $\tilde{i}(n)$, d_l, and d_w are the horizontal index, vertical index, length, and width of the element n, respectively, $i(n) = \text{mod}(n-1, N_H)$, $\tilde{i}(n) = \lfloor (n-1)/N_H \rfloor$. Furthermore, the noise power is assumed to be fixed and identical for all users in C$_1$ and C$_2$, $\sigma^2 = -90$ dBm, $\forall m$, and the simulations are performed with 10^4 random channel realizations.

3.10.2 Search Algorithm Performance

In this subsection, we describe the proposed search algorithms' performance in achieving user fairness and the required search size.

Fig. 3.2 illustrates the performance of the sub-optimal solution to (P1), which is represented by Algorithms 4, 5, and 6 to solve (P1.1) (the reformulated version

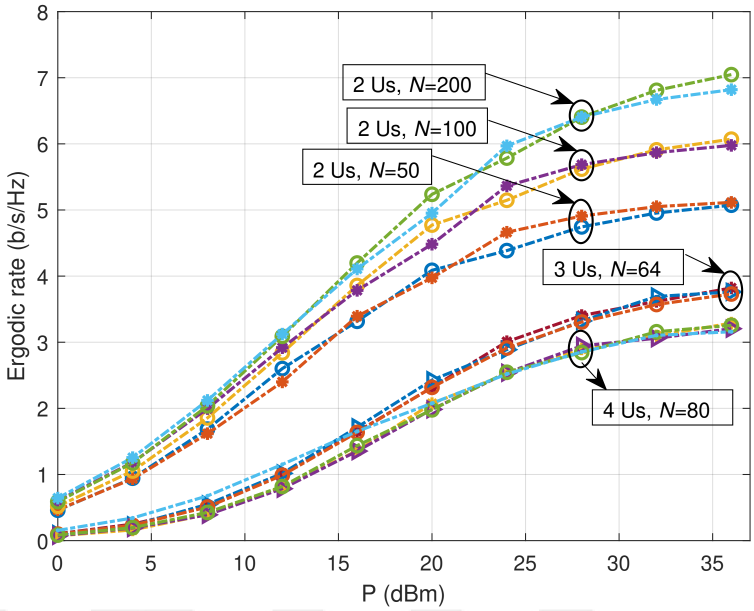

Figure 3.2: The performance of the RIS partitioning algorithms with different N and M_2 values.

Table 3.2: RIS partitioning algoritms: input parameters and outcomes.

N, M_2	N_{thr}, q, ϵ	b, $\bar{r}$	$\lvert\mathcal{S}\rvert/\lvert\tilde{\mathcal{S}}\rvert$
$50, 2$	15, 1.5, 0.1	2, 0.3	5/49
$64, 3$	14, 1, 0.1	1, 0.1	40/210
$80, 4$	15, 1, 0.1	1, 0.1	64/969
$100, 2$	21, 1.5, 0.1	5, 0.5	5/99
$200, 2$	32, 1.5, 0.05	10, 0.7	6/199

of (P1)). Here, for each given P value, we consider multiple users in C_2 where the RIS needs to be partitioned among them to maximize the user fairness in terms of the ergodic-rate. It can be seen that the proposed algorithms achieve a result close to the perfect user fairness between the users with different N values. Furthermore, Table 3.2 shows that Algorithms 4 and 5 reduce the search space for Algorithm 6 significantly, where $|\mathcal{S}|/|\tilde{\mathcal{S}}|$ denote the number of possible partitions provided by the

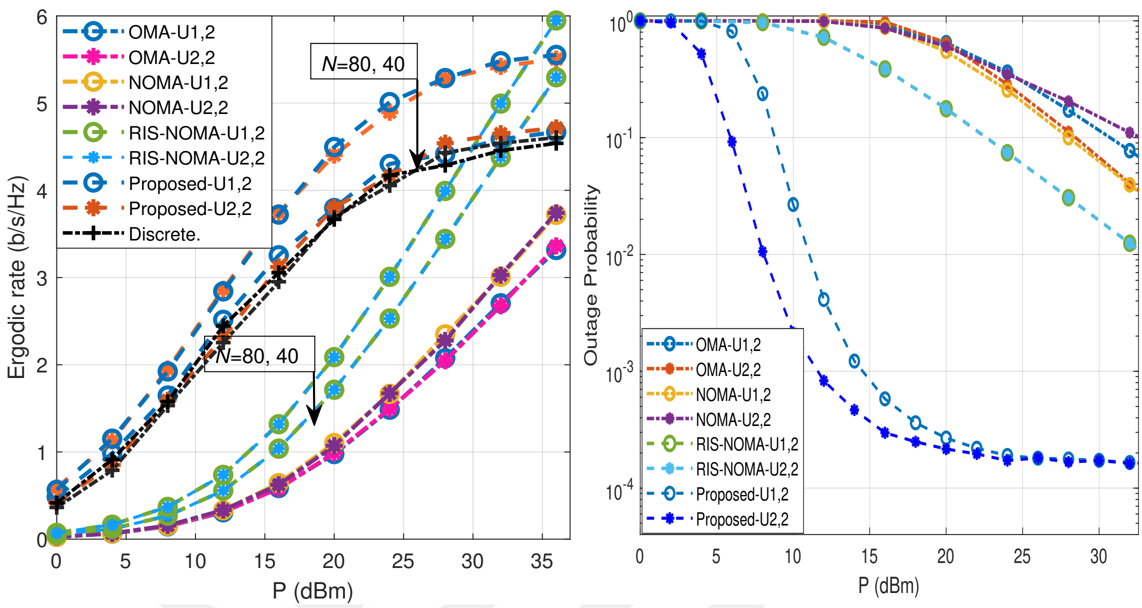

(a) (b)

Figure 3.3: The comparison of the proposed and benchmark schemes with $M_1 = 0$ and $M_2 = 2$, in terms of (a) ergodic rate with $N = 40$, (b) the outage probability, with a targeted transmission rate of 1.2 bpcu for all users, and $N = 40$.

sub-optimal/optimal solution of Algorithm 6. This makes the exhaustive search a practical solution to solve (P1) and find the proper RIS partition.

3.10.3 Special Case 1: All users are located in C_2

In Figs. 3.3 (a) and (b), we consider the first case with $N = 40$, $M_1 = 0$, and $M_2 = 2$. As it is shown in Fig. 3.3(a), all the schemes achieve almost the same user fairness, nevertheless, the proposed scheme shines out with an improvement in the required P of 8 dB compared to the RIS-NOMA scheme and 14 dB compared to TDMA-OMA and PD-NOMA schemes. However, the performance gain achieved by the proposed scheme is bounded by a saturation point due to the mutual sub-surfaces interference. It can be also noted that the discrete phase shift adjustment with only 8 phase shift levels achieves almost the same performance as in the continuous case, where, assuming uniform quantization for the interval $[0, 2\pi)$, 3 bits are used to select the phase shift from $Z = 2^3$ levels in the finite set $\mathcal{F} = \{0, \Delta\Phi, ..., \Delta\Phi(Z-1)\}$,

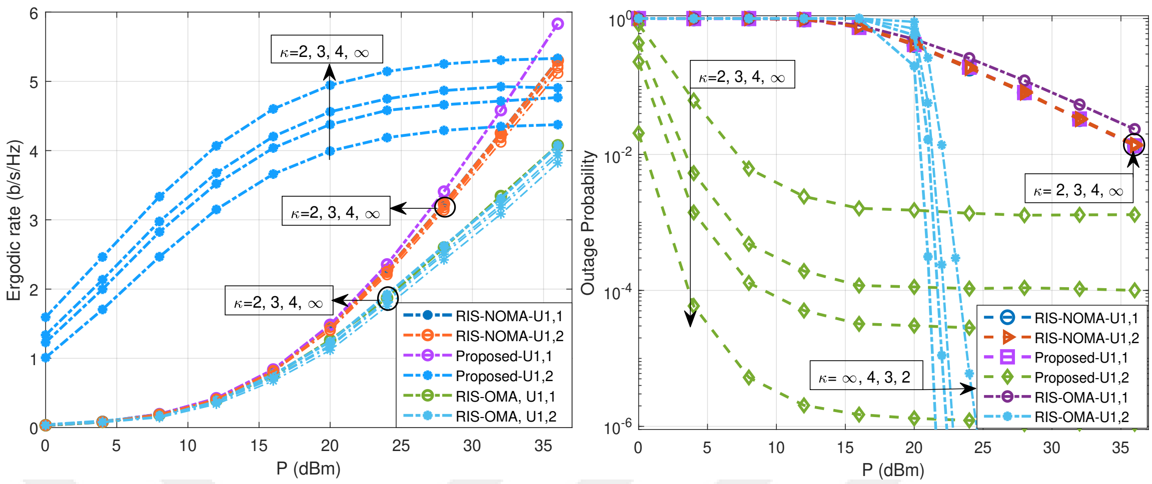

(a) (b)

Figure 3.4: The comparison of the proposed scheme with the RIS-OMA (TDMA) and RIS-NOMA benchmark schemes, with $M_1 = M_2 = 1$ and $N = 40$, in terms of (a) ergodic rate, (b) outage probability, with a targeted transmission rate of 1.2 bpcu for all users.

where $\Delta\Phi = \frac{2\pi}{Z}$ [68]. Fig 3.3 (b) shows the outage probability comparison with a targeted transmission rate of 1.2 bpcu for all users. It can be seen that the proposed scheme outperforms the benchmark schemes with a around 20 dB in the required P for both users before the saturation region.

3.10.4 Special Case 2: Each cluster has a single user

In Figs. 3.4(a) and 3.4(b), we consider the second case with $N = 40$ and $M_1 = M_2 = 1$, as follows. Fig. 3.4(a) shows that $\mathrm{U}_{1,1}$ in the proposed scheme and $\mathrm{U}_{1,1}$ and $\mathrm{U}_{1,2}$ in the RIS-NOMA scheme, achieve almost the same ergodic rate performance, with a 2 dB improvement in the required P for the proposed scheme at the high SNR region. On the other hand, $\mathrm{U}_{1,2}$ in the proposed scheme achieves a 12-24 dB improvement compared to the other users when there is no phase estimation errors, which can be explained by the asymptotic squared power gain of $\mathcal{O}(N^2)$ the RIS provides to $\mathrm{U}_{1,2}$ [106]. However, there is a saturation point for the performance of $\mathrm{U}_{1,2}$ due to the BS-$\mathrm{U}_{1,2}$ interference link. Considering the user fairness, contrary to might be concluded for the first glance from Fig. 3.4(a), the proposed scheme achieves the maximum user fairness, which can be explained as follows. Since the communication link over the RIS is blocked for $U_{1,1}$ in both schemes, the most efficient option, in terms of the sum-rate performance and user fairness, is to fully allocate the RIS to serve $U_{1,2}$ and the BS to serve $U_{1,1}$ in both schemes, which is what the proposed scheme basically does. On the other side, the use of SC in the benchmark scheme makes the RIS amplifies the interference from $U_{1,1}$ to $U_{1,2}$ without any benefit for $U_{1,1}$, which is unfair to $U_{1,2}$. In Fig. 3.4(b), $U_{1,2}$ in the proposed scheme outperforms the other users in both schemes in terms of the outage probability with a remarkable improvement of 20-35 dB in the required P, while the other users achieve the same performance, which agrees with the ergodic rate results shown in Fig. 3.4(a). For the phase estimation errors, we consider the von Mises distribution, where κ is the concentration parameter. It can be seen from Figs. 3.4(a) and 3.4(b) that the benchmark schemes are considerably less sensitive to the phase estimation errors compared to the proposed scheme, which can be explained as follows. The benchmark schemes, unlike the proposed one, have a direct information link which, with this small RIS size, dominates the RIS link and therefore, the performance loss due to the phase estimation errors does not appear clearly. With a larger RIS size that makes the BS-RIS-$U_{m,2}$ reflection link dominate, the benchmark schemes are also expected to experience a similar performance behavior, with the phase estimation errors.

3.10.5 General Case

Here, we show the performance of the proposed system in the general case introduced in Section 3.4, as follows. Fig. 3.5(a) shows the outage probability performance for the general case, with different N values. Note that, as the performance improves with the increase of N, the saturation happens at the high SNR region due to the interference coming from BS and sub-surfaces. It can be also seen that the theoretical and simulation curves are in perfect agreement with each other. Furthermore, it can be noted that the i.i.d. approximation of the RIS-$U_{m,2}$ channels is accurate, where

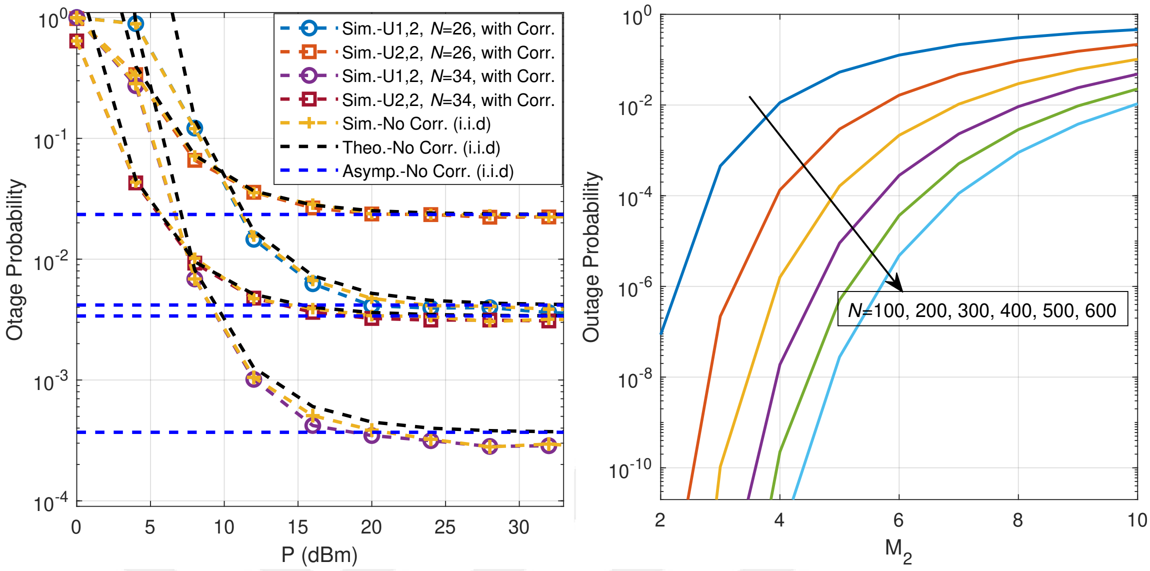

(a) (b)

Figure 3.5: Oubge probability performance with different N values, for (a) the general case, $M_2 = 2$, $M_1 \geq 1$, and a targeted transmission rate of 0.75 bpcu for all users, (b) different numbers of users in C_2 with uniform partitioning, obtained from (3.20).

the curves with/without spatial correlation are perfectly matched. Fig. 3.5(b) shows the outage probability performance of users in C_2 versus the number of users M_2, where the RIS is partitioned uniformly between all users as stated in Corollary 2. It is worth noting that, although the ratio of the amplification to the interferer signals is the same, increasing the RIS size enhances the performance of all users due to the nature of the incoherent interference.

Finally, in Figs. 3.6(a)-(c), we consider the general case of four users for the proposed and NOMA schemes. Fig. 3.6(a) shows the ergodic rate performance for all users, where almost maximum user fairness is achieved by the NOMA scheme. On the other side, the proposed scheme provides a close to the maximum fairness performance when all users are located in C_2, $M_1 = 0, M_2 = 4$, with $N = 80$. A better user fairness performance is noted for $M_1 = 2, M_2 = 2$, and $N = 40$ between the two users in each cluster, which corresponds to the maximum fairness between all the four users due to the same reasons explained in the discussion of

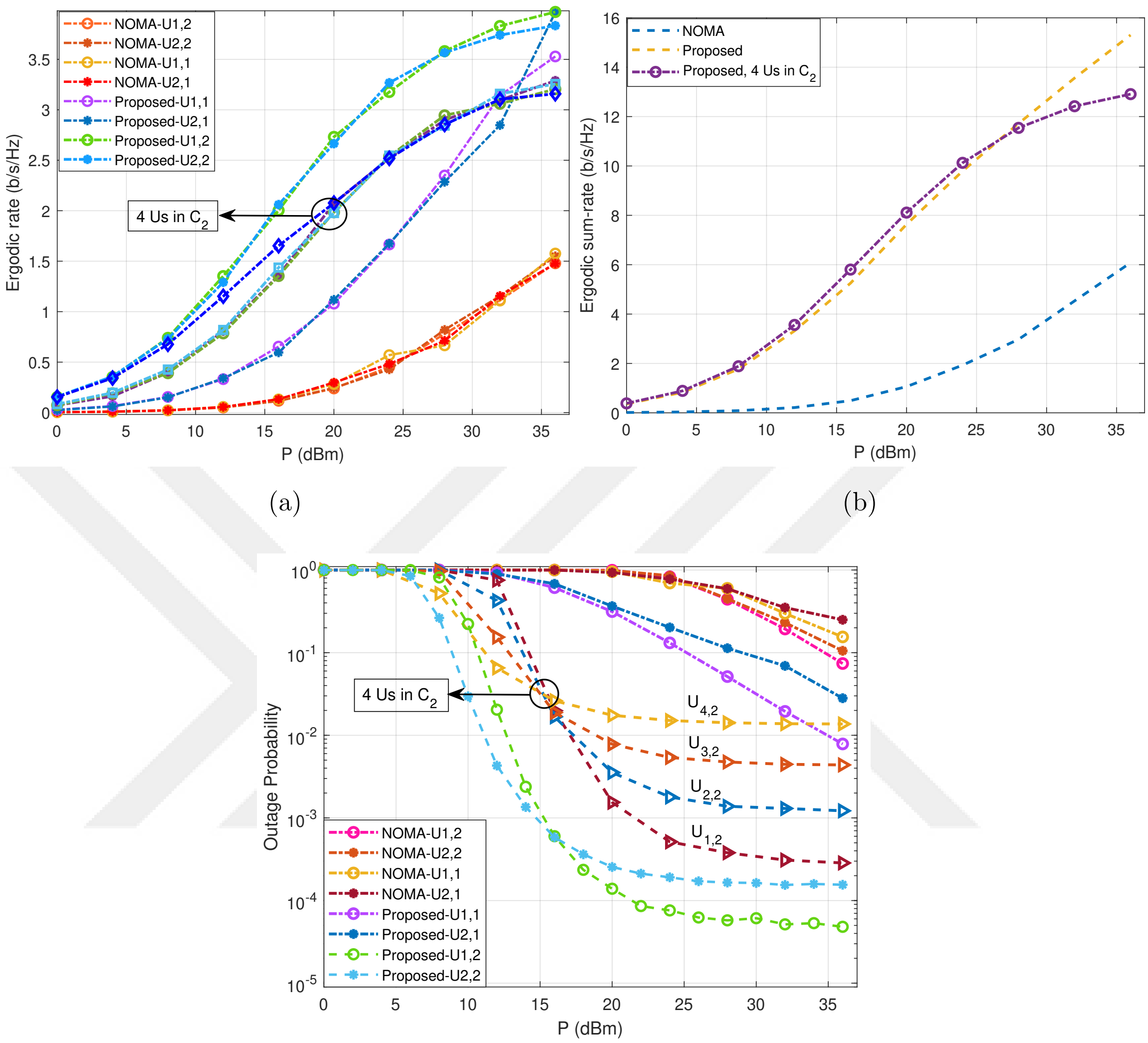

(c)

Figure 3.6: The comparison of the proposed and the NOMA benchmark schemes with $M_1 = M_2 = 2$ and $M_1 = 0, M_2 = 4$ with $N = 40, 80$, respectively, in terms of (a) ergodic rate, (b) ergodic sum-rate, (c) outage probability, with a targeted transmission rate of 0.75 bpcu for all users.

Fig. 3.4(a). Furthermore, when $M_1 = M_2 = 2, N = 40$, the performance of the proposed scheme outperforms the one of NOMA scheme for each user significantly, with more than 12 dB and 22 dB improvement for the two users in C_1 and the two users in C_2, respectively. On the other side, when $M_1 = 0, M_2 = 4, N = 80$, 18 dB gain is observed compared to NOMA scheme, with a 4 dB less gain compared to the previous case due to the mutual sub-surfaces interference. Overall, for both users' deployment scenarios, an improvement of 18 dB in the ergodic sum-rate is achieved by the proposed scheme compared to the NOMA scheme, as shown in Fig. 3.6(b). In Fig. 3.6(c), when $M_1 = M_2 = 2, N = 40$, the proposed scheme outperforms NOMA scheme in the outage probability performance with around 22 dB in the required P for the first and second users in C_2, and around 5 dB and 10 dB for the first and second users in C_1, respectively. For the case where $M_1 = 0, M_2 = 4, N = 80$, the proposed scheme outperforms the NOMA scheme with 22 dB until the saturation region.

3.11 Conclusion

In this chapter, we have introduced a novel downlink NOMA solution with RIS partitioning in order to mitigate the mutual interference between users in a local beyond 5G network. In the proposed system, the ergodic rates and outage probabilities of all users are enhanced and the user fairness is maximized by the fair and efficient distribution of the PR among users. The potential of the proposed PR distribution is perfectly illustrated in Fig. 3.4, where the BS and RIS are used in a very efficient way compared to the classical use of the SC technique. Furthermore, we have proposed three efficient searching algorithms to, sequentially, obtain a sub-optimal solution for the RIS partitioning optimization problem, with insignificant performance degradation. By considering different users' deployment scenarios, it was shown that the proposed system provides remarkable performance gain in all of the considered different environment settings. We have derived the exact and asymptotic outage probability expressions for the proposed system in all the cases including the effect of the number of users in C_2 and the RIS size. The computer simulations show that the proposed system outperforms the OMA, RIS-OMA, NOMA, and RIS-NOMA benchmark systems significantly, in terms of outage probability, ergodic rates of all users, and user fairness. Finally, removing the sub-surfaces and/or the BS interference for C_2 users appears as a future research direction that is worth investigating.

Chapter 4

STAR-RIS-EMPOWERED NOMA NETWORKS: AN ERROR PERFORMANCE PERSPECTIVE

This chapter investigates the BER performance of STAR-RISs-assisted NOMA networks. In the investigated network, a STAR-RIS serves multiple non-orthogonal users located on either side of the surface by utilizing the mode switching protocol. We derive the closed-form BER expressions in perfect and imperfect successive interference cancellation cases. Furthermore, asymptotic analyses are also conducted to provide further insights into the BER behavior in the high signal-to-noise ratio region. Finally, the accuracy of our theoretical analysis is validated through Monte Carlo simulations. The obtained results clearly reveal that the BER performance of STAR-RIS-NOMA outperforms that of the classical NOMA system.

The remaining sections of the chapter are given as follows. We give related studies in Section 4.1, motivation and main contributions in Section 4.2, system model in Section 4.3, BER analysis in Section 4.4, simulation results in Section 4.5, and conclusion in Section 4.6.

4.1 Related Works

Considering relevant studies on BER analysis of NOMA, in [126], the authors analyzed the BER performance of uplink and downlink NOMA networks, where BPSK and QAM modulation schemes are employed for the far and near users, respectively. In [127], the closed-form expressions are derived for the BER of a two-user NOMA system using QAM modulation. In [128, 129], the authors analyzed the BER for a RIS-assisted NOMA system, where the RIS is partitioned into multiple subsurfaces, each allocated to serve a single user. In what follows, we provide the studies related to the STAR-RIS technology, followed by the studies that combine them with NOMA protocol.

4.1.1 Studies on STAR-RIS

RISs can only serve the users located on the same side of the surface as they can not forward impinging EMWs to the opposite side of the surface. Recently, simultaneous transmitting and reflecting RISs (STAR-RISs) are proposed to achieve 360° wireless coverage [130]. Compared to classical RISs, STAR-RISs can serve users located on both sides of their surface. STAR-RISs consist of elements that can produce both electric polarization and magnetization currents, which allows simultaneous control of the transmit and reflect incident signals towards the users located at different sides of the surface. Since the concept of STAR-RIS is relatively new, only a few works in the literature have investigated it so far [12]-[131]. Particularly, in [12], a general hardware model for STAR-RISs was introduced. The channel models for the near- and far-field regions of STAR-RISs were also investigated and the analytical expressions for the channel gains of users were derived in closed-form. Next, the active and passive beamforming optimization problem was considered in [14] for the STAR-RIS-assisted downlink networks in both unicast and multicast transmission cases. Specifically, for three practical operating protocols ES, MS, and TS, the active beamforming at the base station (BS) and the passive transmission/reflection beamforming at the STAR-RIS were jointly optimized in order to minimize the power consumption of the BS and satisfy the quality-of-service (QoS) requirements of different users. In [131], practical hardware implementations and their accurate physical models were investigated for STAR-intelligent omni surfaces (STAR-IOSs). The weighted sum-rate maximization problem of the STAR-RIS-assisted MIMO networks was studied in [132], where the authors proposed to use block coordinate descent algorithm in alternate manner to design the precoding matrices and the transmitting/reflecting coefficients.

4.1.2 Studies on STAR-RIS-NOMA

Recently, a number of works have been reported in the literature incorporating NOMA and STAR-RIS in wireless networks to increase the coverage area and the overall system performance. In particular, in [13], the authors investigated a realistic transmission and reflection coupled phase-shift model for STAR-RISs. The authors in [21] proposed partitioning algorithms for a STAR-RIS-assisted NOMA network, aiming to maximize the sum-rate and guarantee individual users' quality-of-service (QoS) requirements by assigning a proper number of STAR-RIS elements to each of them. The authors in [133] showed that the wireless coverage area can be significantly extended by integrating STAR-RISs into NOMA networks. The authors in [134] took advantage of STAR-RIS to simultaneously eliminate inter-cell interference and enhance desired signals in NOMA enhanced coordinated multi-point transmission networks. In [135] and [136] the authors maximized the weighted sum-rate for the STAR-RIS-assisted MIMO system and the sum secrecy rate for the STAR-RIS-assisted MISO system, respectively. In [137], by jointly optimizing the decoding order, power allocation coefficients, active beamforming, and transmission/reflection beamforming, the achievable sum-rate was maximized for the STAR-RIS-assisted NOMA system. The authors in [138] used a STAR-RIS to enable a heterogeneous network that integrated uplink NOMA and over-the-air federated learning into a unified framework to address the scarcity of system bandwidth. In addition, they minimized the optimality gap while guaranteeing QoS requirements by jointly optimizing the transmit power at users and the configuration mode at the STAR-RIS. In [139] and [140], the authors proposed different approximated mathematical channel models to investigate the outage probability performance for STAR-intelligent omini-surfaces based NOMA and STAR-RIS-NOMA multi-cell networks. In [141], the authors considered STAR-RIS-assisted NOMA networks where the total power consumption is minimized by jointly optimizing the users' transmit power, passive beamforming vectors at the STAR-RIS, and used time slots. In [142], the authors investigated the secrecy design of STAR-RIS-assisted NOMA networks under two scenarios where full or statistical CSI of the eavesdropper is available at the legitimate nodes. For multi-carrier communications networks, the authors in [143] investigated the resource allocation problem in STAR-RIS-assisted OMA and NOMA networks by considering the sum-rate maximization problem in both scenarios. In [144], a deep reinforcement learning-based algorithm is designed to maximize the energy efficiency for a STAR-RIS-NOMA network. The authors in [145] proposed practical phase-shift configuration strategies for STAR-RIS-assisted NOMA networks with correlated phase shifts. In [146], the performance of STAR-RIS-assisted NOMA networks is investigated in terms of OP and ergodic sum-rate.

4.2 Motivation and Contributions

Based on the previous literature review, it can be noted the following. The studies of [126]-[127] assumed a simple scenario of two NOMA users, which might not be practical. Furthermore, the works of [128]-[129] assumed that each user receives the signals reflected from the RIS partition assigned to it only and without interference signals from the other partition, which is physically impossible. Moreover, the performance of STAR-RIS-NOMA networks in [133]-[146] is analyzed in terms of OP and sum-rate only, and no light has been shed on the BER performance aspect yet. These have motivated us to investigate the BER performance for STAR-RIS-NOMA networks, where BS communicates multiple non-orthogonal users with the assistance of a STAR-RIS. The main contributions of this chapter can be summarized as follows. We analyze the BER performance of the STAR-RIS-NOMA network considering the subsurface mutual interference within the RIS transmission or reflection part in the cases of perfect and imperfect SIC. We derive the closed-form expressions of the BER for the users employing a BPSK modulation. Then, asymptotic analyses are carried out to provide further insight into BER behavior at the high SNR regions. Finally, we verify our analytical results by Monte Carlo simulations, which demonstrate the superiority of the STAR-RIS-assisted networks over the classical NOMA.

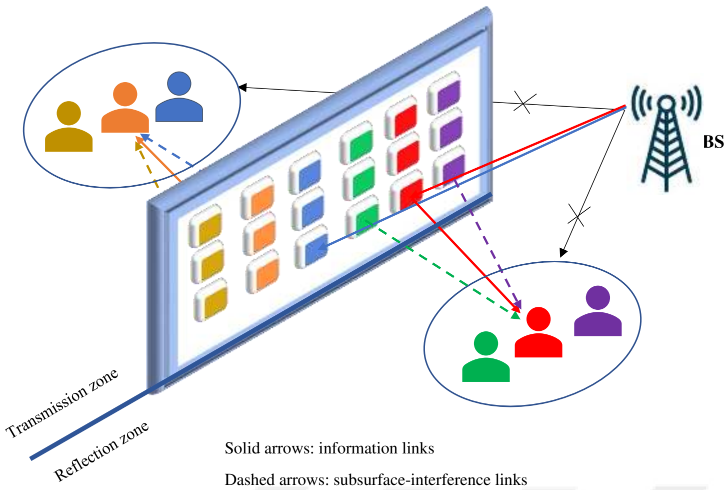

Figure 4.1: A STAR-RIS-assisted NOMA system model.

4.3 System Model

This section introduces the considered channels, STAR-RIS settings, and users' deployment in the investigated system. As illustrated in Fig. 4.1, we consider a STAR-RIS-NOMA network, in which a single-antenna BS communicates simultaneously K single-antenna users with the help of a STAR-RIS equipped with N passive elements. The K users ($\mathrm{U}_1, ..., \mathrm{U}_K$) are deployed on both sides of the STAR-RIS, where K_t and K_r users are located in the transmission and reflection zones, respectively. The direct communication links between the BS and users are assumed to be unavailable due to natural or manmade obstacles and the STAR-RIS is deployed to provide alternative communication links for users through the transmission/reflection elements. The STAR-RIS adopts mode switching (MS) protocol, where each element can operate in full transmission or reflection mode. Thus, the STAR-RIS is partitioned into two main parts, where the first and second parts contain N_t transmitting and N_r reflecting elements to serve the users in transmission and reflection zones, respectively. Both parts of the RIS are partitioned into subsurfaces, where each subsurface is allocated to serve a specific user in the transmission or reflection zone. The BS-STAR-RIS link is assumed to follow Rayleigh fading channel model, where

$\mathbf{h}_i \in \mathbb{C}^{N_i \times 1}$ denotes the BS-ith subsurface vector with N_i refers to the number of elements that belong to the ith subsurface in the transmission (t) or reflection (r) part of the STAR-RIS. $\mathbf{h}_i = \left[h_i^{(1)}, ..., h_i^{(n)}, ..., h_i^{(N_i)}\right]^T$ with $h_i^{(n)} = \sqrt{L_{BS}}\zeta_i^{(n)} e^{-j\phi_i^{(n)}}$ denoting the channel coefficient between the BS and nth STAR-RIS element in the ith subsurface, where L_{BS}, $\zeta_i^{(n)}$, and $\phi_i^{(n)}$ denote the path gain, channel amplitude, and channel phase, respectively, and $h_i^{(n)} \sim \mathcal{CN}(0, L_{BS})$. Likewise, the STAR-RIS-U$_k$ link is assumed to follow Rayleigh fading channel model, where the channel vector between the ith subsurface in the transmission or reflection part of the STAR-RIS and U$_k$ is denoted by $\mathbf{g}_{k,i} \in \mathbb{C}^{N_i \times 1}$, $\mathbf{g}_{k,i} = \left[g_{k,i}^{(1)}, ..., g_{k,i}^{(n)}, ..., g_{k,i}^{(N_i)}\right]^T$, $g_{k,i}^{(n)} = \sqrt{L_{SU,k}}\eta_{k,i}^{(n)} e^{-j\Phi_{k,i}^{(n)}}$ denotes the channel coefficient between nth RIS element in the ith subsurface and U$_k$, where $L_{SU,k}$, $\eta_{k,i}^{(n)}$, and $\Phi_{k,i}^{(n)}$ denote the path gain, channel amplitude, and channel phase, respectively, and $g_{k,i}^{(n)} \sim \mathcal{CN}(0, L_{SU,k})$. The transmission and reflection coefficients for the ith subsurface in the transmission and reflection parts of the STAR-RIS are denoted by the entries of the diagonal matrix $\mathbf{\Theta}_i \in \mathbb{C}^{N_i \times N_i}$, for the nth element we have $\Theta_i^{(n,n)} = e^{j\theta_i^{(n)}}$, where $\theta_i^{(n)} \in [0, 2\pi)$. In the considered setup, the users are ordered according to their channel gains such U$_1$ and U$_K$ are the weakest and strongest channel gains, respectively. Thus, the power allocation are inversely ordered as $a_1 \geq ... \geq a_K$. Given, P is the BS transmit power, x_k and a_k are U$_k$'s symbol and power allocation factor, respectively, $\mathrm{E}\left[|x_k|^2\right] = 1$, $\sum_k a_k = 1$. Then, the BS transmits the superimposed signal $x = \sum_k \sqrt{a_k P} x_k$ to all users and the received signal at U$_k$ is

$$y_k = \mathbf{g}_k^T \mathbf{\Theta}_k \mathbf{h}_k x + \sum_i \mathbf{g}_{k,i}^T \mathbf{\Theta}_i \mathbf{h}_i x + n_k, \tag{4.1}$$

where $\sum_i \mathbf{g}_{k,i}^T \mathbf{\Theta}_i \mathbf{h}_i x$ refers to subsurfaces mutual interference within the transmission or reflection part of the RIS and n_k denotes the AWGN sample at U$_k$, $n_k \sim \mathcal{CN}(0, \sigma^2)$. Notably, U$_1$ has the highest allocated power coefficient, and thus it does not perform the SIC process. It detects its signal directly by considering other users' symbols as noise and implement maximum likelihood detection (MLD). On the other hand, U$_k$ needs the SIC process to detect and subtract $\{1, ..., k-1\}$'s signals and then it implements MLD to detect its signal. Accordingly, the detected $\hat{x}_k$ can be stated as

$$\hat{x}_k = \arg\min_i \left\{ \left| y_k^* - \sqrt{a_k P} \mathbf{g}_k^T \mathbf{\Theta}_k \mathbf{h}_k x_k^{(i)} \right|^2 \right\}, \tag{4.2}$$

where $y_k^* = y_k - \sum_{j=1}^{k-1} \sqrt{a_j P} \mathbf{g}_k^T \mathbf{\Theta}_k \mathbf{h}_k \hat{x}_j$ and $x_k^{(i)}$ denotes ith element in the set of x_k constellation.

4.4 Bit Error Rate Analysis

In this section, we derive theoretical expressions of the BER for user U_k in the perfect and imperfect SIC scenarios, followed by the asymptotic analysis at high SNR regions. The average bit error probability for U_k is given by

$$\mathcal{P}_{e,k} = \int_0^\infty \mathcal{P}(e|\varphi_k) f_{\varphi_k}(x) dx, \tag{4.3}$$

where $\varphi_k = |\mathbf{g}_k^T \mathbf{\Theta}_k \mathbf{h}_k|$, $\mathcal{P}(e|\varphi_k)$ and $f_{\varphi_k}(x)$ denote absolute cascaded channel, conditional BER for U_k in AWGN channel and the PDF of the cascaded channel φ_k, respectively. In what follows, we derive $\mathcal{P}(e|\varphi_k)$ and $f_{\varphi_k}(x)$ in Lemmas 1 and 2, respectively, then we obtain $\mathcal{P}_{e,k}$ in the cases of absence and presence of SIC error in Propositions 2 and 3, respectively.

Lemma 1. *The BER for U_k in AWGN can be given by*

$$\mathcal{P}\left(e|\varphi_k\right) = \sum_i \mathcal{P}\left(A_k^{(i)}\right) Q\left(A_k^{(i)} \varphi_k \sqrt{\varrho_k \gamma}\right), \tag{4.4}$$

where $A_k^{(i)}$ denotes ith combination in $A_k \in \left\{\sqrt{a_k P} \pm ... \pm \sqrt{a_K P}\right\}$ and $\mathcal{P}\left(A_k^{(i)}\right) = 2^{k-K}$. Additionally, $\gamma \triangleq \frac{P}{\sigma^2}$ is the signal-to-noise ratio (SNR), $\varrho_k = \left(1 + L_k \left(N_\chi - N_k\right) \gamma / P\right)^{-1}$. Here, $\chi \in \{t, r\}$, $L_k = L_{BS} L_{SU,k} = d_{BS}^{-\alpha_{BS}} d_{SU,k}^{-\alpha_{SU}}$ is the overall path gain of the BS-RIS-U_k link, where (α_{BS}, d_{BS}), and $(\alpha_{SU}, d_{SU,k})$ refer to (path loss exponents, distances) associated with the BS-RIS and RIS-U_k links, respectively.

Proof: According to the central limit theorem (CLT), for large number of RIS elements, $\sum_i \mathbf{g}_{k,i}^T \mathbf{\Theta}_i \mathbf{h}_i x$ in (4.1) converges to Gaussian RV, i.e., $\sum_i \mathbf{g}_{k,i}^T \mathbf{\Theta}_i \mathbf{h}_i x \sim \mathcal{CN}\left(0, L_k \left(N_\chi - N_k\right)\right)$. Then, $y_k = \mathbf{g}_k^T \mathbf{\Theta}_k \mathbf{h}_k x + w_k$, where $w_k \sim \mathcal{CN}(0, \sigma^2 + L_k \left(N_\chi - N_k\right))$. Following same derivation steps in [126]-[127], the BER for U_k in AWGN can be achieved in (4.4). ■

Lemma 2. *The PDF of φ_k is given by*

$$f_{\varphi_k}(x) = \frac{1}{\sqrt{2\pi v_k}} \exp\left(-\frac{(x-\mu_k)^2}{2v_k}\right), \tag{4.5}$$

where $\mu_k = \frac{\pi}{4}\sqrt{L_k}N_k$ *and* $v_k = \left(1 - \frac{\pi^2}{16}\right) L_k N_k$.

Proof: The SNR can be maximized by letting $\theta_k^{(n)} = \phi_k^{(n)} + \Phi_k^{(n)}$. Thus, φ_k corresponds to the sum of product of two independent Rayleigh RVs. According to the CLT, when $N_k \to \infty$, φ_k follows Gaussian distribution, $\varphi_k \sim \mathcal{N}(\mu_k, v_k)$. Hence, the PDF of φ_k can be finally expressed as in (4.5). ■

Proposition 2. *In the perfect SIC case, the BER of U_k is*

$$\begin{aligned}\mathcal{P}_{e,k} \approx & \frac{\exp\left(-\frac{2cv_k+\mu_k^2}{2v_k}\right)}{\sqrt{2v_k}} \sum_i \mathcal{P}\left(A_k^{(i)}\right) \\ & \exp\left(\frac{\left(bA_k^{(i)}\sqrt{\varrho_k\gamma}v_k - \mu_k\right)^2}{4a\left(A_k^{(i)}\right)^2 \varrho_k\gamma v_k^2 + 2v_k}\right)\sqrt{\frac{v_k}{4\left(A_k^{(i)}\right)^2\varrho_k\gamma v_k + 2}} \\ & \left(1 + erf\left(\sqrt{\frac{\left(bA_k^{(i)}\sqrt{\varrho_k\gamma}v_k - \mu_k\right)^2}{4a\left(A_k^{(i)}\right)^2 \varrho_k\gamma v_k^2 + 2v_k}}\right)\right),\end{aligned} \tag{4.6}$$

where $(a, b, c) = (0.3842, 0.7640, 0.6964)$ *are the fitting coefficients used by Lopez-Benitez and Casadevall in approximating Q-function [147].*

Proof: A tighter and more tractable approximation of Q-function in Lemma 1 can be given by Lopez-Benitez and Casadevall. The integral obtained by substituting this approximation and Lemma 2 into (4.3) can be written in terms of error function [148, Eq. (3.322.2)]. Therefore, the BER of U_k can be finally stated in (4.6). ■

In general scenarios, detection errors can appear at any step of the SIC process. Proposition 3 considers a special case (two-user scenario, where U_1 and U_2 are located at the transmission and reflection zones, respectively), which can be generalized for K users.

Proposition 3. *In the presence of SIC error, the BER for U_1 and U_2 can be given by*

$$\mathcal{P}_{e,1}^{sic} = \mathcal{P}_{e,1} \; and \, \mathcal{P}_{e,2}^{sic} \approx \mathcal{P}_{e,2}\mathcal{P}\left(x_1^c\right) + 0.5\left(1 - \mathcal{P}\left(x_1^c\right)\right), \tag{4.7}$$

where $\mathcal{P}\left(x_1^c\right)$ refers to average bit error probability for U_1 when its signal is detected at U_2 and can be calculated from (4.6) *with related parameters of φ_2.*

Proof: U_1 does not carry out SIC process and hence the BER for U_1 is calculated form (4.6), i.e., $\mathcal{P}_{e,1}^{sic} = \mathcal{P}_{e,1}$. On the other hand, U_2 performs SIC process, and hence the BER for U_2 should be considered for both correct and erroneous SIC cases, $\mathcal{P}_{e,2}^{sic} = \mathcal{P}\left(x_2/x_1^c\right)\mathcal{P}\left(x_1^c\right) + \mathcal{P}\left(x_2/x_1^e\right)\mathcal{P}\left(x_1^e\right)$. Here, $\mathcal{P}\left(x_1^c\right)$ and $\mathcal{P}\left(x_1^e\right)$ denote average bit error probability for correct and erroneous detection of x_1 at U_2, respectively. $\mathcal{P}\left(x_2/x_1^c\right)$ and $\mathcal{P}\left(x_2/x_1^e\right)$ denote average bit error probability for x_2 when x_2 is correctly and erroneously detected at U_2, respectively. $\mathcal{P}\left(x_1^c\right)$ is calculated from (4.6) with related parameters of φ_2, and hence $\mathcal{P}\left(x_1^e\right) = 1 - \mathcal{P}\left(x_1^c\right)$. Form (4.6), $\mathcal{P}\left(x_2/x_1^c\right)$ can be also found, i.e., $\mathcal{P}\left(x_2/x_1^c\right) = \mathcal{P}_{e,2}$ and $\mathcal{P}\left(x_2/x_1^e\right)$ is very close to the worst case, i.e., $\mathcal{P}\left(x_2/x_1^e\right) \approx 0.5$. ■

It is difficult to get an insight from the BER expressions in previous propositions. In Corollary 3, we examine the BER behavior in the high SNR regime.

Corollary 3. *In high SNR region, the BER can be given as*

$$\begin{aligned}\mathcal{P}_{e,k}^{\infty} \approx & \frac{\exp\left(-\frac{2cv_k + \mu_k^2}{2v_k}\right)}{\sqrt{2v_k}} \sum_i \mathcal{P}\left(A_k^{(i)}\right) \\ & \times \exp\left(\frac{\left(bA_k^{(i)}\sqrt{\varpi}v_k - \mu_k\right)^2}{4a\left(A_k^{(i)}\right)^2 \varpi v_k^2 + 2v_k}\right)\sqrt{\frac{v_k}{4\left(A_k^{(i)}\right)^2 \varpi v_k + 2}} \\ & \times \left(1 + erf\left(\sqrt{\frac{\left(bA_k^{(i)}\sqrt{\varpi}v_k - \mu_k\right)^2}{4a\left(A_k^{(i)}\right)^2 \varpi v_k^2 + 2v_k}}\right)\right),\end{aligned} \tag{4.8}$$

where $\varpi = \left(L_k\left(N_\chi - N_k\right)/P\right)^{-1}$.

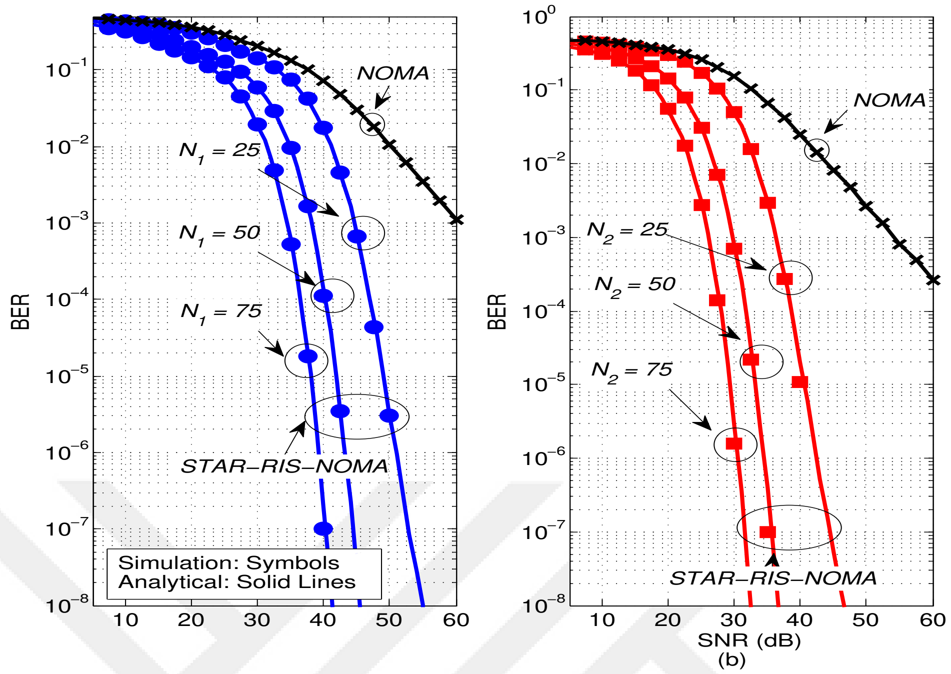

Figure 4.2: The BER versus SNR for (a) U_1 and (b) U_2, in the perfect SIC case, $(a_1, a_2) = (0.7, 0.3)$ and $(d_{BS}, d_{SU,1}, d_{SU,2}) = (50, 6, 4)$ m.

Proof: Let $\varpi = \varrho_k \gamma$, when $\gamma \to \infty$, $\varpi = \left(L_k \left(N_\chi - N_k\right)/P\right)^{-1}$, substituting in (4.6) we obtain (4.8). ■

From Corollary 3, it can be noticed that, due to the subsurface interference, the asymptotic BER does not depend on the SNR. The BER reaches a fixed value (error floor) in the high SNR region, which indicates that the diversity gain is zero.

4.5 Simulation Results

In this section, Monte Carlo simulations are presented to show the performance of the STAR-RIS-NOMA system, and to validate the BER analytical results. Unless stated otherwise, we assume $P = 1$ and $\alpha_{BS} = \alpha_{SU} = 2$. We compare the proposed system with the classical NOMA system by considering the same simulation parameters, and the BS-U_k path gain is modelled as $L_k = d_k^{-\alpha}$, where d_k is the BS-U_k distance and $\alpha = 2$ is the path loss exponent.

Fig. 4.2(a)-(b) show the BER performance versus SNR in the case of perfect

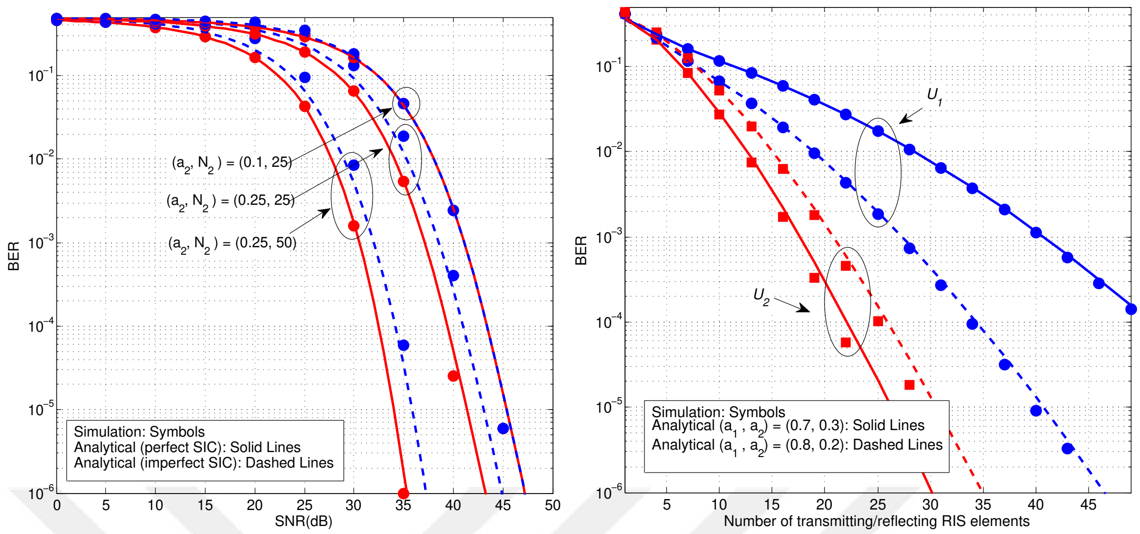

(a)

Figure 4.3: (a) The BER performance versus SNR for U_2 in the perfect and imperfect SIC cases. (b) The BER performance versus number of transmitting/reflecting elements for different power allocation coefficients and $\gamma = 40$ dB.

SIC for two-user scenario, where each user is located at different side of RIS. It can be clearly seen that the obtained analytical results perfectly match the simulations curves. It can be also seen that both users achieve better BER performance as the number of RIS elements increases. Compared to classical NOMA system, Fig. 4.2(b) shows that STAR-RIS NOMA (U_2) achieves 20 dB, 25 dB, and 29 dB performance gains for $N_1 = 25, 50$ and 75, respectively at BER of 10^{-3}.

Fig. 4.3 (a) shows the BER performance versus SNR for U_2 in the cases of perfect and imperfect SIC. It is observed that the BER performance gets worse in the presence of SIC error even when the number of RIS elements increases. However, when a_2 decreases (a_1 increases), the SIC error decreases. This is because increasing a_1 increases the probability of detecting its signal correctly and results in a reduction of SIC error.

Fig. 4.3 (b) depicts the BER performance versus number of RIS elements for different power allocation coefficients. It is observed that U_1 is more sensitive to the change in the power allocation over the change of the number of RIS elements. This

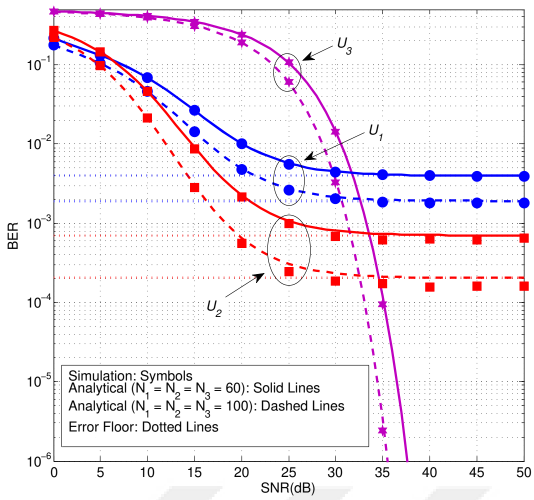

Figure 4.4: The BER versus SNR for three-user scenario, $(a_1, a_2, a_3) = (0.75, 0.248, 0.002)$ and $(d_{BS}, d_{SU,1}, d_{SU,2}, d_{SU,2}) = (20, 3, 2.5, 2)$ m.

is because U_1 does not carry out any SIC process, and hence changes in the power allocation result in variations in the interference level caused by U_2. For instance, an increment of 0.1 in the power allocation makes U_1 need 13 fewer elements to achieve the same BER of 10^{-3}. On the other side, U_2 needs 3 elements more to achieve the same BER of 10^{-3}.

Fig. 4.4 plots the BER performance versus SNR for three-user scenario, where U_1 and U_2 are located at the transmission zone and U_3 is located at the reflection zone. Notice that BER performance enhances as the number of RIS elements increases. However, when SNR increases, the BERs for U_1 and U_2 reach an error floor due to the mutual subsurface-interference. On the other hand, the BER for U_3 does not reach error floor since U_3 does not suffer from any mutual subsurface-interference.

4.6 Conclusion

In this chapter, we have examined the BER performance of STAR-RIS-NOMA network, in which a STAR-RIS utilizes the MS protocol to provide communication between a BS and multiple NOMA users located on both its sides. We have derived closed-form expressions for BER in both perfect and imperfect SIC cases. Then, asymptotic analyses have been carried out to provide further insights into the error rate behavior in the high SNR region. Numerical results show that increasing the number of STAR-RIS elements has a direct effect on the BER performance enhancement, while imperfect SIC still has the same effect as in classical NOMA. Furthermore, the farthest user is more sensitive to changes in the power allocation over the change of numbers of RIS elements. Overall, it has been shown that the BER performance of STAR-RIS-NOMA outperforms that of the classical NOMA system and STAR-RIS based NOMA can be useful candidate for future systems. For a future work, the BER analysis provided here can be extended to the scenario where the STAR-RIS is partitioned between multiple users, and the aim is to find the minimum number of elements needs to be allocated for each user to guarantee a minimum BER threshold for all users.

Chapter 5

STAR-RIS-EMPOWERED NOMA NETWORKS: SYSTEM DESIGN AND RESOURCE ALLOCATION

In this chapter, we propose a novel STAR-RIS-assisted NOMA system. Unlike most of the STAR-RIS-assisted NOMA works, we target scalable phase shift design for our proposed system that requires a reduced channel estimation overhead. Within this perspective, we propose novel algorithms to partition the STAR-RIS surface among the available users. These algorithms aim to determine the proper number of transmitting/reflecting elements needs to be assigned to each user in order to maximize the system sum-rate while guaranteeing QoS requirements for individual users. For the proposed system, we derive closed-form analytical expressions for the outage probability and its corresponding asymptotic behavior under different user deployments. Finally, Monte Carlo simulations are performed in order to verify the correctness of the theoretical analysis. It is shown that the proposed system outperforms the classical NOMA and orthogonal multiple access systems in terms of OP and sum-rate, under spatial correlation and phase errors.

The remaining sections of this chapter are given as follows. In Section 5.1, we provide the motivation and main contributions. Section 5.2 provides the system model and adopted assumptions. Mathematical analyses are given in Section 5.3, partitioning algorithms in Section 5.4, simulation results in Section 5.5, and conclusions in Section 5.6.

5.1 Motivation and Contributions

Considering the phase shift design in the studies of STAR-RIS-assisted NOMA systems introduced in the previous chapter (Section 4.1.2), we note the following. Since the phase shifts are jointly designed for all users, the BS-RIS and RIS-user CSI of all users needs to be available at the BS side. Depending on the considered channel estimation method, KN pilot signals might be required to obtain the RIS-user CSI of all users [149], where N and K are the numbers of STAR-RIS elements and users, respectively, considering a single-input single-output (SISO) multi-user system. Consequently, this approach of phase shift design incurs a huge channel estimation overhead that adversely affects the overall system performance in terms of the data rate. Furthermore, considering the joint optimization of the phase shift design, power allocation at the BS, SIC decoding order, and QoS constraints for all users, the solution for this kind of optimization problem is non-scalable when any of these decision variables changes. Also, due to the heavy computations associated with solving such optimization problems, it is practically challenging to update the phase shift design in real-time.

Against this background and motivated by the work in [20], we propose a reduced channel estimation overhead and scalable phase shift design solution for a STAR-RIS-assisted NOMA system by partitioning the STAR-RIS among the available users to maximize the overall sum-rate while guaranteeing their individual QoS. In the proposed system, the BS communicates multiple users with the assistance of a STAR-RIS. The users are assumed to be randomly deployed on the transmission and reflection sides of the STAR-RIS. According to the STAR-RIS MS protocol[1], each element of the STAR-RIS can operate in transmission or reflection mode. Therefore, in order to serve the users on both sides of the STAR-RIS, we extend the partitioning algorithms proposed in [20] to the STAR-RIS case to partition the surface among users over two stages. First, the RIS surface is partitioned into two parts, transmission and reflection parts, which contain all the elements that operate in transmission and reflection modes, respectively. Second, each STAR-RIS part is partitioned into subsurfaces, where each subsurface is allocated to serve a specific user located on

[1]MS mode is more practical due to its ease of implementation compared to the other modes. In particular, ES mode has a larger number of variables that need to be jointly optimized, while the TS mode has a high hardware implementation complexity [6].

the side of that part. Note that, unlike our proposed system, [20] suffers from strong interference from the direct link due to its transmission mechanism. Furthermore, it is limited to phase shift keying (PSK) modulation. Finally, it requires a high synchronization level between the transmission at the BS and the remodulation process at the STAR-RIS side. The main contributions of this chapter can be summarized as follows:

- We introduce a scalable phase shift design scheme for a STAR-RIS-assisted NOMA system with reduced channel estimation overhead by efficiently partitioning the STAR-RIS surface among users.
- We propose two novel algorithms to partition the STAR-RIS surface among users over two stages to maximize the system sum-rate while fulfilling the different QoS requirements for different users.
- We derive exact and asymptotic expressions of the OP for the STAR-RIS-assisted NOMA network under different user deployments.
- Using comprehensive computer simulations, we verify our theoretical results and show the superiority of the proposed STAR-RIS-assisted NOMA system over the classical NOMA and OMA systems in terms of OP and sum-rate, under spatial correlation and phase errors.

5.2 System Model

In this section, we introduce the signal model and the adopted assumptions for the proposed system. In particular, we consider a downlink STAR-RIS-assisted multi-user wireless network where a single-antenna BS and an RIS with N elements serve K single-antenna users by using PD-NOMA, as shown in Fig. 5.1. The users are grouped into two main clusters, C_t and C_r, which contain K_t users located in the transmission region and K_r users located in the reflection region of the RIS, respectively. In order to reduce the channel estimation overhead associated with the

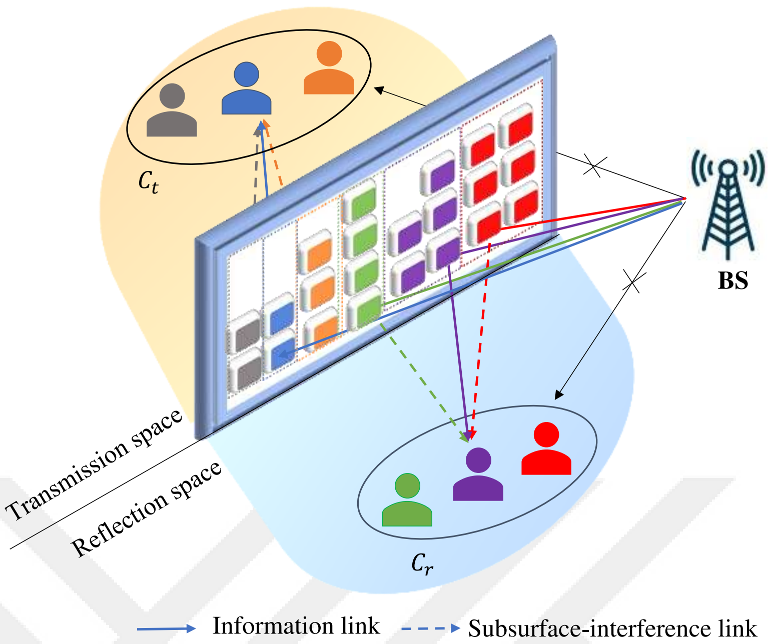

Figure 5.1: A STAR-RIS-assisted NOMA system.

STAR-RIS phase shift design problem and to make the solution for this problem scalable, we partition the STAR-RIS surface among users as follows. To serve the users in both clusters, the RIS is partitioned into two main parts, where the first and second parts contain N_t and N_r elements to serve the users in C_t and C_r, respectively. The elements in the first and second parts are operated in the transmission (t) and reflection (r) modes, respectively, and the whole RIS is assumed to be deployed in the far-field of the BS. Furthermore, the transmission and reflection parts of the RIS are partitioned into subsurfaces, where each subsurface is allocated to serve a specific user in the transmission or reflection region. The BS-U_k direct link is assumed to be blocked by obstacles, where U_k stands for the user k, $k \in \mathbb{K}_\chi$, note that $\chi \in \{t, r\}$, $\mathbb{K}_t = \{1, ..., K_t\}$ and $\mathbb{K}_r = \{K_t + 1, ..., K_t + K_r\}$. The BS-RIS link is assumed to have a Rayleigh fading channel model, where $\mathbf{h}^i \in \mathbb{C}^{N_\chi^i \times 1}$ denotes the BS-ith subsurface channel vector, N_χ^i refers to the number of elements that belong to the ith subsurface in the transmission or reflection part of the RIS, and $\lfloor \mathbf{h}^i \rfloor_n = h^{i,n}$. Here, $h^{i,n} = \sqrt{L_{BS}} \zeta_\chi^{i,n} e^{-j\phi_\chi^{i,n}}$, where L_{BS}, $\zeta_\chi^{i,n}$, and $\phi_\chi^{i,n}$ denote the path gain, channel amplitude, and channel phase, respectively. Note that $\zeta_\chi^{i,n}$ is independently Rayleigh distributed random variable (RV) with a mean $\mathrm{E}\left[\zeta_{\chi}^{i,n}\right] = \frac{\sqrt{\pi}}{2}$, a variance $\mathrm{VAR}\left[\zeta_{\chi}^{i,n}\right] = 1 - \frac{\pi}{4}$, and $\mathrm{E}\left[\left(\zeta_{\chi}^{i,n}\right)^2\right] = 1$. Hence, $h^{i,n}$ can be modelled as complex Gaussian RV with zero mean and a variance L_{BS}, i.e., $h^{i,n} \sim \mathcal{CN}(0, L_{BS})$. Likewise, the RIS-U$_k$ link is assumed to have Rayleigh fading channel model, where the channel vector between the ith subsurface in the transmission or reflection part of the RIS and U_k is denoted by $\mathbf{g}_{\chi,k}^{i}$, where $\lfloor \mathbf{g}_{\chi,k}^{i} \rfloor_n = g_{\chi,k}^{i,n}$ and $\chi \in \{t, r\}$. Here, $g_{\chi,k}^{i,n} = \sqrt{L_{SU,\chi,k}}\eta_{\chi,k}^{i,n} e^{-j\varphi_{\chi,k}^{i,n}}$, where $L_{SU,\chi,k}$, $\eta_{\chi,k}^{i,n}$, and $\varphi_{\chi,k}^{i,n}$ denote the path gain, channel amplitude, and channel phase, respectively. Note that $\eta_{\chi,k}^{i,n}$ is independently Rayleigh distributed RV with a mean $\mathrm{E}\left[\eta_{\chi,k}^{i,n}\right] = \frac{\sqrt{\pi}}{2}$, a variance $\mathrm{VAR}\left[\eta_{\chi,k}^{i,n}\right] = 1 - \frac{\pi}{4}$, and $\mathrm{E}\left[\left(\eta_{\chi,k}^{i,n}\right)^2\right] = 1$. Hence, $g_{\chi,k}^{i,n}$ can be modelled as complex Gaussian RV with zero mean and a variance $L_{SU,\chi,k}$, i.e., $g_{\chi,k}^{i,n} \sim \mathcal{CN}(0, L_{SU,\chi,k})$. All the considered channel coefficients are assumed to be perfectly available at the BS side. Although it is challenging to obtain CSI in RIS-assisted systems, yet, we assume the use of one of the methods proposed in the literature [149, 39, 40]. The transmission/reflection coefficients for the ith subsurface in the transmission or reflection part of the RIS are denoted by the entries of the diagonal matrix $\mathbf{\Theta}_{\chi}^{i} \in \mathbb{C}^{N_{\chi}^{i} \times N_{\chi}^{i}}$, for the nth element we have $\lfloor \mathbf{\Theta}_{\chi}^{i} \rfloor_n = \beta_{\chi}^{i,n} e^{j\theta_{\chi}^{i,n}}$, where $\theta_{\chi}^{i,n} \in [0, 2\pi)$ and $\beta_{\chi}^{i,n} = 1$, under the full transmission/reflection assumption.

Considering PD-NOMA, the BS transmits the signal x, which superimposes the K_t and K_r users' symbols, as follows:

$$\begin{aligned} x &= \sum_{k=1}^{K} \sqrt{a_k P} x_k \\ &= \underbrace{\sum_{k=1}^{K_t} \sqrt{a_k P} x_k}_{K_t \text{ users' symbols}} + \underbrace{\sum_{k=K_t+1}^{K_t+K_r} \sqrt{a_k P} x_k}_{K_r \text{ users' symbols}}, \end{aligned} \tag{5.1}$$

where P is the BS transmit power, x_k and a_k are the user k's symbol and power allocation factor, respectively, $\mathrm{E}\left[|x_k|^2\right] = 1$, $\sum_{k=1}^{K} a_k = 1$. The users are ordered according to their channel gains as $\{U_1, ..., U_{K_t}, U_{K_t+1}, ..., U_{K_t+K_r}\}$, where U_1 and $U_{K_t+K_r}$ are the users with the weakest and strongest channel gains, respectively. Thus, the power allocation coefficients are ordered as $a_1 \geq ... \geq a_k \geq ... \geq a_K$.

By using the SIC process, each user first decodes all strongest signals' users and subtracts them from the received signal, and finally, it decodes its own message. Specifically, the kth user cancels the interfered signals from $U_1, ..., U_{k-1}$ and treats $U_{k+1}, ..., U_K$ as interference. Accordingly, considering successful SIC process at the kth user, the received signal can be expressed as

$$y_k = \underbrace{\left(\mathbf{g}_{\chi,k}^k\right)^T \mathbf{\Theta}_\chi^k \mathbf{h}_\chi^k \sqrt{a_k P} x_k}_{\text{Desired signal term}} + \underbrace{\left(\mathbf{g}_{\chi,k}^k\right)^T \mathbf{\Theta}_\chi^k \mathbf{h}_\chi^k \sum_{l=k+1}^{K} \sqrt{a_l P} x_l}_{\text{User-interference term}}$$
$$+ \underbrace{\sum_{\substack{i\in\mathbb{K}_\chi \\ i\neq k}} \left(\mathbf{g}_{\chi,k}^i\right)^T \mathbf{\Theta}_\chi^i \mathbf{h}_\chi^i x}_{\text{Subsurface-interference term}} + n_k, \tag{5.2}$$

where the first three terms in (5.2) denote the desired signal of the kth user, the interference of other users, and the subsurfaces mutual interference within the transmission or reflection part of the RIS, respectively, while n_k denotes the complex additive white Gaussian noise (AWGN) sample with zero mean and variance σ_k^2 at the kth user, $n_k \sim \mathcal{CN}(0, \sigma_k^2)$.

By letting $r_{\chi,k}^k = \left(\mathbf{g}_{\chi,k}^k\right)^T \mathbf{\Theta}_\chi^k \mathbf{h}_\chi^k$, $r_{\chi,k}^i = \left(\mathbf{g}_{\chi,k}^i\right)^T \mathbf{\Theta}_\chi^i \mathbf{h}_\chi^i$, $\sigma_k^2 = \sigma^2$, and defining $\rho = \frac{P}{\sigma^2}$ is the transmit SNR, then the signal-to-interference-plus-noise ratio (SINR) for user k to detect user j's signal γ_k^j, $\{j \leq k, j \neq K\}$, can be obtained from (5.2) as

$$\gamma_k^j = \frac{\rho \left| r_{\chi,k}^k \right|^2 a_j}{\rho \left| r_{\chi,k}^k \right|^2 \sum_{l=j+1}^{K} a_l + \rho \left| \sum_{\substack{i\in\mathbb{K}_\chi \\ i\neq k}} r_{\chi,k}^i \right|^2 + 1}. \tag{5.3}$$

The phase shift design is considered for each user independent from the others. In this way, each subsurface i tries to maximize γ_k^j by adjusting the phase shifts of its elements to remove the overall BS-STAR-RIS-U$_k$ channel phases, as follows:

$$\theta_\chi^{k,n} = \phi_\chi^{k,n} + \varphi_{\chi,k}^{k,n}. \tag{5.4}$$

Accordingly, changing the CSI of any user and/or the number of users does not affect the phase adjustment of the other users. On the other side, in the joint phase shift design approach adopted in most of the STAR-RIS NOMA works in the literature (for example, [138], [139]), the change in the CSI of even a single individual element requires the redesign of the phase shifts of all the remaining elements in the whole STAR-RIS surface. This gives the proposed partitioning scheme scalability in terms of the phase shift design at the expense of some performance loss compared to the joint phase shift design approach.

By considering (5.4), $\left|r^k_{\chi,k}\right|^2$ and $\left|\sum_{\substack{i\in\mathbb{K}_\chi\\ i\neq k}} r^i_{\chi,k}\right|^2$ can be re-expressed, respectively, as

$$\left|r^k_{\chi,k}\right|^2 = \left|\sqrt{L_k}\sum_{n=1}^{N^k_\chi}\zeta^{k,n}_\chi\eta^{k,n}_{\chi,k}\right|^2, \tag{5.5}$$

$$\left|\sum_{\substack{i\in\mathbb{K}_\chi\\ i\neq k}} r^i_{\chi,k}\right|^2 = \left|\sqrt{L_k}\sum_{\substack{i\in\mathbb{K}_\chi\\ i\neq k}}\sum_{n=1}^{N^i_\chi}\zeta^{i,n}_\chi\eta^{i,n}_{\chi,k}e^{j\Phi^{i,n}_{\chi,k}}\right|^2, \tag{5.6}$$

where $\Phi^{i,n}_{\chi,k} = \theta^{i,n}_\chi - \phi^{i,n}_\chi - \varphi^{i,n}_{\chi,k}$, $L_k = L_{BS}L_{SU,\chi,k}$ is the overall path gain of the BS-STAR-RIS-U_k link, which can be expressed as

$$L_k = \frac{\rho_0^2}{d_{BS}^{\alpha_{BS}}d_{SU,\chi,k}^{\alpha_{SU}}}. \tag{5.7}$$

Here, d_{BS} is the distance between the BS and STAR-RIS and $d_{SU,\chi,k}$ is the distance between the STAR-RIS and the kth user in the transmission or reflection group. Additionally, ρ_0, α_{BS}, and α_{SU} are the path gain at a reference distance of 1 meter, the path loss exponents associated with the BS-STAR-RIS and the STAR-RIS-U_k links, respectively.

By considering SIC, the SINR expression for user k, $k > 1$, after successfully detecting and subtracting the $k-1$ users' signals before it, can be obtained as

$$\gamma_k = \frac{\rho\left|r^k_{\chi,k}\right|^2 a_k}{\rho\left|r^k_{\chi,k}\right|^2\sum_{l=k+1}^{K}a_l + \rho\left|\sum_{\substack{i\in\mathbb{K}_\chi\\ i\neq k}} r^i_{\chi,k}\right|^2 + 1}. \tag{5.8}$$

For the Kth user, we have

$$\gamma_K = \frac{\rho\left|r^K_{\chi,K}\right|^2 a_K}{\rho\left|\sum_{\substack{i\in\mathbb{K}_\chi\\ i\neq K}} r^i_{\chi,K}\right|^2 + 1}. \tag{5.9}$$

Considering the special case of $(K_t, K_r) = (1, 1)$, where one user is located in the transmission region and the other user is located in the reflection region, the SINR of the U_1 to detect its own signal is given by

$$\gamma_1 = \frac{\rho\left|r_{t,1}^1\right|^2 a_1}{\rho\left|r_{t,1}^1\right|^2 a_2 + 1}, \tag{5.10}$$

and the SINR of the U_2 to detect the U_1's signal is given by

$$\gamma_2^1 = \frac{\rho\left|r_{r,2}^2\right|^2 a_1}{\rho\left|r_{r,2}^2\right|^2 a_2 + 1}, \tag{5.11}$$

finally, the SNR of the U_2 to detect its own signal is given by

$$\gamma_2 = \rho\left|r_{r,2}^2\right|^2 a_2. \tag{5.12}$$

5.3 Outage Probability Analysis

In order to reveal the benefits of the proposed STAR-RIS-assisted NOMA system, we examine its performance analytically in terms of OP under different user deployments, as follows.

The OP of user k is the probability that the user cannot successfully detect and remove the signals of the $k-1$ users before it and/or cannot detect its own signal. Let γ_{th}^j denote the SINR threshold for user k to detect user j's signal, $1 \leq j \leq k$, thus, $E_{k\leftarrow j} = \left\{\gamma_k^j < \gamma_{th}^j\right\}$ denotes the event that user k cannot detect user j's signal. Thus, the OP for user k can be obtained as

$$OP_k = 1 - P_r\left(E_{k\leftarrow 1}^c \cap ... \cap E_{k\leftarrow k}^c\right), \tag{5.13}$$

where $E_{k\leftarrow j}^c$ is the complement of the event $E_{k\leftarrow j}$.

Proposition 4. *The OP of the kth user is given by*

$$OP_k\left(\varrho_k^*\right) = 1 - Q_{\frac{1}{2}}\left(\frac{\mu_k}{\nu_k}, \frac{\sqrt{\varrho_k^*}}{\nu_k}\right) + \left(\frac{u_k^2}{\nu_k^2 + u_k^2}\right)^{\frac{1}{2}} e^{\frac{\varrho_k^*}{2u_k^2}} e^{-\frac{\mu_k^2}{2\left(\nu_k^2+u_k^2\right)}} \times Q_{\frac{1}{2}}\left(\frac{\mu_k}{\nu_k}\sqrt{\frac{u_k^2}{\nu_k^2+u_k^2}}, \sqrt{\frac{\varrho_k^*\left(\nu_k^2+u_k^2\right)}{\nu_k^2 u_k^2}}\right), \tag{5.14}$$

where $\varrho_j^* = \max\limits_{j=1,\ldots,k}\{\varrho_j\}$, $\varrho_j = \frac{\gamma_{th}^j}{\rho a_j - \rho\gamma_{th}^j \sum_j}$, $\mu_k = \frac{\pi}{4}\sqrt{L_k}N_\chi^k$, $\sum_j = \sum_{l=j+1}^K a_l$, $\nu_k = \sqrt{\left(1-\frac{\pi^2}{16}\right)L_k N_\chi^k}$ *and* $u_k = \sqrt{0.5\rho\varrho_k^* L_k\left(N_\chi - N_\chi^k\right)}$.

Proof: By considering (5.3), $E_{k\leftarrow j}^c$ can be expressed as

$$E_{k\leftarrow j}^c = \left\{\frac{\rho\left|r_{\chi,k}^k\right|^2 a_j}{\rho\left|r_{\chi,k}^k\right|^2 \sum_j + \rho\left|\sum_{\substack{i\in\mathbb{K}_\chi\\ i\neq k}} r_{\chi,k}^i\right|^2 + 1} > \gamma_{th}^j\right\} \overset{(c)}{=} \left\{\left|r_{\chi,k}^k\right|^2 > \rho\varrho_j\left|\sum_{\substack{i\in\mathbb{K}_\chi\\ i\neq k}} r_{\chi,k}^i\right|^2 + \varrho_j\right\}, \tag{5.15}$$

where $\sum_j = \sum_{l=j+1}^K a_l$, $\varrho_j = \frac{\gamma_{th}^j}{\rho a_j - \rho\gamma_{th}^j \sum_j}$ and the step (c) is obtained under the condition of $a_j > \gamma_{th}^j \sum_{l=j+1}^K a_l$. Now, substituting (5.15) into (5.13) and defining $\varrho_j^* = \max\limits_{j=1,\ldots,k}\{\varrho_j\}$, then the OP of the kth user can be stated as

$$OP_k = 1 - P_r\left(\left|r_{\chi,k}^k\right|^2 > \rho\varrho_k^*\left|\sum_{\substack{i\in\mathbb{K}_\chi\\ i\neq k}} r_{\chi,k}^i\right|^2 + \varrho_k^*\right) = P_r\left(\left|r_{\chi,k}^k\right|^2 < \rho\varrho_k^*\left|\sum_{\substack{i\in\mathbb{K}_\chi\\ i\neq k}} r_{\chi,k}^i\right|^2 + \varrho_k^*\right) = F_{R_k}\left(\varrho_k^*\right). \tag{5.16}$$

Here, $R_k = \left|r_{\chi,k}^k\right|^2 - \rho\varrho_k^*\left|\sum_{\substack{i\in\mathbb{K}_\chi\\ i\neq k}} r_{\chi,k}^i\right|^2 = \left|r_{\chi,k}^k\right|^2 - \left|\sqrt{\rho\varrho_k^*}\sum_{\substack{i\in\mathbb{K}_\chi\\ i\neq k}} r_{\chi,k}^i\right|^2$. It is worth noting that the BS-STAR-RIS-U_k cascaded channel gains are sorted as $\left|r_{\chi,1}^1\right|^2 \leq$

$\ldots \leq \left|r^{k}_{\chi,k}\right|^2 \leq \ldots \leq \left|r^{k}_{\chi,K}\right|^2$, where this users' order can be always guaranteed by allocating the proper START-RIS elements for each user.

Noting $\zeta^{i,n}_{\chi}$ and $\eta^{i,n}_{\chi,k}$ are independently Rayleigh distributed random variables (RVs) with a mean $\mathrm{E}\left[\zeta^{i,n}_{\chi}\right] = \mathrm{E}\left[\eta^{i,n}_{\chi,k}\right] = \frac{\sqrt{\pi}}{2}$ and a variance $\mathrm{VAR}\left[\zeta^{i,n}_{\chi}\right] = \mathrm{VAR}\left[\eta^{i,n}_{\chi,k}\right] = 1-\frac{\pi}{4}$. Then, $\mathrm{E}\left[\zeta^{i,n}_{\chi}\eta^{i,n}_{\chi,k}\right] = \frac{\pi}{4}$ and $\mathrm{VAR}\left[\zeta^{i,n}_{\chi}\eta^{i,n}_{\chi,k}\right] = 1-\frac{\pi^2}{16}$. According to the CLT, for $N^k_{\chi} >> 1$, the cascaded channel $r^k_{\chi,k}$ converges to Gaussian RV. Thus,

$$r^{k}_{\chi,k} \sim \mathcal{N}\left(\frac{\pi}{4}\sqrt{L_k}N^k_{\chi}, \left(1-\frac{\pi^2}{16}\right)L_k N^k_{\chi}\right). \tag{5.17}$$

In addition, for $N_{\chi} - N^k_{\chi} >> 1$, $\sum_{i\neq k}^{K_{\chi}} r^i_{\chi,k}$ converges to Gaussian RV. So,

$$\sum_{\substack{i\in\mathbb{K}_{\chi}\\ i\neq k}} r^{i}_{\chi,k} \sim \mathcal{CN}\left(0, L_k\left(N_{\chi}-N^k_{\chi}\right)\right). \tag{5.18}$$

It is noticed that $\left|r^k_{\chi,k}\right|^2$ is a non-central chi-square RV with one degree of freedom and $\left|\sum_{\substack{i\in\mathbb{K}_{\chi}\\ i\neq k}} r^i_{\chi,k}\right|^2$ is a central chi-square RV with two degrees of freedom. Hence, R_k is the difference of a non-central and central independent chi-square RVs and by using its corresponding CDF $F_{R_k}(x)$ [150], the OP of the kth user can be expressed in closed-form as in (5.14). ■

In order to gain further insights on the OP performance, we give the following Corollary.

Corollary 4. *Considering the asymptotic behavior of OP, for $\rho \to \infty$, i.e., $\varrho^*_k \to 0$, OP is given by*

$$OP^{\infty}_k = \left(\frac{\tilde{u}^2_k}{\nu^2_k + \tilde{u}^2_k}\right)^{\frac{1}{2}} e^{-\frac{\mu^2_k}{2\left(\nu^2_k+\tilde{u}^2_k\right)}}, \tag{5.19}$$

Proof: The proof follows directly from Proposition 4 by considering that $\varrho^*_k = 0$, then we have $Q_{\frac{1}{2}}\left(\frac{\mu_k}{\nu_k}, \frac{\sqrt{0}}{\nu_k}\right) = 1$, $\tilde{u}_k = \sqrt{0.5\varrho^{\dagger}_k L_k\left(N_{\chi}-N^k_{\chi}\right)}$ and $\varrho^{\dagger}_k = \max\limits_{j=1,\ldots,k}\left\{\frac{\gamma^j_{th}}{a_j-\gamma^j_{th}\sum_j}\right\}$. ■

From Corollary 4, it can be noticed that the OP reaches an error floor due to subsurface-interference when the transmit SNR increases.

Proposition 5. *In the case of a two-user STAR-RIS-assisted NOMA network, $(K_t, K_r) = (1, 1)$, the OP of the kth user can be expressed in closed-form as*

$$OP_k = 1 - Q_{\frac{1}{2}}\left(\frac{\mu_k}{\nu_k}, \frac{\sqrt{\varrho_k^*}}{\nu_k}\right). \tag{5.20}$$

Here, considering the asymptotic behavior, for $\rho \to \infty$, i.e., $\varrho_k^* \to 0$, we have $OP_k = 0$.

Proof: By using (5.11), the OP of the kth user can be stated as

$$\begin{aligned} OP_k &= P_r\left(\frac{\rho\left|r_{\chi,k}^k\right|^2 a_j}{\rho\left|r_{\chi,k}^k\right|^2 \sum_j +1} < \gamma_{th}^j\right) \\ &= P_r\left(\left|r_{\chi,k}^k\right|^2\left(\rho a_j - \rho\gamma_{th}^j \sum_j\right) < \gamma_{th}^j\right) \\ &= P_r\left(\left|r_{\chi,k}^k\right|^2 < \varrho_k^*\right) \\ &= F_{\left|r_{\chi,k}^k\right|^2}\left(\varrho_k^*\right). \end{aligned} \tag{5.21}$$

Recall, $\left|\mathbf{r}_{\chi,k}^k\right|^2$ is a non-central chi-square RV with one degree of freedom and its CDF corresponds to the OP expression given in (5.20). ■

From Proposition 5 , it can be noticed that in the case of a two-user STAR-RIS-assisted NOMA network, since there is no subsurface-interference, the OP becomes zero in the high SNR region.

5.4 Partitioning Algorithms

In this section, we provide the partitioning algorithms used to allocate STAR-RIS elements for different users on both sides of the surface. Note that although the general structure of the proposed algorithms is motivated by the one in [20], they are different in the following key aspects. First, unlike the algorithms in [20], which aim to maximize user fairness [Section IV, Eq. (20a)], the proposed algorithms aim to maximize the users' sum rate while guaranteeing quality-of-service (QoS) requirements for all users. In particular, Algorithm 5.4.1 guarantees a unified outage probability requirement for all users, while Algorithm 5.4.1 considers the different rate requirements for individual users. Furthermore, in Algorithm 5.4.1, the OP expression is totally different from the one in the pointed-out work due to obviously different systems models. In what follows, we present the partitioning algorithms considering different users' deployments.

5.4.1 Multi-User STAR-RIS-Assisted NOMA System

In the case of a multi-user STAR-RIS-assisted NOMA system, our partitioning algorithm is carried out in two stages. First, the STAR-RIS surface is partitioned into two parts, transmission and reflection parts, which contain all the elements that operate in transmission and reflection mode, respectively. Second, each STAR-RIS part is partitioned into subsurfaces, where each subsurface is allocated to serve a specific user located on the side of that part. In the following, both stages are explained in detail.

At the first stage, we assign temporary numbers of transmitting ($\tilde{N}_t$) and reflecting ($\tilde{N}_r$) STAR-RIS elements for the transmission and reflection STAR-RIS parts, respectively. Furthermore, the mode of the remaining STAR-RIS elements ($N - \tilde{N}_t - \tilde{N}_r$) will be selected further according to sum-rate and QoS requirements. $\tilde{N}_t$ and $\tilde{N}_r$ can be simply calculated, respectively as $\tilde{N}_t = K_t N_{thr}$ and $\tilde{N}_r = K_r N_{thr}$, where N_{thr} is the minimum number of STAR-RIS elements that needs to be allocated to each user in order to protect it from the subsurface-interference. We use Algorithm 5.4.1 to obtain the value of N_{thr} [20]. Particularly, Algorithm 5.4.1 utilizes a probabilistic approach, where in order to protect the users from the mutual sub-surfaces interference, a common minimum OP is guaranteed for all users by finding the proper N_{thr}. This is achieved by keeping updating N_{thr} until the OP gets below the predetermined threshold ϵ. Note that the asymptotic OP in (5.19) is used to capture the interference effect only and ignore the different SNR levels at different users.

On the other hand, at the second stage, we aim to determine the proper number of transmitting/reflecting STAR-RIS elements that is required for each user to

Algorithm 7 Determination of minimum number of STAR-RIS elements that needs to be allocated to each user (N_{thr}).

Require: $L_{SU,\chi,k}$, K, N, ϵ.

Initialize $N_{thr} = 1$.

repeat

$\mu_k = \frac{\pi}{4}\sqrt{L_k} N_{thr}, \nu_k = \sqrt{\left(1 - \frac{\pi^2}{16}\right) L_k N_{thr}}$, $\tilde{u}_k = \sqrt{0.5 \varrho_k^{\dagger} L_k \left(N - N_{thr}\right)}$.

Obtain the asymptotic OP from (5.19):

$OP_k^{\infty} = \left(\frac{\tilde{u}_k^2}{\nu_k^2 + \tilde{u}_k^2}\right)^{\frac{1}{2}} e^{-\frac{\mu_k^2}{2\left(\nu_k^2 + \tilde{u}_k^2\right)}}$

$N_{thr} = N_{thr} + 1$.

while $OP_k^{\infty} \leq \epsilon$ and $K N_{thr} \leq N$.

return $N_{thr} = N_{thr} - 1$.

maximize the sum-rate and guarantee QoS for individual users. To achieve this goal, at first, Algorithm 5.4.1 is used to determine the number of STAR-RIS elements that need to be added to N_{thr} in order to fulfill the QoS requirement R_k^{min} for each user. According to (5.5), the cascaded channels' gains are proportionate with the number of transmitting or reflecting elements. Therefore, if the cascaded

channels' gains are sorted as $\left|r_{\chi,1}^1\right|^2 \leq ... \leq \left|r_{\chi,k}^k\right|^2 \leq ... \leq \left|r_{\chi,K}^k\right|^2$, then the transmitting/reflecting STAR-RIS elements assigned for the users have to be also ordered as $N_\chi^1 \leq ... \leq N_\chi^k \leq ... \leq N_\chi^K$, which is ensured by Algorithm 5.4.1. Next, in order to maximize the sum-rate, the remaining STAR-RIS elements are added to the closest user to the BS, U_K, which can eliminate the interference of all other users. At the end, the proper values of N_t and N_r are updated, respectively as $N_t = \sum_{k=1}^{K_t} N_t^k$ and $N_r = \sum_{k=K_t+1}^{K} N_r^k$.

5.4.2 Two-User STAR-RIS-Assisted NOMA System

For the case of a two-user STAR-RIS-assisted NOMA system, one user is located in C_t and the other user is located in C_r. Since, in this case, there is no subsurface interference, we skip the first stage of the partitioning process and start directly

Algorithm 8 Determination of proper number of transmitting/reflecting STAR-RIS elements to be assigned to U_k (N_χ^k).

Require: N_{thr}, R_k^{min}.

1: Initialize $N_\chi^k = N_\chi^{k-1}$. If $k = 1$, then $N_\chi^1 = N_{thr}$.
2: **repeat**
3: Obtain the Ergodic rate in the high SNR values:
$R_k = \mathrm{E}\left[\log_2\left(1 + \gamma_k^k\right)\right]$. Perform the expectation over 10^4 random channel realizations.
4: $N_\chi^k = N_\chi^k + 1$.
5: **while** $R_k < R_k^{min}$.
6: **return** $N_\chi^k = N_\chi^k - 1$.

from the second one. That is, Algorithm 5.4.1 is directly applied to fulfill the QoS requirement for U_1, with $N_{thr} = 1$ and (5.10) is used to obtain γ_k^k. Next, the remaining elements need to be allocated to U_2, assuming N is large enough to fulfill both users' QoS requirements.

Remark 4. *As seen from Algorithms 1 and 2, the partitioning scheme does not depend on the instantaneous CSI; rather, it needs to be updated only when K_χ, power allocation at the BS, or distances of users from the STAR-RIS change, where these parameters slowly change over several coherence channel intervals. Furthermore, after the partitioning stage and for a given channel coherence interval, BS needs to know the CSI of the BS-STAR-RIS link, which is the same for all users, and the STAR-RIS (kth sub-surface)-U_k link, for each individual user k. This means that, without loss of generality, for the STAR-RIS-U_k links, a maximum of N pilot signals are required at the channel estimation stage. Compared to the joint phase shift design for all users (where NK pilot signals are required [149]), an effective reduction in the channel estimation overhead is obtained by the proposed system. Furthermore, from Algorithms 1 and 2, the phase shift design problem for all users is scalable as K_χ changes.*

Table 5.1: Parameters used in simulations for the three cases.

Case	Users locations	Power allocation coefficients
1	U_1 in C_t, U_2 in C_r	$(a_1, a_2) = (0.6, 0.4)$.
2	U_1 and U_2 in C_t, U_3 in C_r	$(a_1, a_2, a_3) = (0.6, 0.3, 0.1)$.
3	U_1 in C_t, U_2 and U_3 in C_r.	$(a_1, a_2, a_3) = (0.6, 0.3, 0.1)$

Case	Targeted SINR	Distances (m)
1	$(\gamma_{th}^1, \gamma_{th}^2) = (1, 1)$	$(d_{BS}, d_{SU,t,1}, d_{SU,r,2}) = (50, 50, 40)$
2	$(\gamma_{th}^1, \gamma_{th}^2, \gamma_{th}^3) = (0.7, 0.7, 0.7)$	$(d_{BS}, d_{SU,t,1}, d_{SU,t,2}, d_{SU,r,3}) = (20, 50, 40, 30)$
3	$(\gamma_{th}^1, \gamma_{th}^2, \gamma_{th}^3) = (0.5, 0.5, 0.3)$	$(d_{BS}, d_{SU,t,1}, d_{SU,r,2}, d_{SU,r,3}) = (20, 50, 40, 30)$

5.4.3 Complexity Analysis

In terms of the complexity analysis, it can be readily seen that both algorithms have a finite maximum number of iterations that is upper-bounded by N, which guarantees their convergence. Furthermore, considering the required number of complex multiplications (CMs) as a metric, the complexity level of Algorithm 5.4.1 can be upper-bound by $\mathcal{O}(N^3)$. This can be obtained by noting that Algorithm 5.4.1 requires the calculation of γ_k^k which, in turn, includes the vector-matrix multiplication of $r_{\chi,k}^i, i \neq k$, that requires N^2 CMs for every single iteration. On the other side, Algorithm 5.4.1 has no CM, therefore; its complexity level depends on the type of the used computational algorithm. Accordingly, the proposed Algorithms 1 and 2, require the same complexity level as the ones in [20].

5.5 Simulation Results

In this section, the performance of the considered STAR-RIS-assisted NOMA system is presented via computer simulations in order to validate our theoretical analysis. We consider three cases of users' deployment, namely, $(K_t, K_r) = (1, 1)$, $(K_t, K_r) = (2, 1)$ and $(K_t, K_r) = (1, 2)$. For each case, user locations, power allocation coefficients[2], corresponding target threshold SINR values, distances between the BS and STAR-RIS, and STAR-RIS and users are given in Table 5.1. For all cases, the path gain at a reference distance of 1 meter is assumed as $\rho_0 = -30$ dB and the path loss exponents associated with the BS-STAR-RIS and the STAR-RIS-user links are given as $(\alpha_{BS}, \alpha_{SU}) = (2, 2)$ unless otherwise stated. Furthermore, we compare the proposed system with two benchmark systems, namely the classical OMA and PD-NOMA systems by considering the same simulation parameters. Particularly, for the classical PD-NOMA system, we use the same power allocation that we use in the proposed system. On the other side, for the classical OMA system, we use the time division multiple access (TDMA) scheme, where the time slot allocation equals the power allocation in NOMA case; therefore, we always have the time slots $t_1 = a_1$, $t_2 = a_2$, and $t_3 = a_3$. For the benchmark systems, the BS-U_k path gain is obtained as $L_k = \frac{\rho_0}{d_k^{\alpha}}$, where d_k is the BS-U_k distance and $\alpha = 3.5$ [152].

5.5.1 Case 1: $(K_t, K_r) = (1, 1)$

As shown in Fig. 5.2(a), our theoretical result in (5.20) using the CLT is considerably accurate for increasing N values and the OP performance enhances as number of STAR-RIS elements increases. For instance, to achieve $OP_1 = 10^{-3}$, 10 dBm and 5 dBm gain advantages are obtained in P for $N = 128$ over $N = 64$ and $N = 256$ over 128, respectively. On the other hand, to achieve $OP_2 = 10^{-3}$, about 7.5 dBm and 7 dBm gain advantages are observed in P for $N = 128$ over $N = 64$ and $N = 256$ over 128, respectively. Furthermore, the effect of phase errors is shown to significantly reduce the OP performance as the concentration parameter κ decreases (flatter error distribution)[3], yet, the performance of the proposed system is still

[2]Here, we focus on NOMA with fixed power allocation (F-NOMA), where a fixed amount of transmit power is allocated to each user. In particular, for the two users, the power-allocation coefficients are denoted by a_1 and a_2, where these coefficients are fixed, and $a_1 + a_2 = 1$ and $a_1 \geq a_2$. Likewise, for the three users, $a_1 + a_2 + a_3 = 1$ and $a_1 \geq a_2 \geq a_1$ [151].

[3]We consider Von Mises distribution to simulate the phase errors resulting from phase estimation errors and/or phase quantization in the case of discrete phase shifts [153].

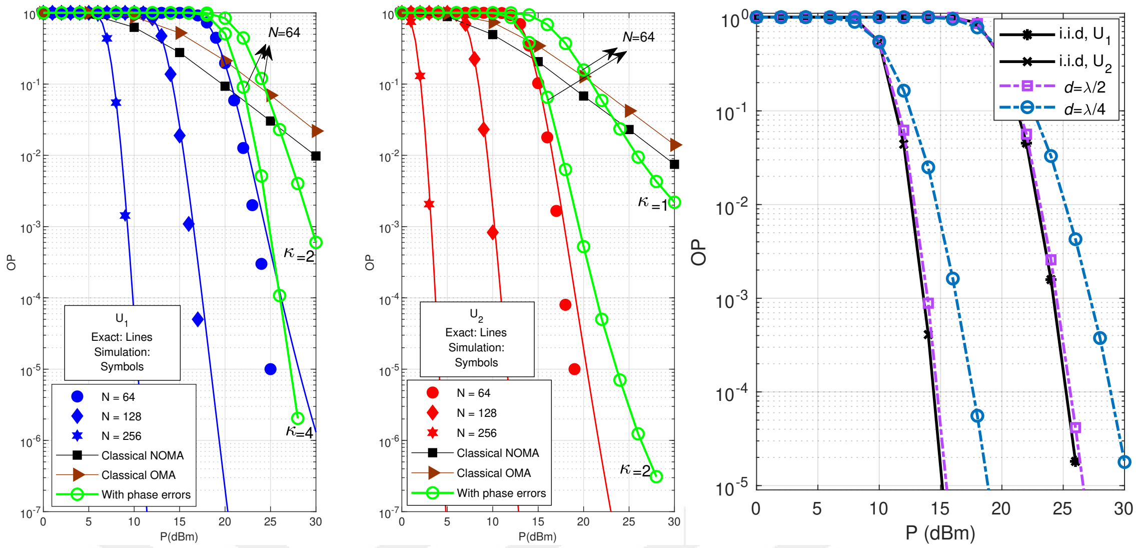

(a) (b)

Figure 5.2: Outage probability performance in case of $(K_t, K_r) = (1, 1)$ (a) under different N values and with/without phase errors, and (b) under spatial correlation effect with $N_t = 24$ and $N_r = 40$, STAR-RIS inter-element spacing d, and 1.8 GHz operating frequency with λ wavelength.

superior to the benchmark ones at the high P region. In Fig. 5.2(b), the spatial correlation effect is shown for two different inter-element spacing values d, where the spatial correlation model proposed for the RIS in [154] is used. Note that, for $d = \lambda/2$, the curve obtained under the spatial correlation assumption is close to the one under the independent and identically distributed (i.i.d.) assumption of the RIS channels, which makes the theoretical OP obtained in Section 5.3 (under the i.i.d. assumption) applicable to the spatial correlation case. Furthermore, the spatial correlation (as d decreases) is shown to have a negative impact on the OP performance due to the lack of diversity in the RIS channels.

Note that in Figs. 5.2-5.3, according to Algorithm 5.4.1, the number of the transmitting STAR-RIS elements for U_1 and the number of the reflecting STAR-RIS elements for U_2 are determined, respectively as $N_t^1 = \{26, 51, 102\}$ and $N_r^2 = \{38, 77, 154\}$. We can clearly notice from Fig. 5.3 that the sum-rate proportionally increases as P increases. This is because the sum-rate depends remarkably on

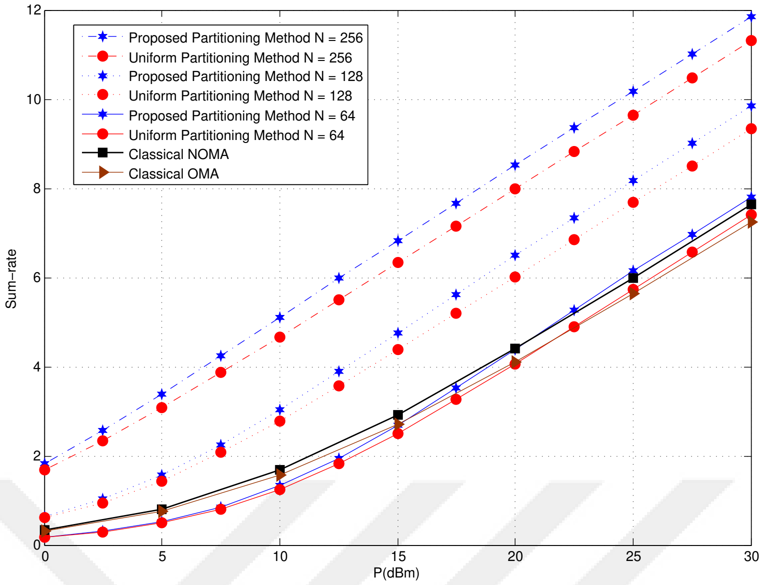

Figure 5.3: The sum-rate versus P for different N in the case of $(K_t, K_r) = (1, 1)$.

Table 5.2: Number of STAR-RIS elements assigned for each user in Case 2 when $N \in \{60, 90, 120, 150\}$.

N	N_t^1	N_t^2	N_r^3	N_t	N_r
60	16	20	24	36	24
90	24	30	36	54	36
120	32	40	48	72	48
150	36	50	64	86	64

the strongest user (U_2) and in this case, U_2 does not suffer from any subsurface-interference. In addition, the proposed partitioning method outperforms the uniform partitioning method. Also, from both figures, we can see the superiority of our proposed system over the classical NOMA and OMA particularly by increasing the total number of the elements of STAR-RIS.

5.5.2 *Case 2:* $(K_t, K_r) = (2, 1)$

Figs. 5.4 and 5.5 demonstrate the performance of the STAR-RIS-assisted NOMA network in terms of OP and sum-rate, respectively for different number of STAR-

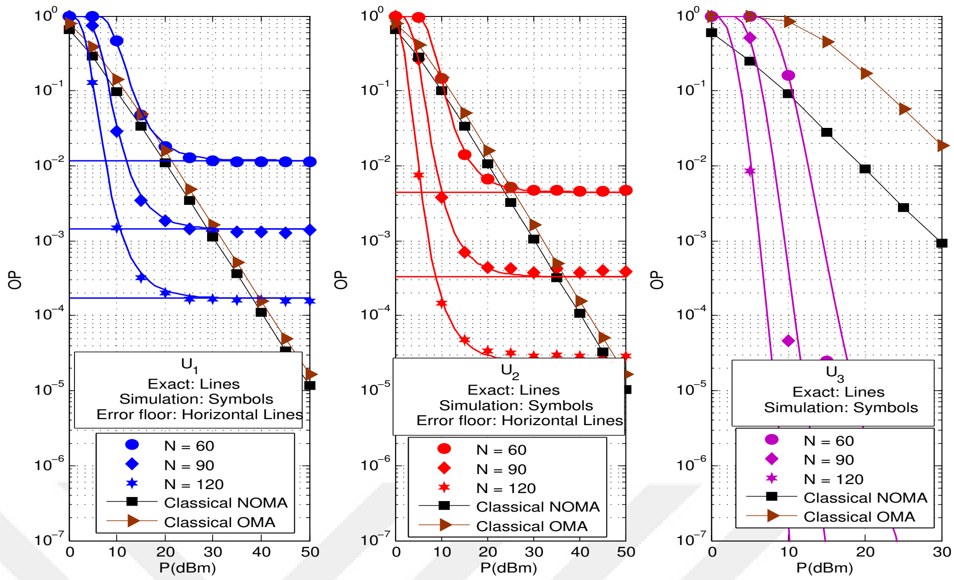

Figure 5.4: The outage probability versus P for different N in the case of $(K_t, K_r) = (2, 1)$.

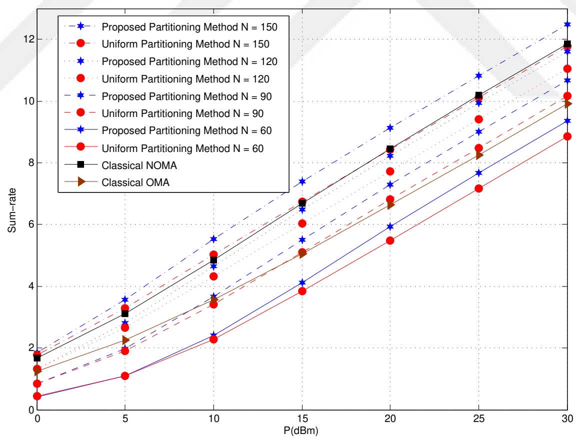

Figure 5.5: The sum-rate versus P for different N in the case of $(K_t, K_r) = (2, 1)$.

RIS elements. The number of transmitting/reflecting STAR-RIS elements assigned for each user is provided in Table 5.2. It can be seen from Fig. 5.4 that when P increases, the OP_1 and OP_2 reach an error floor due to subsurface-interference. On the other hand, OP_3 does not reach error floor since U_3 does not suffer from any subsurface-interference. Compared to the classical NOMA and OMA, the proposed system is always better for U_3 in the whole P range as well as U_1 and U_2 except in

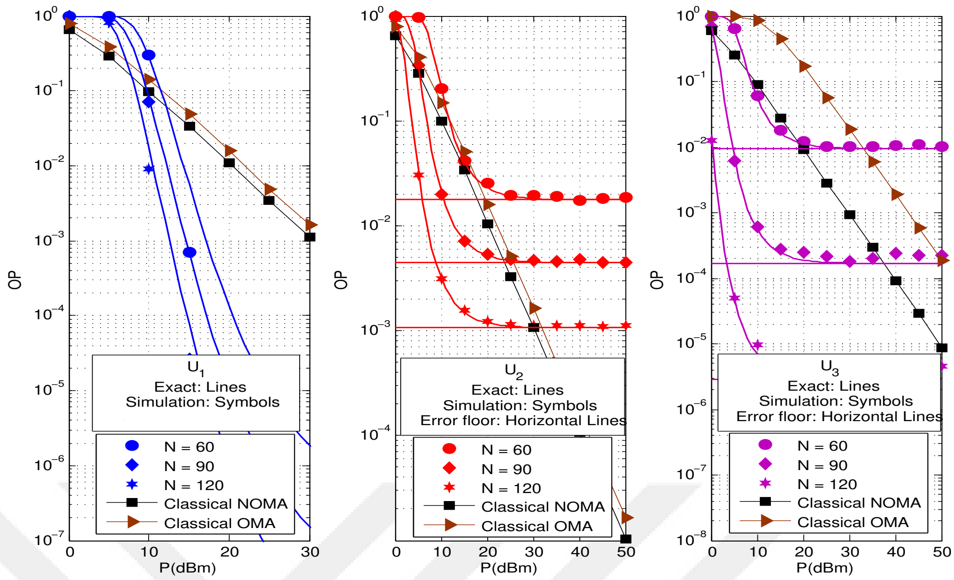

Figure 5.6: The outage probability versus P for different N in the case of $(K_t, K_r) = (1, 2)$.

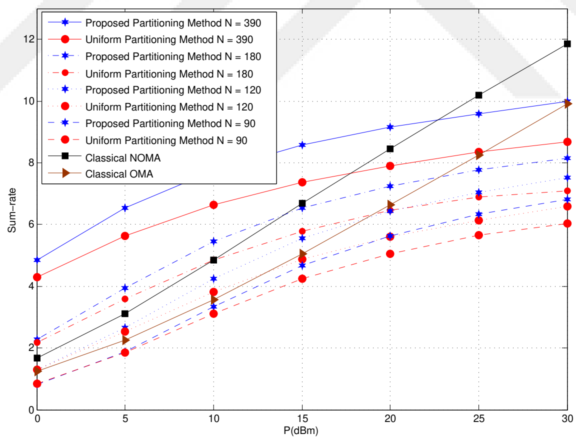

Figure 5.7: The sum-rate versus P for different N in the case of $(K_t, K_r) = (1, 2)$.

the high P regime. As shown in Fig. 5.5, the sum-rate still proportionally increases as P increases since the strongest user (U_3) does not suffer from the subsurface-interference. Furthermore, the STAR-RIS requires about $N = 90$ and $N = 150$ elements to outperform classical OMA and classical NOMA, respectively.

Table 5.3: Number of STAR-RIS elements assigned for each user in Case 3 when $N \in \{60, 90, 120, 180\}$.

N	N_t^1	N_r^2	N_r^3	N_t	N_r
60	16	20	24	16	44
90	19	30	41	19	71
120	22	40	58	22	98
180	35	60	85	35	145
390	52	130	208	52	338

5.5.3 Case 3: $(K_t, K_r) = (1, 2)$

Figs. 5.6 and 5.7 present the OP and sum-rate performance of the STAR-RIS-assisted NOMA network for different number of STAR-RIS elements. The number of transmitting/reflecting STAR-RIS elements assigned for each user is provided in Table 5.3. From Fig. 5.6, it is clearly observed that the OP_2 and OP_3 reach an error floor due to subsurface-interference. On the other hand, the OP_1 does not reach error floor since U_1 does not suffer from any subsurface-interference. As seen from Fig. 5.7, the sum-rate saturates in the high P region. This is because the strongest user (U_3) suffers from subsurface-interference, which significantly affect the sum-rate performance. The proposed partitioning approach is also superior to the uniform partitioning approach. Although classical NOMA and OMA outperform the proposed system in the high SNR region, with a large number of STAR-RIS elements, the proposed system can outperform both classical systems. For instance, the proposed system requires more than $N = 390$ elements to outperform both classical systems.

5.6 Conclusion

In this work, we have proposed a STAR-RIS-assisted NOMA network where the MS operating protocol is utilized to extend the coverage area of classical RIS. Next, we have designed a novel STAR-RIS partitioning algorithm to serve NOMA users on both sides of the STAR-RIS. The proposed algorithm aims to determine the proper number of transmitting/reflecting STAR-RIS elements that requires to be allocated to each user to maximize the sum-rate while fulfilling the QoS requirement. For different NOMA user deployments, we have provided a closed-form expression of the exact OP. Then, a asymptotic analysis has been conducted in order to study the system performance at the high SNR. We note that the OP reaches an error floor in the high SNR region due to the impact of the STAR-RIS's subsurface-interference and it can be reduced by increasing the number of STAR-RIS elements. Finally, simulation results have validated that the proposed partitioning algorithm outperforms the uniform partitioning method. Moreover, the proposed system can achieve better performance in terms of OP and sum-rate than the classical NOMA and OMA systems. We conclude that the use of STAR-RIS NOMA has the potential to provide an enhanced version of classical NOMA systems, where unlike the classical RIS, the STAR-RIS doubled the coverage area. Furthermore, in addition to the STAR-RIS MS mode, our proposed partitioning scheme has added more degrees of freedom to the system design, compared to the classical PD-NOMA protocol, by flexibly and dynamically allocating the physical resources (STAR-RIS elements) among users. In the future, we extend the proposed system to STAR-RIS aided NOMA networks with multiple antennas at the BS.

Chapter 6

PHASE SHIFT-FREE PASSIVE BEAMFORMING FOR RISs

One of the main aspects of using RISs is the exploitation of the so-called passive beamforming (PB), which is carried out by adjusting the reflection coefficients (mainly the phase shifts) of the individual RIS elements. However, practically, this individual phase shift adjustment is associated with many issues in hardware implementation, limiting the RIS achievable gain. In this chapter, we propose a low-cost, phase shift-free and novel PB scheme by only optimizing the on/off states of the RIS elements while fixing their phase shifts. The proposed PB scheme is shown to achieve the same scaling law (quadratic growth with the RIS size) for the signal-to-noise ratio as in the classical phase shift-based PB scheme, yet, with far less sensitivity to spatial correlation and phase errors. We provide a unified mathematical analysis that characterizes the performance of the proposed PB scheme and obtain the outage probability for the considered RIS-assisted system. Based on the provided computer simulations, the proposed PB scheme is shown to have a clear superiority over the classical one under different performance metrics.

The rest of the chapter is organized as follows. In Section 6.1, we provide the literature works related to the reflection phase-based and amplitude-based PB, followed by the motivation and main contributions in Section 6.2. Section 6.3 introduces the general systems' settings and the considered practical phase shift model. In Section 6.4, we formulate the proposed phase shift-free PB problem, followed by our proposed solution in Section 6.5. In Section 6.6, we provide a unified mathematical framework to assess the proposed PB scheme. Comprehensive computer simulations are presented in Section 6.7 and, finally, we conclude in Section 6.8.

6.1 Related Works

In this section, we first provide the studies related to the reflection phase shift-based PB, followed by the studies related to the reflection amplitude-based PB.

6.1.1 Studies on Phase Shift-Based PB Schemes

In RIS-assisted systems, the PB design is achieved by independently adjusting the reflection coefficient associated with each RIS element to align the reflected signals in a particular direction. This can be achieved, for example, by using a tunable impedance that can be continuously adjusted through mixed-signal integrated circuits (ICs) [155] or multilayer surface design [156]. In vast majority of RIS-assisted systems discussed in the literature, the adopted classical PB design fixes the reflection amplitude to unity (to achieve full reflection power) and adjusts only the phase shift associated with each RIS element. The main practical issues related to the classical phase shift-based PB design are discussed next from the hardware implementation perspective.

It is possible, yet, practically challenging to adjust the phase of each RIS element continuously as this requires a sophisticated and expensive hardware design and more control pins connected to each element [157], which overrides the essential features of RISs to be a low-cost and easy-to-deploy solution. Therefore, a discrete phase shift design is considered at implementation, where each RIS element is connected to multiple positive-intrinsic-negative (PIN) diodes, and the combinations of the on/off states (through control signals) of these diodes produce the different required phase shifts [158]. However, since RISs are envisioned to be deployed with a large number (could reach thousands) of elements [19], [8], having multiple control lines for each RIS element to achieve multiple phase shift levels is still a practical issue as it may cause configuration overhead. A common approach to solve this issue is to partition the RIS into multiple sub-surfaces, where a common phase shift can be applied to all the elements within the sub-surface to reduce the overall needed number of control lines [159], [160], at the expense of some degradation in the PB performance. Another issue is the phase shift sensitivity to the incident wave's angle, where it is reported in [19] and [34] that this problem is inherent in the RIS design and can break the channel reciprocity of wireless RIS-assisted systems. Furthermore, the classical phase shift model adopted in most of the literature assumes the independent adjustment of the amplitude and phase reflection coefficients. However, based on the real implementation in [32] and the mathematical modeling in [161], this assumption does not hold practically, and there are always amplitude-phase-dependent variations. In particular, the authors in [161] showed that applying the classical phase shift design and ignoring the amplitude dependency may lead to a 5 dB performance loss compared to the ideal case with no amplitude-phase dependency. Likewise, in studies of [162, 163, 164], it is shown that the amplitude is both phase and frequency-dependent, which necessitates a special phase shift design to capture the correlation between all these variables. In order to mitigate the impact of the reflection amplitude-phase correlation, the authors in [165] proposed a heuristic phase-shift-adjustment algorithm to trade off the phase alignment against the amplitude reflection loss. In the same context, the mutual coupling between RIS elements [30] is another critical issue that affects the phase shift adjustment accuracy and performance. In particular, it is shown in [31] that the actual capacitance, and consequently the phase shift of each RIS element is 45% determined by its intended capacitance and 55% by the capacitance of the neighboring element.

In [166] and [167], it is shown that the classical PB strategy, where the channel phases are all aligned to a particular direction, is not always the best one when considering practical system settings such as spatial correlation and phase errors. In particular, the authors in [167] show that the classical PB under the spatial correlation between RIS elements leads to performance degradation for the information transfer, while it is preferable for energy harvesting. Considering the phase errors, the authors in [166] showed that a blind PB scenario occurs when using classical PB, particularly under high (uniform) phase error levels.

6.1.2 Studies on Reflection Amplitude-Based PB Schemes

In [161] and [162], RIS phase shifts are optimized by considering the phase-amplitude and frequency-amplitude dependent variations, respectively, while in [163] are both phase and frequency-dependent amplitude variations considered. In [8], the authors perform PB by only turning on/off each element using a majority voting algorithm based on the received signal strength indicator (RSSI) measurements. In [168], the authors considered an RIS architecture where a fixed arbitrary phase shift is assigned to each element at the manufacturing stage, while the PB is carried out by jointly optimizing the on/off states of the individual elements. In [169], the authors design their PB vector by optimizing both the amplitude and phase reflection coefficients. Finally, in [170] and [171], each element is allowed to have on/off states that are jointly optimized with the phase shifts to obtain the PB vector.

6.2 Motivation and Contributions

In light of the earlier discussions on hardware implementation and system performance issues associated with the classical phase shift-based PB, we propose a low-complexity phase shift-free novel PB scheme for RISs. In the proposed PB scheme, to achieve full reflection power [32], [161], the RIS elements are assumed to be designed with a common and fixed phase shift (π). Thus, to perform PB, we utilize the CSI of the RIS elements to activate only the elements enhancing the constructive combining effect of the reflected signals. Note that the proposed PB scheme is different than that of[168], which still suffers from arbitrary amplitude reflection loss due to the phase-amplitude dependent variations [161]. Furthermore, unlike our proposed PB scheme, [8] depends on the changes in the RSSI measurements to turn on/off the individual elements; however, it is challenging to track these changes on the level of a single element. Moreover, even when turning on/off a group of elements, the changes in the RSSI measurements cannot be tracked accurately due to the incoherent interference of the signals reflected from these elements. In addition, unlike the statistical CSI-based phase shift design methods [172], our proposed PB scheme is not meant to reduce the channel overhead but instead, aims to overcome the practical issues related to the classical continuous phase shift-based PB. The main contributions of this chapter can be listed as follows:

- We propose a low-complexity, phase shift-free and novel PB scheme to avoid hardware implementation and system performance degradation issues associated with the classical phase shift-based PB [157, 159, 160, 34, 32, 161, 162, 163, 164, 30, 31, 166, 167].

- We provide a unified mathematical analysis that characterizes the performance of the proposed PB scheme. First, we derive the asymptotic activation probability associated with each RIS element. Second, the lower bound for the average number of activated RIS elements is obtained. Third, we obtain lower and upper bounds for the probability of activating a certain number of RIS elements at each transmission. Forth, we show that the proposed scheme provides the same scaling law for the signal-to-noise ratio (SNR) as in the classical phase shift-based PB, where the SNR grows quadratically with the RIS size. This is achieved with a complexity level that is linear in the RIS size.

- We characterize the performance of the proposed RIS-assisted system by obtaining its outage probability and a tight upper bound to the ergodic rate.

- Under spatial correlation and phase errors, we provide comprehensive computer simulations to reveal the superiority of the proposed scheme over the two considered benchmark schemes [161] and [165] in terms of the outage probability and ergodic rate performance.

6.3 System Model

In this section, we provide the general system settings along with the considered practical phase shift model.

6.3.1 General System Settings

Consider a downlink single-input single-output (SISO) system with an N-element reconfigurable intelligent surface (RIS) deployed close to the source (S), providing an alternative communication link to the blocked S-Destination (D) one, as shown in Fig. 6.1. Let η_n and θ_n denote the reflection amplitude and phase of the n^{th} element, respectively, thus; the received signal at D is given as

$$y = \sqrt{PL}\textstyle\sum_{n=1}^{N} h_n \eta_n e^{j\theta_n} g_n x + v, \tag{6.1}$$

where P and x are the transmitted signal and power, respectively, $L = L^{(S)}L^{(D)}$, $L^{(S)}$ and $L^{(D)}$ being the S-RIS and RIS-D path gains. $h_n = \alpha_n e^{-j\phi_n}$ and $g_n = \beta_n e^{-j\psi_n}$ are the S-RIS (n^{th} element) and RIS (n^{th} element)-D channel coefficients, where (α_n, ϕ_n) and (β_n, ψ_n) are the phase and amplitude pairs of h_n and g_n, respectively. h_n and g_n are assumed to be mutually independent and identically distributed (i.i.d.) random variables (RVs), in particular, $h_n, g_n \sim \mathcal{CN}(0,1)$. v is the additive white Gaussian noise (AWGN) sample at D, $v \sim \mathcal{CN}(0,\sigma^2)$.

6.3.2 Practical Phase Shift Model

By considering a practical RIS design (under the narrowband signal assumption), for the n^{th} RIS element, the amplitude η_n and phase θ_n reflection coefficients are correlated such that [161]

$$\eta_n(\theta_n) = (1 - a_{\min})\left(\frac{\sin(\theta_n - b_{hrz}) + 1}{2}\right)^{c_{stp}} + a_{\min}, \tag{6.2}$$

where $a_{\min} \geq 0$, $b_{hrz} \geq 0$, and $c_{stp} \geq 0$ are the constants related to the specific circuit implementation. $a_{\min}$ is the minimum amplitude, b_{hrz} is the horizontal distance between $-\pi/2$ and $a_{\min}$, and c_{stp} controls the steepness of the function curve [161]. In particular, we consider the RIS design in [32], which is also considered in [165], where we have $a_{\min} = 0.2, b_{hrz} = 0.43\pi$, and $c_{stp} = 1.6$. Note that when $a_{\min} = 1$ (or $c_{stp} = 0$), we obtain the ideal case of the phase shift model with full reflection and independent phase and amplitude adjustment. Practically, these parameters are determined at the RIS manufacturing stage, and then, these parameters can be

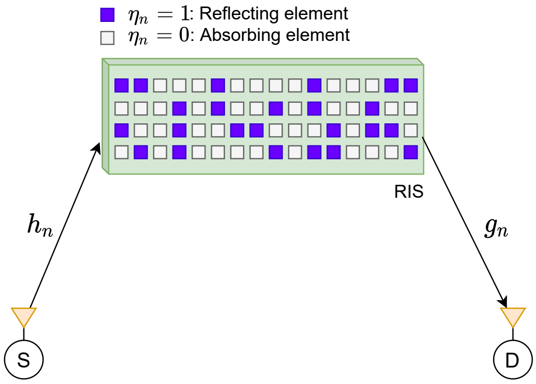

Figure 6.1: RIS-assisted SISO communications system.

obtained by a standard curve fitting tool. Note that the circuit model in [161] is verified with the experimental results reported in [32] and [33]. Furthermore, (6.2) is also adopted in [165], and it is applicable to many of the semiconductor devices usually used to build RISs [161]. Finally, an amplitude-phase-frequency correlation formulas similar to (6.2) are provided in [163].

In the classical PB design, in order to maximize the SNR at D, the RIS phase shifts are adjusted such that $\theta_n = -(\phi_n + \psi_n) + e_n$, where e_n is the residual phase error, and it is assumed to have mutually i.i.d. instances. Note that e_n exists due to the phase estimation errors and/or quantization errors when producing the set of discrete phase shifts [173, 166, 174]. In particular, e_n is assumed to have Von Mises distribution with a zero mean and a concentration parameter κ [175].

6.4 Problem Formulation

In this section, we formulate the phase shift-free PB problem. In the proposed scheme, we avoid all of the aforementioned problems by applying a fixed phase shift to all elements at the manufacturing stage of the RIS. Specifically, we apply a phase shift of π for all elements ($\theta_n = \pi, \forall n$); hence, we guarantee the full reflection of the incident waves [32], [161]. In this way, in order to maximize the SNR, the on/off states of the individual RIS elements need to be jointly optimized to reach the best pattern that enhances the constructive combining of the signals received at D. It is

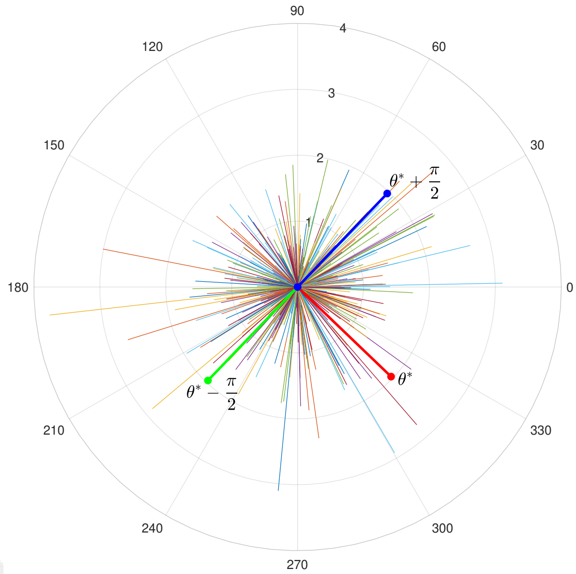

Figure 6.2: Channel coefficients as 2D vectors (amplitudes and phases) in polar coordinates.

not difficult to see that this optimization problem is of the non-convex combinatorial (binary) types which is a non-deterministic polynomial-time (NP) hard problem if we considered the exhaustive search solution [176]. In the following section, we introduce our strategy to solve this problem along with the solution algorithm.

6.5 Proposed Solution

In this section, we propose a sub-optimal solution to find the on/off states pattern of the RIS elements that maximizes the SNR at D.

6.5.1 Solution Strategy

In order to get an intuitive insight, we approach the problem from a geometrical perspective. More specifically, the S-RIS-D channel coefficients are complex numbers that can be represented as 2D vectors in the complex plane, where the real and imaginary parts are the first and second dimensions, respectively. To obtain a geometrical insight, we represent the 2D vectors in polar coordinates as shown in Fig. 6.2, where the length and angle of each vector correspond to the channel amplitude and the phase shift between the real and imaginary parts, respectively. Thus, finding the set of vectors that have the maximum length of the resultant vector associated with their sum is equivalent to finding the on/off state's pattern that maximizes the SNR at D.

6.5.2 Solution Algorithm

We propose Algorithm 9 to find the aforementioned desired set of vectors, as follows. In Algorithm 9, at the first stage, we find the dominant direction (θ^*) where most of the vectors are pointing towards it. Next, we consider only the vectors lie within the span of $\pm\frac{\pi}{2}$ from the dominant direction and activate ($\eta_n = 1$) the RIS elements associated with them, see Fig. 6.2. At the second stage, we seek any vector within the ones excluded at the first stage that can increase the overall sum obtained before. From (6.1), the instantaneous SNR is given by

$$\begin{aligned} \mathrm{SNR} &= \frac{\left|\sqrt{PL}\sum_{n=1}^{N} h_n \eta_n e^{j\theta_n} g_n\right|^2}{\sigma^2} \\ &\overset{(a)}{=} \frac{\left|\sqrt{PL}\sum_{n^*=1}^{N_a} h_{n^*} g_{n^*}\right|^2}{\sigma^2}, \\ &= L\rho\bar{H} \end{aligned} \tag{6.3}$$

where $\rho = \frac{P}{\sigma^2}$ is the transmit SNR, $\bar{H} = |\sum_{n^*=1}^{N_a} h_{n^*} g_{n^*}|^2$. Furthermore, we obtain (a) by applying Algorithm 9, in particular, we set $\theta_n = \pi, \forall n$, where $n^* \in \mathcal{R}^*$ denotes the index of the activated RIS element and $N_a = |\mathcal{R}^*|$ is the total number of the activated elements. In what follows, we provide the steps of Algorithm 9 and give useful insights into its performance.

6.6 Mathematical Analysis and Performance Evaluation

In this section, we characterize the performance of the proposed phase shift-free PB scheme by deriving the probabilities associated with the activation of each RIS element, the minimum number of activated elements at each transmission, the outage probability, and ergodic rate. Finally, we derive the scaling law associated with

Algorithm 9 Phase shift-free PB

Require: h_n, $g_n, \forall n$.

Initialization: $\mathbf{\Gamma} = \text{diag}(\eta_1, ..., \eta_N), \eta_n = 0, \forall n$.
Obtaining the dominant direction: $\theta^* = \arg(\sum_{n=1}^{N} h_n g_n)$.
Specifying the endpoints of the activation region: $c_1 = \theta^* - \frac{\pi}{2}, c_2 = \theta^* + \frac{\pi}{2}$.
Let $\mathcal{R}^* = \{\emptyset\}, Z_n = \arg(h_n g_n)$, and $\Pi(s)$ be the function that maps the value of s to the natural range of an angle, $[0, 2\pi)$, as defined in (6.10).
for $n = 1 : N$ **do**
  if $\Pi(c_1) \leq \Pi(Z_n) \leq \Pi(c_2)$ **then**
    $\eta_n = 1$.
    $\mathcal{R}^* = \mathcal{R}^* \cup \{n\}$.
  end if
end for
Update the entries of $\mathbf{\Gamma}$ according to the above loop, and let $\mathbf{h} = [h_1, ..., h_n, ..., h_N]$ and $\mathbf{g} = [g_1, ..., g_n, ..., g_N]^T$, where $(\cdot)^T$ is the transpose operator.
Construct the new set $\tilde{R} = \{1, ..., N\} \setminus \mathcal{R}^*$.
for $m = 1 : |\tilde{R}|$ **do**
  $n = \tilde{R}^{(m)}$.
  if $|\mathbf{h}\mathbf{\Gamma}\mathbf{g} + h_n \eta_n g_n| > |\mathbf{h}\mathbf{\Gamma}\mathbf{g}|$ **then**
    $\eta_n = 1$.
    $\mathcal{R}^* = \mathcal{R}^* \cup \{n\}$.
  end if
end for
return $\eta_1, ..., \eta_N$.

the growth of the SNR in proportion to N. Note that, in the following analyses, we assume no phase errors ($e_n = 0$), and we consider it later in our computer simulations.

6.6.1 Necessary Lemmas

Here, we provide the necessary lemmas for our main propositions that follow them.

Lemma 3. *The direction of the 2D vector associated with the n^{th} S-RIS-D channel coefficient can be characterized by the random angle $Z_n = \arg(h_n g_n)$, which follows the triangle distribution with the following probability density function (PDF):*

$$f_{Z_n}(z) = \begin{cases} \frac{z+2\pi}{4\pi^2}, & -2\pi \leq z < 0 \\ \frac{-z+2\pi}{4\pi^2}, & 0 \leq z < 2\pi \\ 0, & \textit{otherwise.} \end{cases} \tag{6.4}$$

Proof: Note that ϕ_n and ψ_n are associated with the circular complex Gaussian (CCG) RVs h_n and g_n, respectively, therefore we obtain $\phi_n, \psi_n \sim \mathcal{U}(-\pi, \pi)$ with $f_{\phi_n}(z) = f_{\psi_n}(z) = \frac{1}{2\pi}$, where $\mathcal{U}(a, b)$ denotes the uniform distribution over the interval $[a, b]$. Due to the independence of ϕ_n and ψ_n, the PDF of $Z_n = \arg(h_n g_n) = \phi_n + \psi_n$ can be found as follows:

$$f_{Z_n}(z) = (f_{\phi_n} * f_{\psi_n})(z) = \int_{-\infty}^{\infty} f_{\phi_n}(\tau) f_{\psi_n}(z - \tau) d_\tau. \tag{6.5}$$

Note that (6.5) corresponds to the convolution of a rectangular pulse with itself, which results in a triangular pulse over the interval $[-2\pi, 2\pi]$ as in (6.4). ■

Lemma 3 shows that the direction (phase) associated with the S-RIS-D channel is concentrated around phase zero, for any given RIS element. In general, the S-RIS-D channel's phase is directly determined by the distribution of S-RIS and RIS-D channels.

Lemma 4. *The dominant direction can be characterized as a random angle θ^* which, asymptotically, converges to the uniform distribution, that is, $\theta \xrightarrow{d} \mathcal{U}(-\pi, \pi)$ as $N \to \infty$.*

Proof: The dominant direction can be found by obtaining the resultant vector of the sum of all the channels' coefficients (2D vectors) and then obtaining the angle associated with it. In light of Lemma 3, we obtain

$$\theta^* = \arg\left(\sum_{n=1}^{N} w_n e^{jZ_n}\right), \tag{6.6}$$

where, $w_n = |h_n g_n|$, and the product $h_n g_n$ is the overall S-RIS-D channel. It can be seen that θ^* in (6.6) corresponds to the angle associated with a sum of N weighted 2D unit vectors. Furthermore, irrespective of the distribution of w_n and Z_n, according to the central limit theorem (CLT), the sum in (6.6) converges to the CCG distribution, $\sum_{n=1}^{N} w_n e^{jZ_n} \sim \mathcal{CN}(0, N)$, as $N \to \infty$. Consequently, due to the circular complex property of the sum, its argument is uniformly distributed, $\theta^* \in \mathcal{U}(-\pi, \pi)$, which completes the proof. ■

The result obtained in Lemma 4 shows that when a large RIS is considered, the dominant direction tends to be equally likely in any direction. However, with a small RIS size, the dominant direction directly depends on the wights (channels' amplitudes) associated with their corresponding phases.

Lemma 5. *Asymptotically, $\theta^*, Z_1, ..., Z_n, ..., Z_N$ can be assumed to be pairwise (but not mutually) independent RVs.*

Proof: First, it can be noted that the RVs $\theta^*, Z_1, ..., Z_N$ cannot be mutually independent, where, from (6.6), θ^* is a function of $Z_1, ..., Z_N$. Second, note that $h_1, ..., h_N$ and $g_1, ..., g_N$, by our definition of the S-RIS and RIS-D channels, are mutually independent, which means that the products $h_1 g_1, ..., h_N g_N$ are also mutually independent. Consequently, we conclude that the angles $Z_1, ..., Z_N$ associated with the products are also mutually independent, thus, pairwise independent. In light of these, we need to show that θ^* and Z_n are asymptotically independent (for any given n) to obtain the desired result; $\theta^*, Z_1, ..., Z_N$ are pairwise independent.

Note that the summation in (6.6) can be rewritten as a weighted sum of two unit vectors,

$$\begin{aligned}\theta^* &= \arg\left(\sum_{n=1}^{N} w_n e^{jZ_n}\right)\\ &= \arg(w_{N-1} e^{j\bar{Z}_{N-1}} + w_{\tilde{n}} e^{jZ_{\tilde{n}}}),\ \text{for}\ \tilde{n} \neq n,\end{aligned} \tag{6.7}$$

where $e^{j\bar{Z}_{N-1}}$ and $e^{jZ_{\tilde{n}}}$ are 2D unit vectors, w_{N-1} and $w_{\tilde{n}}$ are the wights associated with them, respectively. Here, $w_{N-1} = |\sum_{n=1}^{N-1} h_n g_n|, w_{\tilde{n}} = |h_{\tilde{n}} g_{\tilde{n}}|$, $\bar{Z}_{N-1} = \arg(\sum_{n=1}^{N-1} h_n g_n)$, and $Z_{\tilde{n}} = \arg(h_{\tilde{n}} g_{\tilde{n}})$. Note that the pairs $(w_{N-1}, \bar{Z}_{N-1})$ and $(w_{\tilde{n}}, Z_{\tilde{n}})$ are independent RVs, and $\tilde{n}$ denotes the index of any particular RIS element. In what follows, we show the asymptotic independence of θ^* and $Z_{\tilde{n}}$ by showing that $w_{\tilde{n}} << w_{N-1}$ as $N \to \infty$, which means that, asymptotically, the direction $Z_{\tilde{n}}$ has a trivial effect on the dominant direction θ^*. This can be shown by evaluating the following limit,

$$\begin{aligned}
\mathcal{L} &= \lim_{N\to\infty} P\left(w_{N-1} > t w_{\tilde{n}}\right) \\
&= \lim_{N\to\infty} P\left(w_{N-1} - t w_{\tilde{n}} > 0\right) \\
&= \lim_{N\to\infty} 1 - F_{\bar{w}}(0),
\end{aligned} \tag{6.8}$$

where $t > 1$, $\bar{w} = w_{N-1} - t w_{\tilde{n}}$, and $F_{\bar{w}}(0)$ is the CDF of $\bar{w}$ evaluated at zero. Note that, as $N \to \infty$, the sum $\sum_{n=1}^{N-1} h_n g_n$ converges in distribution to complex Gaussian and thus, w_{N-1} is a Rayleigh RV. However, it is challenging to derive the PDF associated with the distribution of $\bar{w}$, where it corresponds to the difference of a Rayleigh RV and the products of two other Rayleigh RVs. Therefore, we use the Distribution Fitting Tool in MATLAB to fit the distribution of $\bar{w}$ and then obtain its CDF at zero. As shown in Fig. 6.3, the generalized extreme value (GEV) distribution closely matches the distribution of $\bar{w}$, with $N = 10^5$ and the scale, location, and shape parameters are $k = -0.0717$, $\sigma = 124.464$, and $\mu = 207.635$, respectively, and without loss of generality, $t = 10$. Finally, by evaluating the CDF of the GEV RV with the obtained fitting parameters, we get $F_{\bar{w}}(0) = 0.008$ and $\mathcal{L} = 0.992$. This shows that the weight $w_{\tilde{n}} << w_{N-1}$ as $N \to \infty$, where the dominant direction θ^* does not depend on a specific direction $Z_{\tilde{n}}$, but, on the combination of all N directions. Finally, we obtain that $\theta^*, Z_1, ..., Z_N$ are pairwise independent RVs, which completes the proof. ■

Lemma 5 shows that as the number of RIS elements increases, the dominant direction is determined by the overall contribution of all the individual directions and not by a given single direction (Z_n).

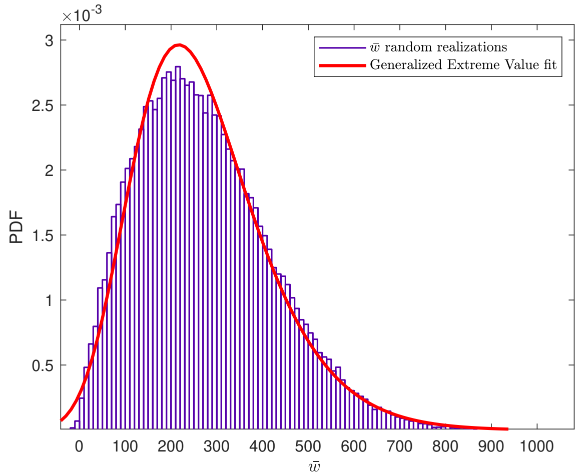

Figure 6.3: Fitting the distribution of $\bar{w}$ to the generalized extreme value distribution.

In what follows, we use the results obtained in Lemmas 3-5 to derive the activation probability in Proposition 6. Note that, activating and deactivating the n^{th} RIS elements equivalent to set its amplitude reflection coefficient as $\eta_n = 1$ and $\eta_n = 0$, respectively. Furthermore, the activation probability in Proposition 6 is derived for the first stage of Algorithm 9 (Steps 5-10), where it is challenging to derive it for the second stage (Steps 13-19) due to the complex distribution of $\mathbf{h\Gamma g}$, as will be discussed later in the proof of Proposition 8. Therefore, the obtained activation probability serves as a lower bound. Also, note that the following results on the RIS elements activation process might be important for the engineering design. In particular, the knowledge of the statistics of the activated/deactivated RIS elements gives useful insight on the electromagnetic wave interference (EMI) [177] associated with the RIS as a whole and the power dissipation/harvesting in autonomous RISs [178].

6.6.2 RIS Elements' Marginal Activation Probability

In this subsection, we derive the activation probability (on-state) for an RIS element according to Algorithm 9.

Proposition 6. *The probability of activating the n^{th} RIS element (according to Algorithm 9) can be lower-bounded as*

$$P_a = P(\Pi(Z_n) \in R) \geq \frac{1}{2}, \ \forall n, \tag{6.9}$$

where the lower bound is achieved as $N \to \infty$. Here, R is the activation (valid) region and $\Pi(s)$ is the function given by

$$\Pi(s) = \begin{cases} s, & 0 \leq s \leq 2\pi \\ s + 2\pi, & s < 0 \\ s - 2\pi, & s > 2\pi. \end{cases} \tag{6.10}$$

Here, $\Pi(s)$ maps the value of s to the natural range of an angle, $[0, 2\pi)$.

Proof: Note that, for the given n^{th} element, its activation probability has the minimum value when θ^* is independent of Z_n, which occurs at the asymptotic range when $N \to \infty$ according to Lemma 5. In contrary to this, the activation probability is higher for smaller N values; for example, it can be readily verified from (6.6) that the activation probability for $N = 1$ is always one. In what follows, we show that the asymptotic value of the activation probability is 0.5, which corresponds to the minimum value as decried earlier.

Note that the n^{th} RIS element is activated ($\eta_n = 1$) according to Algorithm 9 when the phase Z_n associated with its channel coefficient ($h_n g_n$) lies in the valid (activation) region R, which is specified by the endpoints $\Pi(c_1)$ and $\Pi(c_2)$, as shown in Fig. 6.4. It can be also noted form Figs. 6.4(a)-(b) that, depending on the value of $\Pi(\theta^*)$, the endpoints $\Pi(c_1)$ and $\Pi(c_2)$ of R switch their positions. Therefore, in what follows, we calculate the activation probability by considering the two cases shown in Figs. 6.4(a)-(b), separately.

Let $P_{\Pi(c_1) \geq \Pi(c_2)}$ and $P_{\Pi(c_1) \leq \Pi(c_2)}$ denote the activation probability for the first and

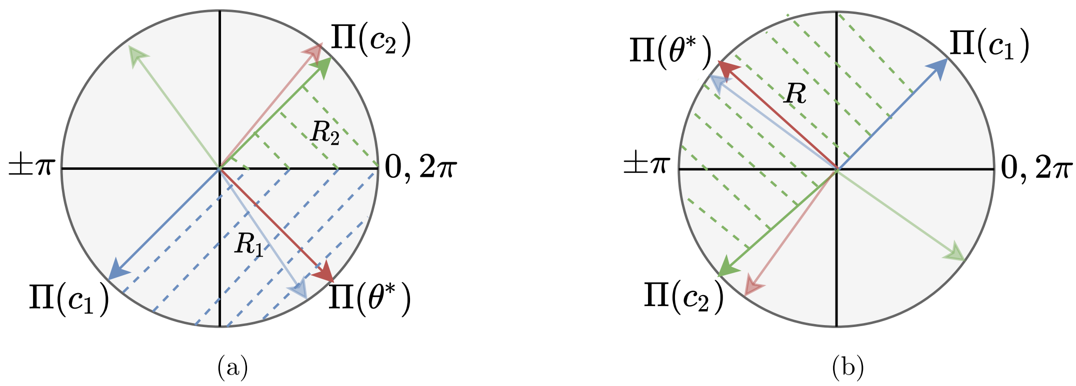

Figure 6.4: The valid (activation) region, shown with dash lines, for the case (a) $\Pi(c_1) \geq \Pi(c_2)$ (b) $\Pi(c_1) \leq \Pi(c_2)$.

second cases shown in Figs. 6.4(a) and (b), respectively, then we have

$$P_{\Pi(c_1)\geq\Pi(c_2)} = P(\Pi(Z_n) \in [\Pi(c_2), \Pi(c_1)], \Pi(c_1) \geq \Pi(c_2)), \tag{6.11}$$

$$P_{\Pi(c_1)\leq\Pi(c_2)} = P(\Pi(Z_n) \in [\Pi(c_1), \Pi(c_2)], \Pi(c_1) \leq \Pi(c_2)), \tag{6.12}$$

consequently, using the total probability law, we obtain

$$P_a = P_{\Pi(c_1)\geq\Pi(c_2)} + P_{\Pi(c_1)\leq\Pi(c_2)}. \tag{6.13}$$

In order to calculate $P_{\Pi(c_1)\geq\Pi(c_2)}$, we note that, as shown in Fig. 6.4(a), the activation region $R = R_1 \cup R_2$, where R_1 and R_2 are the two disjoint regions specified by the pairs of endpoints $[\Pi(c_1), 0]$ and $[0, \Pi(c_2)]$, respectively. Hence, we obtain

$$P_{\Pi(c_1)\geq\Pi(c_2)} = P(\Pi(Z_n) \geq \Pi(c_1)) + P(\Pi(Z_n) \leq \Pi(c_2)). \tag{6.14}$$

In order to calculate $P(\Pi(Z_n) \geq \Pi(c_1))$, we note that when $\Pi(c_1) \geq \Pi(c_2)$, we have θ^* in one of the two intervals $[-\frac{\pi}{2}, 0]$ or $[0, \frac{\pi}{2}]$. On the other side, from Lemma 3, Z_n lies in one of the two intervals $[-2\pi, 0]$ or $[0, 2\pi]$. Also note that, according to (6.10), $\pm 2\pi$ is added whenever Z_n and/or $\theta^* \pm \frac{\pi}{2}$ is out of the natural range of the angle, $[0, 2\pi)$. In light of these, by considering the four different combinations of the two intervals associated with θ^* and Z_n, we obtain

$$P(\Pi(Z_n) \geq \Pi(c_1)) = P_{A1} + P_{A2} + P_{A3} + P_{A4}. \tag{6.15}$$

We define the probabilities P_{Ai} as follows for $i \in \{1, ..., 4\}$:

$$\begin{aligned} P_{A1} &= P(Z_n \geq \theta^* - \frac{\pi}{2} + 2\pi, \theta^* \in [-\frac{\pi}{2}, 0], Z_n \in [0, 2\pi]) \\ &= \int_{-\frac{\pi}{2}}^{0} \int_{\theta+\frac{3\pi}{2}}^{2\pi} f_{Z_n,\theta^*}(z,\theta) d_z d_\theta, \end{aligned} \tag{6.16}$$

by considering Lemma 5, as $N \to \infty$, we have

$$\begin{aligned} P_{A1} &= \int_{-\frac{\pi}{2}}^{0} \int_{\theta+\frac{3\pi}{2}}^{2\pi} f_{Z_n}(z) f_{\theta^*}(\theta) d_z d_\theta \\ &= \int_{-\frac{\pi}{2}}^{0} \int_{\theta+\frac{3\pi}{2}}^{2\pi} \left(\frac{-z+2\pi}{4\pi^2}\right)\left(\frac{1}{2\pi}\right) d_z d_\theta = 0.0182, \end{aligned} \tag{6.17}$$

in the same way, we obtain

$$\begin{aligned} P_{A2} &= P(Z_n \geq \theta^* - \frac{\pi}{2} + 2\pi, \theta^* \in [0, \frac{\pi}{2}], Z_n \in [0, 2\pi]) \\ &= \int_{0}^{\frac{\pi}{2}} \int_{\theta+\frac{3\pi}{2}}^{2\pi} \left(\frac{-z+2\pi}{4\pi^2}\right)\left(\frac{1}{2\pi}\right) d_z d_\theta = 0.0026, \end{aligned} \tag{6.18}$$

$$\begin{aligned} P_{A3} &= P(Z_n + 2\pi \geq \theta^* - \frac{\pi}{2} + 2\pi, \theta^* \in [-\frac{\pi}{2}, 0], Z_n \in [-2\pi, 0]) \\ &= \int_{-\frac{\pi}{2}}^{0} \int_{\theta-\frac{\pi}{2}}^{0} \left(\frac{z+2\pi}{4\pi^2}\right)\left(\frac{1}{2\pi}\right) d_z d_\theta = 0.0755, \end{aligned} \tag{6.19}$$

$$\begin{aligned} P_{A4} &= P(Z_n + 2\pi \geq \theta^* - \frac{\pi}{2} + 2\pi, \theta^* \in [0, \frac{\pi}{2}], Z_n \in [-2\pi, 0]) \\ &= \int_{0}^{\frac{\pi}{2}} \int_{\theta-\frac{\pi}{2}}^{0} \left(\frac{z+2\pi}{4\pi^2}\right)\left(\frac{1}{2\pi}\right) d_z d_\theta = 0.0286, \end{aligned} \tag{6.20}$$

thus, from (6.15), we obtain $P(\Pi(Z_n) \geq \Pi(c_1)) = 0.125$.

For $P(\Pi(Z_n) \leq \Pi(c_2))$, by following the same steps above, we have

$$\begin{aligned} P(\Pi(Z_n) \leq \Pi(c_2)) = &\int_{-\frac{\pi}{2}}^{0}\int_{0}^{\theta+\frac{\pi}{2}} \tilde{f}(z) d_z d_\theta + \int_{0}^{\frac{\pi}{2}}\int_{0}^{\theta+\frac{\pi}{2}} \tilde{f}(z) d_z d_\theta \\ &+ \int_{-\frac{\pi}{2}}^{0}\int_{-2\pi}^{\theta-\frac{3\pi}{2}} f'(z) d_z d_\theta + \int_{0}^{\frac{\pi}{2}}\int_{-2\pi}^{\theta-\frac{3\pi}{2}} f'(z) d_z d_\theta \\ &= 0.125, \end{aligned} \tag{6.21}$$

where, $f'(z) = (\frac{z+2\pi}{4\pi^2})(\frac{1}{2\pi}) = \frac{z+2\pi}{8\pi^3}$ and $\tilde{f}(z) = (\frac{-z+2\pi}{4\pi^2})(\frac{1}{2\pi}) = \frac{-z+2\pi}{8\pi^3}$. Finally, from (6.14), we have $P_{\Pi(c_1) \geq \Pi(c_2)} = 0.25$.

In order to calculate $P_{\Pi(c_1)\leq\Pi(c_2)}$, we note that there is only one activation (valid) region denoted by R, as shown in Fig. 6.4(b). Therefore, the activation probability can be given as

$$\begin{aligned} P_{\Pi(c_1)\leq\Pi(c_2)} &= P(\Pi(Z_n) \in [\Pi(c_1), \Pi(c_2)]) \\ &= P(\Pi(Z_n) \leq \Pi(c_2)) - P(\Pi(Z_n) \leq \Pi(c_1)), \end{aligned} \tag{6.22}$$

where, following the same procedure to compute (6.15), we calculate $P(\Pi(Z_n) \leq \Pi(c_1))$ as follows:

$$\begin{aligned} P(\Pi(Z_n) \leq \Pi(c_1)) =& \int_{\frac{\pi}{2}}^{\pi} \int_{0}^{\theta-\frac{\pi}{2}} \tilde{f}(z) d_z d_\theta + \int_{\frac{\pi}{2}}^{\pi} \int_{-2\pi}^{\theta-\frac{5\pi}{2}} f'(z) d_z d_\theta \\ &+ \int_{-\pi}^{\frac{-\pi}{2}} \int_{0}^{\theta+\frac{3\pi}{2}} \tilde{f}(z) d_z d_\theta + \int_{-\pi}^{\frac{-\pi}{2}} \int_{-2\pi}^{\theta-\frac{\pi}{2}} f'(z) d_z d_\theta \\ =& \, 0.125, \end{aligned} \tag{6.23}$$

and,

$$\begin{aligned} P(\Pi(Z_n) \leq \Pi(c_2)) =& \int_{\frac{\pi}{2}}^{\pi} \int_{0}^{\theta+\frac{\pi}{2}} \tilde{f}(z) d_z d_\theta + \int_{\frac{\pi}{2}}^{\pi} \int_{-2\pi}^{\theta-\frac{3\pi}{2}} f'(z) d_z d_\theta \\ &+ \int_{-\pi}^{\frac{-\pi}{2}} \int_{0}^{\theta+\frac{5\pi}{2}} \tilde{f}(z) d_z d_\theta + \int_{-\pi}^{\frac{-\pi}{2}} \int_{-2\pi}^{\theta+\frac{\pi}{2}} f'(z) d_z d_\theta \\ =& \, 0.3750, \end{aligned} \tag{6.24}$$

thus from (6.22), we obtain $P_{\Pi(c_1)\leq\Pi(c_2)} = 0.375 - 0.125 = 0.25$. Finally, from (6.13), we obtain $P_a = 0.25 + 0.25 = 0.5$, which corresponds to the minimum activation probability as described before, therefore, we obtain $P_a \geq 0.5$. This completes the proof. ∎

Asymptotically, Proposition 6 shows that the probability of activating or deactivating any element is equally likely when the RIS has a large size. This result coincides with Lemma 4, where, when the RIS size is large, the activation region (semi-circle) has an equally likely probability of being in any direction. Furthermore, for a finite N, the activation probability is always higher than 0.5. Finally, note that the obtained lower bound of P_a is still valid under the assumption of spatial correlation between RIS elements, which can be explained as follows. If the RIS elements are spatially correlated, which is practically true, the S-RIS-D channel coefficients (2D vectors) are more concentrated in a specific direction (angle), which increases the number of vectors within the activation window, N_a, and thus, we obtain a higher activation probability P_a.

6.6.3 Average Number of Activated RIS Elements

Corollary 5. *The average number of activated RIS elements can be lower-bounded as*

$$E[N_a] \geq \frac{N}{2}, \tag{6.25}$$

where $E[\cdot]$ is the expectation operator and the lower bound is achieved as $N \to \infty$.

Proof: The proof follows directly from Proposition 6, where $\mathrm{E}[N_a] = \mathrm{E}\left[\sum_{n=1}^{N} \eta_n\right] = \sum_{n=1}^{N} P_n = NP_a \geq \frac{N}{2}$. ■

The result provided in Corollary 5 can be explained as follows. When the number of RIS elements is relatively small, the 2D vectors associated with these elements are more likely to be concentrated within a specific beam, which increases the activation probability above 0.5 and consequently, $\mathrm{E}[N_a] > \frac{N}{2}$. However, as the RIS size increases, the semi-circle activation region can be in any direction (Lemma 4) and the activation probability converges to 0.5 (Proposition 6), therefore, $\mathrm{E}[N_a] \to \frac{N}{2}$.

6.6.4 RIS Elements' Joint Activation Probability

Corollary 6. *The RVs $\eta_1, ..., \eta_n, ..., \eta_N$ are pairwise independent, but not m-wise independent for $2 < m \leq N$.*

Proof: We show that $\eta_1, ..., \eta_n, ..., \eta_N$ are pairwise independent RVs by showing that their probability mass functions (PMFs), for any given pair of elements n and $\tilde{n}$, are independent, $P(\eta_{\tilde{n}} = 1|\eta_n = 1) = P(\eta_{\tilde{n}} = 1)$, where $n, \tilde{n} \in \{1, ..., N\}$, and $n \neq \tilde{n}$. Note that the activation probability of the n^{th} element is the PMF of η_n.

Consider the activation region R specified by the endpoints $[\Pi(c_1), \Pi(c_2)]$, where, without loss of generality, we have $\Pi(c_1) \leq \Pi(c_2)$, as described in the proof of Proposition 6. Therefore, the activation of the n^{th} element ($\eta_n = 1$) corresponds to $\Pi(c_1) \leq \Pi(Z_n) \leq \Pi(c_2)$, however; as it can be seen from the proof of Proposition 6 (Fig. 6.4), giving this information does not change the activation region R for the $\tilde{n}^{th}$ element as $\Pi(c_1)$ and $\Pi(c_2)$ are separated by $\pi/2$ and, therefore, they still span the entire circle. This shows that the activation probabilities (PMF of η_n) for any pair of elements n and $\tilde{n}$ are independent and we have that η_n and $\eta_{\tilde{n}}$ are independent RVs, $\forall n, \tilde{n} \in \{1, ..., N\}$. However, we show that these RVs are not m-wise independent for $2 < m \leq N$, as follows. Consider, without loss of generality, the non-zero probability event where two elements are activated, for example $\eta_1 = \eta_2 = 1$, with $\Pi(Z_1) \leq \Pi(Z_2)$. Consequently, it can be readily seen that given $\eta_1 = \eta_2 = 1$ changes the activation region R for the $\tilde{n}^{th}$ element as the endpoints $\Pi(c_1)$ and $\Pi(c_2)$ do not span the entire circle anymore; more specifically, the endpoints cannot span the interval $[\Pi(Z_1), \Pi(Z_2)]$. This shows that $P(\eta_{\tilde{n}} = 1 | \eta_1 = \eta_2 = 1) \neq P(\eta_{\tilde{n}} = 1)$, thus, η_1, η_2, and $\eta_{\tilde{n}}$ are non-independent RVs. Consequently, the RVs $\eta_1, ..., \eta_N$ are not triple-wise independent, thus, not m-wise independent for $2 < m \leq N$. ■

Corollary 6 shows that the activation probabilities of any two given elements are independent. However, the activation probabilities for $N > 2$ elements are dependent. The result given in Corollary 6 is necessary for the next proposition.

6.6.5 Resources-Based Outage Probability

This subsection, based on Corollary 6, introduces a new physical resources-based outage probability (ROP) metric. The ROP metric is defined to be the probability that the number of activated RIS elements at each transmission is less than a predefined threshold (N_{thr}), ROP $= P(N_a \leq N_{thr})$.

Proposition 7. *For a given N_{thr}, we have $ROP_L \leq ROP \leq ROP_U$, where the lower* *and upper bounds can be given, respectively, as*

$$ROP_L = 1 - U, \tag{6.26}$$

where,

$$U = \begin{cases} 1, \quad N_{thr} < \bar{N}P_a \\ (\bar{N}\bar{P}_a + N_{thr})P_a/N_{thr}, \ \bar{N}P_a \leq N_{thr} \leq 1 + \bar{N}P_a \\ \frac{N\bar{N}P_a^2 + (\zeta-1)(\zeta-2NP_a)}{(N_{thr}-\zeta)^2 + (N_{thr}-\zeta)}, \quad N_{thr} \geq 1 + \bar{N}P_a \\ \zeta = \lceil \frac{NP_a(N_{thr}-1-\bar{N}P_a)}{N_{thr}-NP_a} \rceil, \end{cases} \tag{6.27}$$

$$ROP_U = \sum_{i=0}^{N_{thr}} \binom{N}{i} P_a^i (1 - P_a)^{N-i}, \tag{6.28}$$

where $\bar{N} = N - 1$, $\bar{P}_a = 1 - P_a$, *and* U *corresponds to the upper bound probability of* N_a *exceeding* N_{thr}.

Proof: Note that, from Corollary 6, $N_a = \sum_{n=1}^{N} \eta_n$ corresponds to a sum of pairwise independent Bernoulli RVs. Therefore, for ROP$_L$, U corresponds to the probability of the sum of pairwise independent Bernoulli RVs (N_a) to exceed an integer threshold (N_{thr}), where the proof for U is given in [179, Theorem 4.1].

The upper bound ROP$_U$ is found by approximating N_a to the Binomial distribution, as follows. Note that the sum of pairwise independent Bernoulli RVs can be approximated to the mutually independent case (Binomial distribution) with a total variation distance of $1 - 1/e$, as $N \to \infty$ [180]. Furthermore, it is worth noting that the approximation to the mutual independence case corresponds to the minimum activation probability, where the dominant direction θ^* is not a function of the individual directions Z_n anymore. In light of these, the approximation of N_a to the Binomial distribution serves as a lower bound for N_a and, therefore, its CDF given in (6.28) serves as the upper bound for ROP. ■

In order to get useful insight from Proposition 7, we use Hoeffding's inequality (in light of (6.28)), $P(N_a - \mathrm{E}[N_a] \geq c) \leq e^{-2\frac{c^2}{N}}$, for $c \geq 0$, which shows that the number of activated RIS elements is concentrated around its mean value ($N/2$) and thus, ROP decreases as N_{thr} decreases below the mean value of N_a.

6.6.6 Rate-Based Outage Probability

In this subsection, we derive the outage probability in terms of the communication data rate between S and D, as follows.

Proposition 8. *For a targeted transmission rate r, the outage probability P_{out} of D is given by*

$$P_{out} = \frac{1}{2}\left[1 + erf\left(\frac{\ln(\bar{r}) - \mu}{\sqrt{2}\bar{\sigma}}\right)\right], \tag{6.29}$$

where $\bar{r} = \frac{2^r-1}{L\rho}$, $\mu = a_1 N^{b_1} + c_1$, $\bar{\sigma} = a_2 N^{b_2} + c_2$, and erf$(\cdot)$ is the error function. Considering the spatial correlation between RIS elements with inter-element separation of $\frac{\lambda}{8}$, we have $(a_1, a_2) = (-533.1, 2.928), (b_1, b_2) = (-0.003336, -0.1783)$, and $(c_1, c_2) = (532.3, -0.6076)$. On the other side, ignoring spatial correlation due to inter-element separation much larger than $\frac{\lambda}{2}$ [181], we have $(a_1, a_2) = (39.59, 1.725), (b_1, b_2) = (0.03871, -0.3917)$, and $(c_1, c_2) = (-40.54, -0.0354)$.

Proof: Considering a targeted transmission rate r then, the outage probability is given as

$$P_{out} = P(\log_2(1 + \text{SNR}) < r), \tag{6.30}$$

from (6.3), we obtain

$$\begin{aligned} P_{out} &= P\left(\bar{H} < \frac{2^r - 1}{L\rho}\right) \\ &= F_{\bar{H}}\left(\frac{2^r - 1}{L\rho}\right), \end{aligned} \tag{6.31}$$

where $F_{\bar{H}}$ is the CDF of $\bar{H}$. Note that the S-RIS-D channel coefficients $h_{n^*}g_{n^*}$, $n^* \in \{1, ..., N_a\}$ are correlated through their phases $\Pi(Z_{n^*})$, where $\max_{n^*}(\Pi(Z_{n^*})) \leq \max(\Pi(c_1), \Pi(c_2))$ and $\min_{n^*}(\Pi(Z_{n^*})) \geq \min(\Pi(c_1), \Pi(c_2))$, as demonstrated in the proof of Proposition 6. Accordingly, the terms of the sum of $\bar{H}$ are non-independent, where each term is a product of two Gaussian RVs. Consequently, it is challenging to analytically derive the distribution of $\bar{H}$. Therefore, we use the Distribution Fitting

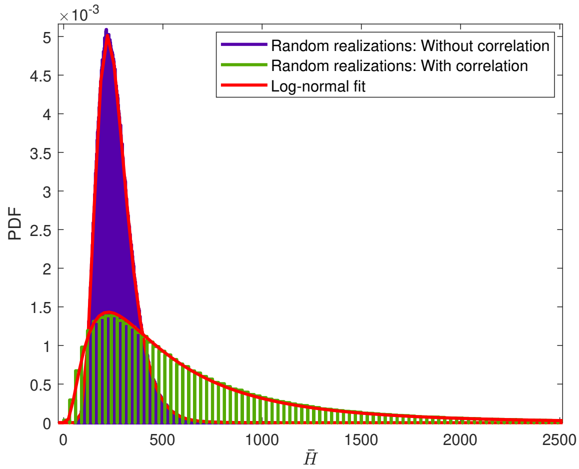

Figure 6.5: Fitting the distribution of $\bar{H}$ to the log-normal distribution.

Tool in MATLAB[1] to fit the distribution of $\bar{H}$ and, accordingly, obtain the outage probability, which is the CDF of $\bar{H}$. Fig. 6.5 shows that the distribution of $\bar{H}$, with/without spatial correlation, perfectly matches the one of the log-normal RV with μ and $\bar{\sigma}$ are the mean and standard deviation of $\ln(\bar{H})$, respectively, $\ln(\bar{H}) \sim \mathcal{N}(\mu, \bar{\sigma}^2)$. Consequently, we obtain the outage probability as the CDF of $\bar{H}$, as given in (6.29). Furthermore, using the Curve Fitter tool in MATLAB, a semi-analytical representation is obtained for μ and $\bar{\sigma}$ as functions of $N \in \{10, 500\}$, where the fitting parameters are given after (6.29). ■

Proposition 8 shows that the outage probability decreases as ρ and/or N increases. In particular, it can be readily verified that, for $N \in \{10, 500\}$, we have $\mu, \bar{\sigma} > 0$, regardless of the spatial correlation assumption. Thus, considering the asymptotic behavior with respect to ρ, as $\rho \to \infty$ ($\bar{r} \to 0$), we obtain $\text{erf}(\frac{\ln(\bar{r})-\mu}{\sqrt{2}\bar{\sigma}}) \to -1$ and $P_{out} \to 0$. Likewise, considering the asymptotic behavior with respect to N, note that as $N \to 500$ we have $\mu \to 10$, $\bar{\sigma} \to 0.36$, accordingly, it can be readily shown that for $r < \log_2(L\rho e^{8.5} + 1)$, we have $\text{erf}(\frac{\ln(\bar{r})-\mu}{\sqrt{2}\bar{\sigma}}) \to -1$, and $P_{out} \to 0$.

[1]Note that this tool uses a maximum likelihood estimator to estimate the assumed distribution's parameters, and the quality of the distribution fit can be measured by the standard error for the estimated parameters and the shape match of the PDFs.

6.6.7 Ergodic Rate

Here, we derive an upper bound for the ergodic rate in the considered system.

Proposition 9. *The ergodic rate of D can be upper-bounded as*

$$R \leq \log_2(1 + L\rho \exp(\mu + \frac{\bar{\sigma}^2}{2})). \tag{6.32}$$

Proof: The ergodic rate of D is given by

$$R = \mathrm{E}[\log_2(1 + \mathrm{SNR})], \tag{6.33}$$

by considering the concavity of the function in (6.33), we use Jensen's inequality to obtain

$$\begin{aligned} R &\leq \log_2(1 + \mathrm{E}[\mathrm{SNR}]), \\ &= \log_2(1 + L\rho \exp(\mu + \frac{\bar{\sigma}^2}{2})), \end{aligned} \tag{6.34}$$

where, from (6.3), we have $\mathrm{E}[\mathrm{SNR}] = L\rho\mathrm{E}[\bar{H}]$, furthermore, from the proof of Proposition 8, we have $\bar{H}$ has log-normal distribution with a mean $\mathrm{E}[\bar{H}] = \exp(\mu + \frac{\bar{\sigma}^2}{2})$. Here, we consider the same semi-analytical representation for μ and $\bar{\sigma}$ given after (6.29). ■

Note that, from the semi-analytical representation for μ and $\bar{\sigma}$ given in the proof of Proposition 8, it can be readily verified that $\mu, \bar{\sigma} > 0$ and the sum $\mu + \frac{\bar{\sigma}^2}{2}$ increases with N, regardless of the spatial correlation assumption. This shows that the ergodic rate is an increasing function in N.

6.6.8 SNR Scaling Law

Proposition 10. *An instantaneous SNR in order of $\mathcal{O}(N^2)$ can be achieved by Algorithm 9 with a complexity level of $\mathcal{O}(N)$.*

Proof: See Appendix C. ■

Proposition 10 shows that the proposed phase shift-free PB scheme preserves the quadratic growth behavior of the beamforming gain associated with the classical

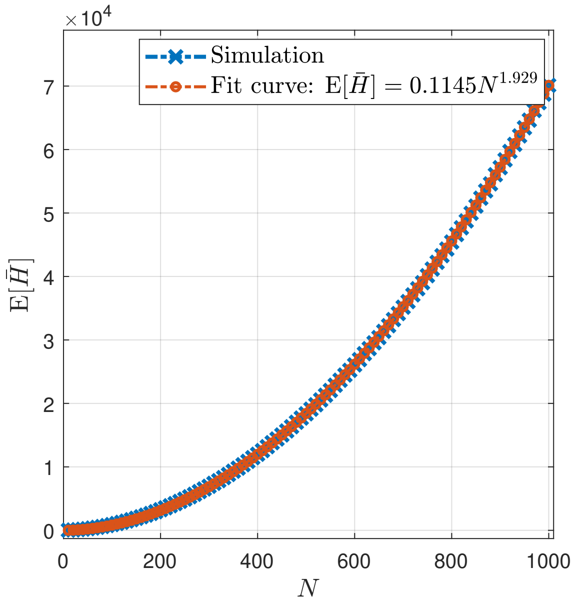

Figure 6.6: The quadratic scaling law of the channel gain $\bar{H}$.

phase shift-based one, see Fig. 6.6. This can be explained as follows. Note that, although the signals reflected from the RIS (according to Algorithm 9) cannot be coherently combined, yet, the overall amplitude of their sum still linearly grows with the number of activated elements N_a. Also, by noting that N_a grows with N, the overall S-RIS-D channel gain ($\bar{H}$) and, thus, the SNR grows quadratically with the RIS size N. Furthermore, contrary to the classical phase shift-based PB, the proposed PB scheme preserves the full power of the reflected signals at the expense of perfectly aligning them. This trade-off, between fully reflecting the signals and perfectly aligning them, gives the superiority to the proposed scheme over the classical one under phase error conditions, where the perfect alignment is inherently impossible.

6.7 Simulation Results

This section presents comprehensive computer simulations to examine the performance of both the proposed and benchmark schemes under different system settings. In what follows, we first provide the simulation parameters and considered benchmark schemes, and then we give the simulation results and discussions under different performance metrics.

6.7.1 Simulation Parameters and Benchmark Schemes

We consider the system performance under phase errors and/or spatial correlation. The adopted RIS size is $N = 40$, where each element has a width d_H and a length d_V, and we used the spatial correlation model presented in [181]. Note that, by default, no spatial correlation or phase errors are assumed in our simulations unless otherwise stated. We consider two different benchmark schemes; first, the classical PB (labeled with classical PB), where the applied phase shift on each RIS element is meant to remove the S-RIS-D channel phase associated with that element.

Second, the reflection phase selection algorithm (RPSA), which is proposed in [165] to mitigate the reflection phase and amplitude correlation issue, is considered. Note that, for the benchmark schemes, the reflection phase and amplitude are correlated through (6.2) [161]. Also, for the benchmark schemes, two phase shift levels are adopted (0 and π) for a fair comparison with the proposed scheme that uses one control bit for the on/off adjustment of each RIS element. The RIS-D distance is $r_D = 10$ m, and the S-RIS distance is given by $r_S = \lceil \frac{N\lambda}{2} \rceil$[19] to ensure that the RIS is in the far-field region of S, where λ is the wavelength associated with the operating frequency (1.8 GHz). The overall S-RIS-D path loss is given by $(L)^{-1} = \lambda^4/(256\pi^2 r_S^2 r_D^2)$ [11], and the noise level is chosen to be $\sigma^2 = -90$ dBm.

Note that, considering the RPSA algorithm, it should be noted that both the RPSA and the proposed Algorithm 9 achieve the quadratic growth of the SNR with N and requires the same complexity level, $\mathcal{O}(N)$. Furthermore, in all of the provided simulations, the proposed scheme activates, on average, around 60% of the RIS elements, while, as stated by Proposition 6, the asymptotic number of activated RIS elements is $N_a = N/2$. This effectively reduces the unavoidable EMI associated with each RIS element [177]. Furthermore, for autonomous RISs [178], the energy consumption associated with the control circuit of the RIS becomes critical. In this regard, our proposed scheme can save more than 50% of the operating energy

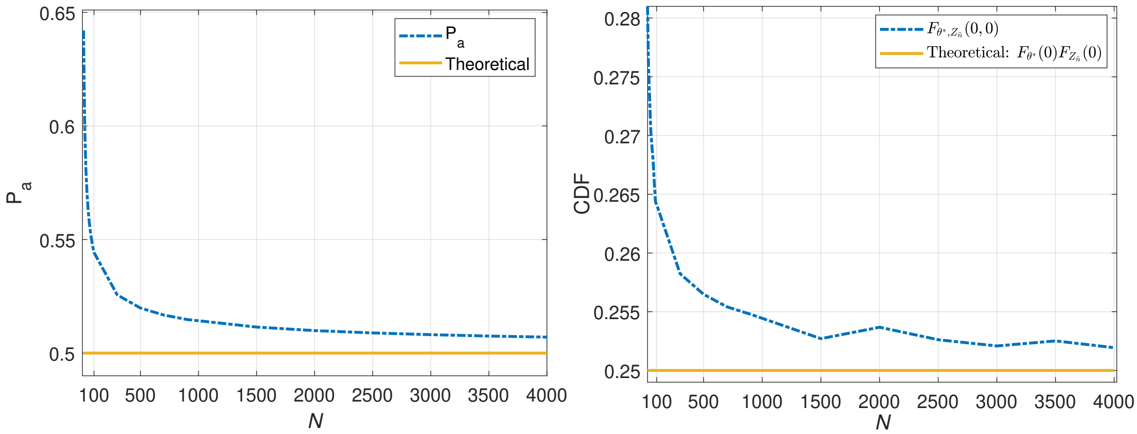

(a) (b)

Figure 6.7: (a) The activation probability and (b) the joint CDF $F_{\theta^*,Z_n}(0,0)$, both versus N.

through the off-state elements. Also, using the energy harvesting strategy provided in [178], the off-state elements can be used as energy harvesters. In light of these, the proposed phase shift-free PB scheme makes the use of the RIS more energy-efficient with less reflection to the EMI interference compared to the benchmark schemes.

6.7.2 Verifying Proposition 6 and Lemma 5

In Figs. 6.7(a) and (b), we verify Proposition 6 and Lemma 5, respectively. In particular, in Fig. 6.7(a), the activation probability P_a converges to the asymptotic value (0.5) as N increases. In Fig. 6.7(b), without loss of generality, we evaluate the joint CDF of θ^* and $Z_{\tilde{n}}$ at the point $(\theta = 0, z = 0)$, where it can be seen that, asymptotically, the product of the individual CDFs converges to the joint CDF.

6.7.3 Verifying Proposition 7

We verify Proposition 7 in Figs. 6.8(a) and (b), where $P_a = 0.5$ is the asymptotic value of the activation probability obtained from Proposition 6, while the other values, $P_a = 0.542$ and 0.5058, are obtained through simulations for $N = 100$ and 5000, respectively. It can be seen that the upper bound curve ROP_{U} gets closer to

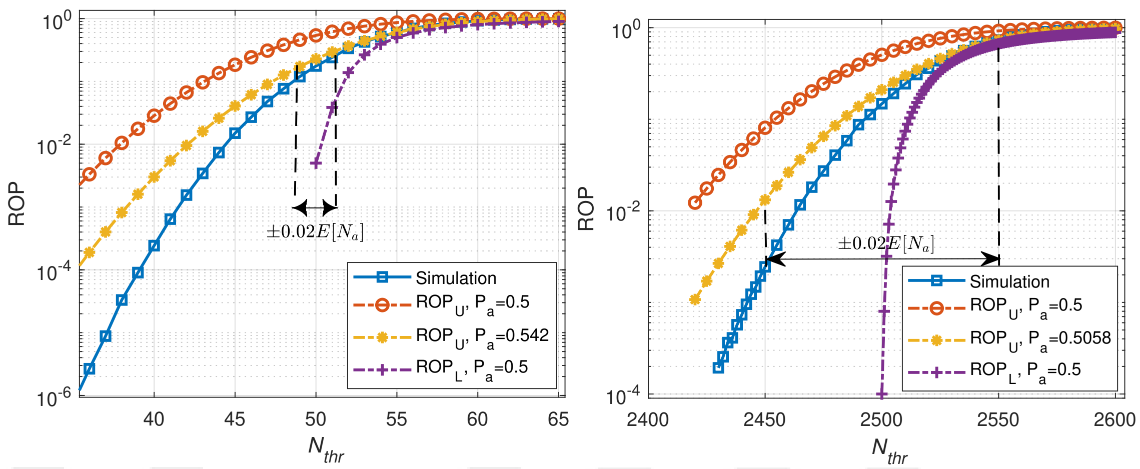

(a) (b)

Figure 6.8: ROP performance with (a) $N = 100$, (b) $N = 5000$.

the simulation curve when using the value of P_a obtained through simulations. This is due to the convergence of P_a and the approximation of ROP_U in Proposition 6 and 2, respectively, requires that $N \to \infty$. Furthermore, it can be noted that the probability that N_a is within $\pm 2\%$ of its mean value increases with N, where it is 0.121 and 0.9102 for $N = 100$ and 5000, respectively.

6.7.4 Verifying Propositions 8 and 9

Fig. 6.9(a) shows the outage probability (OP) performance with different N values, where increasing the RIS size improves the performance effectively. Furthermore, Fig. 6.9(a) verifies Proposition 8, where the theoretical curves converge to those obtained through simulations as N increases, with a perfect match at $N = 200$. Furthermore, it can be seen that the OP performance deteriorates under spatial correlation due to the lack of diversity. Likewise, Fig. 6.9(b) verifies Proposition 9, where the theoretical upper bound is shown to be tight and has a close match to the exact one. Furthermore, the ergodic rate is shown to be an increasing function in N, with, notably, higher performance under spatial correlation, which can be explained as follows. Under spatial correlation, the 2D vectors (S-RIS-D channel coefficients) are more concentrated in a specific direction (angle), which increases the

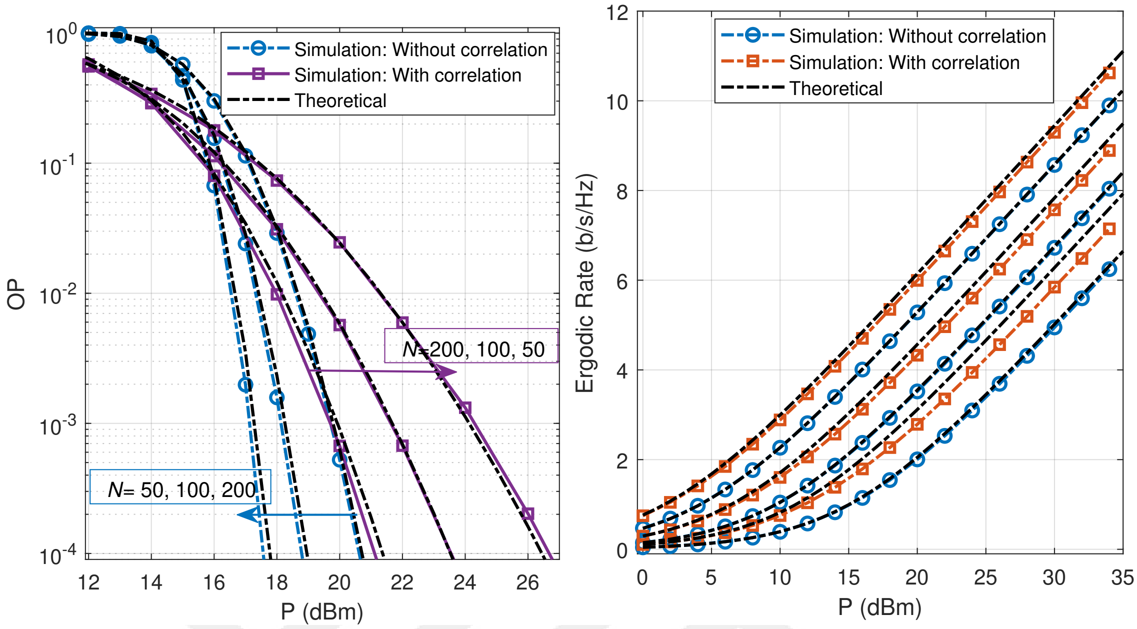

(a) (b)

Figure 6.9: The performance, with/without spatial correlation and with different N values, of (a) outage probability with $r = 1$ bit per channel use (bpcu), and (b) ergodic rate.

number of vectors within the activation window, N_a. Consequently, as N_a increases SNR quadratically increases as stated in Proposition 10, which leads to a better performance in the ergodic rate. Note that, in Fig. 6.9(b), in order to show the effect of increasing N only, we ignore the distance effect by obtaining r_s for $N = 50$ and use it for the other values of N.

6.7.5 Effects of Spatial Correlation and Phase Errors on Outage Probability

In Figs. 6.10(a) and (b), we show the outage probability performance with/without phase error and spatial correlation effects, as follows. In Fig. 6.10(a), it can be seen that the proposed scheme achieves a 2 dB gain in the required P compared to the classical PB, while it is slightly better than RPSA. In Fig. 6.10(b), we show the combined effect of spatial correlation and phase errors, where the proposed scheme achieves around 5 dB performance gain in the required P compared to both

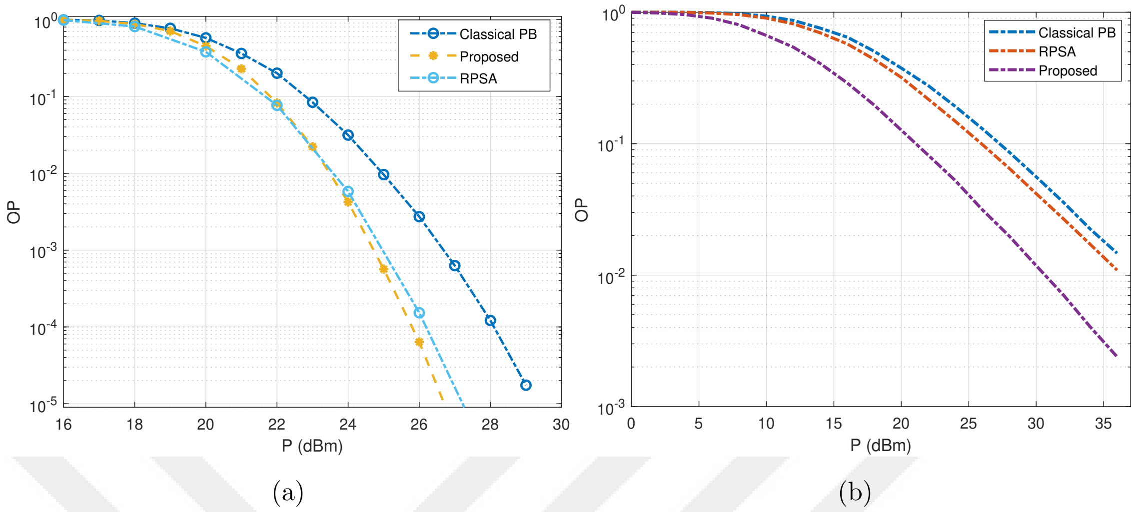

Figure 6.10: Outage probability performance with (a) no phase errors, no spatial correlation, and $r = 2$ bpcu, (b) spatial correlation ($d_H = d_V = d = \lambda/8$) [8], [182], [183], phase errors ($\kappa = 0$) [166], [184], and $r = 0.5$ bpcu.

benchmark schemes.

6.7.6 Effects of Spatial Correlation and Phase Errors on Ergodic Rate

In Figs. 6.11(a) and (b), we show the ergodic rate performance for all schemes with/without phase errors and spatial correlation effects, as follows. In Fig. 6.11(a), all schemes achieve almost the same performance, where neither phase errors or spatial correlation is considered. In Fig. 6.11(b), the combined effect of spatial correlation and phase errors is shown, where the proposed scheme achieves a remarkable performance gain of almost 5 dB in the required P compared to the benchmark schemes. It is worth noting that, as shown in Fig. 6.10(b) and Fig. 6.11(b), unlike the proposed scheme, both benchmark schemes suffer under high spatial correlation and phase errors. In particular, the observed behavior of the classical PB under phase errors is reported in [166], where it is shown that the classical phase shift design (removing the channel phases) may lead to the blind PB scenario, especially when the level of phase errors is high ($\kappa = 0$). Also, it is reported in [167] that classical phase shift design under spatial correlation leads to a worse performance

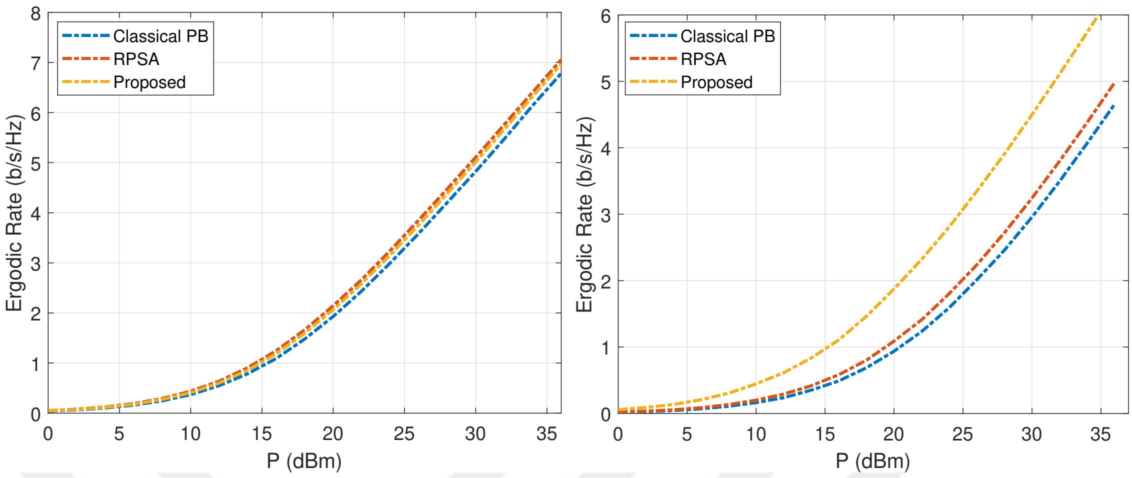

(a) (b)

Figure 6.11: Ergodic rate performance with (a) no spatial correlation and no phase errors, (b) spatial correlation ($d_H = d_V = d = \lambda/8$) and phase errors ($\kappa = 0$).

compared to other phase shift techniques.

6.8 Conclusion

This chapter has proposed a low-complexity and novel phase shift-free PB scheme to avoid the hardware implementation and performance degradation issues associated with the classical phase shift-based PB. The proposed PB scheme requires a complexity level linear in N and achieves the same scaling law for the SNR (quadratic growth with N) as in the classical phase shift-based PB. Computer simulations show that the proposed PB scheme is superior to the considered benchmark schemes (including the classical PB scheme) in terms of the outage probability and ergodic rate performance. Furthermore, the proposed PB scheme exhibits far less sensitivity to practical system settings, such as the spatial correlation between RIS elements and the phase errors. To conclude, extending the proposed PB scheme to the multiple-input multiple-output systems is an appealing future research direction.

Chapter 7

ELECTROMAGNETIC INTERFERENCE CANCELLATION FOR RIS-ASSISTED COMMUNICATIONS

Although RISs have shown the potential of manipulating the wireless channel through passive beamforming, it is shown that they can also bring undesired side effects, such as reflecting the electromagnetic interference (EMI) from the surrounding environment to the receiver side. In this chapter, we propose a novel EMI cancellation scheme to mitigate the impact of the EMI by exploiting its special time-domain structure and considering a clever passive beamforming method at the RIS. Compared to its benchmark, computer simulations show that the proposed scheme achieves superior performance in terms of the average signal-to-interference-plus-noise ratio (SINR) and outage probability (OP), especially when the EMI power is comparable to the power of the information signal impinging on the RIS surface.

The rest of the chapter is organized as follows. In Section 7.1, we provide the related literature works. In Section 7.2, we give the motivation for this work and its main contributions. In Section 7.3, we introduce the system model and explain the proposed EMI cancellation scheme. In Section 7.4, we give outage probability analysis. Section 7.5 provides computer simulations followed by conclusions in Section 7.6.

7.1 Related Works

Due to its inherent physical nature, an RIS cannot selectively reflect the signals impinging its surface; therefore, it also reflects undesired signals from the surrounding environment, causing electromagnetic interference (EMI) at the receiver side [177].

So far, few works have shed light on this problem and took it into consideration while designing RIS-assisted systems. In particular, the authors in [177] provided a mathematical model for an RIS-assisted single-input single-output (SISO) system under EMI interference, where they modeled the EMI as a complex Gaussian random vector with zero mean and a variance corresponding to the EMI power. In [185], the authors compared RIS-assisted and decode-and-forward (DF) relaying systems under EMI in terms of minimizing the total transmit power. In [186], the performance of an RIS-assisted ultra-reliable low-latency communication (URLLC) system is investigated for multi-user scenario in the presence of EMI. In [187], the performance of a multi-pair full-duplex (FD) two-way communication system is considered under RIS hardware impairments, spatial correlation, and EMI.

7.2 Motivation and Contributions

Based on the previous literature review, to the best of the authors' knowledge, no work in the RIS literature has yet investigated the problem of mitigating the EMI in RIS-assisted communications. Against this background, we propose a novel EMI cancellation scheme to mitigate the EMI impact and enhance the signal-to-interference-plus-noise ratio (SINR) at the receiver side. In particular, by exploiting the special structure of the RIS channels and the time-domain behavior of the EMI, we trade off the passive beamforming gain in favor of canceling the EMI through the proper design of the RIS phase shifts. Computer simulations with different system settings show that the proposed scheme has a superior performance in terms of the average SINR and outage probability.

7.3 System Model

In this section, we first introduce the system model then we explain the proposed EMI cancellation scheme in detail. We consider an RIS-assisted SISO system, as shown in Fig. 7.1, where an RIS consisting of N elements is employed. The direct communication link between the source (S) and the destination (D) is assumed to

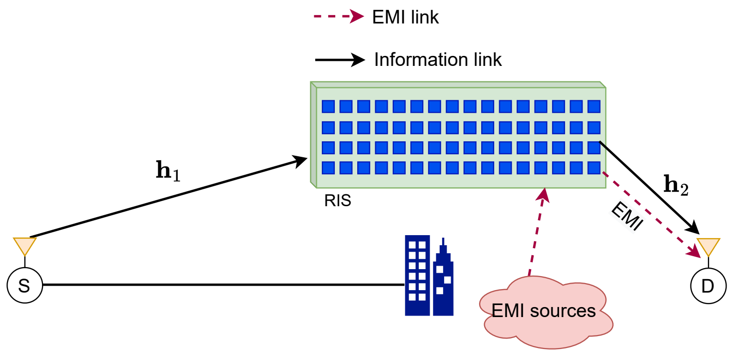

Figure 7.1: RIS-assisted SISO communications system under EMI.

be blocked due to obstacles, and the reflection link over the RIS is the only available link. Furthermore, in addition to the desired transmitted signal, the RIS is assumed to reflect EMI signals from local interference sources close to D [177]. Accordingly, considering only the first reflection from the RIS, at any given time slot t, the received signal at D can be given as [177]

$$y_t = \mathbf{h}_{2,t}^H \mathbf{\Theta}_t^H \mathbf{h}_{1,t} \sqrt{P} s_t + \mathbf{h}_{2,t}^H \mathbf{\Theta}_t^H \mathbf{n}_t + w_t, \tag{7.1}$$

where s_t is the transmitted message at time slot t with a transmit power P. Here, $\mathbf{\Theta}_t \in \mathbb{C}^{N\times N}$ is a diagonal matrix containing the RIS reflection coefficients with $\lfloor \mathbf{\Theta}_t \rfloor_i = \eta_{i,t} e^{j\theta_{i,t}}$, where $\lfloor \mathbf{z} \rfloor_i$ denotes the i-th entry of the vector $\mathbf{z}$, $\eta_{i,t} = 1$ and $\theta_{i,t} \in [0, 2\pi), \forall i, t$, are the i^{th} element applied reflection amplitude and phase shift at time slot t, respectively. $\mathbf{h}_1$ and $\mathbf{h}_2 \in \mathbb{C}^{N\times 1}$ are the S-RIS and RIS-D channel vectors, respectively. $\mathbf{h}_k \sim \mathcal{CN}(\mathbf{0}, A\beta_k \mathbf{R}), k \in \{1, 2\}$ [181], where β_k is the path gain, $A = d_H d_V$ is the RIS element area with d_H and d_V are its length and width, respectively, and $\mathcal{CN}$ represents complex Gaussian random distribution with $\mathbf{R}$ denoting the RIS correlation matrix and $\mathbf{0}$ denoting N-dimensional all-zeros column vector. Assuming isotropic conditions for the EMI, $\mathbf{n} \in \mathbb{C}^{N\times 1}$ is the EMI vector, where $\mathbf{n} \sim \mathcal{CN}(\mathbf{0}, A\sigma^2 \mathbf{R})$ with σ^2 is the EMI power [177]. Accordingly, the ratio of the signal power to the EMI power at each RIS element can be expressed as $\rho = \beta_1 P/\sigma^2$. $w \sim \mathcal{CN}(0, \sigma_w^2)$ is the additive white Gaussian noise (AWGN) sample with zero mean and variance σ_w^2.

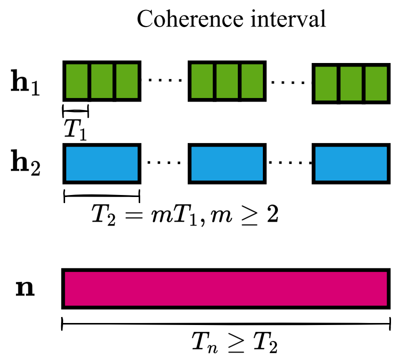

Figure 7.2: The coherence intervals (CIs) T_1 of $\mathbf{h}_1$, T_2 of $\mathbf{h}_2$, and T_n of $\mathbf{n}$ are illustrated relative to each other, where the random realization of each channel/EMI remains constant over its corresponding CI.

Due to the high path loss associated with the reflection link, the RIS needs to be deployed close to D [188], where its position can be optimized with respect to the position of D [189]. In this way, the RIS-D channel $\mathbf{h}_2$ changes less frequently compared to the other channels, where the statistical channel state information (S-CSI) dominates the instantaneous CSI (I-CSI) in terms of the phase shift design [190], [191]. On the other side, depending on the source of interference, the realizations of the EMI vector $\mathbf{n}$ can change faster or slower than those of the other channels. In particular, we consider a specific, yet, realistic case where the coherence interval (CI) for $\mathbf{n}$ spans several CIs of the other channels. This case can be observed when the EMI source is a secondary transmitter in the network, like a backscatter device with a low transmission rate [192]. Fig. 7.2 illustrates the considered CIs for different channels with respect to the EMI, where the realizations of $\mathbf{n}$ and $\mathbf{h}_2$ change slower than that of $\mathbf{h}_1$, due to the reasons explained earlier.

We consider a flat-fading channel where the channel realization remains constant within each CI and independent from the realizations at other CIs. In particular, as shown in Fig. 7.2, the realizations of $\mathbf{h}_1$ and $\mathbf{h}_2$ remain constant over the time durations of T_1 and T_2, respectively, while the realization of $\mathbf{n}$ remains constant for a duration greater than T_2. In order to satisfy the slow fading condition, s is transmitted at each time slot of duration T_1, where, in addition to the EMI realization, all channels remain constant.

From (7.1), the SINR at time slot t (SINR_t) is given by[1]

$$\mathrm{SINR}_t = \frac{P|\mathbf{h}_{2,t}^H \boldsymbol{\Theta}_t^H \mathbf{h}_{1,t}|^2}{A\sigma^2 \mathbf{h}_{2,t}^H \boldsymbol{\Theta}_t^H \mathbf{R} \boldsymbol{\Theta}_t \mathbf{h}_{2,t} + \sigma_w^2}, \tag{7.2}$$

where $\mathrm{E}[|\mathbf{h}_{2,t}^H \boldsymbol{\Theta}_t^H \mathbf{n}_t|^2] = A\sigma^2 \mathbf{h}_{2,t}^H \boldsymbol{\Theta}_t^H \mathbf{R} \boldsymbol{\Theta}_t \mathbf{h}_{2,t}$ [177], and $\mathrm{E}[\cdot]$ is the expectation operator. It can be noted from (7.2) that the presence of EMI has a negative impact on the SINR. In particular, due to the EMI, it has been shown in [177] that the SINR grows linearly with N and not quadratically as in the conventional case without EMI [193] [194].

7.3.1 Proposed EMI Cancellation Scheme

To mitigate the EMI impact on the D side, we exploit the system settings explained earlier to propose a novel interference cancellation scheme. Specifically, since the EMI realization is correlated only with $\boldsymbol{\Theta}_t$ and $\mathbf{h}_2$, and not with $\mathbf{h}_1$, the proposed scheme works within the CI of $\mathbf{h}_2$ (T_2), which can be explained as follows.

Consider the transmission of m symbols within a single CI of $\mathbf{h}_2$. Thus, T_2 is divided into m time slots, each with a duration of T_1 ($T_2 = mT_1, m \geq 2$), where a single symbol s is transmitted at each T_1. Accordingly, the received signal within first time slot of T_2 can be obtained by rewriting (7.1) as

$$\begin{aligned} y_1 = &\left(\sum_{i=1}^{N} |\lfloor \mathbf{h}_{1,1} \rfloor_i| \, |\lfloor \mathbf{h}_{2,1} \rfloor_i|\right) \sqrt{P} s_1 + \mathbf{h}_{2,1}^H \boldsymbol{\Theta}_1^H \mathbf{n}_1 \\ &+ w_1, \end{aligned} \tag{7.3}$$

where, in order to maximize the signal-to-noise ratio (SNR), the RIS phase shifts are adjusted such that $\theta_{i,1} = \arg(\lfloor \mathbf{h}_{1,1} \rfloor_i (\lfloor \mathbf{h}_{2,1} \rfloor_i)^H), \forall i$ [177]. By letting $B = \sum_{i=1}^{N} |\lfloor \mathbf{h}_{1,1} \rfloor_i| \, |\lfloor \mathbf{h}_{2,1} \rfloor_i|$, the transmitted symbol can be detected at D using a maximum likelihood detector, as follows

$$\hat{s}_1 = \arg\min_{s \in \mathcal{S}} |y_1 - Bs|^2, \tag{7.4}$$

[1]Note that, as stated in [177], the EMI interference is treated as a sort of additive noise. However, here, we refer to it as interference for notational convenience.

where $\mathcal{S}$ is the set of all possible transmitted symbols. Accordingly, from (7.3), the SINR to detect s_1 can be obtained as [177]

$$\mathrm{SINR}_1 = \frac{PB^2}{A\sigma^2 \mathbf{h}_{2,1}^H \mathbf{\Theta}_1^H \mathbf{R} \mathbf{\Theta}_1 \mathbf{h}_{2,1} + \sigma_w^2}. \tag{7.5}$$

Next, we extract the EMI sample from y_1 as follows

$$\begin{aligned} \tilde{E} &= y_1 - B\hat{s}_1 \\ &= \mathbf{h}_{2,1}^H \mathbf{\Theta}_1^H \mathbf{n}_1 + I + w_1, \end{aligned} \tag{7.6}$$

where $I = B(s_1 - \hat{s}_1)$ corresponds to the residual interference due to unsuccessful detection of s_1.

At the remaining time slots within T_2, $t^{'} \in \{2, 3, ..., m\}$, the received signal can be obtained by rewriting (7.1) as follows

$$y_{t'} = \mathbf{h}_{2,1}^H \mathbf{\Theta}_{t'}^H \mathbf{h}_{1,t'} \sqrt{P} s_{t'} + \mathbf{h}_{2,1}^H \mathbf{\Theta}_{t'}^H \mathbf{n}_1 + w_{t'}, \tag{7.7}$$

where, as illustrated in Fig. 7.2, $\mathbf{h}_{2,t'} = \mathbf{h}_{2,1}$ and $\mathbf{n}_{t'} = \mathbf{n}_1$, $\forall t^{'} \in \{2, 3, ..., m\}$. In order to cancel the EMI signals at D in the remaining time slots $t^{'}$ within T_2, we destructively add the EMI sample $\tilde{E}$ (obtained at the first time slot) to $y_{t'}$, as follows

$$\begin{aligned} \tilde{y}_{t'} &= y_{t'} + \tilde{E} \\ &= \mathbf{h}_{2,1}^H \mathbf{\Theta}_{t'}^H \mathbf{h}_{1,t'} \sqrt{P} s_{t'} + \mathbf{h}_{2,1}^H (\mathbf{\Theta}_{t'}^H + \mathbf{\Theta}_1^H) \mathbf{n}_1 \\ &+ I + v_{t'}, \end{aligned} \tag{7.8}$$

where $v_{t'} = w_1 + w_{t'}$. In order to fully eliminate the EMI sample, the RIS phase shifts can be adjusted such that $\mathbf{\Theta}_{t'} = e^{j\pi} \mathbf{\Theta}_1, \forall t^{'}$, however; at the expense of having no beamforming gain. Accordingly, the SINR at time slot $t^{'} \in \{2, 3, ..., m\}$ can be obtained as

$$\mathrm{SINR}_{t'} = \frac{P |\mathbf{h}_{2,1}^H \mathbf{\Theta}_{t'}^H \mathbf{h}_{1,t'}|^2}{|I|^2 + \sigma_v^2}, \tag{7.9}$$

where $\sigma_v^2 = 2\sigma_w^2$ is the variance of $v_{t'}$, which corresponds to the sum of the variances of the two independent random variables (RVs) w_1 and $w_{t'}$.

By considering (7.5) and (7.9) together, it can be noted that, in terms of the RIS phase shift design, there is a trade-off between achieving passive beamforming gain and fully eliminating the EMI at D. In our computer simulations, we show that at high EMI levels, sacrificing the beamforming gain in favor of eliminating the EMI provides better results in terms of the average SINR and outage probability performance.

7.4 Outage Probability Analysis

In this section, we provide the outage probability analysis to characterize the performance of the proposed EMI cancellation scheme, as follows. Let SINR_m denotes the average SINR over m CIs such that

$$\mathrm{SINR}_m = \frac{1}{m}\sum_{t=1}^{m} \mathrm{SINR}_t, \tag{7.10}$$

where, for $t = 1$ we have SINR_1 given in (7.5), and for $t > 1$ we have $t = t' \in \{2, 3, ..., m\}$ and $\mathrm{SINR}_{t'}$ is given in (7.9). Accordingly, for a given SINR_m threshold r, the outage probability (OP) can be obtained as

$$\begin{aligned} P_{out} &= P\left(\mathrm{SINR}_m < r\right) \\ &= P\left(\overline{\mathrm{SINR}}_m < \frac{r}{P}\right) \\ &= F_{\overline{\mathrm{SINR}}_m}\left(\frac{r}{P}\right), \end{aligned} \tag{7.11}$$

where $\overline{\mathrm{SINR}}_m = \mathrm{SINR}_m/P$ and $F_{\overline{\mathrm{SINR}}_m}(x)$ is the cumulative distribution function (CDF) of $\overline{\mathrm{SINR}}_m$. It can be noted from (7.5) and (7.9) that $\overline{\mathrm{SINR}}_m$ involves the product and division of multiple correlated RVs, resulting in a very challenging task to obtain its exact probability density function (PDF). Therefore, we use a semi-analytical approach to obtain the PDF of $\overline{\mathrm{SINR}}_m$ using the Distribution Fitting Tool in MATLAB. As shown in Fig. 7.3, the PDF of $\overline{\mathrm{SINR}}_m$ perfectly matches the one of Gamma distribution. Consequently, P_{out} can be obtained as the CDF of $\overline{\mathrm{SINR}}_m$, which is given by

$$F_{\overline{\mathrm{SINR}}_m}\left(\frac{r}{P}\right) = \frac{\gamma(a, \frac{r}{Pb})}{\Gamma(a)}, \tag{7.12}$$

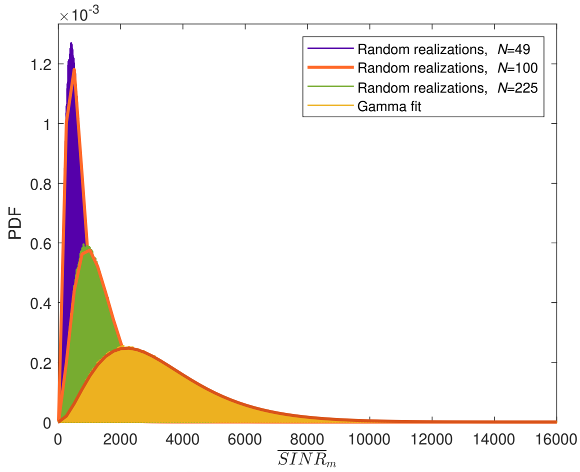

Figure 7.3: Fitting the distribution of $\overline{\text{SINR}}_m$ to Gamma distribution, for $\rho = 0$ dB.

Table 7.1: Shape and scale parameters for different N values.

N	a	b
49	2.853	229
100	2.955	470.391
225	3.01	1089.9

where $\Gamma(\cdot)$ and $\gamma(\cdot)$ are the complete and lower incomplete gamma functions, respectively, with a and b denoting the shape and scale parameters of Gamma distribution, respectively, and these are given in Table 7.1 for $\rho = 0$ dB.

7.5 Simulation Results

This section presents comprehensive computer simulations to examine the performance of both the proposed and benchmark schemes in terms of average SINR and OP, under different system settings. The considered benchmark is the classical passive beamforming scheme, where the RIS phase shifts are adjusted to remove the overall S-RIS-D channel phases, as given in (7.3), at all time slots. In particular, we consider the simulation parameters considered in [177], where $\sigma_w^2 = -114$ dBm,

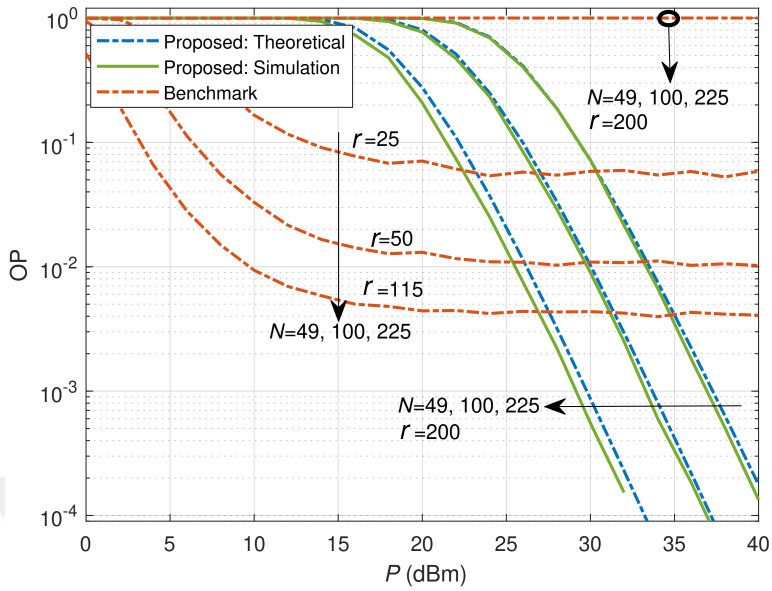

Figure 7.4: Outage probability performance for $\rho = 0$ dB and different N values.

$\beta_1 = -48$ dB, $\beta_2 = -38$ dB. Furthermore, as in [177], we use ρ to control the signal to the EMI power ratio, where $\rho \in \{0, 5, 10\}$ dB. The RIS spatial correlation model in [181] is adopted with $\lambda/2$ separation between elements, where λ is the wavelength associated with the operating frequency 1.8 GHz. The considered CI of $\mathbf{h}_2$ is $T_2 = 4T_1$ $(m = 4)$ unless otherwise stated. Finally, for all of our simulations, we provide the SINR averaged over m time slots (SINR_m); that is, the SINR performance over a full CI of $\mathbf{h}_2$.

In Fig. 7.4, we provide the outage probability performance for different RIS sizes, where the theoretical and simulation curves are shown to have a close match to each other. It can be seen that for an SINR_m threshold $r = 200$, the benchmark scheme has an OP of unity for all considered N values, while the proposed scheme has a superior performance that improves with increasing P and N. Furthermore, to clarify the performance of the benchmark scheme further, we consider different threshold (r) values, since considering a single threshold value does not accurately reflect the performance for different N values due to the sensitivity of the OP to varying N. Accordingly, although the different threshold values of the benchmark scheme are much lower than the one of the proposed scheme, yet, it can be seen

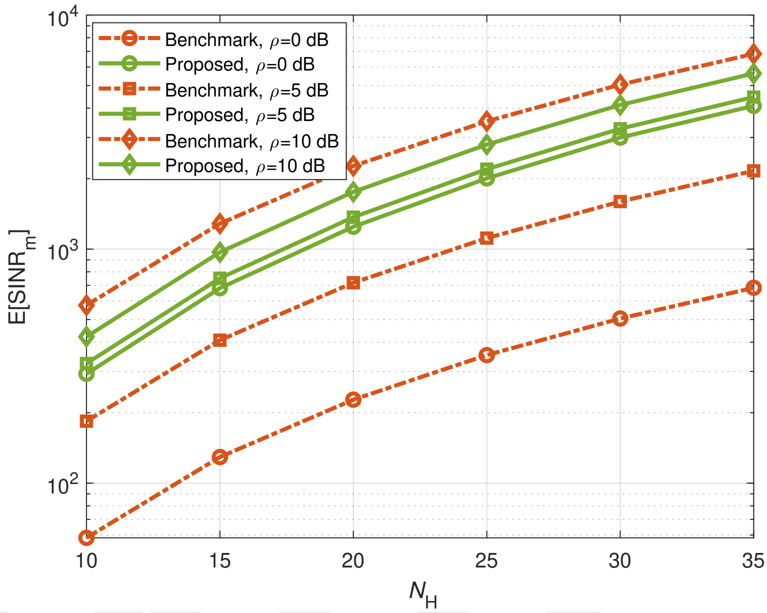

Figure 7.5: Average SINR performance for different RIS sizes and EMI power levels, with $P = 23$ dBm.

that at high P region, the proposed scheme has a superior OP performance. This is because, unlike the proposed scheme that eliminates the EMI, the performance of the benchmark scheme gets saturated due to the EMI, where asymptotically, the average SINR approaches to a constant value as P increases.

In Fig. 7.5, we provide the average SINR versus different RIS sizes and EMI power levels, where the x-axis corresponds to the number of elements per RIS dimension, $N_H = \sqrt{N}$. It can be seen that increasing the RIS size does not affect the SINR gap between the proposed and benchmark scheme, as increasing the RIS size will both increase the beamforming gain and the amount of the EMI reflected to D. Furthermore, it can be noted that our proposed EMI cancellation scheme is more effective when the EMI power is higher, while the benchmark scheme performs better under low levels of EMI power, as expected.

In Fig. 7.6, we show the system performance as the CI of $\mathbf{h}_2$ changes, which means that the CI of $\mathbf{n}$ changes too as the CI of the latter is greater than T_2, as shown in Fig. 7.2. It can be seen that, as T_2/T_1 ratio increases, a better SINR performance is achieved by the proposed scheme, where the SINR values at t' dominate the one

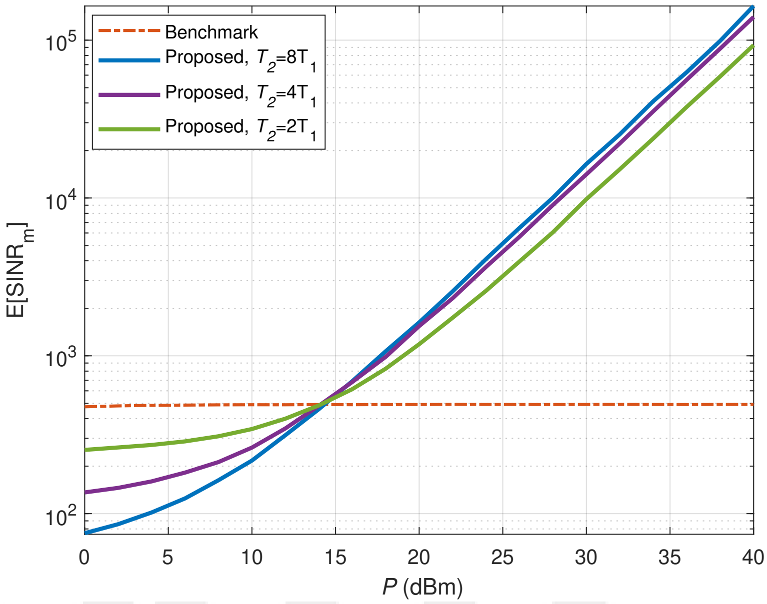

Figure 7.6: Average SINR performance under increasing CI length (T_2) with $N = 900$ and $\rho = 0$ dB.

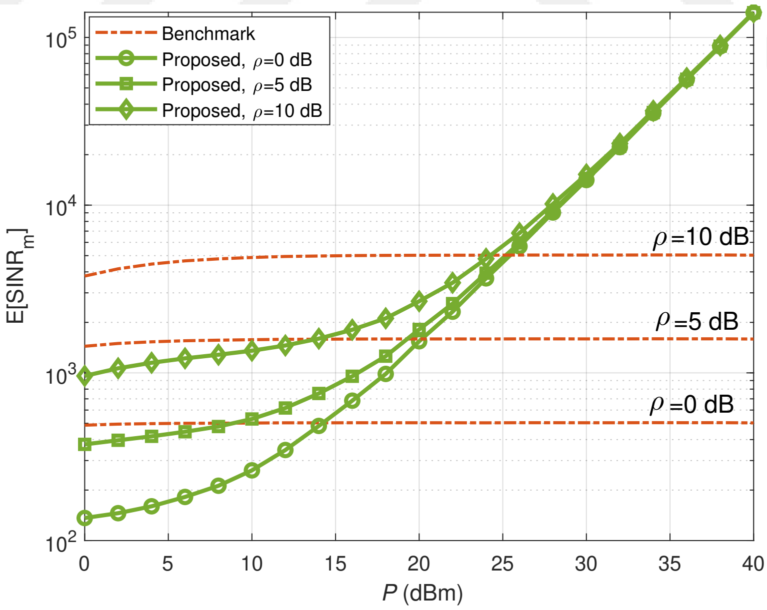

Figure 7.7: Average SINR performance against EMI power level with $N = 900$.

obtained at the first time slot; thus, the overall average over m increases.

Finally, in Fig. 7.7, the effect of the EMI power is investigated for $N = 900$. It can be seen that the proposed scheme performs better as ρ decreases (EMI power increases). Also, the performance of the benchmark scheme gets saturated in a fast manner while the proposed scheme keeps improving with P. Overall, it can be noted that, unless the main signal power is much stronger than the EMI, it is better to adjust the RIS phase shifts to eliminate the EMI instead of steering (beamforming) the main signal to D.

7.6 Conclusion

In this chapter, we have proposed a novel EMI cancellation scheme by trading off the RIS passive beamforming in favor of eliminating the EMI by properly designing the RIS phase shifts over different time slots. Compared to the benchmark scheme that ignores the EMI effects, the proposed scheme is shown to achieve better performance in terms of average SINR and outage probability, particularly when the EMI power is comparable to the main signal power reflected from the RIS surface. For future research, extending the proposed scheme to a MIMO setup seems a promising direction.

Chapter 8

CONCLUSIONS

In this thesis, we have revealed the potential of RISs as enabling technology for 6G and beyond wireless networks. We have shown that, due to their unique capabilities, they can be utilized to improve the performance of existing wireless communications systems or even to redesign them aiming for reduced hardware complexity and cost. Furthermore, by including them in the transceiver architectures of a variety of wireless systems, we have shown that RISs offer high flexibility to be used as a support or main modules to perform a wide range of functions. In particular, based on RISs, this thesis provided the system design and performance analysis of the following novel RIS-based solutions.

- We have proposed an RIS-assisted Alamouti's scheme with reduced hardware complexity and cost. Also, the proposed scheme achieves the same diversity order as in Alamouti's scheme and improves the BER performance as the RIS size increases.

- We have proposed an RIS-assisted and IM-based VBLST system, where we have enhanced the SNR performance and effectively boosted the data rate. Furthermore, the proposed system offers high flexibility to use the RIS for SNR enhancement and/or data rate boosting.

- We have proposed an RIS-assisted NOMA system, where we have reduced the mutual interference between different users clusters by cleverly distributing the physical resources (BS and RIS) among different clusters. Furthermore, we have proposed three novel and efficient search algorithms to partition the RIS among different users in the same cluster, which resulted in improving the ergodic rate of all users and maximizing user fairness for all clusters.

- We have investigated the performance of STAR-RIS-assisted NOMA networks by obtaining the closed-form BER expressions in the case of perfect and imperfect successive interference cancellation. Also, we have provided asymptotic analyses to gain useful insights into the BER performance at high SNR regions.

- We have proposed a novel STAR-RIS-assisted NOMA system, aiming to maximize the sum rate while guaranteeing individual QoS requirements for different users. Also, the proposed system offers a scalable phase shift design for the RIS, which requires a reduced channel estimation overhead.

- We have proposed a low-cost, phase shift-free, and novel PB scheme for RIS-assisted systems. The proposed PB scheme achieves the same SNR scaling law (quadratic growth with the RIS size) similar to the classical phase shift-based PB scheme, yet, it offers far less sensitivity to spatial correlation and phase errors.

- We have proposed an EMI cancellation scheme for RIS-assisted communications by cleverly taking advantage of the EMI time-domain structure and RIS channels. The proposed scheme is shown to effectively mitigate the negative impacts of EMI associated with RIS-assisted transmission and remarkably improves the SINR performance at the receiver side.

A direct and realistic application of this thesis' contributions is to simplify the transceiver architectures, as we have proposed in Chapter 2 for Alamouti's scheme. An interesting future research direction is to generalize our proposed Alamouti's scheme RIS-based transmitter to the STBC MIMO scenario, where a large number of RF chains at the STBC transmitter side can be replaced by a single RF signal generator and the modulation process can be moved to the RIS side. Furthermore, an enhanced version (in terms of BER and data rate performance) of the VBLAST scheme can be obtained by deploying an RIS between the transmitter and receiver, without modifying their hardware architecture.

Considering NOMA, our proposed solution in Chapter 3 can be an effective interference management solution for 5G ultra-dense networks (UDN), by reducing the mutual interference between users in different clusters. A future research direction would be extending the proposed solution to include multiple distributed RISs. Furthermore, the considered STAR-RIS-assisted NOMA systems in Chapters 3 and 4 show the potential of using the STAR-RISs to increase the coverage area in a controlled manner without the need to increase the BS transmit power and causing uncontrolled interference to adjacent cells. Therefore, for future research, the comparison between extending the coverage using STAR-RISs or extending it by increasing BS transmit power can be investigated from the interference management perspective.

For more practical utilization of RISs, the phase shift-free PB scheme proposed in Chapter 6 can be a realistic alternative for the phase shift-based PB scheme associated with hardware implementation problems that limit the RIS achievable gain. Therefore, considering its remarkable performance against the benchmark scheme, the application of the proposed scheme to MIMO system is worth investigating. In the same context, the proposed EMI cancellation scheme in Chapter 7 shows that, practically, the phase shift adjustment of RISs needs not to be limited only to PB, where in case of high EMI, it is better to adjust phase shifts to cancel it. This opens a new research problem about the best strategy for phase shift adjustment under different system settings.

BIBLIOGRAPHY

[1] H. Yang, X. Cao, F. Yang, J. Gao, S. Xu, M. Li, X. Chen, Y. Zhao, Y. Zheng, and S. Li, "A programmable metasurface with dynamic polarization, scattering and focusing control," *Scientific reports*, vol. 6, no. 1, pp. 1–11, 2016.

[2] C. L. Holloway, E. F. Kuester, J. A. Gordon, J. O'Hara, J. Booth, and D. R. Smith, "An overview of the theory and applications of metasurfaces: The two-dimensional equivalents of metamaterials," *IEEE Antennas and Propag. Mag.*, vol. 54, no. 2, pp. 10–35, 2012.

[3] F. Yang and Y. Rahmat-Samii, *Surface electromagnetics: With applications in antenna, microwave, and optical engineering.* Cambridge University Press, 2019.

[4] Y. Liu, X. Liu, X. Mu, T. Hou, J. Xu, M. Di Renzo, and N. Al-Dhahir, "Reconfigurable intelligent surfaces: Principles and opportunities," *IEEE Commun. Surv. Tutor.*, vol. 23, no. 3, pp. 1546–1577, 2021.

[5] S. Basharat, S. A. Hassan, H. Pervaiz, A. Mahmood, Z. Ding, and M. Gidlund, "Reconfigurable intelligent surfaces: Potentials, applications, and challenges for 6G wireless networks," *IEEE Wireless Commun.*, vol. 28, no. 6, pp. 184–191, 2021.

[6] Y. Liu, X. Mu, J. Xu, R. Schober, Y. Hao, H. V. Poor, and L. Hanzo, "STAR: Simultaneous transmission and reflection for 360° coverage by intelligent surfaces," *IEEE Wireless Commun.*, vol. 28, no. 6, pp. 102–109, 2021.

[7] M. Di Renzo, A. Zappone, M. Debbah, M.-S. Alouini, C. Yuen, J. de Rosny, and S. Tretyakov, "Smart radio environments empowered by reconfigurable

intelligent surfaces: How it works, state of research, and the road ahead," *IEEE J. Sel. Areas Commun.*, vol. 38, no. 11, pp. 2450–2525, 2020.

[8] V. Arun and H. Balakrishnan, "RFocus: Beamforming using thousands of passive antennas," in *17th USENIX symposium on networked systems design and implementation (NSDI 20)*, pp. 1047–1061, Feb. 2020.

[9] Z. Zhang, L. Dai, X. Chen, C. Liu, F. Yang, R. Schober, and H. Vincent Poor, "Active RIS vs. passive RIS: Which will prevail in 6G?," *IEEE Trans. Commun.*, pp. 1–1, 2022.

[10] E. Basar, "Transmission through reconfigurable intelligent surfaces: A new frontier in wireless communications," in *Proc. European Conf. Netw. Commun. (EuCNC)*, Valencia, Spain, June 2019.

[11] S.W. Ellingson, "Path loss in reconfigurable intelligent surface-enabled channels," in *Proc. IEEE 32nd Annu. Int. Symp. Per., Indoor Mobile Radio Commun. (PIMRC)*, pp. 829–835, Sep. 2021.

[12] J. Xu, Y. Liu, X. Mu, and O. A. Dobre, "STAR-RISs: Simultaneous transmitting and reflecting reconfigurable intelligent surfaces," *IEEE Commun. Lett.*, vol. 25, no. 9, pp. 3134–3138, 2021.

[13] Y. Liu, X. Mu, R. Schober, and H. V. Poor, "Simultaneously transmitting and reflecting (STAR)-RISs: A coupled phase-shift model," in *ICC 2022 - IEEE Int. Conf. Commun.*, pp. 2840–2845, 2022.

[14] X. Mu, Y. Liu, L. Guo, J. Lin, and R. Schober, "Simultaneously transmitting and reflecting (STAR) RIS aided wireless communications," *IEEE Trans. Wireless Commun.*, vol. 21, no. 5, pp. 3083–3098, 2022.

[15] NTT DOCOMO. (Jan. 2020), "DOCOMO Conducts World's First Successful Trial of Transparent Dynamic Metasurface," [Online]. Avail-

able:https://www.nttdocomo.co.jp/english/info/media_center/pr/2020/0117_00.html.

[16] Y. Liu, X. Liu, X. Mu, T. Hou, J. Xu, M. Di Renzo, and N. Al-Dhahir, "Reconfigurable intelligent surfaces: Principles and opportunities," *IEEE Commun. Surv. Tutor.*, vol. 23, no. 3, pp. 1546–1577, 2021.

[17] E. Basar, "Reconfigurable intelligent surface-based index modulation: A new beyond MIMO paradigm for 6G," *IEEE Trans. Commun.*, vol. 68, no. 5, pp. 3187–3196, Feb. 2020.

[18] A. Khaleel and E. Basar, "Reconfigurable intelligent surface-empowered MIMO systems," *IEEE Sys. J.*, vol. 15, no. 3, pp. 4358–4366, Aug. 2021.

[19] W. Tang *et al.*, "Wireless communications with reconfigurable intelligent surface: Path loss modeling and experimental measurement," *IEEE Trans. Wireless Commun.*, vol. 20, no. 1, pp. 421–439, Jan. 2021.

[20] A. Khaleel and E. Basar, "A novel NOMA solution with RIS partitioning," *IEEE J. Sel. Topics Signal Process.*, vol. 16, no. 1, pp. 70–81, Jan. 2022.

[21] M. Aldababsa, A. Khaleel, and E. Basar, "Simultaneous transmitting and reflectingintelligent surfaces-empowered NOMA networks," Oct. 2021. [Online]. Available: arXiv:2110.05311.

[22] T. Bai, C. Pan, Y. Deng, M. Elkashlan, A. Nallanathan, and L. Hanzo, "Latency minimization for intelligent reflecting surface aided mobile edge computing," *IEEE J. Sel. Areas Commun.*, vol. 38, no. 11, pp. 2666–2682, 2020.

[23] Y. Cao and T. Lv, "Intelligent reflecting surface enhanced resilient design for MEC offloading over millimeter wave links," 2019. [Online]. Available: arXiv:1912.06361.

[24] Y. Cao, T. Lv, W. Ni, and Z. Lin, “Sum-rate maximization for multi-reconfigurable intelligent surface-assisted device-to-device communications,” *IEEE Trans. Commun.*, vol. 69, no. 11, pp. 7283–7296, 2021.

[25] L. Yang, J. Yang, W. Xie, M. O. Hasna, T. Tsiftsis, and M. D. Renzo, “Secrecy performance analysis of RIS-aided wireless communication systems,” *IEEE Trans. Veh. Tech.*, vol. 69, no. 10, pp. 12296–12300, 2020.

[26] C. Pan, H. Ren, K. Wang, W. Xu, M. Elkashlan, A. Nallanathan, and L. Hanzo, “Multicell MIMO communications relying on intelligent reflecting surfaces,” *IEEE Trans. Wireless Commun.*, vol. 19, no. 8, pp. 5218–5233, 2020.

[27] Q. Wu and R. Zhang, “Weighted sum power maximization for intelligent reflecting surface aided swipt,” *IEEE Wireless Commun. Lett.*, vol. 9, no. 5, pp. 586–590, 2020.

[28] S. Li, B. Duo, X. Yuan, Y.-C. Liang, and M. Di Renzo, “Reconfigurable intelligent surface assisted uav communication: Joint trajectory design and passive beamforming,” *IEEE Wireless Commun. Lett.*, vol. 9, no. 5, pp. 716–720, 2020.

[29] Y. Liu, X. Liu, X. Mu, T. Hou, J. Xu, M. Di Renzo, and N. Al-Dhahir, “Reconfigurable intelligent surfaces: Principles and opportunities,” *IEEE Commun. Surv. Tutor.*, vol. 23, no. 3, pp. 1546–1577, 2021.

[30] G. Gradoni and M. Di Renzo, “End-to-end mutual coupling aware communication model for reconfigurable intelligent surfaces: An electromagnetic-compliant approach based on mutual impedances,” *IEEE Wireless Commun. Lett.*, vol. 10, no. 5, pp. 938–942, May 2021.

[31] E. Björnson, “Optimizing a binary intelligent reflecting surface for OFDM communications under mutual coupling,” Sep. 2021. [Online]. Available: arXiv:2106.042802021.

[32] B. O. Zhu, J. Zhao, and Y. Feng, "Active impedance metasurface with full 360° reflection phase tuning," *Scientific Reports*, vol. 3, Oct. 2013.

[33] H. Rajagopalan and Y. Rahmat-Samii, "Loss quantification for microstrip reflectarray: Issue of high fields and currents," in *2008 IEEE Antennas Propag. Soc. Int. Symp.*, pp. 1–4, Jul. 2008.

[34] W. Chen *et al.*, "Angle-dependent phase shifter model for reconfigurable intelligent surfaces: Does the angle-reciprocity hold?," *IEEE Commun. Lett.*, vol. 24, no. 9, pp. 2060–2064, Sep. 2020.

[35] E. Basar, "Reconfigurable intelligent surface-based index modulation: A new beyond MIMO paradigm for 6G," *IEEE Trans. Comm.*, vol. 68, no. 5, May 2020.

[36] A. Zappone, M. Di Renzo, X. Xi, and M. Debbah, "On the optimal number of reflecting elements for reconfigurable intelligent surfaces," *IEEE Wireless Commun. Lett.*, vol. 10, no. 3, pp. 464–468, 2021.

[37] H. Liu, X. Yuan, and Y. J. A. Zhang, "Matrix-calibration-based cascaded channel estimation for reconfigurable intelligent surface assisted multiuser mimo," *IEEE J. Sel. Areas Commun.*, vol. 38, no. 11, pp. 2621–2636, 2020.

[38] Z. Zhou, N. Ge, Z. Wang, and L. Hanzo, "Joint transmit precoding and reconfigurable intelligent surface phase adjustment: A decomposition-aided channel estimation approach," *IEEE Trans. Commun.*, vol. 69, no. 2, pp. 1228–1243, 2021.

[39] L. Wei, C. Huang, G. C. Alexandropoulos, C. Yuen, Z. Zhang, and M. Debbah, "Channel estimation for RIS-empowered multi-user miso wireless communications," *IEEE Trans. Commun.*, vol. 69, no. 6, pp. 4144–4157, 2021.

[40] L. Wei, C. Huang, G. C. Alexandropoulos, and C. Yuen, "Parallel factor decomposition channel estimation in RIS-assisted multi-user miso communication," in *2020 IEEE 11th Sensor Array and Multichannel Signal Process. Workshop (SAM)*, pp. 1–5, 2020.

[41] W. Tang, J. Y. Dai, M. Zheng Chen, Y. Han, X. Li, C.-K. Wen, S. Jin, Q. Cheng, and T. J. Cui, "Realization of reconfigurable intelligent surface-based alamouti space-time transmission," in *2020 Int. Conf. Wireless Commun. Signal Process. (WCSP)*, pp. 904–909, 2020.

[42] A. E. Canbilen, E. Basar, S. S. Ikki, "Reconfigurable intelligent surface-assisted space shift keying," *IEEE Wireless Commun. Lett. (to appear)*.

[43] X. Tan, Z. Sun, J. M. Jornet, and D. Pados, "Increasing indoor spectrum sharing capacity using smart reflect-array," pp. 1–6, in *Proc. 2016 IEEE Int. Conf. Commun. (ICC)*, Kuala Lumpur, Malaysia, May 2016.

[44] C. Huang, G. C. Alexandropoulos, A. Zappone, M. Debbah, and C. Yuen, "Energy efficient multi-user MISO communication using low resolution large intelligent surfaces," in *Proc. IEEE Global Commun. Conf.*, Abu Dhabi, UAE, Dec. 2018.

[45] Q. Wu, R. Zhang, "Weighted sum power maximization for intelligent reflecting surface aided SWIPT," *IEEE Wireless Commun. Lett.*, vol. 9, no. 5, pp. 586-590, May 2020.

[46] X. Guan, Q. Wu, R. Zhang, "Intelligent reflecting surface assisted secrecy communication: Is artificial noise helpful or not?," *IEEE Wireless Commun. Lett.*, vol. 9, no. 6, pp. 778-782, June 2020.

[47] Q. Wu, R. Zhang, "Intelligent reflecting surface enhanced wireless network: Joint active and passive beamforming design," in *Proc. IEEE Global Commun. Conf.*, Abu Dhabi, UAE, Dec. 2018. [Online]. Available:arXiv:1809.01423.

[48] Q. Wu, R. Zhang, "Intelligent reflecting surface enhanced wireless network via joint active and passive beamforming," *IEEE Trans. Wireless Commun.*, vol. 18, no. 11, pp. 5394-5409. Nov. 2019.

[49] X. Yu, D. Xu, and R. Schober, "MISO wireless communication systems via intelligent reflecting surfaces," *in Proc. 2019 IEEE/CIC Int. Conf. Commun. (ICCC)*, Changchun, China, Aug. 2019. [Online]. Available: arXiv:1904.12199.

[50] Q.-U.-A. Nadeem, A. Kammoun, A. Chaaban, M. Debbah, and M.-S. Alouini, "Asymptotic max-min sinr analysis of reconfigurable intelligent surface assisted MISO systems," *IEEE Trans. Wireless Commun.*, vol. 19, no. 12, pp. 7748–7764, Dec. 2020.

[51] Ö. Özdogan, E. Björnson, E. G. Larsson, "Using intelligent reflecting surfaces for rank improvement in MIMO communications," *in Proc. IEEE Int. Conf. on Acoustics, Speech and Signal Process. (ICASSP)*. Barcelona, Spain. May 2020.

[52] S. Zhang and R. Zhang, "Capacity characterization for intelligent reflecting surface aided mimo communication," *IEEE J. Sel. Areas Commun.*, vol. 38, no. 8, pp. 1823–1838, Aug. 2020.

[53] J. Chen, Y.-C Liang, H. V. Cheng, W. Yu, "Channel estimation for reconfigurable intelligent surface aided multi-user MIMO systems," Dec. 2019 [Online]. Available: arXiv: 1912.03619.

[54] C. Huang, A. Zappone, M. Debbah, C. Yuen, "Achievable Rate Maximization by Passive Intelligent Mirrors," *in Proc. IEEE Int. Conf. on Acoustics, Speech and Signal Process. (ICASSP)*. Calgary, AB, Canada, Apr. 2018.

[55] C. Huang, S. Hu, G. C. Alexandropoulos, A. Zappone, C. Yuen, R. Zhang, M. D. Renzo, and M. Debbah, "Holographic mimo surfaces for 6g wireless

networks: Opportunities, challenges, and trends," *IEEE Wireless Commun.*, vol. 27, no. 5, pp. 118–125, Oct. 2020.

[56] C. Huang, R. Mo, and C. Yuen, "Reconfigurable intelligent surface assisted multiuser MISO systems exploiting deep reinforcement learning," *IEEE J. Sel. Areas Commun.*, vol. 38, no. 8, pp. 1839–1850, Aug. 2020.

[57] Z. Yigit, E. Basar, and I. Altunbas, "Low complexity adaptation for reconfigurable intelligent surface-based mimo systems," *IEEE Commun. Lett.*, vol. 24, no. 12, pp. 2946–2950, Dec. 2020.

[58] E. Basar, I. Yildirim, and F. Kilinc, "Indoor and outdoor physical channel modeling and efficient positioning for reconfigurable intelligent surfaces in mmwave bands," *IEEE Trans. Commun.*, vol. 69, no. 12, pp. 8600–8611, Dec. 2021.

[59] E. Basar and I. Yildirim, "Simris channel simulator for reconfigurable intelligent surface-empowered communication systems," in *2020 IEEE Latin-American Conf. Commun. (LATINCOM)*, pp. 1–6, 2020.

[60] P. Wolniansky, G. Foschini, G. Golden, and R. Valenzuela, "V-BLAST: an architecture for realizing very high data rates over the rich-scattering wireless channel," in *1998 URSI Int. Symp. on Signals, Systems, and Electronics. Conf. Proc (Cat. No.98EX167)*, pp. 295–300, 1998.

[61] S. Alamouti, "A simple transmit diversity technique for wireless communications," *IEEE J. Sel. Areas Commun.*, vol. 16, no. 8, pp. 1451–1458, 1998.

[62] J. G. Proakis, "*Digital Communications*," 5th ed. New York: McGrawHill, 2008.

[63] M. Simon, M. S. Alaouni, *Digital Communications over Fading Channels.* 2nd ed. New Jersey: John Wiley and Sons, 2005.

[64] E. Damosso, L. M. Coreia, *COST Action 231: Digital Mobile Radio Towards Future Generation Systems: Final Report.* 1999.

[65] L. Wei, C. Huang, G. C. Alexandropoulos, C. Yuen, "Parallel factor decomposition channel estimation in RIS-assisted multi-user MISO communication," *IEEE 11th Sensor Array and Multichannel Signal Process. Workshop (SAM).* Hangzhou, China. Jun. 2020.

[66] J. He, M. Leinonen, H. Wymeersch, M. Juntti, "Channel estimation for RIS-aided mmWave MIMO channels," Feb. 2020. [Online]. Available: arXiv:2002.06453.

[67] C. Huang, A. Zappone, G. C. Alexandropoulos, M. Debbah, C. Yuen, "Reconfigurable intelligent surfaces for energy efficiency in wireless communication," *IEEE Trans. Wireless Commun.*, vol. 18, no. 8. Aug. 2019.

[68] Q. Wu, R. Zhang, "Beamforming optimization for wireless network aided by intelligent reflecting surface with discrete phase shifts," *IEEE Trans. Commun.*, vol. 68, no. 3, March 2020.

[69] C.H.Y. Eugene, K. Sakaguchi , K. Araki, "Experimental and analytical investigation of MIMO channel capacity in an indoor line-of-sight (LOS) environment," *in Proc. IEEE Int. Symp. Pers. Indoor Mobile Radio Commun. (IEEE Cat. No.04TH8754)*, Barcelona, Spain, Sep. 2004.

[70] H. Zhang, B. Di, L. Song, Z. Han, "Reconfigurable intelligent surfaces assisted communications with limited phase shifts: How many phase shifts are enough?," *IEEE Trans. Veh. Tech.*, vol. 69, no. 4. Apr. 2020.

[71] W. Tang *et al.*, "Wireless communications with reconfigurable intelligent surface: Path loss modeling and experimental measurement," *IEEE Trans. Wireless Commun.*, vol. 20, no. 1, pp. 421–439, 2021.

[72] Y. Liu, W. Yi, Z. Ding, X. Liu, O. Dobre, and N. Al-Dhahir, "Developing NOMA to next generation multiple access (NGMA): Future vision and research opportunities," May 2022. [Online]. Available: arXiv:2103.02334.

[73] M. Aldababsa, M. Toka, S. Gökçeli, G. K. Kurt, and O. Kucur, "A tutorial on nonorthogonal multiple access for 5g and beyond," *Wireless communications and mobile computing*, vol. 2018, 2018.

[74] S. M. R. Islam, N. Avazov, O. A. Dobre, and K.-s. Kwak, "Power-domain non-orthogonal multiple access (noma) in 5g systems: Potentials and challenges," *IEEE Commun. Surv. Tutor.*, vol. 19, no. 2, pp. 721–742, 2017.

[75] Z. Ding, Z. Yang, P. Fan, and H. V. Poor, "On the performance of non-orthogonal multiple access in 5G systems with randomly deployed users," *IEEE Signal Process. Lett.*, vol. 21, no. 12, pp. 1501–1505, Jul. 2014.

[76] X. Yue, Z. Qin, Y. Liu, S. Kang, and Y. Chen, "A unified framework for non-orthogonal multiple access," *IEEE Trans. Commun.*, vol. 66, no. 11, pp. 5346–5359, May 2018.

[77] Z. Wei, L. Yang, D. W. K. Ng, J. Yuan, and L. Hanzo, "On the performance gain of NOMA over OMA in uplink communication systems," *IEEE Trans. Commun.*, vol. 68, no. 1, pp. 536–568, 2020.

[78] "Feasibility study on temporary spectrum access for local high-quality wireless networks," ETSI, Sophia Antipolis, France, Rep. TR 103 588, p. 30. Feb. 2018.

[79] L. Dai, B. Wang, Z. Ding, Z. Wang, S. Chen, and L. Hanzo, "A survey of non-orthogonal multiple access for 5G," *IEEE Commun. Surv. Tutor.*, vol. 20, no. 3, pp. 2294–2323, 2018.

[80] Y. Saito *et al.*, "Non-orthogonal multiple access (NOMA) for cellular future radio access," in *2013 IEEE 77th Veh. Technol. Conf. (VTC Spring)*, pp. 1–5, June 2013.

[81] G. Yang, X. Xu, Y.-C. Liang, "Intelligent reflecting surface assisted non-orthogonal multiple access," Dec. 2019. [Online]. Available: arXiv:1907.03133.

[82] G. Yang, X. Xu, and Y. -C. Liang, "Intelligent reflecting surface assisted non-orthogonal multiple access," in *2020 IEEE Wireless Commun. Netw. Conf. (WCNC)*, pp. 1–6, May 2020.

[83] Z. Ding and H. V. Poor, "A simple design of IRS-NOMA transmission," *IEEE Commun. Lett.*, vol. 24, no. 5, pp. 1119–1123, Feb. 2020.

[84] T. Hou *et al.*, "Reconfigurable intelligent surface aided NOMA networks," *IEEE J. Sel. Areas Commun.*, vol. 38, no. 11, pp. 2575–2588, Jul. 2020.

[85] M. Zhang, M. Chen, Z. Yang, H. Asgari, and M. Shikh-Bahaei, "Joint user clustering and passive beamforming for downlink NOMA system with reconfigurable intelligent surface," in *2020 IEEE 31st Annual Int. Symposium on Personal, Indoor and Mobile Radio Commun.*, pp. 1–6, Aug. 2020.

[86] Y. Xu *et al.*, "Fair non-orthogonal multiple access communication systems with reconfigurable intelligent surface," in *2020 IEEE 31st Annual Int. Symposium on Personal, Indoor and Mobile Radio Commun.*, pp. 1–6, Aug. 2020.

[87] X. Liu, Y. Liu, Y. Chen, and H. V. Poor, "RIS enhanced massive non-orthogonal multiple access networks: Deployment and passive beamforming design," *IEEE J. Sel. Areas Commun.*, pp. 1–1, Aug. 2020.

[88] Y. Li, M. Jiang, Q. Zhang, and J. Qin, "Joint beamforming design in multi-cluster MISO NOMA reconfigurable intelligent surface-aided downlink communication networks," *IEEE Trans. Commun.*, pp. 1–1, Oct. 2020.

[89] T. Hou, Y. Liu, Z. Song, X. Sun, and Y. Chen, "MIMO-NOMA networks relying on reconfigurable intelligent surface: A signal cancellation based design," *IEEE Trans. Commun.*, pp. 1–1, Aug. 2020.

[90] C. Zhang, W. Yi, Y. Liu, "Reconfigurable intelligent surfaces aided multi-cell NOMA networks: A stochastic geometry model," Aug. 2020. [Online]. Available: arXiv:2008.08457.

[91] C. Zhang, W. Yi, Y. Liu, Z. Qin, K.K. Chai, "Downlink analysis for reconfigurable intelligent surfaces aided NOMA networks," Jun. 2020. [Online]. Available: arXiv:2006.13260.

[92] M. Elhattab, M. A. Arfaoui, C. Assi, and A. Ghrayeb, "Reconfigurable intelligent surface assisted coordinated multipoint in downlink NOMA networks," *IEEE Commun. Lett.*, pp. 1–1, Oct. 2020.

[93] Z. Ding, R. Schober, and H. V. Poor, "On the impact of phase shifting designs on IRS-NOMA," *IEEE Wireless Commun. Lett.*, vol. 9, no. 10, pp. 1596–1600, Apr. 2020.

[94] J. Zuo, Y. Liu, Z. Qin, and N. Al-Dhahir, "Resource allocation in intelligent reflecting surface assisted NOMA systems," *IEEE Trans. Commun.*, pp. 1–1, Aug. 2020.

[95] M. Najafi, V. Jamali, R. Schober, and H. V. Poor, "Physics-based modeling and scalable optimization of large intelligent reflecting surfaces," Apr. 2020. [Online]. Available: arXiv:2004.12957.

[96] D. Xu, V. Jamali, X. Yu, D. W. K. Ng, and R. Schober, "Optimal resource allocation design for large IRS-assisted SWIPT systems: A scalable optimization framework," Apr. 2021. [Online]. Available: arXiv:2104.03346.

[97] Q. U. A. Nadeem, A. Kammoun, A. Chaaban, M. Debbah, and M. S. Alouini, "Asymptotic max-min sinr analysis of reconfigurable intelligent surface assisted miso systems," *IEEE Trans. Wireless Commun.*, vol. 19, no. 12, pp. 7748–7764, 2020.

[98] M. S. Ali, H. Tabassum, and E. Hossain, "Dynamic user clustering and power allocation for uplink and downlink non-orthogonal multiple access (NOMA) systems," *IEEE Access*, vol. 4, pp. 6325–6343, 2016.

[99] A. de Jesus Torres, L. Sanguinetti, and E. Björnson, "Near- and far-field communications with large intelligent surfaces," Nov. 2020. [Online]. Available: arXiv:2011.13835.

[100] H. Yu, H. D. Tuan, A. A. Nasir, T. Q. Duong, and H. V. Poor, "Joint design of reconfigurable intelligent surfaces and transmit beamforming under proper and improper gaussian signaling," *IEEE J. Sel. Areas Commun.*, vol. 38, no. 11, pp. 2589–2603, 2020.

[101] C. Pan, H. Ren, K. Wang, M. Elkashlan, A. Nallanathan, J. Wang, and L. Hanzo, "Intelligent reflecting surface aided MIMO broadcasting for simultaneous wireless information and power transfer," *IEEE J. Sel. Areas Commun.*, vol. 38, no. 8, pp. 1719–1734, 2020.

[102] Q. U. A. Nadeem, H. Alwazani, A. Kammoun, A. Chaaban, M. Debbah, and M. S. Alouini, "Intelligent reflecting surface-assisted multi-user miso communication: Channel estimation and beamforming design," *IEEE Open J. Commun. Soc.*, vol. 1, pp. 661–680, 2020.

[103] H. Alwazani, Q. U. A. Nadeem, and A. Chaaban, "Channel estimation for distributed intelligent reflecting surfaces assisted multi-user miso systems," in *2020 IEEE Globecom Workshops (GC Wkshps)*, pp. 1–6, Dec. 2020.

[104] W. Xia, Y. Zhou, G. Yang, and R. T. Chen, "Optimal minimum euclidean distance-based precoder for NOMA with finite-alphabet inputs," *IEEE Access*, vol. 7, pp. 45123–45136, Apr. 2019.

[105] J. Zhang, X. Wang, T. Hasegawa, and T. Kubo, "Downlink non-orthogonal

multiple access (NOMA) constellation rotation," in *2016 IEEE 84th Veh. Technol. Conf. (VTC-Fall)*, pp. 1–5, Sep. 2016.

[106] Q. Wu and R. Zhang, "Intelligent reflecting surface enhanced wireless network via joint active and passive beamforming," *IEEE Trans. Wireless Commun.*, vol. 18, no. 11, pp. 5394–5409, Aug. 2019.

[107] Q.-U.-A. Nadeem, A. Zappone, and A. Chaaban, "Intelligent reflecting surface enabled random rotations scheme for the MISO broadcast channel," Mar. 2021. [Online]. Available: arXiv:2103.09898.

[108] S. Abeywickrama, R. Zhang, Q. Wu, and C. Yuen, "Intelligent reflecting surface: Practical phase shift model and beamforming optimization," *IEEE Trans. Commun.*, vol. 68, no. 9, pp. 5849–5863, 2020.

[109] U. Siddique, H. Tabassum, and E. Hossain, "Downlink spectrum allocation for in-band and out-band wireless backhauling of full-duplex small cells," *IEEE Trans. Commun.*, vol. 65, no. 8, pp. 3538–3554, 2017.

[110] S. Atapattu, R. Fan, P. Dharmawansa, G. Wang, J. Evans, and T. A. Tsiftsis, "Reconfigurable intelligent surface assisted two–way communications: Performance analysis and optimization," *IEEE Trans. Commun.*, vol. 68, no. 10, pp. 6552–6567, 2020.

[111] A. Osseiran, J. Monserrat, and W. Mohr, "*Mobile and Wireless Communications for IMT-Advanced and Beyond*," Hoboken, NJ, USA: Wiley, 2011.

[112] X. Kang, H. F. Chong, Y. Chia, and S. Sun, "Ergodic sum-rate maximization for fading cognitive multiple-access channels without successive interference cancelation," *IEEE Trans. Veh. Techno.*, vol. 64, no. 9, pp. 4009–4018, Oct. 2014.

[113] T. Hou *et al.*, "Reconfigurable intelligent surface aided NOMA networks," *IEEE J. Sel. Areas Commun.*, vol. 38, no. 11, pp. 2575–2588, Jul. 2020.

[114] A. Papazafeiropoulos, C. Pan, A. Elbir, P. Kourtessis, S. Chatzinotas, and J. M. Senior, “Coverage probability of distributed IRS systems under spatially correlated channels,” Feb. 2021. [Online]. Available: arXiv:2102.09416.

[115] T. V. Chien, A. K. Papazafeiropoulos, L. T. Tu, R. Chopra, S. Chatzinotas, and B. Ottersten, “Outage probability analysis of IRS-assisted systems under spatially correlated channels,” Feb. 2021. [Online]. Available: arXiv:2102.11408.

[116] E. Björnson and L. Sanguinetti, “Rayleigh fading modeling and channel hardening for reconfigurable intelligent surfaces,” *IEEE Wireless Commun. Lett.*, pp. 1–1, 2020.

[117] A. Annamalai, C. Tellambura, and J. Matyjas, “A new twist on the generalized marcum q-function qm(a, b) with fractional-order m and its applications,” in *2009 6th IEEE Consumer Commun. Netw. Conf.*, pp. 1–5, Jan. 2009.

[118] M. Simon, “*Probability Distributions Involving Gaussian Random Variables*,” New York, NY, USA: Springer, 2002.

[119] M. Simon, “*Probability Distributions Involving Gaussian Random Variables*,” New York, NY, USA: Springer, 2002.

[120] A. Mathai and S. B. Provost, “ *Quadratic Forms in Random Variables: Theory and Applications*,” New York, NY, USA: Marcel Dekker, 1992.

[121] R. Jain, D.-M. Chiu, W. R. Hawe, “A quantitative measure of fairness and discrimination for resource allocation in shared computer system,” Eastern Research Laboratory, Digital Equipment Corporation Hudson, MA, 1984, vol. 38.

[122] L. A. Wolsey and G. L. Nemhauser, *Integer and Combinatorial Optimization.* New York: John Wiley & Sons, 1988.

[123] S. Burer and A. N. Letchford, "Non-convex mixed-integer nonlinear programming: A survey," *Surv. Oper. Res. Manage. Sci.*, vol. 17, no. 2, pp. 97–106, Jun. 2012.

[124] S. Haykin, "Cognitive radio: Brain-empowered wireless communications," *IEEE J. Sel. Areas Commun.*, vol. 23, no. 2, pp. 201–220, Feb. 2005.

[125] R. Zhang, S. Cui, and Y. Liang, "On ergodic sum capacity of fading cognitive multiple-access and broadcast channels," *IEEE Trans. Inf. Theory*, vol. 55, no. 11, pp. 5161–5178, Oct. 2009.

[126] F. Kara and H. Kaya, "Ber performances of downlink and uplink NOMA in the presence of sic errors over fading channels," *IET Communications*, vol. 12, no. 15, pp. 1834–1844, 2018.

[127] T. Assaf, A. J. Al-Dweik, M. S. E. Moursi, H. Zeineldin, and M. Al-Jarrah, "Exact bit error-rate analysis of two-user NOMA using QAM with arbitrary modulation orders," *IEEE Commun. Lett.*, vol. 24, no. 12, pp. 2705–2709, 2020.

[128] V. C. Thirumavalavan and T. S. Jayaraman, "Ber analysis of reconfigurable intelligent surface assisted downlink power domain NOMA system," in *2020 Int. Conf. Commun. Sys. & Net. (COMSNETS)*, pp. 519–522, 2020.

[129] L. Bariah, S. Muhaidat, P. C. Sofotasios, F. E. Bouanani, O. A. Dobre, and W. Hamouda, "Large intelligent surface-assisted nonorthogonal multiple access for 6G networks: Performance analysis," *IEEE Internet of Things J.*, vol. 8, no. 7, pp. 5129–5140, 2021.

[130] Y. Liu, X. Mu, J. Xu, R. Schober, Y. Hao, H. V. Poor, and L. Hanzo, "STAR: Simultaneous transmission and reflection for 360° coverage by intelligent surfaces," *IEEE Wireless Commun.*, vol. 28, pp. 102–109, dec 2021.

[131] J. Xu, Y. Liu, X. Mu, J. T. Zhou, L. Song, H. V. Poor, and L. Hanzo, "Simultaneously transmitting and reflecting (STAR) intelligent omni-surfaces, their modeling and implementation," 2021. [Online]. Available: arXiv 2108.06233.

[132] H. Niu, Z. Chu, F. Zhou, P. Xiao, and N. Al-Dhahir, "Simultaneous transmission and reflection reconfigurable intelligent surface assisted MIMO systems," 2021. [Online]. Available: arXiv: 2106.09450.

[133] C. Wu, Y. Liu, X. Mu, X. Gu, and O. A. Dobre, "Coverage characterization of STAR-RIS networks: NOMA and OMA," *IEEE Commun. Lett.*, vol. 25, no. 9, pp. 3036–3040, 2021.

[134] T. Hou, J. Wang, Y. Liu, X. Sun, A. Li, and B. Ai, "A joint design for STAR-RIS enhanced NOMA-CoMP networks: A simultaneous-signal-enhancement-and-cancellation-based (SSECB) design," *IEEE Trans. Veh. Tech.*, vol. 71, no. 1, pp. 1043–1048, 2022.

[135] H. Niu, Z. Chu, F. Zhou, P. Xiao, and N. Al-Dhahir, "Weighted sum rate optimization for STAR-RIS-assisted MIMO system," *IEEE Trans. Veh. Tech.*, vol. 71, no. 2, pp. 2122–2127, 2022.

[136] H. Niu, Z. Chu, F. Zhou, and Z. Zhu, "Simultaneous transmission and reflection reconfigurable intelligent surface assisted secrecy miso networks," *IEEE Commun. Lett.*, vol. 25, no. 11, pp. 3498–3502, 2021.

[137] J. Zuo, Y. Liu, Z. Ding, L. Song, and H. Vincent Poor, "Joint design for simultaneously transmitting and reflecting (STAR) RIS assisted NOMA systems," *IEEE Trans. Wireless Commun.*, pp. 1–1, 2022.

[138] W. Ni, Y. Liu, Y. C. Eldar, Z. Yang, and H. Tian, "STAR-RIS integrated nonorthogonal multiple access and over-the-air federated learning: Framework, analysis, and optimization," *IEEE Internet of Things Journal*, vol. 9, pp. 17136–17156, sep 2022.

[139] C. Zhang, W. Yi, Y. Liu, Z. Ding, and L. Song, “STAR-IOS aided NOMA networks: Channel model approximation and performance analysis,” *IEEE Trans. Wireless Commun.*, vol. 21, no. 9, pp. 6861–6876, 2022.

[140] Z. Xie, W. Yi, X. Wu, Y. Liu, and A. Nallanathan, “STAR-RIS aided NOMA in multicell networks: A general analytical framework with gamma distributed channel modeling,” *IEEE Trans. Commun.*, vol. 70, no. 8, pp. 5629–5644, 2022.

[141] J. Zuo, Y. Liu, Z. Ding, and X. Wang, “Uplink NOMA for STAR-RIS networks,” 2021. [Online]. Available:arXiv:2110.05686.

[142] Z. Zhang, J. Chen, Y. Liu, Q. Wu, B. He, and L. Yang, “On the secrecy design of STAR-RIS assisted uplink NOMA networks,” *IEEE Trans. Wireless Commun.*, vol. 21, no. 12, pp. 11207–11221, 2022.

[143] C. Wu, X. Mu, Y. Liu, X. Gu, and X. Wang, “Resource allocation in STAR-RIS-aided networks: OMA and NOMA,” *IEEE Trans. Wireless Commun.*, vol. 21, no. 9, pp. 7653–7667, 2022.

[144] Y. Guo, F. Fang, D. Cai, and Z. Ding, “Energy-efficient design for a NOMA assisted STAR-RIS network with deep reinforcement learning,” *IEEE Trans. Veh. Tech.*, pp. 1–5, 2022.

[145] J. Xu, Y. Liu, X. Mu, R. Schober, and H. V. Poor, “Star-riss: A correlated t&r phase-shift model and practical phase-shift configuration strategies,” *IEEE J. Sel. Topics Signal Process.*, vol. 16, no. 5, pp. 1097–1111, 2022.

[146] X. Yue, J. Xie, Y. Liu, Z. Han, R. Liu, and Z. Ding, “Simultaneously transmitting and reflecting reconfigurable intelligent surface assisted NOMA networks,” *IEEE Trans. Wireless Commun.*, pp. 1–1, 2022.

[147] M. López-Benítez and F. Casadevall, “Versatile, accurate, and analytically tractable approximation for the gaussian q-function,” *IEEE Trans. Commun.*, vol. 59, no. 4, pp. 917–922, 2011.

[148] I. S. Gradshteyn and I. M. Ryzhik, *Table of integrals, series, and products.* Academic press, 2014.

[149] A. L. Swindlehurst, G. Zhou, R. Liu, C. Pan, and M. Li, “Channel estimation with reconfigurable intelligent surfaces—a general framework,” *Proceedings of the IEEE*, vol. 110, no. 9, pp. 1312–1338, 2022.

[150] M. K. Simon, *Probability distributions involving Gaussian random variables: A handbook for engineers and scientists.* Springer, 2002.

[151] Z. Ding, P. Fan, and H. V. Poor, “Impact of user pairing on 5g nonorthogonal multiple-access downlink transmissions,” *IEEE Trans. Veh. Tech.*, vol. 65, no. 8, pp. 6010–6023, 2016.

[152] Q. Wu and R. Zhang, “Intelligent reflecting surface enhanced wireless network via joint active and passive beamforming,” *IEEE Trans. Wireless Commun.*, vol. 18, no. 11, pp. 5394–5409, 2019.

[153] M.-A. Badiu and J. P. Coon, “Communication through a large reflecting surface with phase errors,” *IEEE Wireless Commun. Lett.*, vol. 9, no. 2, pp. 184–188, 2020.

[154] E. Björnson and L. Sanguinetti, “Rayleigh fading modeling and channel hardening for reconfigurable intelligent surfaces,” *IEEE Wireless Commun. Lett.*, vol. 10, no. 4, pp. 830–834, 2021.

[155] F. Liu *et al.*, “Intelligent metasurfaces with continuously tunable local surface impedance for multiple reconfigurable functions,” *Phys. Rev. Applied*, vol. 11, Apr. 2019.

[156] P. Nayeri, F. Yang, and A. Z. Elsherbeni, *Analysis and Design of Reflectarray Elements*. John Wiley & Sons, Feb. 2018.

[157] Q. Wu and R. Zhang, “Towards smart and reconfigurable environment: Intelligent reflecting surface aided wireless network,” *IEEE Commun. Mag.*, vol. 58, no. 1, pp. 106–112, Jan. 2020.

[158] L. Li *et al.*, “Machine-learning reprogrammable metasurface imager,” *Nature commun.*, vol. 10, no. 1, pp. 1–8, Mar. 2019.

[159] R. Zhong, Y. Liu, X. Mu, Y. Chen, and L. Song, “AI empowered RIS-assisted NOMA networks: Deep learning or reinforcement learning?,” *IEEE J. Sel. Areas Commun.*, vol. 40, no. 1, pp. 182–196, Jan. 2022.

[160] Z. Mao *et al.*, “Element-grouping intelligent reflecting surface: Electromagnetic-compliant model and geometry-based optimization,” *IEEE Trans. Wireless Commun.*, pp. 1–1, Jan. 2022.

[161] S. Abeywickrama, R. Zhang, Q. Wu, and C. Yuen, “Intelligent reflecting surface: Practical phase shift model and beamforming optimization,” *IEEE Trans. Commun.*, vol. 68, no. 9, pp. 5849–5863, June. 2020.

[162] W. Cai, H. Li, M. Li, and Q. Liu, “Practical modeling and beamforming for intelligent reflecting surface aided wideband systems,” *IEEE Commun. Lett.*, vol. 24, no. 7, pp. 1568–1571, Jul. 2020.

[163] H. Li *et al.*, “Intelligent reflecting surface enhanced wideband MIMO-OFDM communications: From practical model to reflection optimization,” *IEEE Trans. Commun.*, vol. 69, no. 7, pp. 4807–4820, Jul. 2021.

[164] F. Costa and M. Borgese, “Electromagnetic model of reflective intelligent surfaces,” *IEEE Open J. Commun. Soc.*, vol. 2, pp. 1577–1589, June 2021.

[165] M. Jung, W. Saad, M. Debbah, and C. S. Hong, "On the optimality of reconfigurable intelligent surfaces (RISs): Passive beamforming, modulation, and resource allocation," *IEEE Trans. Wireless Commun.*, vol. 20, no. 7, pp. 4347–4363, Jul. 2021.

[166] M.-A. Badiu and J. P. Coon, "Communication through a large reflecting surface with phase errors," *IEEE Wireless Commun. Lett.*, vol. 9, no. 2, pp. 184–188, Feb. 2020.

[167] C. Psomas and I. Krikidis, "SWIPT with intelligent reflecting surfaces under spatial correlation," *IEEE Wireless Commun. Lett.*, vol. 10, no. 9, pp. 1924–1928, Sep. 2021.

[168] Z. Sattar and A. Haghighat, "Nearly passive reconfigurable intelligent surface with constant phase-shifts," in *Proc. IEEE 32nd Annu. Int. Symp. Pers., Indoor Mobile Radio Commun. (PIMRC)*, pp. 794–799, Sep. 2021.

[169] M.-M. Zhao, Q. Wu, M.-J. Zhao, and R. Zhang, "Exploiting amplitude control in intelligent reflecting surface aided wireless communication with imperfect CSI," *IEEE Trans. Commun.*, vol. 69, no. 6, pp. 4216–4231, June 2021.

[170] A. Li, L. Song, B. Vucetic, and Y. Li, "Interference exploitation precoding for reconfigurable intelligent surface aided multi-user communications with direct links," *IEEE Wireless Commun. Lett.*, vol. 9, no. 11, pp. 1937–1941, Nov. 2020.

[171] P. Mursia *et al.*, "RISMA: Reconfigurable intelligent surfaces enabling beamforming for IoT massive access," *IEEE J. Sel. Areas Commun.*, vol. 39, no. 4, pp. 1072–1085, Apr. 2021.

[172] T. V. Chien *et al.*, "Controlling smart propagation environments: Long-term versus short-term phase shift optimization," in *IEEE . Int. Conf. Acoust.*

Speech, Signal Process. (ICASSP), pp. 5348–5352, Singapore, Singapore, Apr. 2022.

[173] L. Kong, S. Kisseleff, S. Chatzinotas, B. Ottersten, and M. Erol-Kantarci, "Effective rate of RIS-aided networks with location and phase estimation uncertainty," in *IEEE Wireless Commun. Netw. Conf. (WCNC)*, pp. 2071–2075, Austin, TX, USA, May. 2022.

[174] T. Wang, M.-A. Badiu, G. Chen, and J. P. Coon, "Outage probability analysis of RIS-assisted wireless networks with Von Mises phase errors," *IEEE Wireless Commun. Lett.*, vol. 10, no. 12, pp. 2737–2741, Dec. 2021.

[175] K. V. Mardia and P. E. Jupp, *Directional Statistics*, vol. 494. John Wiley & Sons, 2009.

[176] L. A. Wolsey and G. L. Nemhauser, *Integer and Combinatorial Optimization.* New York: John Wiley & Sons, 1988.

[177] A. d. J. Torres, L. Sanguinetti, and E. Björnson, "Electromagnetic interference in RIS-aided communications," *IEEE Wireless Commun. Lett.*, pp. 1–1, Nov. 2021.

[178] K. Ntontin *et al.*, "Toward autonomous reconfigurable intelligent surfaces through wireless energy harvesting," Aug. 2021. [Online]. Available: arXiv preprint arXiv:2108.07953.

[179] A. Ramachandra, K. Natarajan, "Tight probability bounds with pairwise independence," May. 2020. [Online]. Available: arXiv:2006.00516.

[180] J. M. Gonzalez-Barrios, "Sums of nonindependent Bernoulli random variables," *Brazilian J. Probab. Stat.*, pp. 55–64, June 1998.

[181] E. Björnson and L. Sanguinetti, "Rayleigh fading modeling and channel hardening for reconfigurable intelligent surfaces," *IEEE Wireless Commun. Lett.*, vol. 10, no. 4, pp. 830–834, Apr. 2021.

[182] O. Tsilipakos *et al.*, "Toward intelligent metasurfaces: The progress from globally tunable metasurfaces to software-defined metasurfaces with an embedded network of controllers," *Advanced Optical Materials*, vol. 8, no. 17, p. 2000783, Jul. 2020.

[183] Ö. Özdogan, E. Björnson, and E. G. Larsson, "Intelligent reflecting surfaces: Physics, propagation, and pathloss modeling," *IEEE Wireless Commun. Lett.*, vol. 9, no. 5, pp. 581–585, May. 2020.

[184] R. C. Ferreira, M. S. P. Facina, F. A. P. De Figueiredo, G. Fraidenraich, and E. R. De Lima, "Bit error probability for large intelligent surfaces under double-Nakagami fading channels," *IEEE Open J. Commun. Soc.*, vol. 1, pp. 750–759, May 2020.

[185] A. d. J. Torres, L. Sanguinetti, and E. Björnson, "Intelligent reconfigurable surfaces vs. decode-and-forward: What is the impact of electromagnetic interference?," in *2022 IEEE 23rd Int. Workshop Signal Process. Advances Wireless Commun. (SPAWC)*, pp. 1–5, Jul. 2022.

[186] G. S. Chandra, R. K. Singh, S. Dhok, P. K. Sharma, and P. Kumar, "Downlink URLLC system over spatially correlated RIS channels and electromagnetic interference," *IEEE Wireless Commun. Lett.*, vol. 11, no. 9, pp. 1950–1954, Sep. 2022.

[187] S. R. Kudumala, A. K. Dubey, P. Gupta, S. Gupta, and E. Sharma, "Hardware impaired RIS assisted multipair FD communication with spatial correlation," *IEEE Commun. Lett.*, vol. 26, no. 9, pp. 2200–2204, Sep. 2022.

[188] E. Ibrahim, R. Nilsson, and J. van de Beek, "On the position of intelligent reflecting surfaces," in *2021 Joint European Conf. Netw. Commun. & 6G Summit (EuCNC/6G Summit)*, pp. 66–71, 2021.

[189] E. Basar, I. Yildirim, and F. Kilinc, "Indoor and outdoor physical channel modeling and efficient positioning for reconfigurable intelligent surfaces in mmwave bands," *IEEE Trans. Commun.*, vol. 69, no. 12, pp. 8600–8611, Dec. 2021.

[190] H. Liu, X. Yuan, and Y.-J. A. Zhang, "Matrix-calibration-based cascaded channel estimation for reconfigurable intelligent surface assisted multiuser MIMO," *IEEE J. Sel. Areas Commun.*, vol. 38, no. 11, pp. 2621–2636, Nov. 2020.

[191] C. Hu, L. Dai, S. Han, and X. Wang, "Two-timescale channel estimation for reconfigurable intelligent surface aided wireless communications," *IEEE Trans. Commun.*, vol. 69, no. 11, pp. 7736–7747, Nov. 2021.

[192] R. Long, Y.-C. Liang, H. Guo, G. Yang, and R. Zhang, "Symbiotic radio: A new communication paradigm for passive internet of things," *IEEE Internet Things J.*, vol. 7, no. 2, pp. 1350–1363, Feb. 2020.

[193] Q. Wu and R. Zhang, "Towards smart and reconfigurable environment: Intelligent reflecting surface aided wireless network," *IEEE Commun. Mag.*, vol. 58, no. 1, pp. 106–112, Jan. 2020.

[194] E. Basar and H. V. Poor, "Present and future of reconfigurable intelligent surface-empowered communications [perspectives]," *IEEE Signal Process. Mag.*, vol. 38, no. 6, pp. 146–152, Nov. 2021.